The Dissertation Committee for Owen Anders Callahan Certifies that this is the approved version of the following dissertation:

INTERACTIONS BETWEEN CHEMICAL ALTERATION, FRACTURE MECHANICS, AND FLUID FLOW IN HYDROTHERMAL SYSTEMS

Committee:

Peter Eichhubl, Supervisor

Jaime D. Barnes

Whitney M. Behr

Nicholas C. Davatzes

Jon E. Olson

Daniel F. Stockli

Interactions between chemical alteration, fracture mechanics, and fluid flow in hydrothermal systems

by

Owen Anders Callahan

Dissertation

Presented to the Faculty of the Graduate School of
The University of Texas at Austin
in Partial Fulfillment
of the Requirements
for the Degree of

Doctor of Philosophy

The University of Texas at Austin
August 2018

Dedication

This work is dedicated to Amy and our boys, Macsen and Avery.

Acknowledgements

I am grateful for the time and attention given to me and this work by my advisor, Peter Eichhubl, and my committee members, Jaime Barnes, Whitney Behr, Nicholas Davatzes, Jon Olson, and Daniel Stockli. Peter always made himself available for discussion and asked hard questions that advanced my thinking and writing on chemical-mechanical interactions in geologic systems. Jaime offered a genuine interest in hydrothermal systems and useful advice on managing research, family, and career. Whitney lent a skeptical ear to my ideas on fault rock rheology. Nick participated in field work, helped refine discussion topics, and provided insights for the geothermal audience. Jon patiently explained fracture mechanics concepts and modeling; all fracture mechanics tests were conducted in his lab. Danny provided thoughtful comments regarding Basin and Range systems and a proper field vehicle.

I was joined in the field by Sol Cooperdock, Adenike Tokan-Lawal, and Alison MacNamee. They endured sandstorms, blistering heat, freezing nights, ankle-twisting talus, stinking fumaroles, and tedious scanlines. I am grateful for their patience.

Xiaofeng Chen and Jonathan Major helped improve the double torsion testing apparatus and methodology. Jonathan also offered advice on sample preparation for and interpretation of X-ray diffraction analyses. Esti Ukar entertained numerous questions about minerals in thin section. András Fall provided guidance on fluid inclusion microthermometry. Sara Elliot tolerated repeated SEM-CL and SEM-EDS training sessions. Jon Holder and Donnie Brooks both provided technical assistance and Christopher Zahm and Brent Elliot volunteered field equipment. Toti Larson helped with analysis of stable isotopes of calcite. J. Richard Kyle showed an early interest in this work and provided suggestions on possible field sites. Richard Ketcham helped with apatite fission track modeling on an early research project that was ultimately set aside. Robin Zuza with Ormat Technologies, Inc. shared trajectories and subsurface geology from geothermal exploration drilling at Dixie Comstock.

Philip Guerrero and Dori Coy streamlined administrative hurdles and bore many spontaneous visits to discuss everything and nothing.

This work was funded by graduate student research grants from the GDL foundation, the Geothermal Resource Council, and the American Association of Petroleum Geoscientists Foundation. Additional support was provided by matching funds from The Jackson School of Geosciences, as well as off campus research and analytical fees grants, and the Fracture Research and Application Consortium (FRAC) at the Bureau of Economic Geology. While at The University of Texas at Austin I was supported by a William C. Powers Graduate Fellowship, as well as teaching and research assistantships.

I also wish to thank my family. My mother, Daren Callahan, for allowing me the opportunity to pursue my interests to the end. And my amazing wife, Amy Keeling, for her support and encouragement, without which none of this work would have been possible.

Interactions between chemical alteration, fracture mechanics, and fluid flow in hydrothermal systems

Owen Anders Callahan, Ph.D.
The University of Texas at Austin, 2018

Supervisor: Peter Eichhubl

The hydromechanical properties of fault zones reflect evolving feedback between chemical, hydrological, and mechanical processes. These processes are evident in differences in fault zone architecture and the mineralogical, textural, and mechanical properties of the constituent parts. In this study, I quantify each of these attributes and explore feedback pathways evident in the Dixie Valley-Stillwater fault zone, Nevada, USA. I conducted 1) double-torsion load-relaxation tests to measure mode-I fracture toughness (K_{IC}) and subcritical fracture growth index (SCI) in ambient and aqueous conditions, 2) uniaxial testing to measure unconfined compressive strength (UCS) and static elastic parameters, 3) mineralogical and textural characterization of altered and damaged rock, and 4) field observations focused on the role of alteration in fault zone evolution. The first investigation explored the impact of alteration on fracture mechanical properties of exhumed alteration assemblages, including: fumarole-related acid-sulfate alteration and silicification, silicification in an epithermal environment, quartz-kaolinite-carbonate alteration in an intermediate depth system, and calcite-chlorite-hematite alteration. The second investigation examined the impact of physiochemical conditions on fracture growth in silicified rocks. Environments included: ambient air, deionized water, dilute HCl, NaOH, and NaCl solutions, and deionized water at elevated temperature. The third investigation employed field observations to assess the impact of alteration on fault

evolution. The results from these complimentary investigations show that fault-proximal weakening or strengthening are strongly influenced by hydrothermal processes. Silicification is associated with increased K_{IC}, SCI, UCS, and brittleness, producing fault cores as strong or stronger than adjacent damage zone material. Calcite-chlorite-hematite assemblages containing abundant unsealed microfractures are approximately six times weaker than silicified rocks. All measures of strength increase when sealing of microfractures surpasses ~85%. SCI in silicified rocks is reduced in aqueous environments, with >60% reduction in alkaline solutions, suggesting that physiochemical conditions in hydrothermal systems may facilitate fracture growth. Field observations support the importance of alteration and precipitation in fault zone development; silicification and precipitation-strengthening contribute to thick fault cores, whereas damage and alteration-weakening promote strain localization. Together, results from these investigations highlight the important and underappreciated role of hydrothermal processes in the development of hydromechanical properties in fault zones.

Table of Contents

List of Tables

List of Figures

1. Introduction

1.1 MOTIVATION

Fractures, fracture networks, and faults composed of opening-mode and sheared fractures are the dominant flow pathways controlling the distribution of fluids and heat in hydrothermal and epithermal systems, and related geothermal and mineral resources (Cox, 2005). Fault geometry is often invoked as a first-order control on hydrothermal flow, with thermal anomalies and mineral deposits localized in dilational fault jogs and step-overs, or at fault tips (Curewitz and Karson, 1997; Eichhubl and Boles, 2000; Cox et al., 2001; Faulds et al., 2006; Anderson and Fairley, 2008; Eichhubl et al., 2009; Micklethwaite, 2009; Micklethwaite et al., 2010). Studies of fault-fluid flow behavior reveal that conductive fault segments are characterized by well-developed damage zones composed of opening-mode fractures and sheared fractures, whereas fault segments composed of deformation bands and clay gouge generally inhibit flow (Brown and Bruhn, 1996; Caine et al., 1996; Sibson, 1996; Caine, 1999; Nelson et al., 1999; Davatzes et al., 2003b; Eichhubl et al., 2009; Ikari et al., 2009; Caine et al., 2010). The occurrence of opening-mode fractures in fault zones and fracture networks, and the evolution of these flow systems from single fractures to complex interconnected networks by fracture propagation, reactivation, and coalescence therefore provides a fundamental control on the permeability evolution of fault-controlled hydrothermal and epithermal systems (Wong and Zhu, 1999; Bourne and Willemse, 2001; Crider and Peacock, 2004; Davatzes et al., 2005; Blenkinsop, 2008; Crider, 2015).

Chemical controls on conduit evolution are likewise well documented, with dissolution, precipitation, and chemical alteration potentially changing the hydrologic properties of fault-facture networks (Facca and Tonani, 1967; Gherardi et al., 2007; Dempsey et al., 2012; Lester et al., 2012). Some degree of alteration is common in most fault zones, where fracture-enhanced fluid flow and mechanical grain size reduction encourage chemical reactions (Bruhn et al., 1994; Solum et al., 2010). These effects are more pronounced in chemically reactive environments encountered in high temperature hydrothermal systems (Ord et al., 2012). As a result, large regions of alteration are commonly associated with active hydrothermal systems (Browne, 1978) and around fossil

conduits associated with magmatic and hydrothermal ore deposits (Henley and Ellis, 1983; Simmons et al., 2005; Sillitoe, 2010).

Less well understood are the impacts of chemical alteration on the mechanical properties governing fracture growth and fault-fracture network geometry, despite clear evidence indicating a complex relationship between mechanical and chemical processes (Sornette, 1999; Eichhubl et al., 2004; Gratier and Gueydan, 2006; Jamtveit et al., 2008; Eichhubl et al., 2009; Davatzes and Hickman, 2010; Laubach et al., 2010; Finzi et al., 2011; Gratier, 2011). Numerical simulations of thermo-hydrologic-mechanical-chemical processes tend to neglect fracture growth and coalescence, ignore the chemical processes influencing fracture propagation, and rarely account for spatial or temporal changes in rock and fracture mechanical properties due to hydrothermal alteration (Taron and Elsworth, 2009, 2010; Sonnenthal et al., 2012).

The chemical-mechanical interactions influencing fracture growth and network evolution have broad impacts across a range of geosciences, from fault zone behavior to advanced recovery of hydrocarbons and CO_2 storage, from the localization of epithermal and porphyry ore systems to the development of hydrothermal and engineered geothermal power production and reinjection strategies (Takahashi and Abé, 1987). Despite these broad impacts, a thorough review of the literature reveals no systematic investigations of fracture mechanical properties from geochemically well-characterized hydrothermally altered samples. The work presented in this dissertation aims to close the observational gap through a combination of field and laboratory investigations exploring interactions between chemical alteration and physiochemical environment, evolving fracture mechanical properties, and the geometric evolution of fault-fracture conduits in hydrothermal system.

1.2 BACKGROUND

1.2.1 Hydrothermal Systems and Hydrothermal Alteration

In this dissertation I consider *hydrothermal* systems to include the heat source, conduits, and advective flow associated with local or regional temperature anomalies. Hydrothermal systems are found in a variety of tectonic settings, from oceanic and continental rifts to magmatic arcs. Active hydrothermal systems in the shallow crust

associated with commercially viable hot water or steam reserves are referred to as *geothermal* resources and yet-to-be financially viable engineered geothermal systems. A worldwide survey of electricity generating geothermal fields shows conditions in the most productive systems are located close to the boiling point with depth for pure water (Figure 1.1); average reservoir conditions are 230 °C at 1.5 km, ranging from ~150-350 °C at depths from 0.5 to 3 km (Bertani, 2005, 2012). These conditions are analogous to epithermal ore forming environments (White, 1981; White and Hedenquist, 1990; Simmons et al., 2005), and similar to shallow portions of ore producing magmatic porphyry systems (Sillitoe, 2010).

Dissolution and precipitation of rock forming minerals are ubiquitous around hydrothermal systems (Nishimoto and Yoshida, 2010). The spatial distribution of hydrothermal reaction products is governed by the physical, chemical, and hydrologic conditions around hydrothermal systems, and results in common alteration assemblages (Lindgren, 1933), including potassic, phyllic, propylitic, and intermediate and advanced argillic alteration (Table 1.1) (Guilbert and Park, 1986; Thompson and Thompson, 1996; Robb, 2005; Simmons et al., 2005). Reaction kinetics are controlled in part by water-rock ratio and temperature, which are in turned influenced by the permeability distribution in fault-fracture networks. Reactions are thus enhanced in the vicinity of high permeability fault-fracture conduits, resulting in distinct zones of characteristic alteration assemblages (Figure 1.2). These zones are frequently mappable on the outcrop to reservoir scale. Davatzes and Hickman (2010) hypothesized that the distribution of alteration zones around hydrothermal systems results in spatial variability of hydro-mechanical properties, creating a complex feedback between fluid flow, enhanced chemical reactions, and fault behavior. Of significance to this dissertation is 1) the variety of reaction products, ranging from soft minerals (kaolinite, sericite, chlorite) to brittle quartz, and 2) the spatial distribution of these products resulting from physical, chemical, and hydrological gradients across hydrothermal systems.

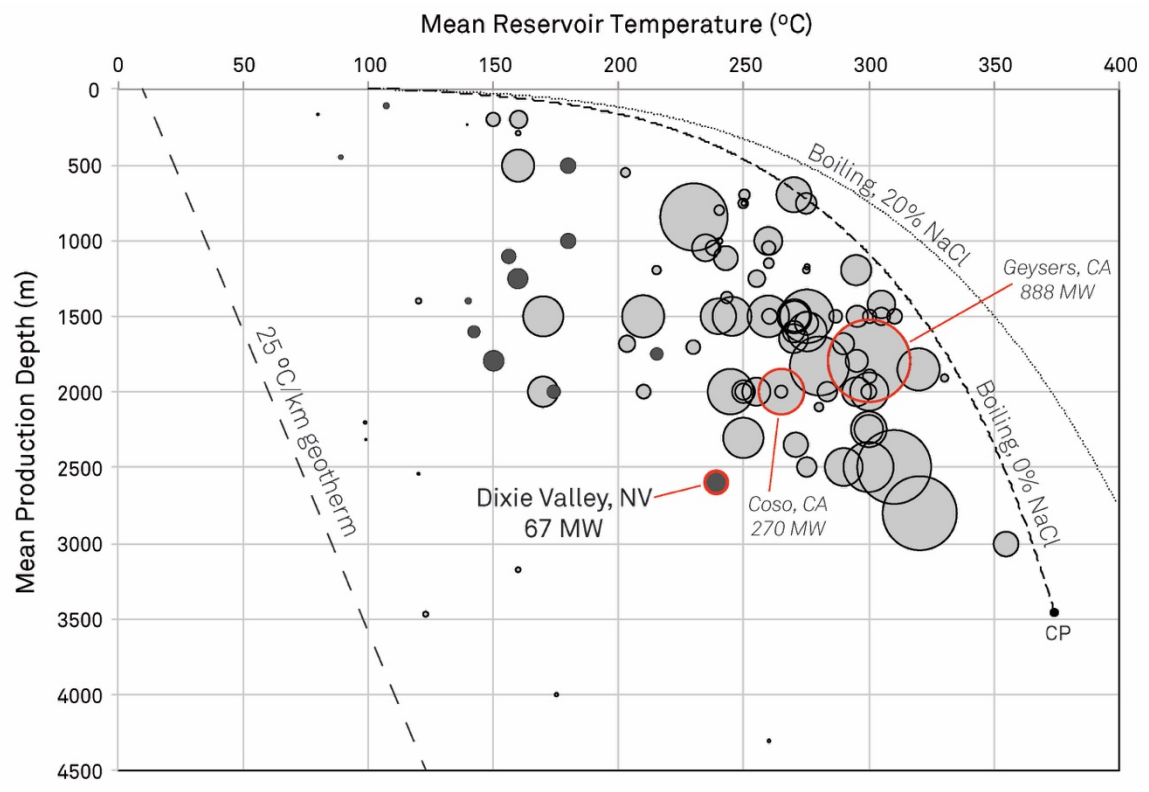

Figure 1.1. Temperature and depth for producing hydrothermal systems. Circles are scaled to generating capacity. Dark circles represent fault-hosted, Basin and Range systems. Based in part on Bertani (2005, 2012). Boiling point with depth curves from Haas (1971).

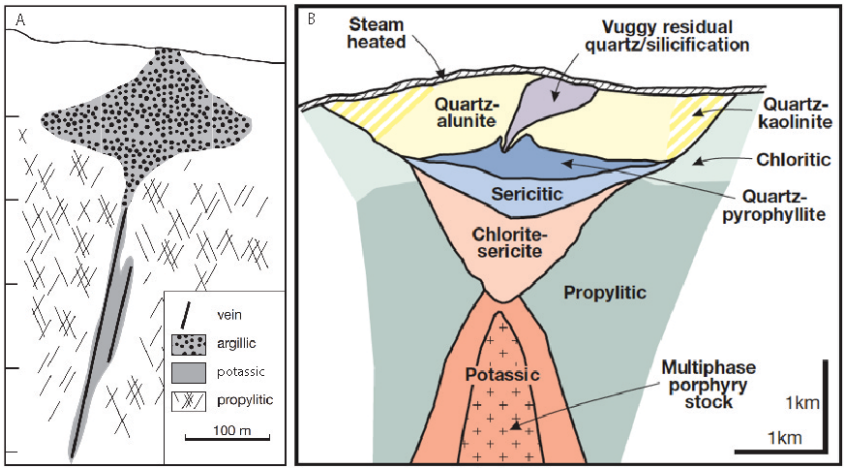

Figure 1.2. Illustrations showing the spatial relationships between alteration assemblages in A) epithermal systems and B) magmatic systems. After Simmons et al. (2005) and Sillitoe (2010).

Table 1.1. Common Alteration Assemblages in Epithermal Systems (from Simmons et al., 2005)

Alteration	Mineralogy	Occurrence and origin
Propylitic	Quartz, K-feldspar (adularia), albite, illite, chlorite, calcite, epidote, pyrite	Develops at >240°C deep in the epithermal environment through alteration by near-neutral pH waters
Argillic	Illite, smectite, chlorite, inter-layered clays, pyrite, calcite (siderite), chalcedony	Develops at <180°C on the periphery and in the shallow epithermal environment through alteration by steam-heated CO_2-rich waters
Adv. Argillic (steam-heated)	Opal, alunite (white, powdery, fine-grained, pseudocubic), kaolinite, pyrite, marcasite	Develops at <120°C near the water table and in the sha llowest epithermal environment through alteration by steam-heated acid-sulfate waters; locally associated with silica sinter but only in geothermal systems
Adv. Argillic (magmatic hydrothermal)	Quartz, alunite (tabular), dickite, pyrophyllite, (diaspore, zunyite)	Develops at >200°C within the epithermal environment through alteration by magmatic-derived acidic waters

1.2.2 Fracture Mechanics

In this dissertation, I measure variations in fracture toughness, subcritical fracture growth index, and static elastic properties with variation in chemical alteration around hydrothermal flow conduits. The choice to emphasize fracture mechanics testing is based on the significance of opening-mode fractures as the fundamental hydrologically conductive structure in hydrothermal flow conduits. Furthermore, fracture mechanics testing isolates the fundamental processes of fracture initiation and growth in hydrothermally altered rock and underlies more complex processes of fracture interaction and coalescence that lead to shear failure in triaxial experiments.

Fracture toughness, K_{IC}, is a rock property that quantifies the stress required for mechanical opening-mode fracture propagation as a function of loading stress, loading geometry, and fracture length (Schmidt, 1975; Atkinson, 1979a; Atkinson, 1982, 1984). Although the influence of fracture toughness as a control on fracture growth diminishes with increasing fracture length, fracture toughness controls fracture initiation and early fracture growth (Engelder et al., 1993). Variations in fracture toughness among alteration zones are thus expected to result in quantifiably different size distributions of fracture length, aperture, and intensity for different fracture size classes under given stress or strain boundary conditions.

Below the critical fracture toughness threshold, chemical corrosion at the fracture tip can promote fracture propagation and the accumulation of damage. Subcritical fracture growth is characterized by the subcritical fracture growth index, SCI, which describes the velocity dependence of fractures propagating in subcritical conditions (Atkinson, 1984; Swanson, 1984) as given by the expression

$$V = A(\frac{K_I}{K_{IC}})^{SCI} \quad \text{Eq. 1.1}$$

where V designates the subcritical fracture propagation velocity, K_I is the mode-I stress intensity factor at the fracture tip, and A is a pre-exponential constant. Olson (1993, 2004) showed in numerical models that the subcritical fracture growth index impacts the geometry of evolving fracture patterns, with increasing subcritical index resulting in transitions from irregularly spaced fractures, to regularly spaced fractures, and finally to clustered sets. Consequently, the subcritical fracture growth index may be a key parameter in relating fracture mechanics to fracture network connectivity because, for a given number of fractures in a rock volume, clustering favors fracture-to-fracture elastic interaction, fracture coalescence, and thus the formation of hydraulically conductive fracture systems.

The subcritical fracture growth index is also of particular interest because chemical processes may influence subcritical fracture propagation. Chemically-aided fracture growth by stress corrosion (Figure 1.3) or increase fracture toughness by tip blunting and cementation are both possible mechanisms operating in hydrothermal systems. Atkinson (1979a) and Atkinson and Meredith (1987) were among the first to discuss the role of chemical reactions in facilitating subcritical fracture propagation in rocks. Fracture behavior of rocks under varying environmental conditions, including elevated temperature, confining pressure, and pore pressure, has since been investigated by several researchers, including Meredith and Atkinson (1985), Balme et al. (2004), Funatsu et al. (2004), and Nasseri et al. (2009), and in the presence of reactive fluids (Karfakis and Akram, 1993; Feng and Ding, 2007; Feng et al., 2009; Nara et al., 2012; Nara et al., 2013; Nara et al., 2014; Chen et al., 2017; Nara et al., 2017a; Nara et al., 2017b; Chen et al., submitted). Although there is substantial work describing fracture mechanical properties in sedimentary rocks of particular interest to oil and gas exploration and CO_2 sequestration (Schmidt, 1975; Atkinson, 1979b; Rijken, 2005; Nara et al., 2014; Chandler et al., 2016; Chen et al., 2017; Major et al., 2018; Chen et al., submitted) the impact of chemical environment on fracture growth in altered rocks commonly encountered in and around high temperature hydrothermal systems has not been evaluated in detail.

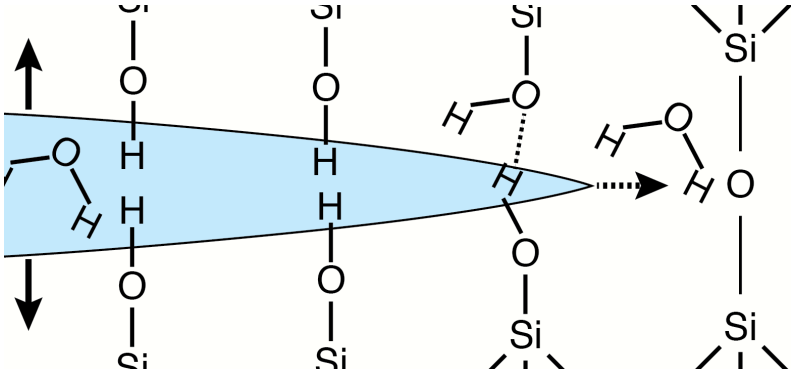

Figure 1.3. Schematic illustration of molecular mechanism of water weakening in silicate. After Michalske and Freiman (1982).

1.3 Research Questions

I postulate that the spatial zonation of alteration assemblages around hydrothermal systems results in spatial variation of fracture mechanical properties. Because of fracture mechanical controls on the evolution of fracture networks, feedback mechanisms may exist between chemical alteration and the hydro-mechanical attributes of evolving fault-fracture conduits. Specific research questions about the interaction between alteration, rock and fracture mechanics, and fault-fracture systems emerged as the focus of different parts of this dissertation:

1. How do fracture mechanical properties vary between different alteration assemblages?
2. How do changes in physio-chemical environment impact subcritical fracture growth in common hydrothermal assemblages?
3. What impact does hydrothermal alteration have on the evolution of fault-fracture networks?

1.4 Investigations

The body of this dissertation consists of three chapters prepared as manuscripts exploring the different research questions posed above. Chapter 2, *Fracture-mechanical properties of damaged and hydrothermally altered rocks, Dixie Valley - Stillwater fault zone, Nevada, USA*, presents results from rock and fracture mechanical testing of fault zone rocks exhumed from different hydrothermal environments. This manuscript was written for submission to the *Journal of Geophysical Research – Solid Earth*. A subset of this

investigation was presented as a conference paper at the 2017 Stanford Geothermal Workshop. Chapter 3, *Experimental investigation of chemically aided fracture growth in silicified rocks*, focuses on the impact of different physiochemical environments on fracture growth in silicified fault material from the Dixie Comstock epithermal deposit. This manuscript was written for submission to *Geothermics*. Chapter 4, *Precipitation-strengthening and fault zone evolution, Dixie Comstock epithermal deposit, Dixie Valley, NV,* explores the role of hydrothermal alteration in the evolution of fault-fracture networks from field observations and informed by the petrographic and mechanical characterization presented in Chapters 2 and 3. The target journal for this manuscript was the *Journal of Structural Geology*. Chapter 5 consists of a brief review of key findings and additional observations, a discussion of some of the limitations, and a short closing statement. Supplemental information, including sample locations and catalogs, rock mechanical test results, fracture mechanical test results, structural measurements and scanline data, stable isotope data, and fluid inclusion analysis are included in Appendices A – K.

The manuscripts presented as Chapters 2-4 were co-authored with my advisor, Peter Eichhubl, and Nicholas C. Davatzes. Jon E. Olson is an additional co-author on Chapters 2 and 3. All three co-authors contributed to grant writing in the early stages of these investigations, provided useful discussions that guided the overall path of the research, and reviewed the manuscripts prior to submission. In addition, Peter Eichhubl and Nicholas C. Davatzes participated in field work and shared field photographs. Fracture mechanics tests were conducted in Dr. Olson's laboratory in the Hildebrand Department of Petroleum and Geosystems Engineering at The University of Texas at Austin.

Together these chapters form a body of work investigating chemical-mechanical interactions in materials and conditions relevant to hydrothermal systems, mineral deposits, and fault zones more generally.

2. Fracture-Mechanical Properties of Damaged and Hydrothermally Altered Rocks, Dixie Valley - Stillwater Fault Zone, Nevada, USA[1]

ABSTRACT

Damaged and hydrothermally altered rocks are ubiquitous in fault zones. However, the degree of damage and the type and intensity of alteration vary significantly in space and time. The impact of damage and alteration on hydromechanical behavior of fault zones is difficult to assess without characterizing the associated changes to rock and fracture mechanical properties. To evaluate the mechanical properties of fault rocks in different alteration regimes, we conducted 1) double-torsion load relaxation tests to measure mode-I fracture toughness (K_{IC}) and subcritical fracture growth index (SCI), 2) uniaxial testing to measure unconfined compressive strength (UCS) and static elastic parameters, and 3) mineralogic and textural characterization of rock from four different sites in the footwall of the Dixie Valley-Stillwater fault zone. Alteration at these sites includes: acid-sulfate alteration and silicification associated with active fumaroles, intense silicification after calcite and chlorite alteration in an epithermal setting, quartz-kaolinite-carbonate alteration in an intermediate depth system, and a calcite-chlorite-hematite assemblage containing abundant unhealed damage. Silicification is associated with high K_{IC}, SCI, UCS, and increased brittleness, and in precipitation-dominated settings produces fault cores that are as strong or stronger than adjacent damage zone material. Calcite-chlorite-hematite assemblages containing abundant unsealed microfractures are approximately six times weaker than silicified fault rocks. Mechanical properties are not predicted by mineralogical composition alone; a key control is the accumulation of damage and degree of healing. Measures of strength increase when mineral precipitation reduces microfracture porosity to <15%. These results show that fault-proximal weakening or strengthening is influenced by hydrothermal setting.

---

[1] Authors and affiliations: Owen A. Callahan and Peter Eichhubl, Bureau of Economic Geology, The University of Texas at Austin, Austin, TX; Jon E. Olson, Hildebrand Department of Petroleum and Geosystems Engineering, The University of Texas at Austin, Austin, TX; Nicholas C. Davatzes, Earth and Environmental Sciences, Temple University, Philadelphia, PA

HIGHLIGHTS

1. Rock- and fracture-mechanical properties of altered and damaged fault zone rocks differ significantly from those of the protolith.
2. Silicification increases compressive strength, fracture toughness, and subcritical index relative to chlorite-calcite altered rocks.
3. Sealing of microfractures by quartz and calcite is associated with strength recovery when fracture porosity drops below ~15%.

KEYWORDS

fracture toughness, subcritical fracture, silicification, strength, elastic, geothermal

2.1 INTRODUCTION

Fault-fracture networks contribute critically to fluid flow in low-porosity crystalline rock, impacting the distribution of heat, fluid, and minerals in the upper crust. Hydraulically conductive faults and fault segments are characterized by well-developed damage zones composed of opening-mode fractures and sheared fractures (Brown and Bruhn, 1996; Caine et al., 1996; Sibson, 1996; Nelson et al., 1999; Davatzes and Aydin, 2003; Davatzes et al., 2003a; Eichhubl et al., 2009; 2010; Anders et al., 2013). The occurrence of opening-mode fractures in fault zones and fracture networks, and the evolution of these flow systems from single fractures to complex interconnected networks by fracture reactivation, propagation, and coalescence provide a fundamental control on the permeability evolution of faults and fault-controlled hydrothermal and epithermal systems (Sornette, 1999; Davatzes et al., 2003a; Davatzes et al., 2005; Blenkinsop, 2008).

Chemical controls on conduit evolution are well documented in field, experimental, and numerical studies, with dissolution, precipitation, and chemical alteration impacting the hydrologic properties of fault-facture networks (Summers et al., 1978; Moore et al., 1983; Berkowitz, 2002; Eichhubl et al., 2004; Eichhubl et al., 2009). These effects are particularly pronounced in chemically reactive environments encountered in high temperature hydrothermal systems (Lowell et al., 1993), where dissolution, advection, and precipitation of different mineral species in response to thermal and chemical disequilibrium and water-rock reactions lead to the development of distinct alteration assemblages (Facca and Tonani, 1967; Henley and Ellis, 1983; Simmons et al., 2005;

Gherardi et al., 2007; Tosdal et al., 2009; Sillitoe, 2010). Large regions of alteration are commonly associated with active hydrothermal systems (Browne, 1978) and around fossil conduits associated with magmatic and hydrothermal ore deposits (Henley and Ellis, 1983). However, some degree of alteration is common in most fault zones, where fracture-enhanced fluid flow and mechanical grain size reduction promote chemical reactions (Bruhn et al., 1994; Solum et al., 2010).

The mineralogical and textural changes encountered in hydrothermal alteration assemblages result in mechanical rock properties that differ from those of relatively pristine samples commonly used in geomechanical laboratory tests. For example, Seront et al. (1998) showed a decrease in compressive strength of altered and damaged fault-proximal granite compared to unaltered granite in parts of the Dixie Valley-Stillwater fault zone, Nevada. Wyering et al. (2014) and Siratovich et al. (2014) reported higher UCS in calcite and quartz ± propylitic altered volcanic rocks than in the same rocks dominated by quartz and clay alteration in the Taupo Volcanic Zone, New Zealand. Less work addresses the impact of damage and alteration on the fracture mechanical properties fracture toughness (K_{IC}) and subcritical crack index (SCI) (Atkinson, 1984; Kobayashi et al., 1986; Major et al., 2018), despite 1) the role of fractures and fracture growth in fault systems and 2) the differences between naturally altered and damaged fault rocks and relatively pristine geomechanical materials.

For opening-mode (mode-I) fractures, the stress intensity at the fracture tip, K_I, may be written as a function of remote applied stress, σ_r, fracture length or height, a, and fracture geometry, Y (Brown and Strawley, 1966):

$$K_I = \sigma_r Y \sqrt{a} \qquad \text{Eq. 2.1}$$

Mechanical fracture propagation occurs when K_I reaches a critical threshold, known as fracture toughness (K_{IC}). K_{IC} is particularly important during early fracture growth (Engelder et al., 1993). Cyclic loading and chemical corrosion at the fracture tip can lead to fracture growth below the critical stress intensity threshold, referred to as subcritical fracture growth and quantified by the SCI parameter which describes the relationship between fracture propagation velocity and stress intensity for fracture propagation below K_{IC} (Pletka et al., 1979):

$$V = V^* \left(\frac{K_I}{K_0}\right)^{SCI} \quad \text{Eq. 2.3}$$

where V is velocity, V^* is a constant, and K_0 is used to normalize K_I. Subcritical fracture growth has been invoked to explain long-term strength of the crust (Anderson and Grew, 1977; Rudnicki, 1980; Brantut et al., 2013), and differences in SCI may influence fracture spatial arrangements (Olson, 1993, 2004). Together, K_{IC} and SCI characterize fracture mechanical properties in a deforming rock volume.

Here we present experimental measurements of K_{IC} and SCI from double torsion load relaxation (DT-LR) fracture mechanical tests of a series of variably hydrothermally altered and damaged rocks collected from four sites in the Dixie Valley – Stillwater fault zone, Nevada (Figure 2.1)[2]. Sample sites represent a variety of hydrothermal settings, including: 1) a shallow acid sulfate fumarole setting at Dixie Meadows Fumaroles, 2) silicification after chlorite-calcite alteration in an epithermal setting at Dixie Comstock, 3) quartz-kaolinite-carbonate alteration and cementation in the "Mirrors" normal fault exposure, and 4) chlorite-calcite-hematite dominated assemblages at the Box Canyons. Alteration and deformation histories at these sites record processes during exhumation from different paleo temperature and depth conditions (Figure 2.2) and illustrate the relative impact of damage-dominated versus healing-dominated alteration on fracture-mechanical behavior. We demonstrate that hydrothermal alteration, previously recognized as an important factor influencing rock mechanical properties, also impacts the fracture mechanical properties influencing initiation, growth, and coalescence in fault-fracture networks.

2.2 METHODS

2.2.1 Mineralogical and Textural Characterization

We evaluated bulk mineralogy of damaged and altered rocks with X-ray diffractometry (XRD) using a Bruker D8 Advanced X-Ray Diffractometer with LynxEye detector. Samples were prepared as randomly oriented spray-dried powders (Hillier, 1999) and scanned at ~0.01° increments from 4-66° 2-theta for 1.5-2 hrs. Initial analysis of XRD

[2] Sample numbers in this chapter correspond to the following samples in the appendices: 1 = 052615-3a, 2 = 052615-3b, 3 = 083114-2a, 4 = 052815-3b, 5 = 052815-3a, 6 = 061114-4b, 7 = 052815-2, 8 = 030914-1, 9 = 052715-7, 10 = 052615-1a, 11 = 052615-1b, 12 = 071813-3, 13 = 071813-2, 14 = 052615-2.

spectra was conducted with EVA software, followed by Rietveld analysis using TOPAS 4.2 software (Table 2.1).

Alteration, porosity, and microfracture intensity were quantified from thin section petrography and point counting of blue-epoxy impregnated samples. Porosity and microfracture intensity were obtained from ~400 points at 120X magnification (Table 2.2). Microfracture intensity was calculated from the percentage of points encountering microfracture porosity or fracture-filling cement. Thin sections were oriented approximately perpendicular to the dominant structural fabric.

2.2.2 Unconfined Compressive Strength and Static Elastic Characterization

We measured static elastic properties and unconfined compressive strength (UCS) with uniaxial compressive strength tests using a GCTS rock mechanics system (Table 2.3). Plug orientations were vertical (V), parallel to strike (H), down dip (D), or mutually perpendicular to strike and dip (P) of local range front faults. Loading was conducted at an axial strain rate of 0.055%/minute. UCS is reported from peak, area-corrected load. Young's modulus and Poisson's ratio were calculated from the middle portion of the loading curve where the relationship between stress and strain was approximately linear.

2.2.3 Double Torsion Load Relaxation Fracture Mechanics Testing

We used double-torsion load relaxation (DT-LR) tests to measure K_{IC} and SCI using multiple specimens of altered rocks prepared as thin wafers. All specimens were cut from the same blocks of material used for petrographic, mineralogic, and mechanical characterization of each sample. DT-LR tests were conducted by repeatedly propagating a fracture down the axis of a specimen prepared as a thin rectangular wafer (Figure 2.3). Detailed descriptions of the testing apparatus, method, and data reduction procedure used here can be found in Chen et al. (2017), and are summarized below.

The DT testing apparatus consists of a base plate, specimen supports, a loading ram with internal force sensor, and a linear variable displacement transducer to record displacement (Figure 2.3). K_I at the fracture tip was calculated using the equation (Williams and Evans, 1973):

$$K_I = PW_m\sqrt{\frac{3(1+\nu)}{\varphi W t_n t^3}} \qquad \text{Eq. 2.4}$$

where P is load supported by a pre-fractured specimen, W_m is the moment arm of the DT apparatus, ν is Poisson's ratio, W is specimen width, t is specimen thickness, and t_n is the reduced thickness along the axial groove created by pulling the specimen across a recessed diamond saw prior to testing. If insufficient sample material existed for UCS tests, ν was estimated from similarly altered and damaged samples. The geometric correction factor, ψ, is based on individual specimen geometry (Fuller, 1979):

$$\psi = 1 - 0.6302\frac{2t}{W} + 1.2\frac{2t}{W}e^{\left(\frac{-\pi W}{2t}\right)} \quad \text{Eq. 2.5}$$

We tested specimens with thickness (t), width (W), and length (L) dimensions of approximately 1.8 mm x 30 mm x 75 mm, respectively (Figure 2.3), meeting dimensional requirements of ~24t<2W<L (Nara and Kaneko, 2005). Absolute specimen dimensions were similar to those used by Atkinson (1979b), Sano et al. (1992), and Chen et al. (2017) and were limited in part by sample size and load cell capacity (Appendices E and F) . Pre-fractures were induced using the DT apparatus at low displacement rates (<1 μm/s) until a distinct load drop was observed, indicating the formation of an edge crack.

DT tests for fracture toughness were conducted on pre-fractured specimens at fast displacement rates (~180-220 μm/sec) to total failure (Figure 2.4). DT-LR tests for SCI were conducted by loading pre-fractured specimens at low displacement rates (1-2 μm/s) until fracture propagation was indicated by a rapid drop in supported load. Displacement was stopped, and the load allowed to decay for 5-10 minutes. Ideal DT-LR test patterns included a high pre-fracture load, a subsequent plateau region of lower peak loads and load-decay curves that were used to calculate SCI, and a final load drop upon complete specimen failure (Figure 2.4). A separate estimate of fracture toughness (K_{IC}*), based on the stress intensity from peak loads in the plateau region during slow displacement tests, was evaluated as a proxy for K_{IC} calculated from rapid displacement tests. Load and displacement were recorded at 14 Hz for K_{IC} tests and 5 Hz for DT-LR tests. All tests were conducted under ambient conditions at 23-24°C. Relative humidity was not measured for all tests, but commonly ranged between 58-75%.

Fracture propagation velocity was calculated from the load relaxation curve (Evans, 1972):

$$V = -\phi\left(\frac{a_0 P_i}{P^2}\right)\frac{dP}{dT} \quad \text{Eq. 2.6}$$

where a_0 is initial fracture length, and P_i is load at the start of each load-decay cycle. The correction factor for fracture front geometry, ϕ, is assumed to be 0.2 (Williams and Evans, 1973; Atkinson, 1979a; Chen et al., 2017). Because pre-fracture lengths are difficult to observe in our materials, we follow Chen et al. (2017) and use a_0 of 12.7 mm, with later cycles using $a_n = a_0 + n*12.7$ mm, a nominal value that accounts for the average number of fracture growth increments and specimen length. Variation of a_0 has minimum impact on calculated fracture front velocity (Chen et al., 2017). SCI was calculated from K-V curves using an in-house LabView script for smoothing and fitting following derivations described in Holder et al. (2001).

2.3 Sample Sites and Materials

2.3.1 Acid Sulfate Alteration and Silicification at Dixie Meadows Fumaroles

The Dixie Meadows Fumaroles site exposes fumarole-related alteration in Oligocene tuff in the footwall of the Stillwater Fault Zone west of Dixie Meadows Hot Springs (Figure 2.1). Alteration products here include native sulfur, sulfate minerals, kaolin group minerals, montmorillonite, calcite, and quartz (Kennedy-Bowdoin et al., 2004; Lamb et al., 2011; Schwering, 2013), a suite of minerals reflecting shallow acid-sulfate alteration related to ongoing fumarole activity and boiling or near boiling conditions in the shallow subsurface (Figure 2.2).

We tested multiple plugs and DT specimens from two samples from Dixie Meadows Fumaroles: a moderately altered tuff (sample 1), and a portion of exhumed fault core composed of weakly silicified bladed calcite and microquartz (sample 2) (Figure 2.5, Table 2.1). Sample 1 is a pale, non-welded, devitrified tuff, with partially dissolved feldspar phenocrysts. The dominant mineral species are quartz and feldspar, with lesser kaolinite and undifferentiated clay. Vugs in pumice are commonly filled with kaolinite, whereas vugs in partially dissolved feldspar grains contain small euhedral quartz crystals. Hematite occurs as disseminated grains and as fracture fill. Pores are typically smaller than 0.5 mm, with some secondary pores in dissolved grains exceeding 2 mm. Total porosity is ~7.1%, and microfracture intensity is low (~0.7%) (Table 2.2). Sample 2 is coarse-grained fault breccia, mineralogically and texturally dominated by multiple generations of quartz and calcite, with minor hematite and sericite. Calcite occurs as bladed laths, and as

disseminated, fine-grained, and occasionally laminated intergrowths with microquartz. Microquartz occurs as clasts and as cement between clasts. Clast sizes range from ~1 cm to <1 mm. Total porosity and microfracture intensity are low (~0.3% and 2.7%).

2.3.2 Na-Ca Alteration and Silicification at Dixie Comstock Epithermal Gold Deposit

The Dixie Comstock epithermal gold deposit is located along a north-south portion of the Dixie Valley - Stillwater fault zone (Figure 2.1). Several temporally distinct episodes of alteration are preserved in the Dixie Comstock area. Early and widespread sodic and calcic alteration of the Jurassic Humboldt Igneous Complex (Dilek and Moores, 1995; Johnson and Barton, 2000) is overprinted by aureoles of quartz, albite, sericite, kaolinite, and iron oxide around apophyses of Cretaceous granite (Vikre, 1993). Alteration in the mine area is dominated by silicification of the range front fault, with portions of the silicified fault core exceeding 2 m in thickness and approaching 100% quartz. Silicification overprints and entrains earlier assemblages. Intense silicification extends ~300 m north and south of the mine workings, with quartz veins in the footwall and minor silicification of fault breccia extending 1.5 km along strike and at least several hundred meters down dip. Bladed calcite (this study) and liquid- and vapor-rich inclusions (Vikre, 1993) indicate boiling conditions existed in shallow parts of the system, and fluid inclusion microthermometry indicate temperatures between ~160-180 °C (Vikre, 1993). Boiling near 170 °C suggests exhumation from as shallow as ~76 m (Haas, 1971) (Figure 2.2).

Dixie Comstock samples were obtained from a distal portion of the footwall (sample 3), from the footwall behind the main mineralized deposit (samples 4 and 5), and from the silicified fault core (samples 6 and 7) (Figure 2.6). Alteration reactions are dominated by replacement of feldspars with chlorite, calcite, and sericite and intense silicification (Table 2.1). Sample 3 is a medium-grained quartz gabbro, dominated by plagioclase and albite with minor quartz. Alteration minerals include chlorite, minor epidote, sericite, sulfides, oxides, and trace calcite. Plagioclase is partially replaced by chlorite and exhibits minor sericitization. Quartz and plagioclase laths are broken, but intragrain fractures have no observable porosity. Total porosity is low (~0.7%) and microfracture intensity is intermediate (~6%). Samples 4 and 5 retain primary textures, but plagioclase and mafic minerals are increasingly replaced by chlorite in sample 4 and by

calcite in sample 5. Plagioclase and albite laths are cloudy. Calcite occurs as replacement and as thin cements lining fractures. Cataclastic zones contain crushed plagioclase and calcite with hematite and pyrite. Sample 4 has low microfracture intensity (1.8%) and intermediate porosity (1.8%), whereas Sample 3 has higher microfracture intensity (3.6%) and lower porosity (0.7%) (Table 2.2). Samples 6 and 7 were collected from different locations within the silicified fault core to capture large scale heterogeneity and reproducibility in this material. The samples are dominated by fine-grained, intergrown, microquartz with minor chlorite, feldspar, and plagioclase, and trace sericite, calcite, and sulfides and oxides. Both samples contain evidence of multiple generations of brecciation and quartz cementation in the form of broken and rounded clasts of earlier microquartz breccia. Microfracture intensity in Sample 6 is intermediate (6.9%) and porosity is low (0.5%). Microfracture intensity in Sample 7 is high (12.6%), but intense silicification has reduced porosity to 1.6%. In both samples, porosity is restricted to quartz lined and nearly occluded vugs and minor partially quartz- or calcite-cemented fractures.

2.3.3 Quartz-Kaolinite-Carbonate Alteration at the Mirrors Fault Zone Exposure

The Mirrors site is located along a NE-SW striking section of the Stillwater Fault Zone southwest of the producing geothermal field (Figure 2.1). The protoliths at the Mirrors are intrusive and extrusive components of the Jurassic Humboldt Igneous Complex (Page, 1965; Speed, 1976; Dilek and Moores, 1995). Alteration includes regional sodic, calcic, and chlorite alteration, with later kaolinite, carbonate, and quartz after mafic minerals and feldspar in a well-developed damage zone and fault core (Lutz and Moore, 1996; Caine et al., 2010). Physical conditions during the dominate phase of alteration are constrained by post-Miocene exhumation of <2 km (Power and Tullis, 1989, 1992), and the occurrence of quartz with kaolinite indicating temperatures <270 °C (Figure 2.2). Ferroan dolomite, chalcedony, goethite, and barite (Lutz and Moore, 1996) and chalcedony with kaolinite (this study) indicate that at least some alteration occurred at temperatures <180 °C.

Samples from the Mirrors include altered and moderately silicified fault damage zone (sample 8) and fault core material (sample 9) (Figure 2.7, Table 2.1). Sample 8 is an argillic/silicic altered fine to medium grained mafic plutonic rock. Mineralogy is

dominated by quartz and kaolinite, with less carbonate (calcite, ankerite), sericite, and trace hematite. Primary magmatic textures are cryptic, with kaolinite replacing feldspars, calcite replacing amphibole, and degraded pyroxene. Quartz is dominantly fine grained, intergrown microquartz, with rare chalcedony lined, kaolinite filled pockets. Carbonate occurs as small (<50 μm), disseminated grains, as fill in thin, discontinuous fractures, and replacing amphibole grains <2 mm long. Sample 9 was obtained from the cemented fault core. Sample texture is heterogenous at the thin section scale. Cement is dominantly fine grained, interlocking microquartz, with angular to sub-angular clasts <2 cm long of broken calcite and ankerite veins. Macroscopic textures indicate repeated brecciation, alteration, and cementation during exhumation, with little primary texture preserved. Kaolinite, sericite, and calcite occur in the matrix, with some sericite and carbonate replacing clasts. Samples 8 and 9 both contain intermediate microfracture intensity (3.2 and 5.0%, respectively), and low total porosity (0.6 and 0.3%), similar to porosity ~0.3-0.4% previously measured in Mirrors fault core samples (Seront et al., 1998).

2.3.4 Chlorite-Calcite-Hematite Alteration and Damage at the "Box Canyons"

The Box Canyons site in southern Dixie Valley is located along a portion of the Dixie Valley - Stillwater Fault Zone that ruptured in the 1954 Fairview Peak – Dixie Valley earthquake sequence (Figure 2.1). Host lithology is Oligocene-Miocene granite and granodiorite (John, 1995). Fault proximal alteration records progressive exhumation, with early, deep, potassium feldspar-biotite to chlorite-calcite-hematite ±epidote alteration, sericite-quartz-kaolinite-smectite and zeolite alteration (Parry et al., 1991; Bruhn et al., 1994; Hedderly-Smith, 1997). K-Ar ages from sericite are coeval with magmatism (25.0 ±1.0 Ma and 21.8 ±0.9 Ma (Parry et al., 1991). Alteration occurred across a range of depth and temperature conditions. (Figure 2.2). Mineral equilibrium and fluid inclusion studies indicate potassic alteration occurred at <6 km and 300-350 °C (Parry and Bruhn, 1990; Parry et al., 1991). Epidote, chlorite, calcite assemblages record alteration >240 °C. Parry et al. (1991) reported homogenization temperatures in fluid inclusions in microfractures in quartz as low as 180-190 °C and stilbite in outcrop, suggesting alteration continued <140 °C and <2.5 km, although we did not observe zeolite locally.

Box Canyon samples (10-14) record increasing alteration and damage of granite and granodiorite (Figure 2.8, Table 2.1). Background samples include two plutonic phases: a less altered granodiorite (sample 10) and a more altered granite (sample 11). Quartz grains in sample 10 contain minor deformation. Plagioclase laths up to 1.5 mm in length contain small, uneven fractures, but no rotation and only minor sericitization. Biotite and amphibole are relatively pristine. All crystals are intergrown, with little interstitial space, no observed porosity, and low microfracture intensity (0.2%). In sample 11 feldspars contain patches of albite, and cloudy, vacuolized cores. Damage includes transgranular fractures with minor, early hydrothermal biotite. Microfracture intensity is intermediate (3.3%) with low porosity (0.5%). Sample 12 was collected near the range front fault, but away from the chlorite-calcite-hematite altered area. Hydrothermal biotite replaces mafic minerals and occurs as fracture fill in orthoclase. Feldspars and some plagioclase laths contain cloudy, vacuolized cores, large sericite grains, and increased albitization. Porosity (2%) is comparable to 1.2% previously reported for Box Canyon damage zone samples (Seront et al., 1998), and occurs in microfractures and in dissolved feldspars. Microfracture intensity is intermediate (5.5%). Samples 13 and 14 were both collected from the most altered area in the Box Canyons site, and help to constrain reproducibility among similarly altered and damaged materials. Alteration minerals include carbonate and chlorite, with lesser sericite, epidote, and sulfides/oxides and damage includes multiple cross-cutting cataclastic bands, broken grains, and thin, partially calcite- and hematite-filled fractures (Figure 2.8). Microfracture density is high (19.4-23.3%). Porosity (2.5-5.6%) occurs in late, partially calcite-filled fractures, and along the edges of cataclastic bands. These samples likely represent the "ultradamage zone" of Seront et al. (1998), but the porosity is two to four times higher. These samples contain among the highest microstructural heterogeneity at the thin section and specimen scale.

2.4 Experimental Results and Analysis

2.4.1 UCS and Static Elastic Properties

We conducted UCS tests on 24 plugs from 11 samples of crystalline rock with varying degrees of alteration and damage (Table 2.3). The amount of material in each sample and sample integrity limited the number of successful repeat tests in some

materials. Strength and elastic measurements from plugs with different orientations generally overlapped. Test results from each plug are included in Appendix D.

Samples with the highest UCS and Young's modulus include minimally altered granodiorite (sample 10), silicified samples (6 and 7), and the calcified sample (5). Silicified samples have the highest compressive strength (286.5 MPa) and Young's modulus (62.8 GPa), and among the lowest Poisson's ratios (0.11-0.13). The strength of the silicified material is greater than minimally altered granodiorite, and six times higher than the weakest altered and damaged samples. The weakest materials contained disseminated chlorite and calcite alteration and a higher percentage of partially and uncemented microfractures.

2.4.2 Fracture Mechanical Properties

We calculated K_{IC} for 13 samples (6-21 specimens per sample) using rapid displacement to total failure (Table 2.4), and K_{IC}* for 13 samples from 337 plateau loads (6-73 per sample) during slow displacement DT-LR tests (Table 2.5). Twelve samples were tested for both K_{IC} and K_{IC}*. Despite experimental work indicating loading rate dependence on K_{IC} in some materials (Atkinson and Meredith, 1987), we observed no consistent difference between toughness calculated from rapid or slow displacement tests (Figure 2.9). The average standard deviation for K_{IC} is ~21%. When K_{IC} and K_{IC}* are combined, the average standard deviation is reduced to 17%. However, all figures use K_{IC} from rapid displacement tests unless otherwise noted. Test conditions and failure parameters for each specimen are included in Appendices E-F.

We observed significant variation in K_{IC} between background and more damaged, altered, and cemented fault core and fault proximal material (Figure 2.10). The highest maximum K_{IC} (3.84 MPa$\sqrt{m}$) and the highest mean K_{IC} (3.20 MPa$\sqrt{m}$) were measured in silicified samples from Dixie Comstock. These K_{IC} values are greater than relative pristine granodiorite (2.08 MPa$\sqrt{m}$), and as much as six times higher than the weakest altered and damaged material (0.56 MPa$\sqrt{m}$). Moderate silicification (~50-60 wt% quartz) in fault core material from the Mirrors had an intermediate K_{IC}, similar to that of fresh granodiorite. The transect from least altered granodiorite to damage zone samples at the Box Canyons records a reduction in K_{IC} from >2.0 to <0.7 MPa$\sqrt{m}$. Similarly altered plutonic rocks from both

Dixie Comstock and the Box Canyons, characterized by minor chlorite, calcite, hematite, ±epidote alteration and unhealed damage, had similarly low K_{IC} (~0.7 MPa√m). A positive correlation between K_{IC} and UCS (Figure 2.11) is consistent with the underlying mechanism of failure in UCS tests, microfracture growth and coalescence, which is in turn influenced by K_{IC}.

We calculated SCI for 13 samples, using 4 to 19 specimens per sample (Table 2.6). In some tests induced fractures propagated out of the axial groove, either due to interaction with existing microstructures or unbalanced loading. These decay curves were not included in SCI calculations. The number of selected decay curves per sample ranged from 1 to 53. The minimum and maximum standard deviations were 23-38%, with an average standard deviation for SCI ~30%. The highest mean SCI was calculated for silicified fault core and damage zone material from Dixie Comstock, the Mirrors, and Dixie Meadows (92.3 - 144.6), although the range of mean SCI in other material is smaller (51.6-76.0). Calculated fracture growth velocities (Eqs. 3 and 5) were generally between 10^{-5} to 10^{-7} m/s (Figure 2.10). This range in fracture propagation velocity is similar to values calculated for rocks under ambient conditions by other researchers (Atkinson, 1979a; Wilkins, 1980; Swanson, 1984; Nara and Kaneko, 2005; Chen et al., 2017), and is in part limited by sampling rate and signal to noise ratios. Stress intensity – velocity (K-V) plots show 1) fracture propagation at lower stress intensities in weaker material and 2) steeper K-V curves in more altered, fault proximal material with greater microstructural complexity.

2.5 DISCUSSION

2.5.1 Mechanical Properties in Altered vs. Pristine Rocks

We observed both increases and decreases in K_{IC}, SCI, and elastic properties in damaged, altered, and cemented fault zone material compared to the local protolith. Mean K_{IC} in relatively unaltered granodiorite from the Box Canyons is similar to reported values of K_{IC} from Westerly granite (1.74 MPa√m (Atkinson, 1984); 1.79 ±0.02 MPa√m (Meredith and Atkinson, 1985); 1.43±0.05 MPa√m (Nasseri et al., 2009)). SCI is similar to reported values for Lac du Bonnet granodiorite (55.9, 58.5, (Wilkins, 1980); 56 (Lajtai and Bielus, 1986) and Westerly granite (35.9-39 (Atkinson, 1982); 69 (Swanson, 1984)). However, the most altered and damaged granitic and gabbroic rocks in our dataset show a

significant reduction in K_{IC} (<0.7 MPa√m), and silicification resulted in significant increases in mean K_{IC}, SCI, and UCS (up to 3.2 MPa√m, 144.7, and 286.5 MPa, respectively). Silicification of altered damage zone material at the Dixie Comstock site in particular corresponds to an approximately 600% increase in strength over the weakest footwall samples that we tested.

The observed fracture mechanical values in altered and damaged samples are within ranges previous measured in rocks in general (Atkinson, 1984; Swanson, 1984), but mineral composition alone is a poor predictor of these properties. K_{IC} in silicified material is similar to "black gabbro" (2.88 MPa√m, (Atkinson, 1984); 2.9 MPa√m; (Atkinson, 1982); 2.71-3.03 MPa√m, (Meredith and Atkinson, 1985)) and quartzite (2.1-2.65 MPa√m (Atkinson, 1984)). However, novaculite, which is mineralogically similar to the most silicified samples has less than half of the strength (K_{IC} of 1.335 ±0.075 MPa√m) and lower SCI (25.1) (Atkinson, 1980). These finding suggest that experimental analogs based solely on rock type or mineralogy are likely to be inadequate.

Instead, the reduction in toughness we observed in altered and damaged fault proximal samples is comparable to strength reductions measured in other naturally and experimentally damaged material. Meredith and Atkinson (1985) and Nasseri et al. (2009) measured reduced K_{IC} in thermally treated Westerly granite containing experimentally induced microfractures. Siratovich et al. (2014) observed a factor of four reduction in UCS with a tripling of connected porosity in volcanic rocks from the Taupo hydrothermal field, NZ. Pola et al. (2014) reported a 45-50% reduction in UCS and Young's modulus in altered and weathered samples from dissolution-dominated volcanic environments. Heap et al. (2015) reported a correlation between increasing connected porosity and reduced compressive strength for lava and tuff with different degrees of advanced argillic (acid sulfate) alteration from the White Island volcanically-hosted hydrothermal system, New Zealand.

Despite the occurrence of some degree of damage and alteration in most natural systems, systematic investigations of the impact of alteration on fracture mechanical properties are limited. Atkinson (1984) included a reference to dunite and serpentinized dunite, with serpentinization resulting in a >50% reduction in K_{IC}, from 3.74 to 1.39 MPa√m. Kobayashi et al. (1986) reported low K_{IC} in smectite/zeolite altered Ogino tuff

(~0.7 MPa√m); Ogino tuff has a lower density, lower UCS, and lower E than the material we tested, suggesting a greater degree of argillic alteration. Major et al. (2018) reported bleached sandstone from the Crystal Geyser system, Utah, USA, has a lower K_{IC} than adjacent hematite-cemented sandstone.

In the materials that we tested, sealing of ~85-90% of fracture porosity with mineral cement is associated with a significant increase in all measures of toughness (UCS, K_{IC}, SCI) (Figure 2.12). The observation that damaged rocks can regain significant strength and resistant to fracture growth is consistent with other researchers that observed strengthening as a result of mineral precipitation (quartz or calcite (our dataset); alunite (del Potro and Hürlimann, 2009; Heap et al., 2015); hematite and calcite (Major et al., 2018)). Our sample base is too small to probe the full range of impacts on strength recovery resulting from different fracture cement types, textures, or distributions. However, the addition of fracture-filling mineral cements in some hydrothermal settings clearly impacts strength distribution in these systems.

2.5.2 Implications for Strength Distribution in Fault-Hosted Hydrothermal Systems

Hydrothermal alteration results in changing rock properties, introducing competition between healing and strengthening against damage and weakening, with different mechanism dominating at different times and in different places. These processes occurred repeatedly in these samples, indicated by multiple generations of fractures and fracture-filling cements, cross-cutting mineral assemblages from different alteration regimes (Figure 2.6 E, H) and by brecciation of previously cemented fault rock. If precipitation outpaces deformation, fault rocks will experience interseismic strengthening in precipitation-dominated environments. Conversely, periods experiencing frequent deformation, or when precipitation is less effective at healing damage, will tend to undergo progressive weakening. Because hydrothermal systems commonly show spatial variation in the dominant alteration mechanisms related to temperature, fluid chemistry, and fluid-rock ratios (Simmons et al., 2005; Tosdal et al., 2009; Nishimoto and Yoshida, 2010; Sillitoe, 2010), the spatial distribution of mechanical properties in and around fault-fracture conduits is likewise expected to change depending on the type of alteration. Based on depth and temperature reconstructions for the Dixie Valley field sites (Figure 2.2), the fault-

hosted hydrothermal systems we examined show a depth-dependent inversion in mechanical contrast between fault conduit and host rock (Figure 2.13). In the exhumed chlorite-calcite-hematite assemblage preserved at the Box Canyons we see a reduction in K_{IC} and UCS near the fault. Notably, the fault core at this site is not preserved in outcrop, suggesting the material is particularly weak or susceptible to erosion. In the shallow, precipitation-dominated epithermal setting at Dixie Comstock samples from the thick, silicified fault core are up to six times stronger than chloritized footwall samples. This distribution of mechanical properties has implications for fault zone architecture and behavior. In portions of hydrothermal systems dominated by dissolution and the accumulation of unhealed damage, we expect deformation to become increasingly focused. In contrast, rapid advection, cooling, and enhanced precipitation in shallow portions fault-hosted hydrothermal systems, where conditions approach the boiling point with depth curve (Figure 2.2) may inhibit fracture growth in the primary conduits and promote fracture growth in adjacent material, ultimately contributing to large volumes of fractured rock and distributed alteration in shallow portions of the system.

2.5.3 Broader Impacts of Alteration, Damage, and Healing

Hydrothermal alteration and the resulting preservation or healing of damage may impact several geologic systems of particular interest to society, including mineral deposits, volcano-magmatic systems, and fault systems more generally. Moir et al. (2013) showed that dilatant damage around mineralized fault zones could be related to contrasting mechanical properties in different host lithologies. Our results suggest that the distribution of fracture growth and fracture strength parameters will be heterogeneous in both space and time around mineral deposits due to alteration-induced mechanical contrast. Acid sulfate and argillic alteration in volcanic edifices has been linked to flank collapse (Lopez and Williams, 1993; Watters et al., 2000; Reid et al., 2001; del Potro and Hürlimann, 2009). However, cementation by quartz or alunite in these environments may also result in local densification and strengthening, with physical and mechanical contrast between different alteration products potentially influencing where flank collapse ultimately occurs. Opening-mode fractures are fundamental parts of fault initiation in crystalline rock (Crider, 2015) and persistent elements in damage zones in mature fault systems (Wilson et al., 2003;

Davatzes et al., 2005). Subcritical fracture growth in damage zones has been implemented in pre-and post-seismic behavior of fault systems (Anderson and Grew, 1977; Rudnicki, 1980; Brantut et al., 2013). However, because some degree of hydrothermal alteration is common in large seismogenic faults (e.g. Parry et al. (1991); Bruhn et al. (1994)), the fracture mechanical properties of fault zones are poorly constrained by geomechanical tests of pristine material. The threshold that we observe, where healing of ~85-90% fracture healing results in a significant increase in material strength, represents a gross approximation that may be applied to models of spatial and temporal changes in strength, fracture formation, and fracture growth in these different systems.

2.6 CONCLUSIONS

We combined unconfined compressive strength tests, mineralogical and textural characterization, and double torsion load relaxation tests to measure elastic and fracture mechanical properties in suites of rocks from different hydrothermal alteration regimes preserved in the footwall of the Dixie Valley – Stillwater fault zone. The alteration regimes include 1) a shallow acid-sulfate regime dominated by quartz and calcite precipitation, 2) an epithermal regime dominated by intense silicification after earlier sodic and calcic alteration, 3) a moderate depth and temperature silicic-argillic regime dominated by quartz, kaolinite, and carbonates, and 4) a retrograde alteration regime dominated by chlorite-calcite-hematite assemblages and unhealed damage. Silicification is associated with high unconfined compressive strength (286.5 MPa), Young's modulus (62.8 GPa), K_{IC} (3.20 MPa$\sqrt{m}$), SCI (144.7), and low Poisson's ratio (0.11-0.13). Silicified fault rocks are stronger than minimally altered granodiorite, and up to six times tougher than unhealed chlorite-calcite-hematite fault damage zone samples. Based on the alteration assemblages that we tested, the mechanical contrast among fault core, damage zone, and protolith changes between precipitation- vs damage-dominated regimes. Sealing of >85% of initial microfracture porosity by quartz and/or calcite in the fault zone in the epithermal regime is associated with a significant increase in UCS, K_{IC}, and SCI above values of altered protolith in the footwall. The mechanical properties that we measured in altered, damaged, and healed fault zone samples are not readily predicted from geomechanical tests of pristine rocks.

ACKNOWLEDGMENTS

Donnie Brooks assisted with rock mechanics testing at the Rock Mechanics Lab, Bureau of Economic Geology, Austin, TX. Xiaofeng Chen greatly improved the double torsion testing apparatus, method, and data reduction routine. Jonathan Major helped with sample preparation and XRD analysis. Sol Cooperdock, Alison MacNamee, and Adenike Tokan-Lawal provided field assistance. Funding was provided by grants from The GDL Foundation, The Geothermal Resources Council, and The American Association of Petroleum Geologists Foundation. Additional support was provided by The Jackson School of Geosciences and the Fracture Research and Application Consortium (FRAC) at The University of Texas at Austin. Publication authorized by the Director, Bureau of Economic Geology.

Table 2.1. Bulk Mineralogy from X-Ray Diffraction of Spray Dried Powders

Site	ID	Cor spike (wt%)	Cor (wt%)	Normalized wt%												
				QTZ	PLAG + FELD	ALB	AMPH	Px	BIO	CARB	EPI	CHL	MUSC/SER	KAOL	Other CLAY	Oxides, Sulfides
DM	1	10.14%	10	50	38	-	-	-	-	-	-	-	-	6	7	<1
	2	9.98%	10	40	7	-	-	-	-	54	-	-	-	-	-	-
DC	3	10.00%	9	10	30	46	-	-	-	<1	2	8	2	-	-	2
	4	9.98%	9	2	33	26	-	-	-	1	1	32	4	-	-	-
	5	10.16%	9	1	36	21	-	-	-	19	-	22	-	-	-	1
	6	10.00%	7	91	5	<1	-	-	-	-	-	4	-	-	-	<1
	7	10.00%	6	97	-	<1	-	-	-	<1	-	3	-	-	-	<1
M	8	10.00%	10	49	-	-	-	-	-	8	-	-	3	40	-	<1
	9	10.00%	10	60	-	-	-	-	-	10	-	-	2	28	-	<1
BC	10	9.98%	10	23	44	18	7	2	4	-	-	-	1	-	-	-
	11	10.00%	10	33	46	20	-	-	<1	-	-	-	1	-	-	<1
	12	10.00%	10	24	51	14	2	6	1	-	-	-	2	-	-	<1
	13	10.00%	10	29	40	14	-	-	-	7	1	9	-	-	-	-
	14	10.00%	10	19	46	21	-	-	-	2	<1	6	5	-	-	1

- = not included in final Rietveld solution

% Cor = wt% corundum in final Rietveld solution; compare to wt% in spike

Table 2.2. Sample Properties from Plugs and Point Counting

Site	ID	Density (g/cm^3)			Total Porosity (%)			Fracture Porosity (%)			Microfracture Density (%)			n
		wt mean*	± std dev †	n		+ error	-error		+ error	-error		+ error	- error	
DM	1	2.19	0.02	4	7.1	2.4	1.9	0.0	0.7	0.0	0.7	1.1	0.5	400
	2	2.50	0.02	4	0.3	1.0	0.3	0.0	0.8	0.0	2.7	1.8	1.2	360
DC	3	-	-	-	0.7	1.2	0.5	0.7	1.2	0.5	6.0	2.4	1.9	383
	4	2.56	0.00	1	1.8	1.4	0.9	1.1	1.2	0.7	1.8	1.4	0.9	418
	5	2.69	0.00	1	0.7	1.1	0.5	0.0	0.7	0.0	3.6	1.9	1.4	451
	6	2.64	0.00	1	0.5	1.1	0.4	0.2	0.9	0.2	6.9	2.4	2.0	404
	7	2.62	0.01	2	1.6	1.5	0.9	0.8	1.3	0.6	12.6	3.1	2.7	381
M	8	2.65	0.00	1	0.6	1.0	0.5	0.4	0.8	0.3	3.2	1.6	1.2	504
	9	2.57	0.01	6	0.3	0.6	0.2	0.0	0.5	0.0	5.0	1.6	1.3	659
BC	10	2.68	0.01	3	0.0	0.7	0.0	0.0	0.7	0.0	0.2	0.9	0.2	410
	11	2.58	0.01	3	0.5	1.0	0.4	0.3	0.9	0.3	3.3	1.8	1.3	428
	12	-	-	-	2.0	1.6	1.0	1.7	1.6	0.9	5.5	2.3	1.8	382
	13	-	-	-	5.6	2.2	1.7	5.1	2.1	1.6	19.4	3.5	3.1	418
	14	2.58	0.01	3	2.5	1.7	1.1	2.5	1.7	1.1	23.3	3.7	3.4	412

* from single calculation when n = 1

† from propagated error when n = 1

Table 2.3. Static Elastic Properties and Unconfined Compressive Strength

Site	ID	UCS (MPa)		E (GPa)		*v*		G (GPa)		n	Orientation
		mean*	± std dev ‡	mean*	± std dev ‡	mean*	± std dev ‡	mean*	± std dev ‡		
DM	1	62.4	10.3	15.1	0.8	0.10	0.06	6.9	0.0	2	H
	2	68.1	11.3	27.2	7.0	0.16	0.05	11.6	2.7	4	H, P
DC	3	-	-	-	-	-	-	-	-	-	-
	4	50.7	-	22.8	-	0.20	-	9.5	-	1	V
	5	148.0	-	48.2	-	0.22	-	19.7	-	1	V
	6	187.8	-	51.1	-	0.13	-	22.6	-	1	H
	7	286.5	12.7	62.8	1.6	0.11	0.02	28.3	0.3	2	H
M	8	67.1	-	27.0	-	0.38	-	9.8	-	1	V
	9	109.0	8.9	38.9	3.0	0.13	0.03	17.3	1.5	5	H, P, D
BC	10	256.2	14.4	59.4	2.2	0.29	0.03	23.1	0.3	2	H, V
	11	99.8	20.8	40.0	5.6	0.24	0.04	16.1	1.7	2	H
	12	-	-	-	-	-	-	-	-	-	-
	13	-	-	-	-	-	-	-	-	-	-
	14	51.1	5.5	17.6	2.2	0.25	0.10	7.0	0.4	3	H, V

* from single calculation when n = 1
‡ from stdev.p, not reported when n = 1
8 sample 8 failed on a pre-existing axial fracture

Table 2.4. K_{IC} from Rapid Displacement Using Double Torsion Configuration

Site	ID	Fracture Toughness (MPa m^1/2)							
		Min	Q1	Med	Q3	Max	Mean ± std dev		n
DM	1	0.45	1.15	1.25	1.45	1.87	1.24	0.29	21
	2	0.75	0.90	1.17	1.47	1.54	1.16	0.31	12
DC	3	0.25	0.55	0.73	0.84	0.95	0.68	0.20	14
	4	0.30	0.46	0.60	0.66	0.70	0.56	0.13	8
	5	1.81	1.94	2.13	2.25	2.48	2.12	0.23	7
	6	1.84	2.38	2.77	2.93	3.39	2.67	0.44	10
	7	2.88	2.93	3.07	3.45	3.84	3.20	0.33	10
M	8	1.86	1.99	2.20	2.33	2.66	2.20	0.27	6
	9	1.11	1.92	2.09	2.24	2.47	1.98	0.40	15
BC	10	1.53	1.85	2.01	2.27	2.79	2.08	0.32	16
	11	0.33	0.83	0.99	1.22	1.41	1.01	0.26	19
	12	0.74	0.97	1.12	1.20	1.34	1.07	0.18	10
	13	-	-	-	-	-	-	-	-
	14	0.31	0.43	0.62	0.85	1.24	0.67	0.28	11

Table 2.5. K_{IC}* from Fracturing Loads During Slow Displacement DT-LR Tests

Site	ID	Peak Stress Intensity, Slow Loading (MPa m^1/2)							
		Min	Q1	Med	Q3	Max	Mean ± std dev		n
DM	1	1.02	1.11	1.16	1.20	1.31	1.16	0.08	26
	2	1.16	1.31	1.46	1.57	2.05	1.46	0.21	16
DC	3	0.22	0.53	0.73	0.90	1.08	0.70	0.27	12
	4	-	-	-	-	-	-	-	-
	5	1.04	1.35	1.85	2.01	2.30	1.77	0.39	20
	6	2.60	2.90	3.00	3.08	3.49	3.01	0.18	25
	7	1.82	2.79	2.93	3.10	3.58	2.94	0.36	21
M	8	1.74	1.90	1.99	2.12	2.43	2.01	0.15	36
	9	1.17	1.56	1.84	1.96	2.69	1.79	0.32	73
BC	10	1.61	1.81	1.83	2.03	3.07	2.02	0.41	16
	11	0.96	1.09	1.17	1.30	1.45	1.18	0.15	24
	12	1.23	1.35	1.47	1.56	1.71	1.46	0.16	6
	13	0.35	0.48	0.51	0.58	0.74	0.53	0.13	13
	14	0.44	0.54	0.62	0.70	0.79	0.62	0.11	18

Table 2.6. Subcritical Fracture Growth Index (SCI) from DT-LR Tests

Site	ID	SCI							
		Min	Q1	Med	Q3	Max	Mean ± std dev		n
DM	1	15.2	48.1	60.2	68.9	111.6	59.8	21.9	27
	2	67.6	77.0	89.5	109.1	122.3	92.9	19.9	6
DC	3	36.8	37.0	50.0	50.9	83.3	51.6	17.0	5
	4	-	-	-	-	-	-	-	-
	5	31.8	64.4	74.7	85.3	141.7	74.3	24.8	18
	6	54.9	107.0	123.7	145.4	182.9	123.7	31.9	24
	7	72.4	114.0	142.9	175.4	202.1	144.7	38.5	15
M	8	39.7	68.0	89.4	110.7	166.5	92.3	31.0	31
	9	35.8	68.0	98.2	111.5	172.2	94.4	30.2	53
BC	10	34.9	50.5	58.7	65.2	83.8	59.0	13.4	10
	11	43.1	60.9	74.2	89.6	109.4	74.9	18.7	16
	12	29.1	51.3	64.1	71.2	81.5	60.3	16.8	8
	13	36.5	63.1	70.0	93.0	107.0	75.0	19.1	13
	14	76.0	76.0	76.0	76.0	76.0	76.0	-	1

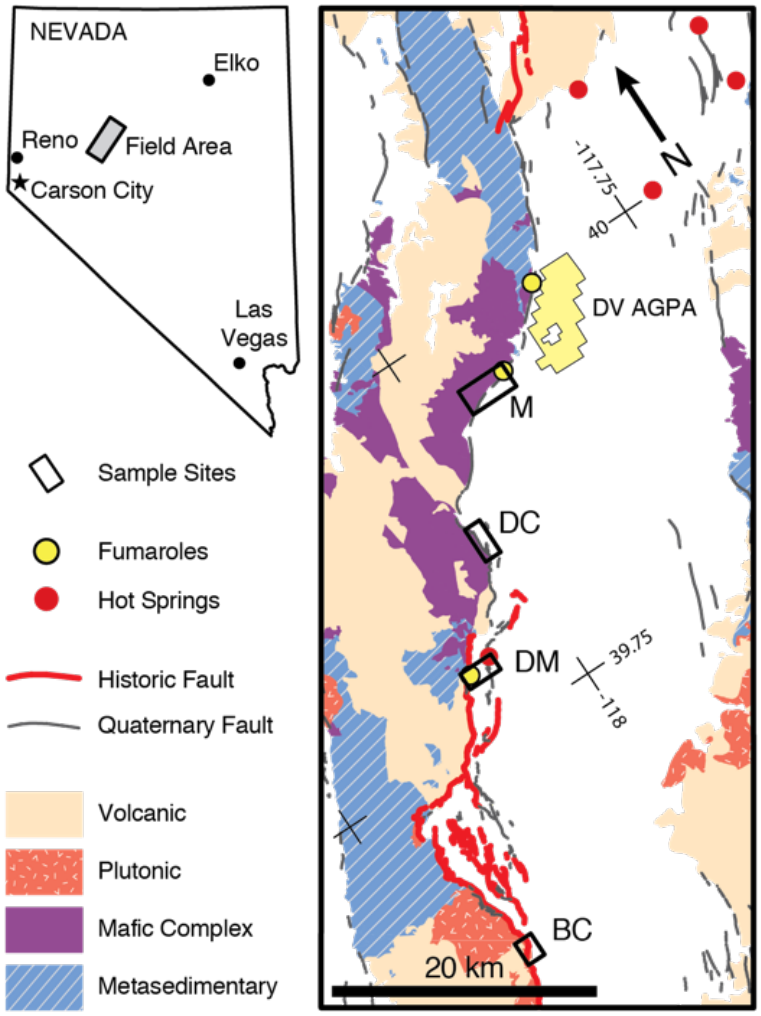

Figure 2.1. Field sites in the Dixie Valley – Stillwater fault zone include the Mirrors (M), Dixie Comstock epithermal gold deposit (DC), Dixie Meadows fumaroles (DM), and the Box Canyons (BC). Active hydrothermal features include the Dixie Valley geothermal production area (NREL, 2016), hot springs, and fumaroles (Berry et al., 1980). Quaternary faults after USGS and NBMG (2010). Geology modified from Crafford (2007).

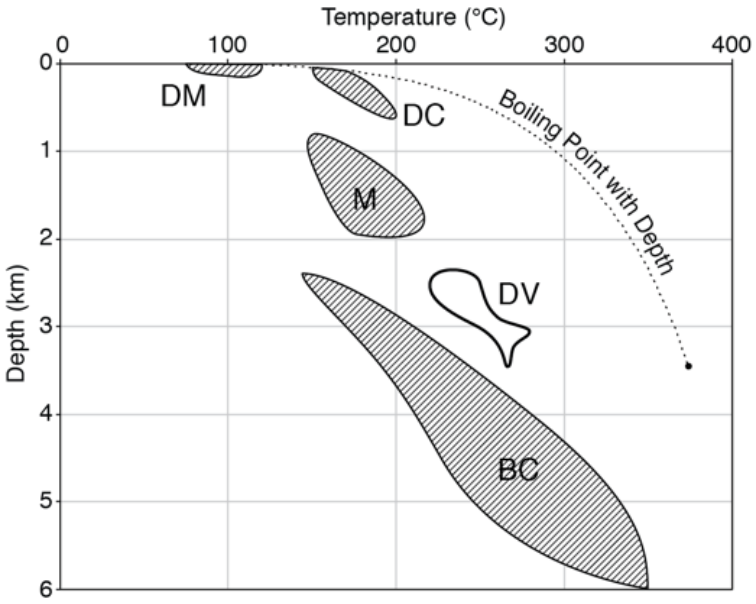

Figure 2.2. Temperature-depth conditions during development of dominant alteration assemblages. DM = Dixie Meadows, DC = Dixie Comstock, M = Mirrors, BC = Box Canyons. Temperature-depth constraints for each sample site are discussed in the text. Average temperature in the producing Dixie Valley geothermal reservoir (DV) is ~248 °C at 2.5-3 km, with recorded temperatures as high as 285 °C (Blackwell et al., 2007). Boiling point with depth for pure water from Haas (1971).

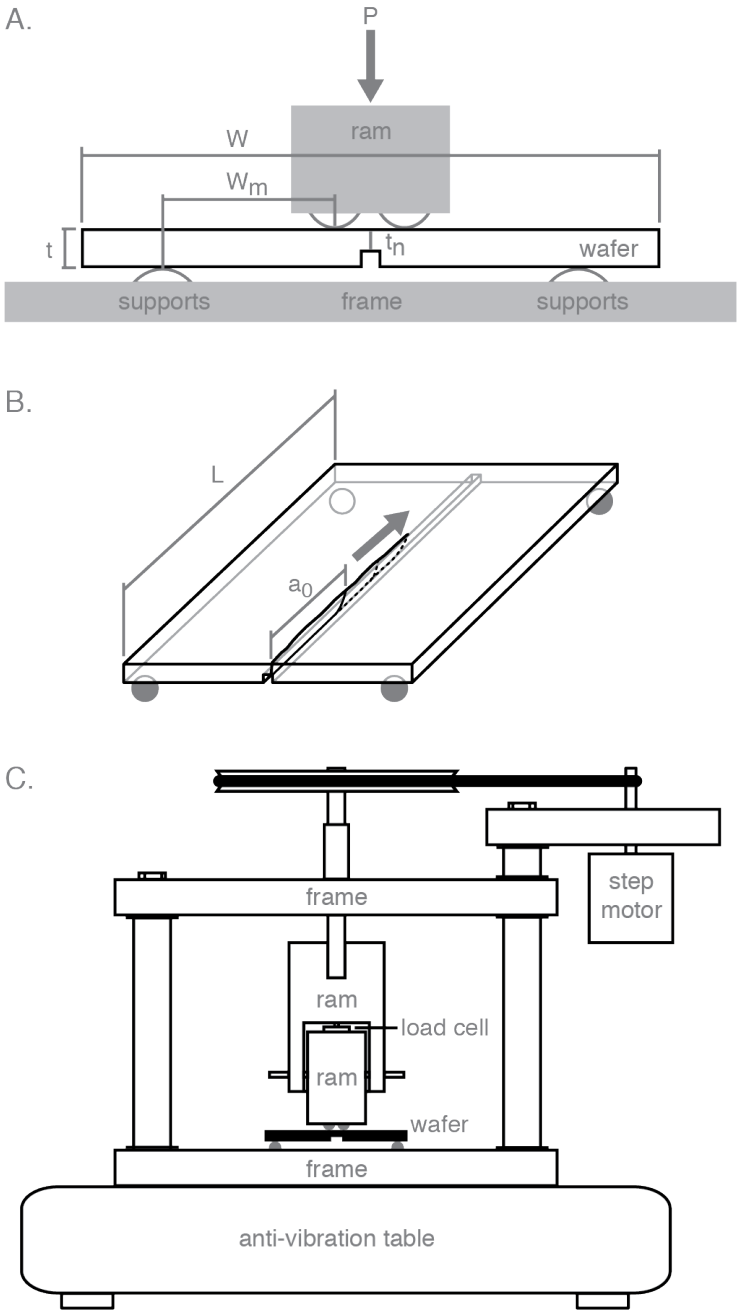

Figure 2.3. Double-torsion specimen schematic and test geometry. A) Cross-section of double torsion specimen, with load and support points (semicircles) and dimensions: W = width, W_m = moment arm, t = thickness, t_n = reduced thickness. B) Oblique view of specimen showing pre-fracture length (a_0) and subsequent fracture growth increments. Arrow indicates direction of fracture propagation. C) Double torsion apparatus.

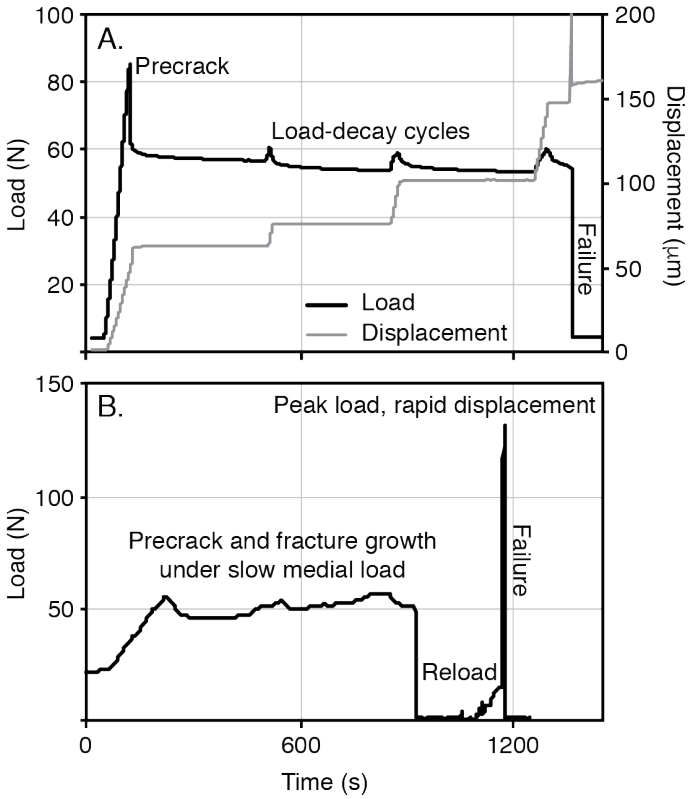

Figure 2.4. Load and displacement patterns from DT tests. A) DT-LR tests used to derive SCI and K_{IC}* under slow loading. SCI is derived from load-decay cycles at constant displacement. K_{IC}* is derived from local load maxima sustained before each load-decay cycle. B) DT tests used to derive K_{IC} from peak load during rapid loading to failure.

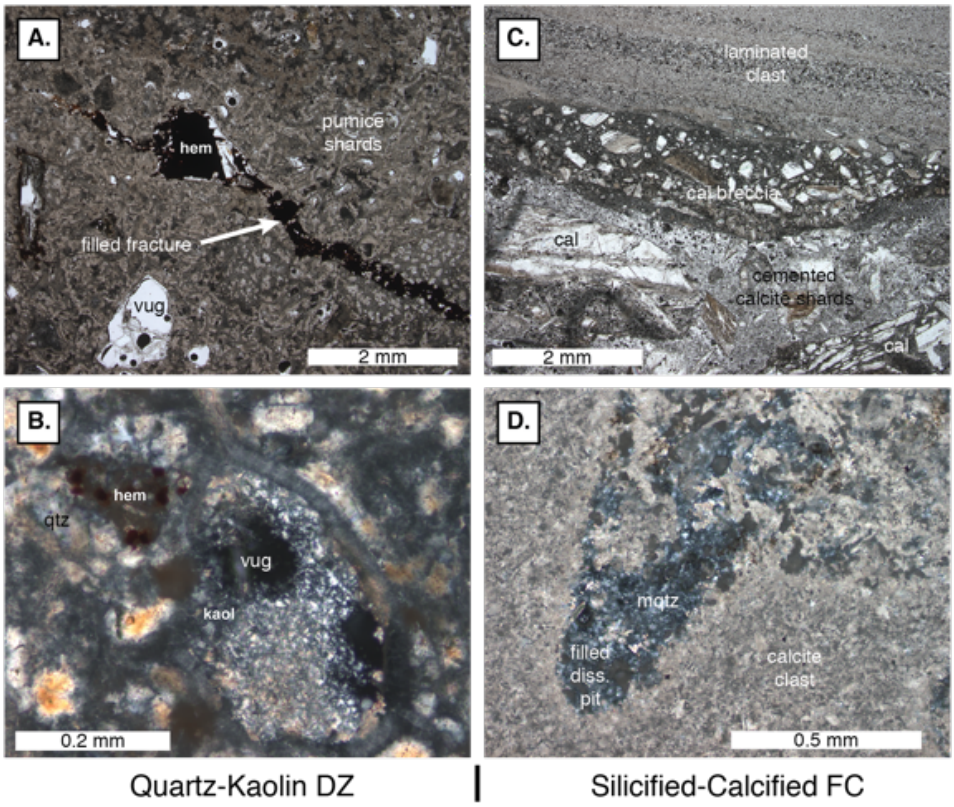

Figure 2.5. Photomicrographs of Dixie Meadows samples (1 and 2). Sample 1 (A, B) contains quartz (qtz), hematite (hem), kaolinite (kaol) alteration of Oligocene tuff in the damage zone at Dixie Meadows. Sample 2 (C, D) is a microquartz- (mqtz) cemented fault core breccia.

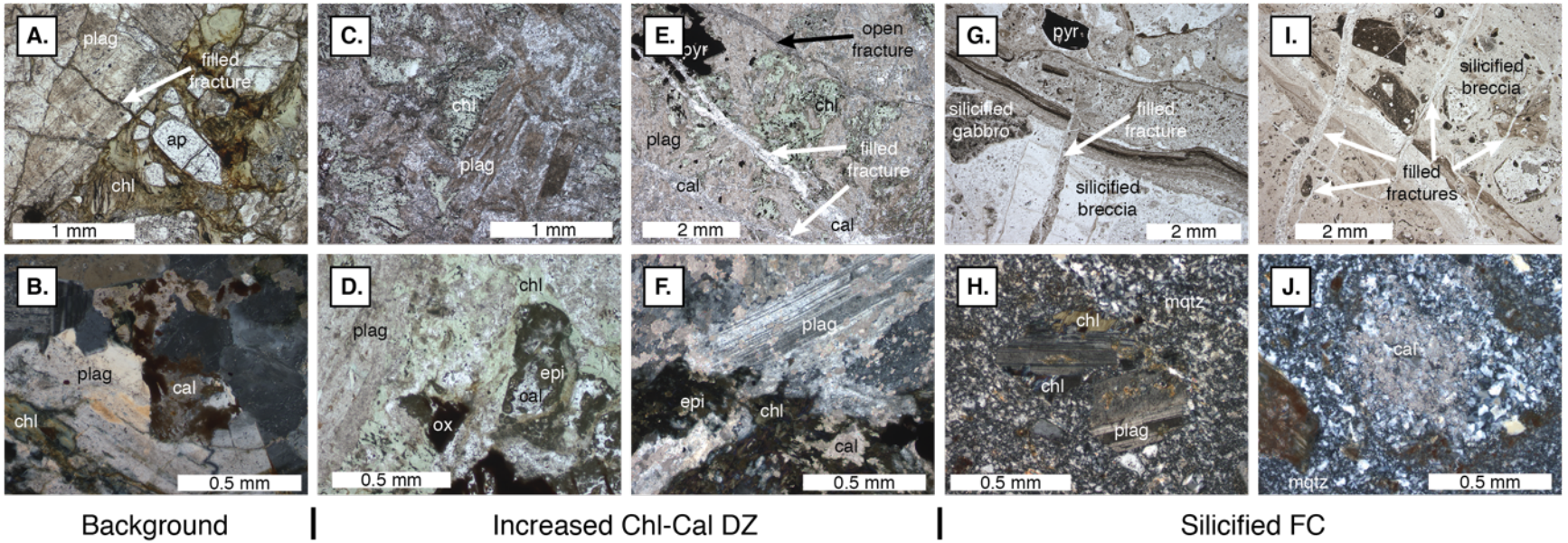

Figure 2.6. Photomicrographs of Dixie Comstock samples (3-7). Dixie Comstock samples show progressive alteration from background propylitic and Na-Ca altered gabbro through increase calcite-chlorite alteration and late silicification. Sample 3 (A, B) with chlorite (chl) and calcite (cal) after mafic minerals and Ca-rich plagioclase. Samples 4 (C, D) and 5 (E, F) record increasing chloritization and calcification of plagioclase and mafic minerals and calcite-filled fractures near the main deposit. G, H and I, J represent massive silicification and quartz-filled fractures with relict altered grains in fault core samples 6 and 7.

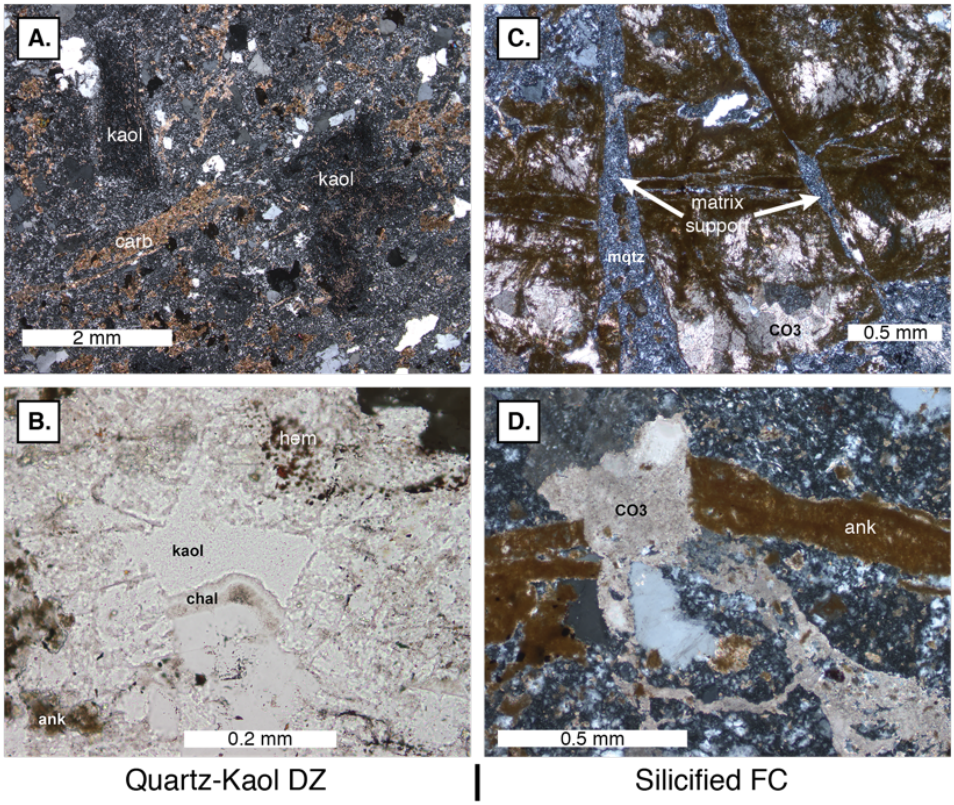

Figure 2.7. Photomicrographs of Mirrors samples (8 and 9). Sample 8 (A, B) records replacement of feldspars by kaolinite (kaol) and amphiboles by carbonate (ankerite, calcite) in the fault damage zone. Kaolinite + chalcedony (chal) indicates alteration continued <180 °C. Sample 9 (C, D) records multiple cycles of deformation and cementation by calcite, ankerite, and microquartz in the fault core.

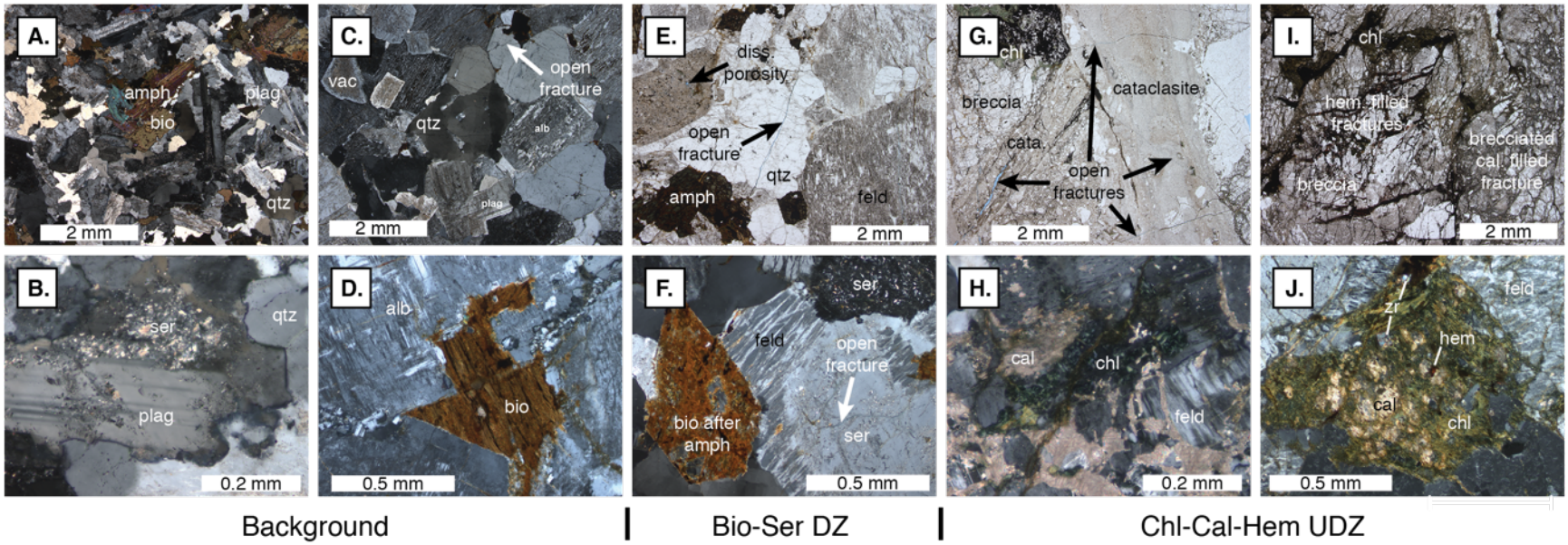

Figure 2.8. Photomicrographs from Box Canyon samples (10-14). Alteration in background granodiorite (sample 10; A, B) and granite (sample 11; C, D) includes minor sericitization (ser) and albitization (alb) of plagioclase (plag). Damage zone sample 12 (E, F) contains biotite (bio) after amphibole (amph), sericite in plagioclase. Samples 13 and 14 are obtained from the most altered area at the box canyons and include extensive replacement of plagioclase with calcite and chlorite, and calcite and hematite veins (G-J). Damage increases from isolated open fracture (C) to cataclastic bands (G) and brecciation or fragmentation of grains (I).

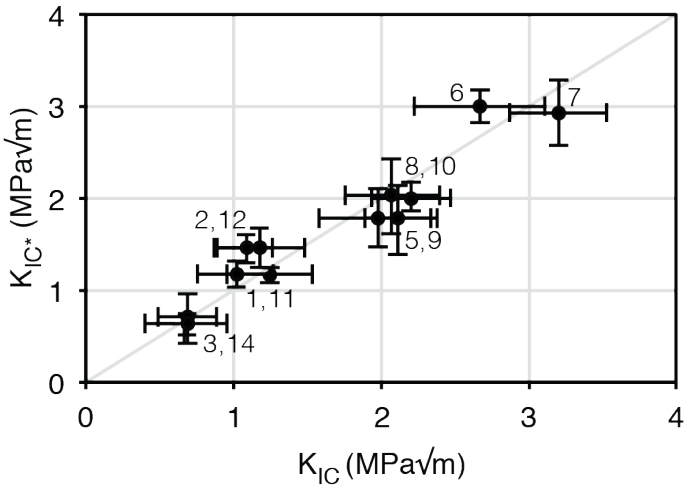

Figure 2.9. Relationship between K_{IC} and K_{IC}*. Mean K_{IC} and K_{IC}* from rapid and slow displacement tests, respectively, are within error of one another internally and fall along a 1:1 line as a group (Table 2.4, Table 2.5). Samples identified by numbers. Sample 13 was not tested with rapid loading and Figures 2.10-2.12 show K_{IC}* for this sample. Sample 4 was not tested with slow loading. Error bars are standard deviations of n samples.

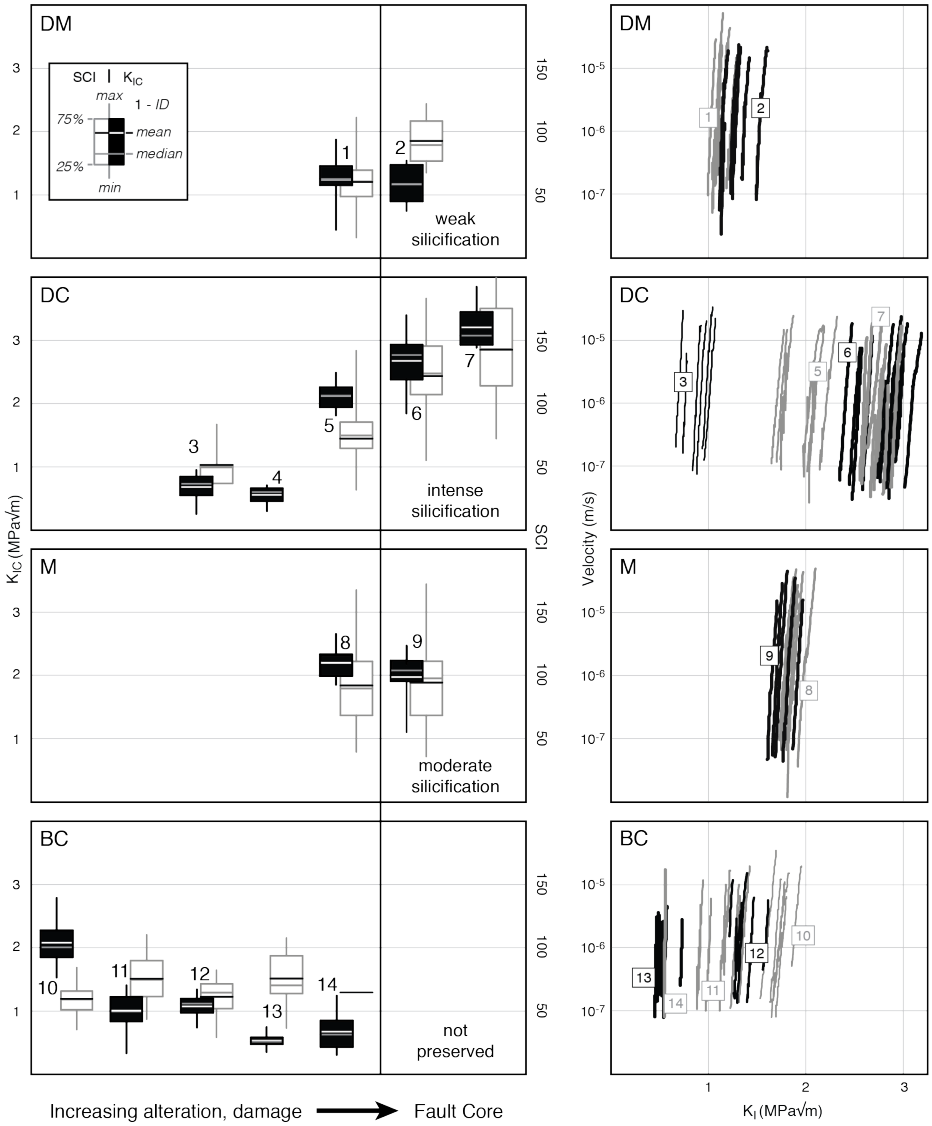

Figure 2.10. Structural setting, alteration, K_{IC}, SCI, and representative K-v curves for each site. Box plots for K_{IC} and SCI show the complete range of DT test results (Table 2.4, Table 2.6). Alteration increases from left to right at each site, with increasing alteration represented by heavier K-v curves. Numbers match sample IDs discussed in the text. K_{IC}* is plotted for Sample 13. Alteration and unhealed damage at the Box Canyons (BC) result in a decrease in toughness, and a subsequent shift left of the K-v curves. Healing by silicification (±calcite) at the other sites results in an increase in toughness and SCI values in and near the fault core.

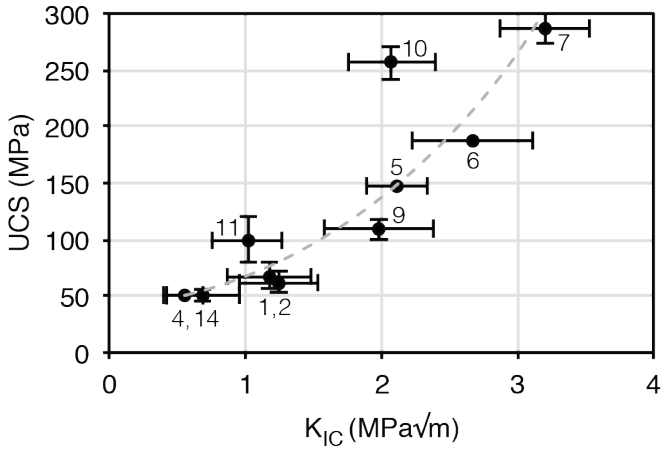

Figure 2.11. Fracture toughness and unconfined compressive strength. Positive correlation between mean K_{IC} and mean UCS suggests microfracture growth is an underlying failure mechanism in UCS tests. Samples identified by number. Errors bars show standard deviation of n samples.

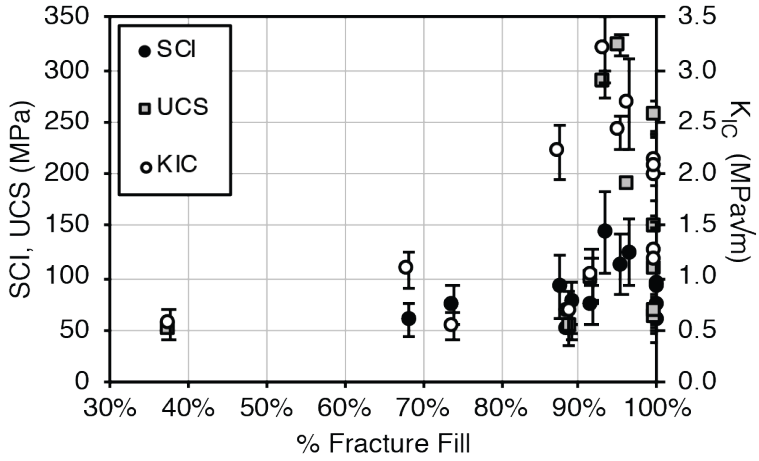

Figure 2.12. Mechanical properties and fracture fill. Abundant open microfractures results in mechanically weak samples. Cementation, indicated by reduction of remnant fracture porosity to <15%, results in substantial increases in K_{IC}, SCI, and UCS.

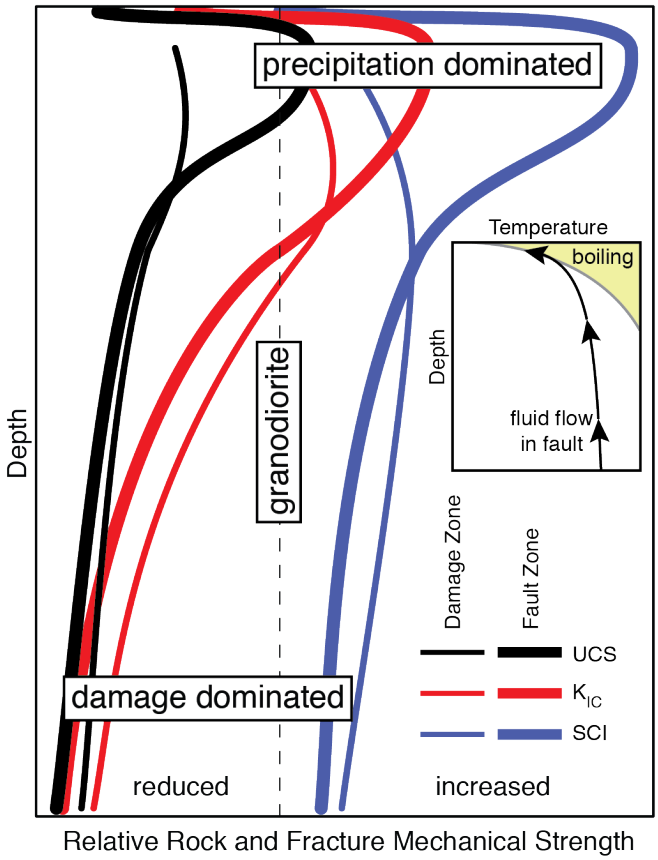

Figure 2.13. Schematic mechanical properties with depth for fault core and fault damage zone with advective, high temperature fluid flow. Measures of strength and resistance to fracture propagation (UCS, K_{IC}, SCI) are generally lower in the fault core than in the damage zone. In precipitation dominated hydrothermal regimes, cementation of the fault core by silicification (±calcification) increase rock strength relative to the less cemented damage zone. Increased dissolution in the near surface fumarole environment is associated with a relative loss of strength. Inset shows upward migration of fluid in fault interacting with boiling point with depth curve.

3. Experimental Investigation of Chemically Aided Fracture Growth in Silicified Fault Rocks[3]

ABSTRACT

Using double-torsion load relaxation tests, we evaluated the effect of chemical environment on fracture toughness and subcritical fracture growth index (SCI) in silicified fault rocks collected in the vicinity of the Dixie Valley, NV, geothermal system. Testing environments included: ambient air, deionized water, dilute HCl, NaOH, and NaCl solutions, and deionized water at elevated temperatures. We observed reductions in SCI in all aqueous environments, with >60% reduction in alkaline solutions. These results suggest that physiochemical conditions in hydrothermal systems may facilitate fracture growth, with chemically aided fracture growth and flow conduit formation competing with precipitation and sealing in reactive systems.

HIGHLIGHTS

1. Subcritical fracture growth in silicified rocks depends on chemical environment.
2. Aqueous conditions increase fracture velocity by up to 2 orders of magnitude.
3. Fracture velocity depends on dissolution rate at fracture tips.
4. Elevated temperature, pH, salinity promote fracture growth in silicified rocks.

KEYWORDS

fracture toughness, subcritical, hydrothermal, alteration, fault, Dixie Valley

3.1 INTRODUCTION

The location and lifecycle of hydrothermal systems are often considered through one of two lenses: either the mechanical properties or the chemical processes influencing

[3] Authors and affiliations: Owen A. Callahan and Peter Eichhubl, Bureau of Economic Geology, The University of Texas at Austin, Austin, TX; Jon E. Olson, Hildebrand Department of Petroleum and Geosystems Engineering, The University of Texas at Austin, Austin, TX; Nicholas C. Davatzes, Earth and Environmental Sciences, Temple University, Philadelphia, PA

permeability. Fault geometry commonly exerts a first-order control on hydrothermal flow, with thermal anomalies and mineral deposits commonly localized in dilational fault jogs, stepovers, intersections, and tips (Curewitz and Karson, 1997; Cox et al., 2001; Faulds et al., 2006; Anderson and Fairley, 2008; Eichhubl et al., 2009; Micklethwaite, 2009). However, the evolution of permeability in hydrothermal systems is modified by enhanced dissolution and precipitation, and associated mineralogical and textural changes, encountered in and around hydrothermal cells (Facca and Tonani, 1967; Browne, 1978; Nishimoto and Yoshida, 2010; Dempsey et al., 2012). There is growing interest in the interaction between these two paradigms, with the observation that chemical alteration changes the mechanical behavior of the host rock (e.g. Davatzes and Hickman (2010); Wyering et al. (2014)) and that mechanical processes may enhance chemical reactions (Gratier and Gueydan, 2006; Gratier, 2011).

Chemical-mechanical interactions may also manifest as changing rock strength and elastic properties in response to different fluid environments. Deformation in the presence of water has a well-known weakening effect, particularly during slow loading and under sustained loads (Hadizadeh and Law, 1991; Lockner, 1993; Baud et al., 2000; Wong et al., 2016). In hydrothermal systems, which commonly contain spatially zoned fluid conditions (Henley and Ellis, 1983), the influence of fluid composition on deformation, and thus permeability, represents a possible feedback mechanism between chemical and mechanical process and fluid flow. However, little is known about the impact that chemical environment may have on the mechanical properties governing fracture growth in hydrothermally altered rocks commonly encountered in hydrothermal systems.

The occurrence of opening-mode fractures in fault zones and fracture networks, and the evolution of these flow systems from single fractures to complex interconnected networks by fracture propagation, reactivation, and coalescence provides a fundamental control on the permeability evolution of fault-controlled hydrothermal and epithermal systems (Wong and Zhu, 1999; Bourne and Willemse, 2001; Crider and Peacock, 2004; Davatzes et al., 2005; Blenkinsop, 2008; Crider, 2015). Furthermore, fracture mechanics testing isolates the fundamental processes of fracture initiation and growth in

hydrothermally altered rock and underlies more complex processes of fracture interaction and coalescence that lead to shear failure in triaxial experiments.

Linear elastic fracture mechanics describes the stress intensity at the tip of an opening-mode (mode-I) fracture, K_I, as a function of remote stress, σ_r, the radius of the fracture, r, and a fracture and loading geometry constant, Y (Brown and Strawley, 1966):

$$K_I = \sigma_r Y \sqrt{r} \qquad \text{Eq. 2.1}$$

The maximum K_I that a material can sustain before critical failure and mechanical fracture propagation is known as fracture toughness, K_{IC}.

Fracture growth may occur below the critical threshold due to chemically-aided failure of the loaded and stretched bonds at the fracture tip. The relationship between stress intensity at the fracture tip, physiochemical condition, and the velocity, V, of subcritical fracture growth is (Charles, 1958; Evans, 1972; Wiederhorn, 1974; Atkinson, 1979a):

$$V = V_0' exp \frac{-\Delta H}{RT} K_I^{SCI} \qquad \text{Eq. 3.2}$$

where V_0' is a pre-exponential constant, $-\Delta H$ is the activation enthalpy, R is the gas constant, T is the absolute temperature, and SCI is the subcritical crack growth or stress corrosion index. SCI describes the slope of the stress intensity – velocity (K-V) relationship when fracture growth is governed by chemical reaction rates (Figure 3.1) (Wiederhorn and Johnson, 1973), before fracture propagation velocity outpaces diffusion of reactive species to the fracture tip. Lower values of SCI imply fracture propagation at lower stress intensities, or at greater velocity at the same stress intensity. Furthermore, changes in SCI may manifest as changes in fracture patterns, with lower SCI resulting in increased fracture abundance and reduced spacing and higher SCI leading to fracture clusters (Olson, 1993, 2004). Because subcritical fracture growth is sensitive to physiochemical environment and occurs at lower stress intensities than critical fracture failure, subcritical fracture growth may be an important but generally underappreciated mechanism of chemical-mechanical coupling in hydrothermal systems.

From Equation 3.2, a change in temperature or chemical fluid composition that reduces activation enthalpy promotes faster fracture propagation. However, fracture

mechanics testing of various rocks has shown a complex dependence of this behavior on physio-chemical environment, with mineralogic composition and rock texture influencing the response in ways that are not always predictable *a priori* (Atkinson, 1979a; Waza et al., 1980; Meredith and Atkinson, 1985; Karfakis and Akram, 1993; Funatsu et al., 2004; Feng and Ding, 2007; Feng et al., 2009; Kumar, 2010; Nara et al., 2012; Rostom et al., 2012; Brantut et al., 2013; Nara et al., 2013; Nara et al., 2014; Chen et al., 2017; Chen et al., submitted). Mechanisms invoked to explain observed effects of chemical-mechanical interactions include changes in elastic parameters of the sample in the process zone of the propagating fracture (Balme et al., 2004; Funatsu et al., 2004; Nasseri et al., 2009; Erarslan, 2016), localized stress-enhanced chemical corrosion (Anderson and Grew, 1977; Atkinson, 1979a; Atkinson and Meredith, 1981; Karfakis and Akram, 1993), fracture tip blunting or sharpening (Rostom et al., 2012), and cohesive or repulsive forces between the fracture walls (Karfakis and Akram, 1993; Rostom et al., 2012). These mechanisms are not mutually exclusive and may all be important in chemically reactive subsurface environments. Although there is substantial work describing fracture mechanical properties in sedimentary rocks of particular interest to oil and gas exploration and CO_2 sequestration (Schmidt, 1975; Atkinson, 1979b; Holder et al., 2001; Rijken, 2005; Nara et al., 2014; Chandler et al., 2016; Chen et al., 2017; Major et al., 2018) the impact of chemical environment on fracture growth in hydrothermally altered rocks encountered in and around high temperature hydrothermal systems has not been evaluated in detail.

Fracture mechanical properties in hydrothermal systems may be influenced 1) by hydrothermal alteration changing rock composition and texture, and thus the rock mechanical properties, and 2) by spatial and temporal variation in chemical environment and chemically-aided deformation across hydrothermal systems. Here we focus on the latter scenario, by measuring fracture mechanical properties of silicified fault rocks in different physiochemical conditions. We used double torsion load relaxation (DT-LR) tests to quantify the peak stress intensity (K_{IC*}), a proxy for K_{IC}, and SCI in silicified rocks in different chemical environments. Samples were collected from the Dixie Comstock epithermal deposit, Dixie Valley, Nevada, USA (Figure 3.2). Testing environments

included room temperature ambient air conditions, room temperature aqueous conditions, including deionized (DI) water, hydrochloric acid, sodium hydroxide, sodium chloride, and DI water at elevated temperature. We discuss the impacts that chemical environments have on fracture growth and possible implications for feedback between fluid composition, fracture growth, and fluid flow in hydrothermal systems.

3.2 SAMPLE MATERIALS

We tested multiple rock and fracture mechanics specimens from three samples of silicified fault rock (052815-4b, 061114-4b, and 052815-2, herein Samples 1, 2, and 3) from the Dixie Comstock epithermal gold deposit in Dixie Valley, Nevada (Figure 3.2, Figure 3.3). Several temporally distinct episodes of alteration are preserved in the Dixie Comstock area, including early widespread sodic and calcic alteration of the Jurassic Humboldt Igneous Complex (Dilek and Moores, 1995), and aureoles of quartz, albite, sericite, kaolinite, and iron oxide above and around apophyses of Cretaceous granite (Vikre, 1993). Alteration in the mine area is dominated by silicification along the range front fault (Figure 3.3), with some silicified fault breccia exceeding 2 m in thickness. Intense silicification extends ~300 m north and south of the mine workings, with quartz veins and minor silicification of fault breccia occurring ~1.5 km along strike and >600 m down dip (R. Zuza, personal communication).

Samples were obtained from the silicified fault core and represent the most intense phase of deformation, alteration, and silicification. Mineral composition, texture, and paragenesis were characterized by powder X-ray diffractometry (XRD) and transmitted-light thin section petrography. Porosity was calculated by point counting standard petrographic thin sections with blue-dyed epoxy at 120X magnification. Total points counted per thin section ranged from 381 to 555. Unconfined compressive strength (UCS) and static elastic parameters were measured with uniaxial compressive strength tests using a GCTS rock mechanics system.

All samples are dominated by fine-grained, intergrown microquartz and euhedral quartz-lined fractures, with minor chlorite, feldspar and plagioclase, calcite, and trace

sericite, sulfides, and oxides (Figure 3.4, Table 3.1). Calcite occurs as late fracture fill in the most silicified sample, and as broken lathes in the least silicified sample. In all samples, porosity is <1.6% and heterogeneous, hosted by quartz lined vugs and partially quartz- or calcite-cemented fractures (Table 3.2). All samples contain evidence for multiple generations of deformation and quartz cementation in the form of entrained and recrystallized silicified clasts and cross-cutting fractures. However, silicification in these samples appears to have reduced mechanical anisotropy at the scale of rock and fracture mechanics specimens. Mean UCS and Young's modulus (E) of samples are high, up to 301.3 MPa and 62.8 GPa, respectively, and Poisson's ratio is between 0.11-0.18 (Table 3.3).

3.3 DOUBLE TORSION LOAD RELAXATION TESTING

3.3.1 Double Torsion Load Relaxation Method

We used the DT-LR fracture mechanics testing configuration to measure K_I, K_{IC}*, and SCI of 3 samples of silicified material in different chemical environments. The DT testing apparatus consists of a base plate, ball bearings that function as specimen supports, a loading ram with internal force sensor, and a linear variable displacement transducer to record displacement (Figure 3.5). K_I is calculated from DT tests using the equation from Williams and Evans (1973):

$$K_I = PW_m\sqrt{\frac{3(1+\nu)}{\varphi W t_n t^3}} \qquad \text{Eq. 3.3}$$

where P is load, W_m is moment arm, W is width of a pre-fractured specimen of sample material, t is specimen thickness, and t_n is the reduced thickness along the axial groove. Poisson's ratio, ν, was obtained from UCS tests. The geometric correction factor, ψ, is based on individual specimen geometry and is derived from Fuller (1979):

$$\psi = 1 - 0.6302\frac{2t}{W} + 1.2\frac{2t}{W}e^{\left(\frac{-\pi W}{2t}\right)} \qquad \text{Eq. 3.4}$$

Specimen thickness (t), width (W), and length (L) dimensions were approximately 1.8 mm x 30 mm x 75 mm, respectively (Figure 3.5), meeting dimensional requirements of ~24t<2W<L (Nara and Kaneko, 2005). Absolute specimen dimensions were similar to

Atkinson (1979a), Sano and Kudo (1992), and Chen et al. (2017) and were influenced by sample size and load cell capacity (Appendix G). A 0.5 mm deep axial guide groove was cut into the base of each specimen. Specimens were placed in the DT apparatus with the axial guide groove facing down (Evans, 1972; Pletka et al., 1979) and loaded from above (Figure 3.5). A starting fracture ("pre-fracture") was introduced into the sample using the DT apparatus under ambient conditions at low displacement rates (<1 μm/s) until a distinct load drop indicated the formation of an edge-crack. DT-LR tests were conducted by loading the pre-fractured specimen at a displacement rate between 1-2 μm/s until fracture propagation was indicated by a rapid drop in supported load. Displacement was stopped, and the load allowed to decay for ~10 minutes. Load-cycles were repeated until the fracture propagated across the full length of the specimen. Load and displacement were recorded at 5 Hz.

Fracture toughness (K_{IC}) is calculated from peak load sustained by pre-fractured specimens under rapid loading conditions. Low displacement rates used in our DT-LR tests allowed for controlled fracturing and multiple load-decay cycles per specimen, improving the overall number of measurements without additional material expense. However, low displacement rates may underestimate intrinsic fracture toughness in some materials (see discussion in Atkinson and Meredith (1987)). We find no significant difference between peak load sustained under rapid vs slow displacement conditions in our tests and consider stress intensity during peak loads in slow displacement tests, K_{IC}*, a reasonable proxy for K_{IC}. We include the unique nomenclature for this measurement throughout.

Fracture propagation velocity, V, was calculated from the load relaxation curve after Evans (1972):

$$V = -\phi \left(\frac{a_0 P_i}{P^2}\right) \frac{dP}{d\mathrm{T}} \qquad \text{Eq. 3.5}$$

where a_0 is fracture length at the start of each load-decay cycle, P_i is initial load, and T is time. We used 0.2 for the fracture front geometry correction factor, ϕ (Chen et al., 2017). Initial fracture length for the first load-decay cycles was measured along the induced pre-fracture, with later cycles using $a_n = a_0 + (n-1)*12.7$ mm, a nominal value accounting for a

typical number of fracture growth increments and L. Variation of a_0 does not affect the calculation of SCI, and has limited impact on calculated fracture front velocity (Chen et al., 2017). SCI was calculated from stress intensity – velocity (K-V) plots using smoothing and fitting functions using an in house LabView script based in part on derivations described in Holder et al. (2001).

3.3.2 Testing Conditions

We tested specimens in room temperature ambient air conditions, in room temperature aqueous conditions, including DI water (pH~6.3-7.5), 0.001 M HCl (pH=3), 0.01 M NaOH (pH=12), 0.1 wt% NaCl, and in DI water at elevated temperatures (~60-65 °C). Aqueous conditions were selected to identify trends resulting from changes in fluid environment and do not represent specific hydrothermal fluids. The range of fluid pH is similar to that used in double torsion tests of synthetic quartz crystal by Atkinson and Meredith (1981), and designed to produce observable changes in short duration (~10 minute) load-decay experiments. Conditions during elevated temperature tests were limited by low signal to noise ratios at temperatures above ~70 °C. Relative humidity during ambient tests was not controlled and typically varied from 63-79%. Aqueous conditions were controlled by placing the DT apparatus in a stainless-steel basin filled with 3.5 liters of solution so that the specimen was submerged ~7 mm below the surface (Figure 3.5). Temperature was recorded with two thermocouples. Elevated temperature tests were conducted with the basin and DT apparatus on a hotplate. To avoid thermal gradients in the sample, the solution containing the sample was heated from ambient to ~60-65 °C at a rate of <1 °C/min, consistent with the rate of temperature change reported in Meredith and Atkinson (1985) and Balme et al. (2004). Mean temperature during individual specimen tests varied by less than 0.3° C. During elevated temperature tests, a polycarbonate loading ram was used to reduce noise from thermal fluctuations. For all tests conducted in aqueous solution, specimens were first vacuum dried for >48 hrs then pre-fractured and immersed in DI water for >1 hour before testing to avoid transient wetting effects. Duration and conditions for presoaking vary by author; some authors do not explicitly specify the

duration of immersion (Atkinson, 1979a; Atkinson and Meredith, 1981; Karfakis and Akram, 1993), and others report samples were stored in testing fluids for hours to days (Waza et al., 1980; Nara and Kaneko, 2005; Nara et al., 2012; Rostom et al., 2012; Nara et al., 2014; Hao et al., 2015). Because specimens are thin (<2 mm) and the pre-fractures full thickness, we are confident that fluids had rapid access to the fracture tip; we found no consistent difference between dry samples tested immediately upon immersion and those soaked in DI water for >24 hours prior to testing.

3.4 Experimental Results

3.4.1 SCI and K_{IC}* Values in Different Testing Environments

We tested 3 sample of silicified fault rock from the Dixie Comstock epithermal deposit in different chemical environments. Five to twelve specimens per sample were tested in each chemical environment, with the total number of valid K_{IC}* and SCI measurements in each environment between 7-28 and 5-24, respectively. Tests that resulted in fractures that propagated out of the axial guide groove, exceeded load cell capacity, or failed on pre-fracturing were not included. We observed high K_{IC}* and SCI in silicified fault rock in ambient air conditions. Mean K_{IC}* in ambient conditions is 2.40 to 3.01 MPa $\sqrt{m}$, and mean SCI in ambient conditions is 113.3 to 142.2 (Table 3.4, Table 3.5).

Testing environment had limited impact on K_{IC}* in these samples. Mean K_{IC}* is 2.13 – 2.73 MPa $\sqrt{m}$ for all samples in aqueous conditions (Figure 3.6). The standard deviations of K_{IC}* overlap for the same sample tested in different environments, except sample 2, where K_{IC}* in NaOH tests are 29% lower than in ambient conditions. The largest relative standard deviations for K_{IC}* and SCI (22% and 60%, respectively) for any environment were observed in sample 2, suggesting inter-specimen heterogeneity in this sample may have negatively impacted the results.

SCI was more sensitive to chemical environment. Mean SCI was reduced in aqueous environments compared to ambient conditions for all samples, with the degree of reduction dependent on the environmental conditions (Figure 3.7). Reduction in SCI below ambient conditions was most pronounced in NaOH environments, where we saw a 46-66%

reduction below mean ambient SCI (Figure 3.7). P values from t-tests between SCI in ambient and NaOH conditions are <<0.05 for all samples. In sample 1, SCI in NaOH was also significantly lower than DI and HCl tests, but not compared to NaCl test. In sample 3, SCI from NaOH tests was significantly lower than DI conditions, but not significantly different from HCl or NaCl conditions. Mean SCI values at elevated temperature were comparable to SCI in NaOH and NaCl conditions (Figure 3.7). Despite some mineralogical, textural, and mechanical differences between samples (Table 3.1, Table 3.2, Table 3.3), there is little difference in SCI between samples tested in the same environment; SCI measured in ambient, NaCl, HCl, and NaOH conditions are all statistically similar between samples.

3.4.2 K-V Curves and Fracture Propagation Velocity

Calculated fracture propagation velocities are between 10^{-8} and 10^{-4} m/s (Figure 3.8), which generally overlap with other subcritical fracture growth velocities for rocks derived from DT tests (Atkinson, 1979a; Nara et al., 2014; Chen et al., 2017). Due to the high SCI in these samples, individual fracture growth curves occur across a narrow range of high mode-I stress intensity (K_I). K-V curves for different environments overlap, reflecting scatter in K_{IC}* and limited impact of chemical environment on toughness. However, in samples 2 and 3 a clear reduction in stress intensity in K-V curves from aqueous tests indicates subcritical fracture propagation at lower K_I compared to ambient conditions. K-V curves normalized to peak velocity and stress intensity highlight the reduction in SCI (slope) in aqueous conditions, particularly NaOH, NaCl, and at elevate temperature (Figure 3.8). We attribute noisy K-V curves from elevated temperature tests to thermal transients affecting the DT apparatus and/or load cell, even with mean temperature fluctuation during each decay period <0.3 °C.

3.5 DISCUSSION

3.5.1 Physiochemical Effects and Mechanisms

3.5.1.1 Water vs. Ambient Air Conditions

The water-weakening effect that we observe as reduced SCI is also described for glass and ceramics (Freiman et al., 2009), single synthetic quartz crystals (Atkinson, 1979a), and igneous, metamorphic, and sedimentary rocks (Nara et al., 2013; Nara et al., 2014; Chen et al., 2017; Nara et al., 2017a). Chemical-mechanical interaction at the fracture tip is commonly invoked to describe the mechanics of the water-weakening effect in silicates (Waza et al., 1980; Michalske and Freiman, 1982). In this model, mechanically stressed Si-O bonds enable penetration of H_2O molecules. The polar water molecular bonds with the Si-O-Si molecule, producing a weaker, short-lived OH bond that enables fracture propagation at lower stress intensity. Any condition that accelerates penetration of water molecules into the fracture tip region will favor increased subcritical growth. Particularly sensitive materials may exhibit a water-weakening effect with changing relative humidity (Wiederhorn, 1967; Nara et al., 2012). We did not control relative humidity in our experiments, which may have contributed to scatter in SCI in ambient conditions. However, the influence of changing humidity on SCI is more pronounced in clay-rich material (Nara et al., 2012).

3.5.1.2 Effect of Changing pH

The 60% reduction in SCI we observed in silicified samples in strong base, conditions under which quartz is more soluble, is consistent with other reported reductions in SCI in environments that enhance solubility or dissolution rate of material at the fracture tip. Reduced SCI in environments that increased solubility is observed at high pH in glass (Wiederhorn and Johnson, 1973), at high pH in single synthetic quartz crystals and silicate rocks (Atkinson and Meredith, 1981), and at low pH in carbonate-rich shales (Chen et al., submitted), although there are exceptions. Rostom et al. (2012) described an increase in toughness of calcite in low pH conditions, conditions under which calcite is more soluble, which they partially attribute to fracture tip blunting. In silicates, and in our samples,

fracture growth is generally promoted in high pH conditions, due to the increased availability of OH^- facilitating the breaking of Si-O-Si bonds (Atkinson and Meredith, 1981; Karfakis and Akram, 1993). Although pH=12 is not representative of subsurface conditions, our intent was to observe effects over geologically short timescales. Weak bases are encountered in hydrothermal systems with chloride and chloride-bicarbonate fluids (Henley et al., 1984; Berger and Bethke, 1985). The effects we observe are expected to be more pronounced in more soluble phases of silica (e.g. amorphous silica or chalcedony (Fournier, 1985)).

SCI in our silicified samples in acidic conditions is statistically indistinguishable from DI water tests, whereas Atkinson and Meredith (1981) reported an increase in SCI in acidic environments relative to DI water for single synthetic quartz crystals. The difference between single synthetic quartz crystals and the behavior of the aggregate samples we tested may arise from the presence of 2-4 wt% calcite, which would have become more soluble at lower pH. Acidic conditions with pH <3 are encountered in hydrothermal systems, particularly in shallow, fumarole, acid-sulfate alteration environments (Berger and Bethke, 1985; Hedenquist and Henley, 1985), settings commonly associated with vuggy silica deposits, residual material that has not dissolved in acidic conditions.

3.5.1.3 Effect of Increased Salinity

The effect of solution salinity on fracture propagation velocity in rocks varies widely. Clay-rich materials and some carbonates show non-linear relationships between toughness, SCI, and salinity, with both the concentration and type of cation influencing results (Rostom et al., 2012; Nara et al., 2014; Chen et al., submitted). Rostom et al. (2012) related increases in SCI in calcite at salt concentration below ~1 M NaCl to enhanced calcite solubility, whereas Chen et al. (submitted) and Nara et al. (2014) both inferred that observed toughening in salt solutions was related to reduced clay-swelling ahead of the fracture tip.

In our samples, dilute NaCl concentrations resulted in a reduction in SCI compared to DI water. We attribute this response to increased dissolution rates in silica with increase

NaCl concentration at intermediate to elevated pH, as predicted by Dove (1995) for pure quartz. The behavior of the silicified material is best explained by the dissolution kinetics of the dominant mineral species in these samples, with an additive influence of minor components on behavior in different environments.

3.5.1.4 Effect of Increased Temperature

Temperature effects on K_{IC} and SCI are typically attributed to 1) increased microstructural complexity due to damage caused by differential thermal expansion and cracking in test environments 2) increased activity of reactive agents, and 3) faster reaction kinetics at elevated temperature. The impact on K_{IC} from increasing microstructural complexity by thermal treatments is commonly non-linear; Meredith and Atkinson (1985), Balme et al. (2004), and Nasseri et al. (2009) all reported initial toughening with increased temperature of thermally treated samples and then a decrease in material strength and fracture resistance. Initial toughening is attributed to the development of small misaligned cracks that arrest fracture propagation, and the decrease in strength is attributed to the growth and coalescence of experimentally induce microfractures throughout the sample. Physio-chemical effects at higher temperatures include toughening in response to dehydration of clays in oil baths > 125 °C (Funatsu et al., 2004), and increased dissolution rate at elevated temperature (Dove, 1995).

In our experiments, we observed a significant reduction in SCI and no significant change in K_{IC}* in DI water at elevated temperature up to 65 °C. The reduction in SCI at elevated temperatures that we observed in silicified rocks is similar to those reported by Nara et al. (2013) for granite. Because the total change in temperature was small and the rate of warming was slow, we do not think that observed temperature effects resulted from thermal cracking in our specimens. Instead, we attribute the reduction in SCI to increased solubility of silica at higher temperature and increased dissolution rate at the fracture tip. If solubility of silica is the dominant mechanism, the effect should be more pronounced in silicified rocks in hydrothermal systems up until the point of retrograde solubility ~340 °C (Fournier and Rowe, 1977).

3.5.1.5 Subcritical Fracture Growth Behavior in Silicified Fault Rocks

The influence of chemical environment on SCI is similar between samples: SCI is reduced in aqueous conditions relative to ambient conditions, with the most pronounced reductions in NaOH, at elevated temperature, and in dilute NaCl solutions. Synthetic K-V curves based on mean SCI in each environment and reduction below a nominal K_{IC} (2.5 MPa $\sqrt{m}$) illustrate the relative change in subcritical fracture growth behavior in different environments (Figure 3.9). NaOH tests have the lowest slopes on average, representing faster fracture front velocities at a given stress intensity and fracture propagation at lower stress intensities. Silica solubility increases with increasing pH (Fournier, 1985), but increased temperature and salinity also increase dissolution rate. The observation that environments that favor increased solubility and dissolution rate promote subcritical fracture growth in silicified materials is consistent with predictions by Dove (1995) based on single synthetic quartz crystals, although silicified rocks are approximately three times tougher than single crystals of synthetic quartz.

Although the trends that we observed are well described by quartz and silica kinetics, the absolute fracture mechanical properties of silicified fault rocks differ from single synthetic quartz crystals. In the silicified rocks we tested, the presence of minor amounts of plagioclase, feldspar, calcite, and sericite, which have different dissolution behavior, had negligible effect on bulk fracture mechanics compared to the dominant mineral phase, and instead appear to have an additive effect. Compared to increased SCI and reduction of fracture propagation velocity in single synthetic quartz crystals in acidic environments (Atkinson, 1979a; Atkinson and Meredith, 1981), the presence of minor amounts of calcite in our samples may have helped reduce SCI in acidic solutions. The textural complexity found in silicified rocks (Figure 3.4) may also contribute to the high toughness we observed in our samples, which are approximately three times tougher than single synthetic quartz crystals described by Atkinson (1979a).

3.5.2 Feedback Between Physiochemical Condition and Fracture Processes in Hydrothermal Systems

Permeability in many hydrothermal systems evolves through competition between dilatant damage and sealing. Negative feedback between focused hydrothermal alteration and reduction in permeability is well documented, with argillic alteration and silicification both cited as a mechanism that ultimately reduce fluid flow in hydrothermal systems (Facca and Tonani, 1967; Henley and Ellis, 1983; Lowell et al., 1993; Olsen et al., 1998; Dempsey et al., 2012). Yet permeability in some fault-hosted systems persists long after the last demonstrable episode of seismic deformation (Caskey, 2000; Howald et al., 2015; Siler et al., 2018). Our results suggest that positive feedback between chemical environment, subcritical fracture growth, and enhanced permeability may operate in some hydrothermal settings.

To illustrate the possible impact of different physiochemical conditions on fracture growth, we conducted a limited set of boundary element models using JOINTS, a pseudo-3D numerical fracture pattern simulator (Olson, 1993). We used two model geometries (representing 1 and 2-meter-thick silicified bodies), low strain rates (10^{-16}/s) designed to minimize purely mechanical (critical) fracture propagation, and model run times ~10 kyr. Model run times are nominally representative of interseismic periods >2.5 kyr in the fault segment hosting the Dixie Valley geothermal field and Dixie Comstock epithermal deposit (Bell et al., 2004). We used SCI = 130, 90, and 50, representative of values we measured in silicified rocks in ambient, DI, and NaOH environments, respectively. The direct application of these model results to fracture networks in the subsurface is limited by specific subsurface conditions and deformation history, rock and fracture mechanical properties, and fracture reactivation or inheritance in real systems. However, in these models, changing SCI resulted in measurable differences in fracture development: fracture growth was favored in models with lower SCI and suppressed in models with higher SCI (Figure 3.10).

Based on our experimental observations and results of our heuristic model, reduced SCI, enhanced subcritical fracture growth, and thus higher fracture intensity, may be found

in quartz-rich rocks in parts of hydrothermal systems where the physiochemical environment favors increased quartz dissolution rates, i.e., at higher temperature, higher pH, and higher salinity conditions. Chemically-aided subcritical fracture growth may be inhibited by interaction with cooler, more dilute meteoric fluids, in vapor-dominated systems, or in precipitation-dominated settings (i.e., boiling interfaces, shallow outflow zones). In addition to the spatial variation in subcritical fracture growth arising from different chemical environments encountered in hydrothermal systems, the relative role of subcritical processes may change through time. This may manifest as evolving chemical conditions as hydrothermal systems mature, or in relation to external forces, such as seismic cycles. Coseismic failure in hydrothermal systems may be dominated by critical fracture failure and rapid post-seismic healing (Sheldon and Micklethwaite, 2007) with subcritical fracture growth gaining influence in the interseismic period, or in off-fault areas with less advection and precipitation.

Our predictions of enhanced fracture growth at hydrothermal reservoir conditions diverge from other experimental results showing faster rates of fracture *healing* in quartz at elevated temperatures (Brantley et al., 1990; Brantley, 1992; Morrow et al., 2001; Beeler and Hickman, 2004). A critical difference between these analysis and ours, which predict enhanced fracture growth in hydrothermal condition, is the introduction of concentrated tensile stress at a fracture tip. This difference suggests that fracture healing vs. fracture growth in hydrothermal reservoirs may be particularly sensitive to mismatches between load and fracture orientations.

3.5.3 Implications for Operating Geothermal Fields

Correctly characterizing fracture mechanical behavior in altered rock improves our understanding of the lifecycle of hydrothermal systems and promotes better management of producing geothermal fields (Demarest, 1976). Production and injection in geothermal fields induce complex hydrologic, thermal, chemical, and mechanical interactions affecting overall productivity. These interactions are the focus of extensive research and modeling efforts, such as the DOE Geothermal Technologies Office Code Comparison project

(White and others, 2016). Fracture mechanical attributes based on experimental investigations of hydrothermally altered rocks are rarely included in subsurface models, because few such measurements exist. Experimental fracture mechanics investigations using pristine rock samples, such as the work presented by Takahashi and Abé (1987), may *overestimate or underestimate* the toughness of altered reservoir rock (Callahan et al., submitted), and tests conducted in ambient conditions cannot address coupled chemical-mechanical interactions occurring during subcritical fracture growth. Our results help constrain fracture growth behavior in operating geothermal reservoirs by 1) measuring K_{IC}^* and SCI in altered rocks commonly encountered in hydrothermal systems and 2) exploring the role of chemically-aided fracture growth in hydrothermal reservoirs.

3.6 CONCLUSION

Productivity of many hydrothermal systems is controlled by fluid flow in fault-fracture networks. Fracture mechanical properties, fracture toughness and subcritical index, likely influence the hydro-mechanical properties of these systems. However, little work has been done to measure these properties in damaged and altered rocks in hydrothermal systems or to quantify the effect that chemically aided fracture growth may have in common hydrothermal alteration products. We present results from double torsion load relaxation tests of silicified fault zone material conducted in various chemical environments. We find that subcritical index in this material is reduced by >60% in aqueous environments compared to tests conducted in ambient air conditions and that the largest reductions are associated high pH NaOH, dilute NaCl solutions and at elevated temperature. Peak stress intensity during slow loading, a proxy for fracture toughness, is less affected by chemical environment. In this end member material, with high strength, high resistance to fracture growth, and low chemical sensitivity, water-weakening and enhanced stress corrosion under favorable chemical environments still produce measurable reductions in subcritical fracture index, indicating faster fracture growth at lower stress intensities. These results indicate that alkaline, higher temperature dilute brines encountered in hydrothermal upflow zones may promote subcritical fracture growth,

providing a positive feedback mechanism that would contribute to localization of hydrothermal fluid flow and help sustain permeability.

ACKNOWLEDGMENTS

Xiaofeng Chen aided with fracture mechanics testing and data reduction. Donnie Brooks helped with UCS testing. Jeff Cullen and Ben Larson provided insight on silica solubility in high pH conditions. This work was supported by grants from The GDL Foundation; AAPG Foundation; and the Geothermal Resources Council. Additional supported was provided by the Jackson School of Geosciences and the Fracture Research and Application Consortium (FRAC) at the Bureau of Economic Geology, Austin, Texas. Publication authorized by the Director, Bureau of Economic Geology.

Table 3.1. Normalized Weight Percent Mineralogy from X-Ray Diffraction

Sample	Corundum, spike	Corundum, analyzed	quartz	plagioclase+feldspar	calcite	chlorite	muscovite/sericite	oxides, sulfides
1	10	8	88	5	4	4	-	<1
2	10	7	91	2	-	4	<1	<1
3	10	6	97	<1	<1	3	<1	<1

Table 3.2. Physical Properties of Samples from Plugs and Point Counting

	Density (g/cm^3)			Porosity (%)			
Sample	wt mean	± std dev	n		+ error	-error	n
1	2.61	0.00	2	0.4	0.8	0.3	555
2	2.64	-	1	0.5	1.1	0.4	404
3	2.62	0.01	2	1.6	1.5	0.9	381

Table 3.3. Unconfined Compressive Strength and Static Elastic Properties

Sample	UCS (MPa)		E (GPa)		ν		G (GPa)		n
	mean	± std dev	mean	± std dev	mean	± std dev	mean	± std dev	
1	301.3	38.4	58.1	0.8	0.18	0.01	24.7	0.4	3
2	187.8	-	51.1	-	0.13	-	22.6	-	1
3	286.5	12.7	62.8	1.6	0.11	0.02	28.3	0.3	2

Table 3.4. Mean Peak Stress Intensity (K_{IC}*)

Sample	K_{IC}* †					
	air @ RT	DI water @ RT	HCl (pH 3) @ RT	NaOH (pH 12) @ RT	0.1% NaCl @ RT	DI water @70 °C
1	2.40 ±0.16, n = 16	2.59 ±0.27, n = 16	2.33 ±0.39, n = 15	2.51 ±0.17, n = 13	2.51 ±0.27, n = 16	N.T.
2	3.01 ±0.18, n = 25	2.61 ±0.38, n = 17	N.T.	2.13 ±0.45, n = 11	N.T.	N.T.
3	2.89 ±0.38, n = 28	2.73 ±0.23, n = 7	2.33 ±0.35, n = 9	2.45 ±0.28, n = 15	2.44 ±0.37, n = 14	2.53 ±0.32, n = 13

† RT = room temperature (22-23 °C). N.T. = not tested.

Table 3.5. Mean Subcritical Fracture Growth Index (SCI)

Sample	SCI †					
	air @ RT	DI water @ RT	HCl (pH 3) @ RT	NaOH (pH 12) @ RT	0.1% NaCl @ RT	DI water @70 °C
1	113.3 ±29.2, n = 12	106.3 ±20.2, n = 7	89.8 ±25.1, n = 7	61.4 ±16.3, n = 8	63.6 ±18.8, n = 13	N.T.
2	123.7 ±31.9, n = 24	86.6 ±50.0, n = 12	N.T.	44.0 ±21.7, n = 11	N.T.	N.T.
3	142.2 ±37.7, n = 17	73.3 ±19.3, n = 5	63.8 ±19.0, n = 6	48.3 ±17.5, n = 13	53.9 ±18.8, n = 12	58.6 ±14.4, n = 17

† RT = room temperature (22-23 °C). N.T. = not tested.

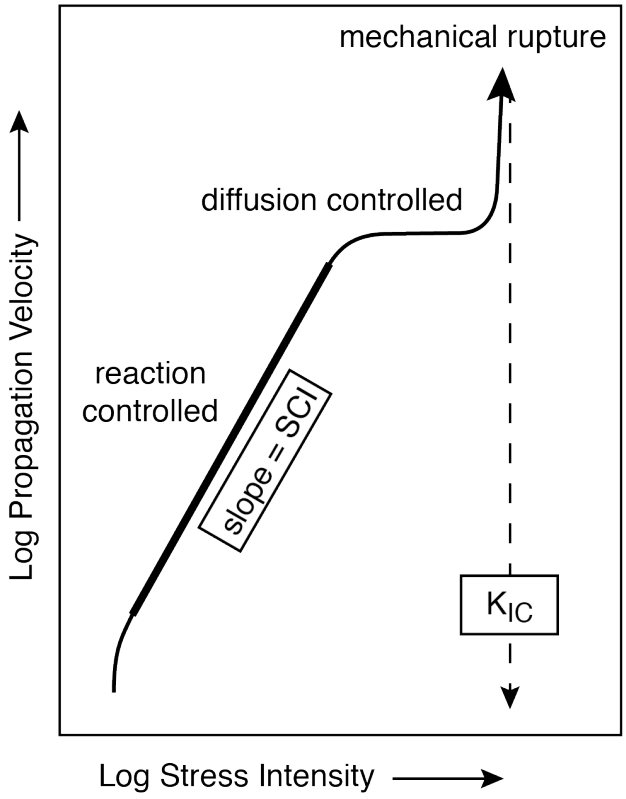

Figure 3.1. Schematic K-V curve. At low stress intensity, chemical reactions at the fracture tip control fracture propagation velocity. As stress intensity increases, fracture propagation velocity outpaces chemical reactions and eventually diffusion of reactive species to the fracture tip. Fracture toughness, K_{IC}, is the maximum stress intensity that a material can sustain before mechanical rupture. After Atkinson (1979a).

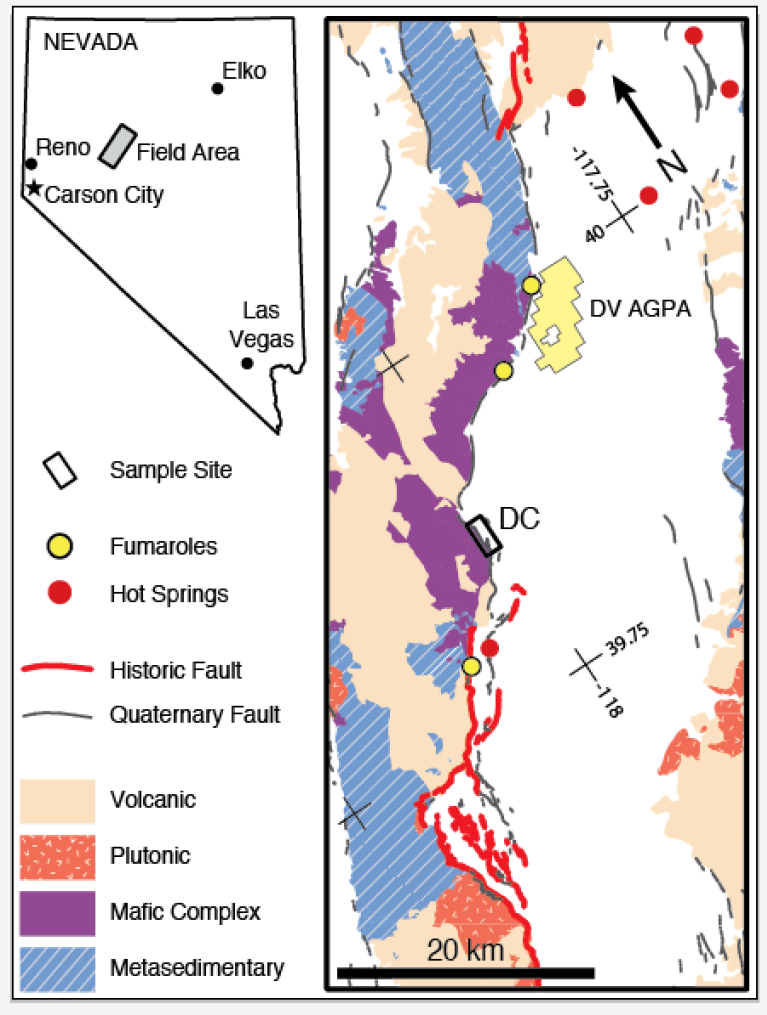

Figure 3.2. Field location and generalized geology, Dixie Valley, NV. Samples were obtained from the Dixie Comstock epithermal deposit (DC), located along a north-south trending portion of the Dixie Valley – Stillwater fault zone, north of the 1954 Dixie Valley fault scarps and south of the producing geothermal field.

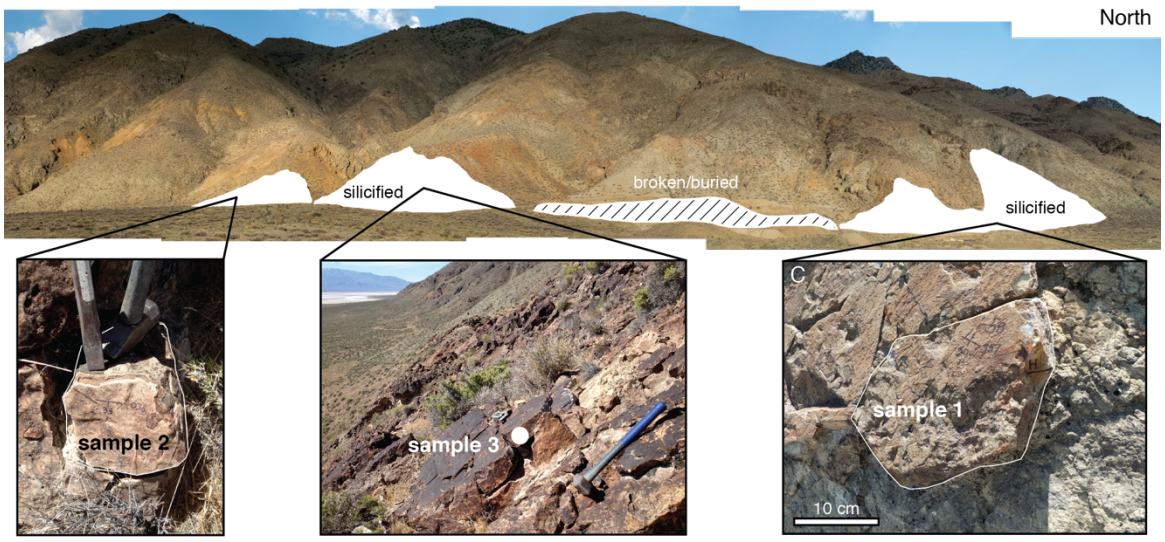

Figure 3.3. Field setting and photographs of samples 1, 2, and 3. Samples were collected from the main silicified range front fault north and south of the Dixie Comstock mine site.

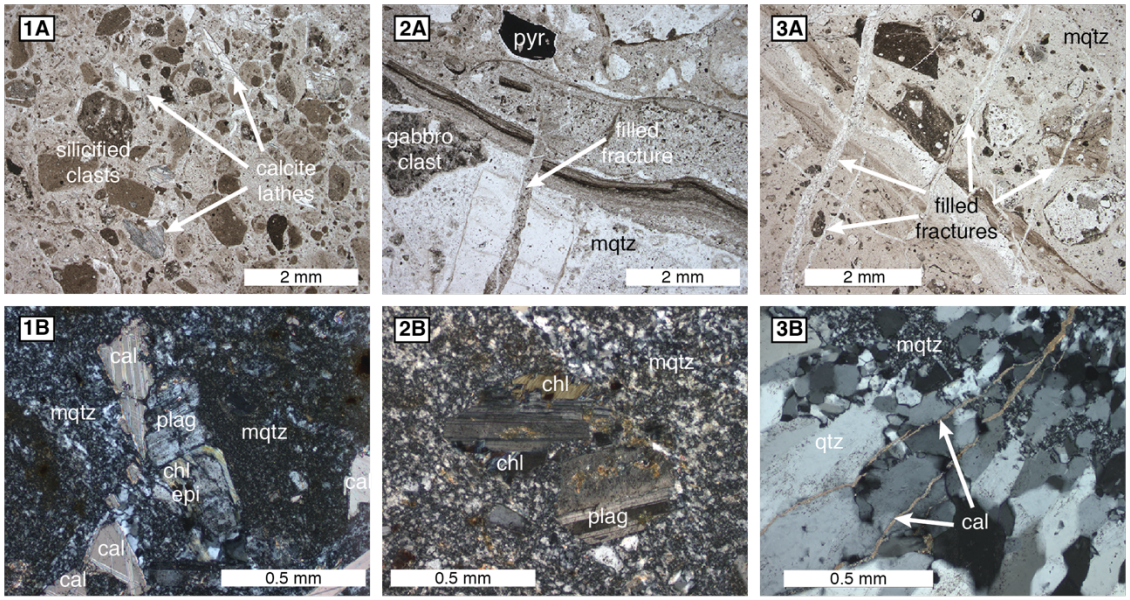

Figure 3.4. Plain light and polarized light photomicrographs of sample material. Variation in sample texture (clast shape, microfractures, micro- vs euhedral quartz) and composition arises from changes in degree of silicification and minor changes in protolith composition. Sample 1 (A, B) includes broken calcite lathes incorporated from calcite breccia in the adjacent footwall. Samples 2 (C, D) and 3 (E, F) reflect increasing amounts of silicification, but contain relict plagioclase and chlorite from the adjacent altered gabbro. All samples contain quartz-filled fractures, with some late calcite-filled fractures (F), and open fractures and vugs, although these are not evening distributed.

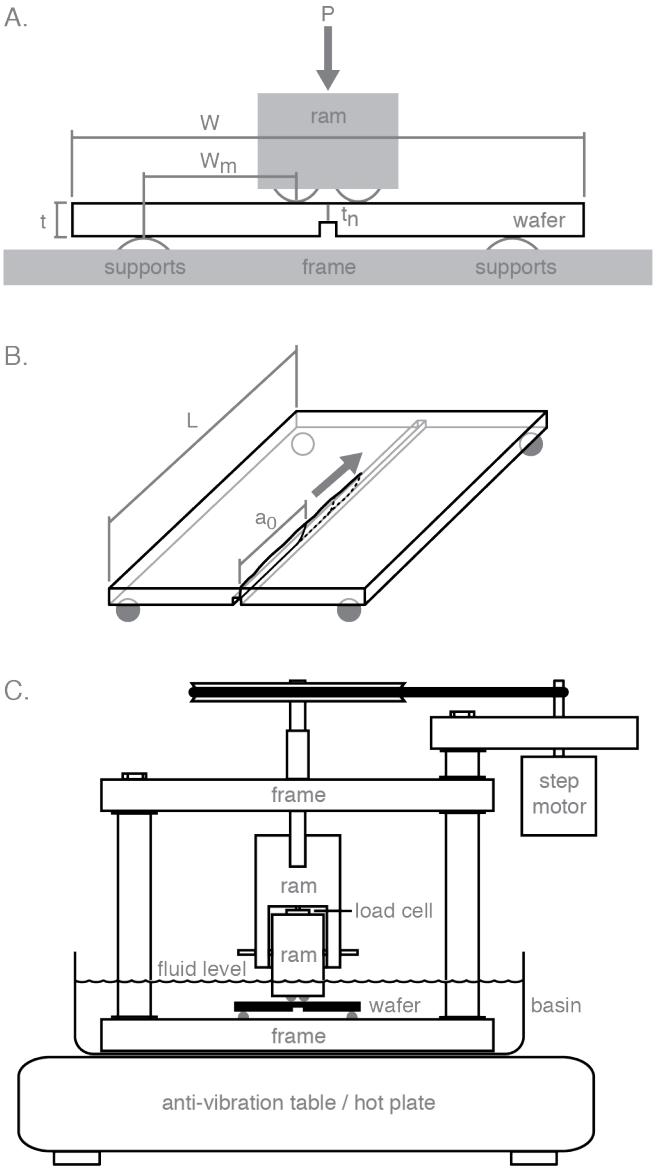

Figure 3.5. Double torsion sample geometry and environmental testing configuration. A) Cross-section of double torsion specimen, with load and support points (semicircles) and dimensions: W = width, W_m = moment arm, t = thickness, tn = reduced thickness. B) Oblique view of specimen showing pre-fracture length (a_0) and subsequent fracture growth increments. Arrow indicates direction of fracture propagation. C) Double torsion apparatus and specimen partially submerged in testing fluid.

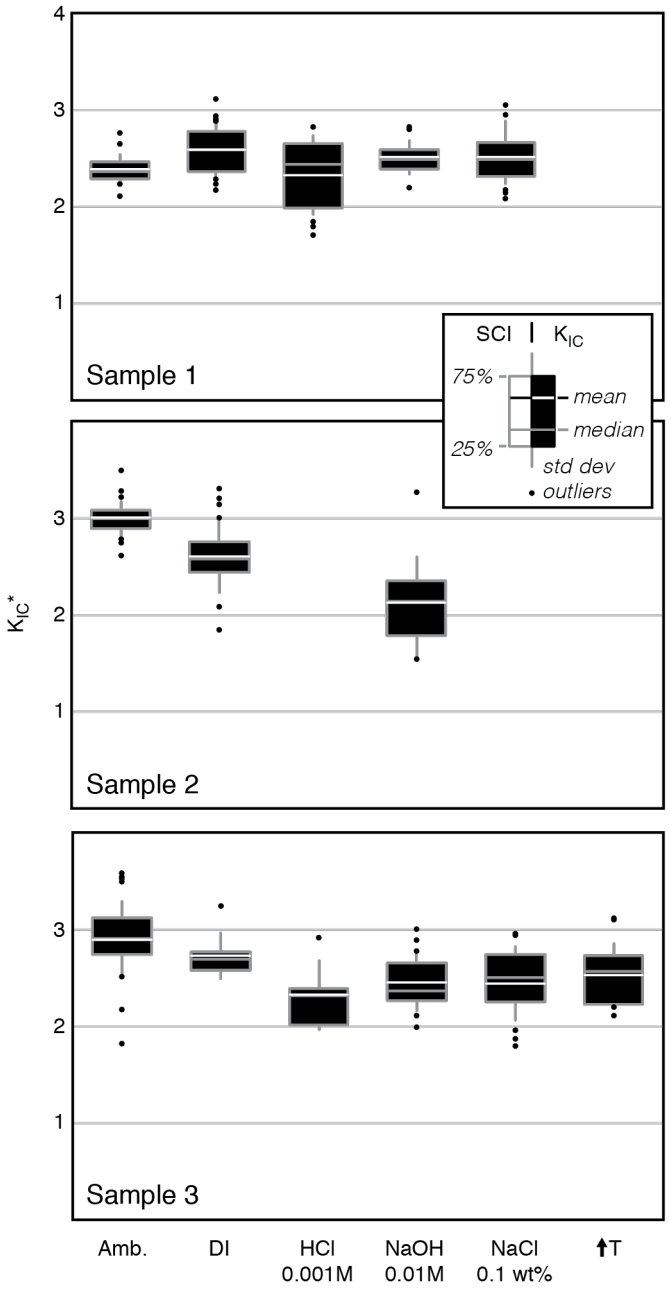

Figure 3.6. Box plots showing K_{IC}* results in different testing environments. Boxes show interquartile range, bars show standard deviations, and dots show outliers. Number of tests in Table 3.4. Testing conditions have limited impact on K_{IC}*, except for sample 2, which may be a result of poor specimen quality in later tests.

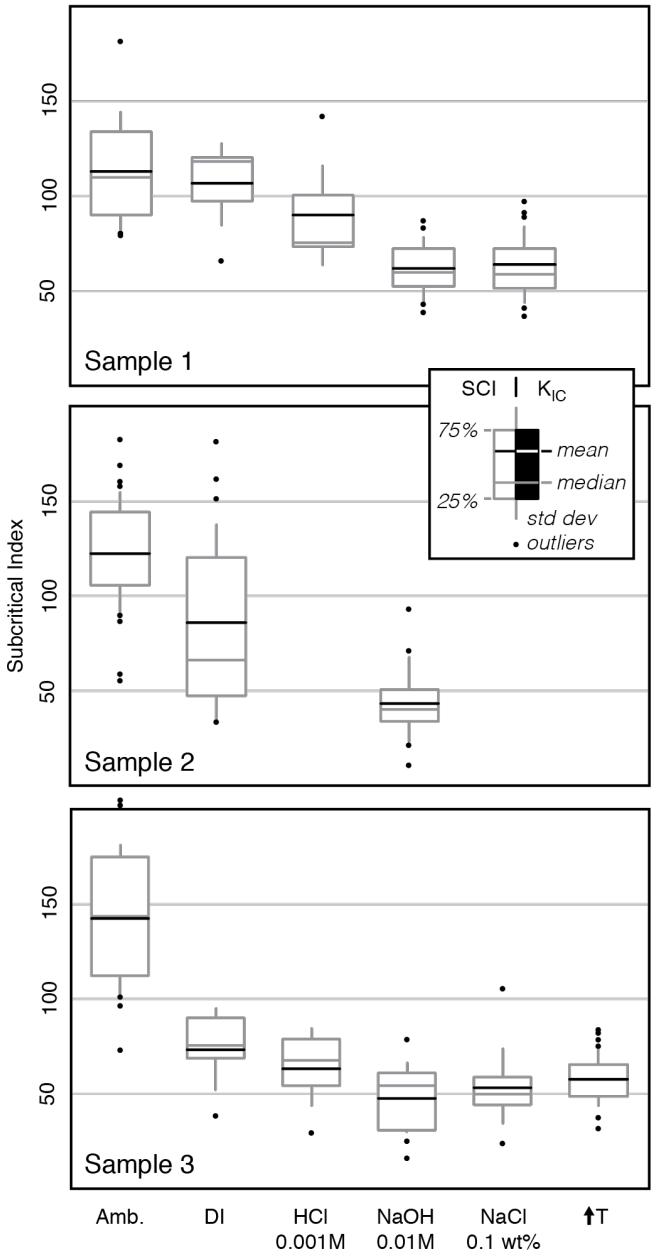

Figure 3.7. Box plots showing SCI results for in different testing environments. Boxes show interquartile range, bars show standard deviations, and dots show outliers. Number of tests in Table 3.5. Aqueous conditions result in reduction in mean SCI compared to ambient tests for all samples. The largest reduction in mean SCI compared to ambient tests is observed in dilute NaOH conditions.

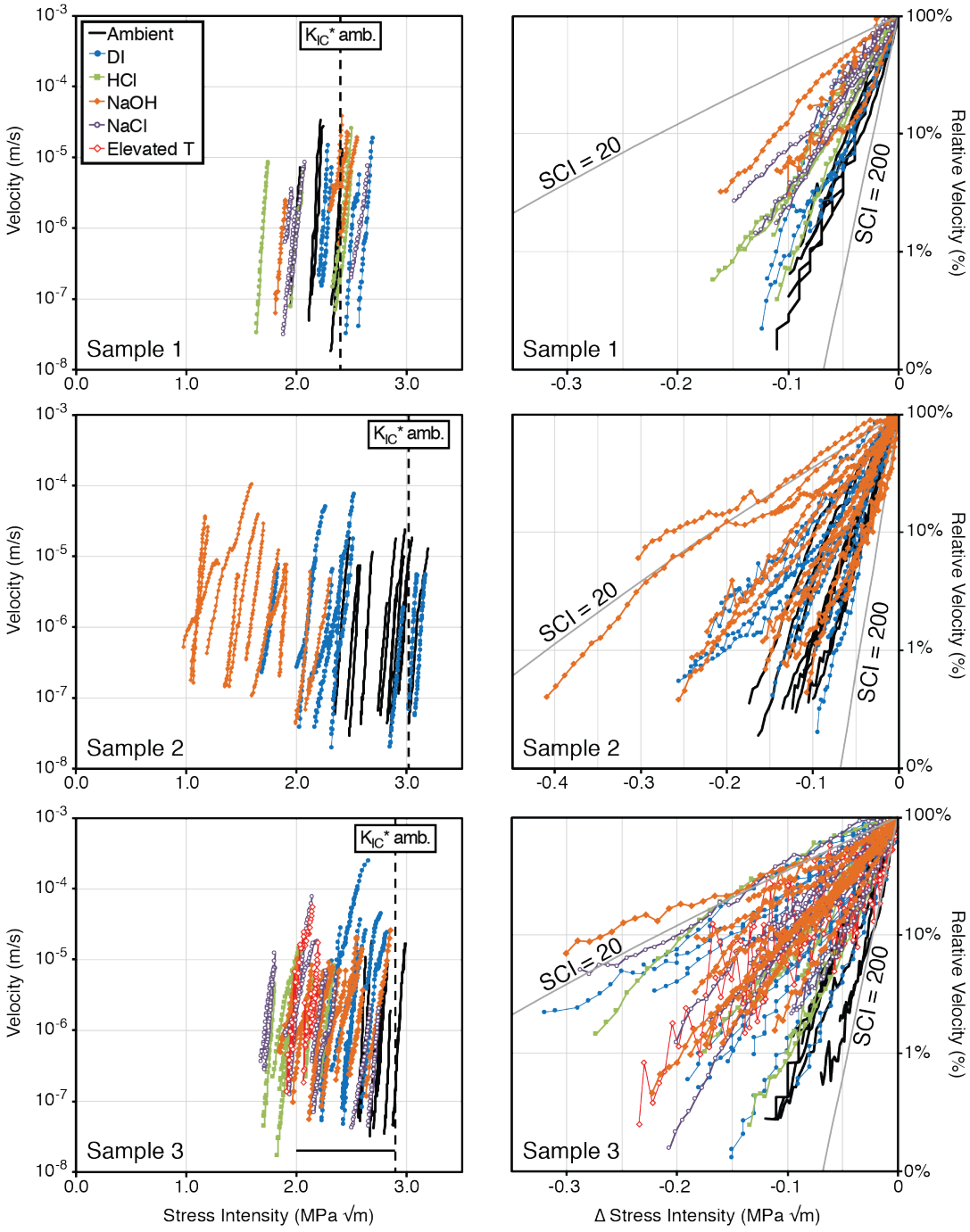

Figure 3.8. Linear-log and normalized K-V curves. Shift in K-V curves is typically to lower stress intensity and to shallower slope (lower SCI) as the testing environment changes from ambient to aqueous conditions.

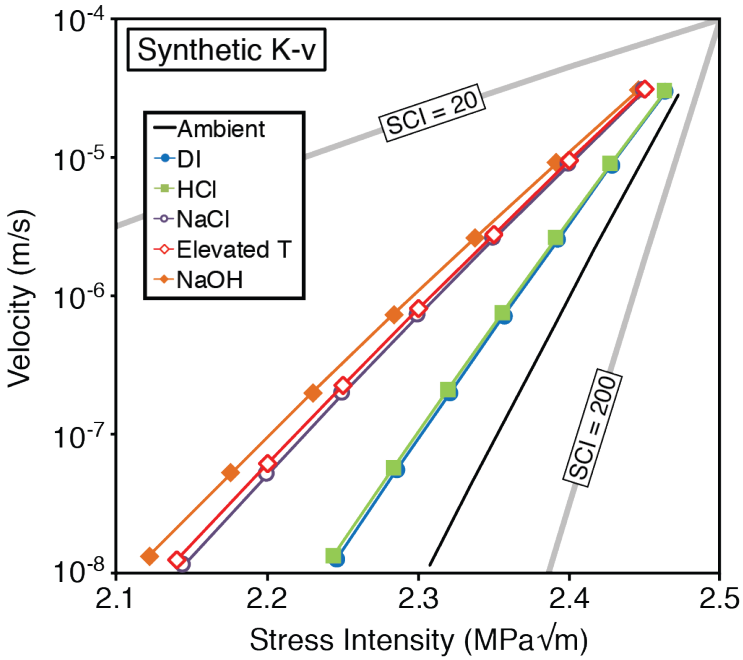

Figure 3.9. Synthetic K-V curve showing mean SCI for silicified fault material in different physio-chemical environments for a nominal K_{IC}. A change in chemical environment from ambient to DI water increases fracture propagation velocity by more than an order of magnitude at lower stress intensity. Fractures in NaOH conditions may propagate at the same velocity as ambient fractures, but at lower stress intensity.

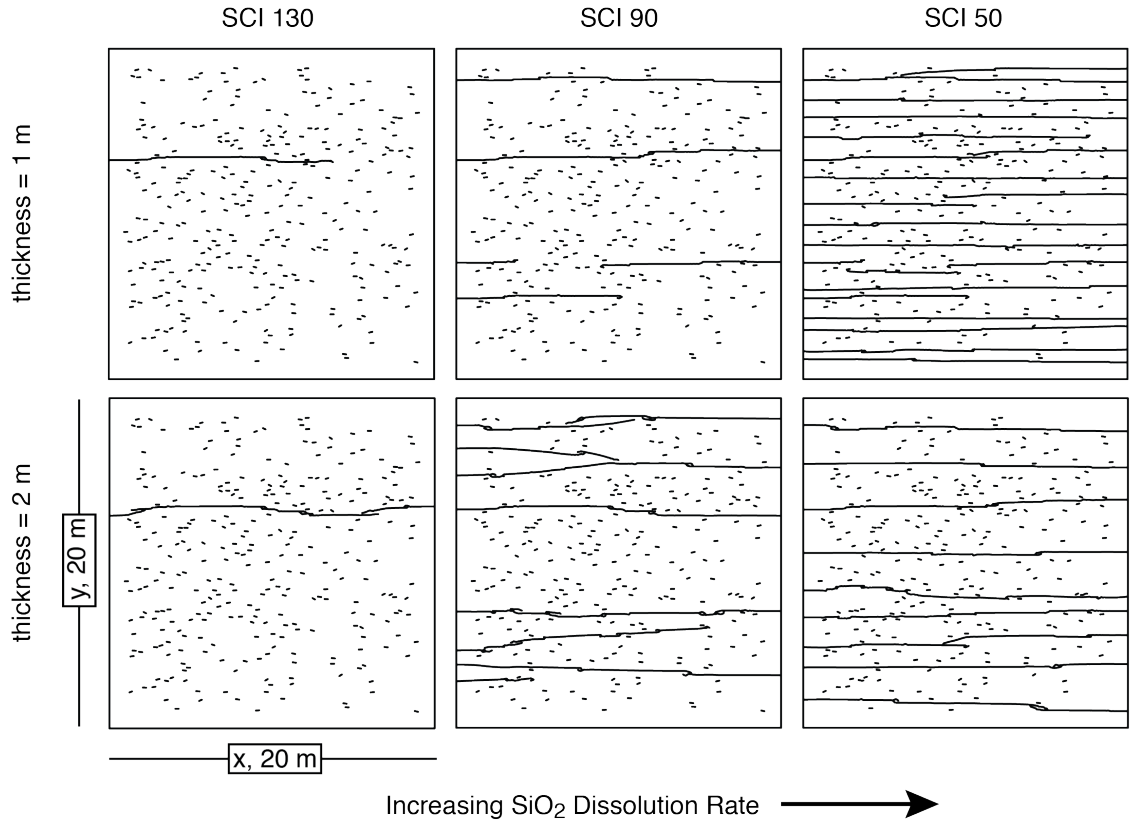

Figure 3.10. JOINTS models showing potential influence of SCI and body thickness on fracture network development. Decreasing SCI with changes from ambient, aqueous, to strong base conditions is associated with an increase in fracture intensity. Small tick marks are non-propagating seed flaws. SCI and body thickness are varied in these models. Fixed model parameters include seed flaw location and orientation, strain boundary conditions, number of strain increments, model run time (~10 kyr), and material mechanical properties.

4. Precipitation-Strengthening and Fault Zone Evolution, Dixie Comstock Epithermal Deposit, Dixie Valley, NV[4]

ABSTRACT

Fault-fracture networks vary from single planes to wide, complex core and damage zones. Various mechanisms are invoked to explain difference in fault zone width, from growth and linkage of antecedent structures to the amount of accumulated slip. Water-rock interaction is typically attributed with weakening and shear localization. However, we hypothesize that hydrothermal alteration resulting in mineral precipitation and strengthening contributes to the development of thick fault cores. We conducted field mapping and petrographic, mineralogical, and mechanical characterization to assess the impact of alteration and cementation on brittle deformation in chloritized footwall gabbro and silicified fault breccia at the Dixie Comstock epithermal gold deposit, Dixie Valley, Nevada, USA. We observed 1) strong, thick silicified fault cores and wide, weak damage zones, 2) evidence for widening of the silicified core through embrittlement and dilation as well as entrainment of damage zone material, 3) repeated fracturing and sealing recorded by multiple breccia and cement types and textures, and 4) breakup of the fault core as deformation outpaced cementation. Based on these observations, we present a conceptual model of fault zone evolution in crystalline rock that includes alteration-weakening and precipitation-strengthening paths with observable differences in fault zone architecture and implications for hydromechanical properties. Alteration-weakening favors localization of the fault zone into thinner, clay-rich, low permeability fault cores. Precipitation-strengthening promotes thick, strong-yet-brittle, low permeability fault cores, and enhances transient permeability following co-seismic failure and dilation.

HIGHLIGHTS

- Mineral precipitation contributes to complex fault zone architecture.

---

[4] Authors and affiliations: Owen A. Callahan and Peter Eichhubl, Bureau of Economic Geology, The University of Texas at Austin, Austin, TX; Nicholas C. Davatzes, Earth and Environmental Sciences, Temple University, Philadelphia, PA

- Silicification creates strong, brittle, dilatant fault cores.
- Precipitation around ripouts, pinnate fractures facilitates fault core growth.
- Breakup of the core occurs when deformation outpaces precipitation and healing.

KEYWORDS
alteration, silicification, hydrothermal, deformation, fault architecture

4.1 INTRODUCTION

Fault-fracture networks vary from single planes to complex core and damage zones (Caine et al., 1996). Fault cores are commonly composed of variably cemented fault rock, including gouge and breccia, and multiple slip surfaces, and have accommodated the most strain. Fault damage zones are composed of opening mode and sheared fractures, veins, small faults, and fragmented, pulverized, or altered protolith (Kim et al., 2004; Mitchell and Faulkner, 2009). The fault damage zone grades into protolith, which lacks distinct fault-related damage. Well-developed damage zones comprised of opening-mode and sheared fractures may facilitate fault-parallel flow, whereas fault cores consisting of deformation bands and clay gouge generally inhibit flow (Brown and Bruhn, 1996; Sibson, 1996; Caine et al., 1996; Barton et al., 1998; Caine et al., 1999, 2010; Nelson et al., 1999; Ikari et al., 2009; Davatzes et al, 2003a, b; Eichhubl et al., 2009; Anders et al., 2013).

Various mechanisms are employed to explain the development of fault zone architecture. Linkage and the formation of subsidiary faults at fault segment boundaries are principal controls on fault zone architecture and fault zone width (Myers and Aydin, 2004; Childs et al., 2009). Fault width, including fault core and damage zone, may also grow as a function of accumulated slip (Hull, 1988; Watterson et al., 1998; Savage and Brodsky, 2011), although this relationship is not always well defined (Evans, 1990). Mineralogy of host lithology and lithologic contrast can both influence fault zone geometry, with weaker, clay-rich lithologies contributing to fault localization and sealing and stronger, clay-poor lithologies contributing to fault zone complexity (Heynekamp et al., 1999; Solum et al., 2010; Moir et al., 2013; Laubach et al., 2014). Most of these fault growth models focus on

the mechanical and geometric controls, assuming that rock properties remain unaffected by fault-controlled chemical fluid-rock interaction.

Less well understood are the effects of hydrothermal alteration and mineralization on fault zone architecture and fault structural evolution. Chemical fluid-rock interaction and resulting alteration have been associated with fault-rock weakening in laboratory tests (Sleep and Blanpied, 1992; Blanpied et al., 1995; Blanpied et al., 1998; Lockner et al., 2011) and with fault-zone localization in field-structural investigations (Blenkinsop and Sibson, 1992; Chester et al., 1993; Bruhn et al., 1994; Solum et al., 2010; Backeberg et al., 2016). In these investigations, increasing amounts of damage and alteration through time and with increasing proximity to the fault core result in reduced fault strength through mechanical and chemical development of alteration products such as clay minerals and zeolites that have lower frictional resistance than the unaltered protolith (Sleep and Blanpied, 1992; Wintsch et al., 1995; Blanpied et al., 1998; Lockner et al., 2011). We refer to this process as alteration weakening. Although fault-controlled cementation is well documented as a control on fault zone hydrology (Eichhubl et al., 2004; Eichhubl et al., 2009; Bense et al., 2013), the mechanical aspects of fault rock strengthening by cementation are largely limited to laboratory tests (Olsen et al., 1998; Tenthorey et al., 2003; Yasuhara, 2005), with fewer field studies exploring the impact of precipitation-strengthening on fault zone architectural elements (Woodcock et al., 2007; Faulkner et al., 2008; Caine et al., 2010).

In this study, we address the question of how fluid-rock interactions resulting in alteration and precipitation impact fault zone architecture and fault zone evolution. We hypothesize that hydrothermal alteration and precipitation result in fundamental changes in mechanical properties of fault rocks. These changes contribute to, not just arise from, complex fault zone architecture. If precipitation of quartz dominates, then fault cores and damage zones will tend to thicken due to increased rock strength and toughness. If alteration increases the abundance of phyllosilicate and clay minerals, then the fault zone will thin and become less complex in response to reduced strength and fracture toughness. Similarly, if precipitation cannot keep up with deformation, then the fault will weaken.

These hypotheses are tested by correlating fault architecture with (a) mineralogical and textural analysis that document the history of deformation and alteration and (b) rock mechanical testing of these materials. We conducted field observations, and petrographic, mineralogic, and mechanical characterization of a well-exposed fault system preserved at the Dixie Comstock epithermal deposit, Dixie Valley, Nevada, USA (Figure 4.1). We present evidence for the growth of the fault core by silicification, embrittlement, and dilation as well as through incorporation of previously altered and damaged footwall material when precipitation outpaced deformation. The strengthening stage is followed by break up and distribution, or dislocation, of previous cemented fault core when deformation outpaces mineralization during active exhumation. The spatial and temporal relationships we observed are synthesized into a conceptual model that explores fault zone evolution arising from interaction between hydrothermal alteration and deformation and includes paths through alteration-weakening and precipitation-strengthening stages.

4.2 Regional Geologic Setting

4.2.1 Dixie Valley – Stillwater Fault Zone

The Dixie Valley - Stillwater fault zone is a ~NE striking, east dipping basin-bounding fault system in north central Nevada, USA (Figure 4.1). The Stillwater Range front is sinuous, with changes in geometry associated with reactivation of older N-S striking normal faults (Parry et al., 1991) and changing lithology (Caskey et al., 1996). The basin hosts a series of buried, nested grabens and >1.8 km of Quaternary lacustrine and alluvial fan deposits (Okaya and Thompson, 1985; Bell and Katzer, 1990). Post 8 Ma dip-slip displacement is 2.2-2.9 km in the northern valley (Okaya and Thompson, 1985) and there is up to 6 km of post-Oligocene fault-related exhumation in southern Dixie Valley (Thompson et al., 1967; Parry and Bruhn, 1990). Exhumed portions of the Dixie Valley – Stillwater fault zone have been loci of extensive research on fault zone architecture, mechanics, and processes (Okaya and Thompson, 1985; Power and Tullis, 1989; Parry and Bruhn, 1990; Parry et al., 1991; Zhang et al., 1991; Power and Tullis, 1992; Bruhn et al.,

1994; Hedderly-Smith, 1997; Seront et al., 1998; Caine, 1999; Caine et al., 2010; Candela and Renard, 2012).

The Dixie Valley – Stillwater fault zone is located in the northern part of the Central Nevada Seismic belt, with historic seismicity in the region including a sequence of large earthquakes that culminated with the 1954 Fairview Peak-Dixie Valley sequence (M 7.2-6.8) (Wallace, 1984; Caskey et al., 1996; Caskey, 2002; Bell et al., 2004). Older fault scarps resulting from similarly sized prehistoric earthquakes are found along most of the Dixie Valley – Stillwater fault zone (Wallace, 1984; Wallace and Whitney, 1984; Bell and Katzer, 1990; Zhang et al., 1991; Caskey, 2002; Bell et al., 2004). Based on fault scarp orientations and displacement associated with the 1954 Dixie Valley earthquake, the extension direction in the southern Dixie Valley-Stillwater fault zone is estimated to be ~94 ±15° (Whitten, 1957; Caskey et al., 1996) and in the central Dixie Valley 124-125° (Thompson and Burke, 1973; Caskey et al., 1996). Geologic extension directions within Dixie Valley based on fault striations are 116-140° (Thompson and Burke, 1973; Okaya and Thompson, 1985; Caine, 1999). The orientation of minimum horizontal stress in the Dixie Valley geothermal field is 123-160°, and maximum horizontal stress is oriented to 033 ±10° (Hickman et al., 1998; Hickman et al., 2007), consistent with the extension direction over recent geologic time.

4.2.2 Dixie Valley Hydrothermal Setting

The Dixie Valley – Stillwater fault zone hosts active hydrothermal circulation and preserved hydrothermal assemblages in exhumed portions of the footwall along much of its length. The Dixie Valley geothermal field has been in operation since 1988, generating ~62 MWe from 245 °C fluids produced from fault and fracture networks in Miocene basalt and Jurassic and Cretaceous crystalline rocks at ~2.5-3 km depth (Benoit, 1992; Blackwell et al., 2000; Blackwell et al., 2007). Active and extinct surface hydrothermal features occur along the range front both north and south of the producing field, including fumaroles, hot springs, sinter, and travertine deposits (Lutz and Hulen, 2000; Lutz et al., 2002). Exhumed alteration in the footwall includes regional sodic and calcic metasomatism of Jurassic mafic

rocks (Dilek and Moores, 1995; Johnson and Barton, 2000), syn-magmatic potassic and sericite alteration of Oligocene granitic rocks (Parry et al., 1991; John, 1995), and a variety of retrograde, fault-related sericite, chlorite-carbonate-hematite, quartz-kaolinite, smectite, zeolite, and silicic assemblages in local segments of the fault system (Power and Tullis, 1989; Parry et al., 1991; Vikre, 1993; Bruhn et al., 1994; Caine et al., 2010).

4.3 Faulting, Alteration, and Mineralization At Dixie Comstock

The Dixie Comstock epithermal gold deposit located in the central portion of the Dixie Valley – Stillwater fault zone was discovered in 1934 and operated intermittently from 1938 to 1970 (Vanderburg, 1940; Wilden and Speed, 1974; Vikre, 1993). Total yield was approximately 4,600 - 5,000 oz of gold from 10,000-17,000 tons of altered gabbro, quartz stockwork, silicified fault rocks, and low-grade mineralized hanging wall alluvium (Wilden and Speed, 1974; Vikre, 1993). Drilling between 1982 and 1984 defined an additional 1.8 million tons of ore at 0.058 oz/ton in a 5-30 m thick fault zone mullion (Vikre, 1993).

The location of epithermal alteration and mineralization is associated with an extensional fault step and releasing bend caused by normal-oblique displacement across a 10-30° change in fault strike (Figure 4.2 and Figure 4.3). Extension direction based on striations on silicified fault rocks, partially mineralized sheared joints, and unmineralized gouge is ~130° (this study). In the southern part of the mine area prominent triangular facets armored by <1 to >2 m thick silicified breccia strike ~025° and dip ~28-52° southeast. In the northern part of the mine area the range front fault strikes ~000° and dips 43-55° east. The range front south of the mine strikes ~N-S, but the fault is poorly exposed due to erosion and onlap of lacustrine shoreline deposits.

Faults controlling mineralization at Dixie Comstock have been active since at least the middle Miocene. The range front at Dixie Comstock is partially defined by the north-striking White Rock Canyon fault that transects the Stillwater Range and juxtaposes Jurassic and Oligocene rocks (Figure 4.1). K-Ar sericite ages record faulting and alteration between 15 ±0.5 and 11.1 ±0.3 Ma (Vikre, 1993), corresponding with Miocene volcanism

and a shift in extension direction from E-W to NW-SE around 10-13 Ma (Zoback et al., 1981; Hudson and Geissman, 1991; Parry et al., 1991). The most recent fault slip is preserved in 2.0-2.5 ka scarps with 3-5 m of normal displacement that displace alluvial and lacustrine deposits in the southern part of the map area and Quaternary and Oligocene units north of the mine (Thompson and Burke, 1973; Wallace and Whitney, 1984; Bell et al., 2004; Caskey and Ramelli, 2004). Faults in alluvium exposed in mine workings record down to the east dip slip, but Quaternary scarps through the middle of the field site are obscured by past mining activity.

The Humboldt Igneous Complex is the dominant protolith now exposed in the footwall of the Dixie Comstock deposit. This tectonically imbricated mafic volcanic-arc complex includes coeval intrusive units, from anorthosite to monzonite, basaltic to andesitic dikes, and volcanics units ranging from basalt to dacite (Wilden and Speed, 1974; Dilek and Moores, 1995). Hornblende K-Ar and $^{40}Ar/^{39}Ar$ ages are mid Jurassic (170 ±2 Ma), with younger biotite ages reflecting Cretaceous and Cenozoic reheating (Kistler and Speed, 2000). Lithologies in the immediate vicinity of Dixie Comstock range from fine to coarse grained plagioclase- and pyroxene-rich hornblende gabbro and anorthosites, and minor basalt (Wilden and Speed, 1974; Speed, 1976; Vikre, 1993). Small bodies of pink, fine grained granite intrude the Humboldt Igneous Complex in the southern part of the map area. K-Ar ages from albite associated with the granite intrusions are 93.2 ±7.8 Ma (Vikre, 1993). Unaltered, steeply east-dipping dikes in the northern part of the map area are tentatively correlated with regionally extensive 13-17 Ma basalt flows (Nosker, 1981; Gonsior and Dilles, 2008).

Several distinct episodes of alteration are preserved in the Dixie Comstock area. Early widespread sodic and calcic alteration of the Jurassic Humboldt Igneous Complex (Dilek and Moores, 1995; Johnson and Barton, 2000) manifests as chlorite, calcite ±epidote and albite replacing plagioclase and mafic minerals, and calcite-hematite ±quartz and cataclasite veins (Table 4.1, Figure 4.4). Background alteration in the southern part of the map area is overprinted by large masses (>10 m) of barite, calcite, and pyrite and aureoles

of quartz, albite, sericite, kaolinite, and iron oxide around apophyses of Cretaceous granite (Vikre, 1993).

The epithermal phase of alteration is dominated by silicification of the range front fault, with portions of the silicified fault core exceeding 2 m in thickness and approaching 100% quartz (Table 4.1, Figure 4.5). Intense silicification is focused in the releasing bend and along the dilational portion of the fault, with quartz veins in the footwall and minor quartz-cemented fault breccia extending 1.5 km along strike and >400 m down dip (Figure 4.3). Late calcite precipitation occurs as massive calcite-supported breccia in the northern part of the mine area, as rhombic fill in quartz-lined fractures, and as bladed crystals in cockade breccia. Liquid- and vapor-rich inclusions (Vikre, 1993) and bladed calcite in outcrop (this study) indicate boiling conditions existed in shallow parts of the system. Fluid inclusion microthermometry indicates temperatures between ~160-180 °C (Vikre, 1993); Appendix K). Boiling near 170 °C suggests exhumation from as shallow as ~76 m (Haas, 1971). Vikre (1993) proposed a mid-Pleistocene age for gold mineralization based on minor silicification of Pleistocene Lake Dixie gravels and U-Pb calcite >0.35 Ma. MacNamee (2015) reported 0.3 Ma ±0.2 Ma and 0.9 ±0.4 Ma apatite (U-Th)/He cooling ages north of Dixie Comstock, in good agreement with Vikre's (1993) suggested age.

4.4 Field Observations of Fault Zones at Dixie Comstock

Hydrothermal alteration and fault zone architecture vary along strike around the Dixie Comstock deposit. We describe the relationship between the type and intensity of alteration with fault zone elements including the fault core and fractures and veins in the core and damage zone at four distinct field areas, 1-4 in Figure 4.2. From least to most structurally evolved, we describe 1) small uncemented faults in sodic and calcic metasomatized and damaged gabbro in Area 1, 2) a thin body of moderately quartz-cemented breccia along the White Rock Canyon fault in Area 2, 3) thick silicified and mineralized portion of the range front fault in the dilational fault jog in Area 3, and 4) dislocated cemented fault breccia distributed in a matrix of clay-rich fault gouge in Area 4.

4.4.1 Uncemented Faults in Area 1

Area 1, located 500 m north of the Dixie Comstock mine and 200-300 m west of the range front fault, exposes small, northeast- to northwest-striking, moderately east-dipping faults (Figure 4.2). These faults are traceable for tens of meters and, where they offset compositional variation in the gabbro, show less then ~5 m of normal displacement. Uncemented fault gouge is <10 cm thick (Figure 4.6). Striations in fault gouge indicate oblique right-lateral slip (Figure 4.6, inset). Fault related damage is mostly limited to steeply-dipping uncemented opening-mode fractures in the hanging wall. The orientations of these faults and joints are consistent with range front normal faulting in the stress state measured by Hickman et al. (2007).

4.4.2 Faults with Minor Quartz Cement in Area 2

Area 2, located 500 m north of the Dixie Comstock Mine and 100-200 m west of the range front fault, contains exposures of the White Rock Canyon fault. The fault core contains quartz-cemented breccia and gouge in 10-30 cm thick sheets adjacent to 2 m thick weakly cemented breccia (Figure 4.7a). The fault is broadly corrugated over hundreds of meters, and dips between 29-55° east. The northern segment of this fault contains coarse, partially quartz-cemented gabbro breccia structurally above thin (<10 cm) partially mineralized and oxidized slip surfaces in cemented gouge underlain by a competent plagioclase-rich gabbro in the footwall (Figure 4.7b). The southern White Rock Canyon fault segment contains a thin (10-30 cm), laterally extensive (~10 m) tightly quartz-cemented fault breccia with well-developed slickensides and a veneer of late calcite-cemented clasts (Figure 4.7). Slickensides record oblique dextral normal slip. The main slip surface grades into a 1 m thick body of incompletely quartz-cemented, chloritized gabbro breccia with through-going anastomosing slip surfaces. The lower slip surfaces separate the sheared breccia from quartz-cemented mosaic breccia that grades into chloritized gabbro 1-3 m into the footwall (Figure 4.7). 25-30 Ma Oligocene volcaniclastic units above the White Rock Canyon fault segment are fractured and sheared, with isolated hydrothermal quartz breccia veins.

4.4.3 Silicified Faults in Area 3

Area 3 includes the region adjacent to the Dixie Comstock mine, extending approximately 600 m along the range front and 200 m into the footwall (Figure 4.2). The range front fault in this area changes orientation from north-striking, moderately east-dipping (40-55°) in the northern part of the area to north-northeast striking with shallower east-southeast dips (28-50°) in the southern part of the area. Striations in this interval show normal, dextral slip to the southeast (110-155°). Intense silicification of the range front fault preserves prominent triangular facets north and south of the mine, but intact silicified fault core is not exposed at the surface in the immediate vicinity of the mine. Silicified fault core grows in thickness and extent to the south, approaching ~5 m in the southern facets (Figure 4.8, Figure 4.9). Thick fault core is comprised of subparallel sheets of silicified fault breccias, inverse graded breccia, massive silica, and matrix supported blocks (<0.5 m) of variably altered gabbro clasts (Figure 4.5). The base of the silicified fault core is generally sharp. However, wide (1-20 cm), quartz-cemented fractures extend from the fault core into and around blocks of altered and sheared footwall, completely surrounding this material in some areas (Figure 4.9, Figure 4.10). The silicified body is cut by long (>10 m), steep, wide (1-20 cm), partially quartz, chalcedony, or calcite-filled, east-west striking fractures and unmineralized fractures that strike subparallel to the range front and curve into a sheared interval at the base of the silicified blocks (Figure 4.10). The interval below the silicified portion is highly sheared, and grades into course, oxidized, chlorite-calcite altered gabbro with multiple generations of cataclastic, quartz, and chalcedony veins (Figure 4.10). Locally intense areas of open prismatic veins, graded quartz supported breccias, chalcedony, quartz stockwork, and shearing extend >30 m into the footwall (Figure 4.9). North of the mine silicified triangular facets contain repeated layers of 10-50 cm thick, laterally extensive (>5 m), sheets of silicified fault breccia and chalcedony, pods of graded breccia and chalcedony in cemented dilatant pinnate fractures, and massive, calcite-supported breccia (Figure 4.11). Clasts in the calcite breccia include broken silicified fault core and altered gabbro (Figure 4.11c).

4.4.4 Post-Silicification Faults in Area 4

Area 4, located in the footwall of the range front fault in the vicinity of the Dixie Comstock mine (Figure 4.2), is structurally most evolved. The range front fault juxtaposes Quaternary deposits against a >10 m thick interval of clay-rich fault gouge containing large (>1 m) blocks of silicified fault breccia (Figure 4.12). Fault gouge is composed of montmorillonite, sericite, kaolinite, feldspar, and quartz (Vikre, 1993). Multiple ~dip-slip oxide-coated slickensides occur throughout the clay-rich interval. Alteration minerals in the adjacent footwall includes calcite, chlorite, hematite, sulfide, and clay in sheared gabbro. The topography of the range front in this interval steps into the footwall, reflecting collapse of the silicified facet and increased susceptibility of the footwall to erosion.

4.5 DISCUSSION

4.5.1 Mechanisms of Fault Core Widening

Based on characteristic breccia textures and footwall features, we infer two mechanisms of fault zone widening: 1) embrittlement, deformation, dilation, and cementation of fault rocks, and 2) stepping by plucking and entrainment of the silicified interval into the footwall. Silicification resulted in increased strength, stiffness, and brittleness (Table 4.2), thus promoting dilatancy upon failure. Evidence for dilation includes re-brecciation of cemented breccia components, cockade breccia, and multiple generations of mutually crosscutting veins that cut previously cemented clasts (Figure 4.13). Repeated stages of dilation and cementation indicate that the fault zone locally widened over time. Mass balance considerations require that the mass of precipitate equals mass of dissolved material in other parts of the hydrothermal system, with advective transport of dissolved material to the dilatant portion of the fault. Evidence for footwall erosion includes incorporation of altered footwall material into silicified breccia (Figure 4.5, Figure 4.10). Footwall erosion and incorporation occur through cementation of footwall fractures and isolation of intervening footwall blocks. Various geometries are observed at Dixie Comstock, including ripout clasts and lozenges bound by footwall fractures (Figure 4.10, Figure 4.11). Footwall ripout clasts in the Dixie Comstock deposit

share geometry with ripout features described in strike slip faults (Swanson, 1989, 2005), with fragmented wall rock in other mineralizing systems (Micklethwaite, 2009), and with millimeter-scale injection features in the footwall at the Dixie Valley Mirrors normal fault exposure (Candela and Renard, 2012). In the epithermal environment ripout clasts are initially displaced into the silicified fault core through dilation and cementation along the basal fracture, resulting in the incorporation of damage zone material into the silicified body and stepping of the silicified interval into the footwall. Likewise, cementation of wide, deeply penetrating, sub-vertical, fault-perpendicular cross-fractures and curving upward, dilatant fractures bound by subparallel slip surface resembling pinnate fractures (Bruhn et al., 1994) encapsulated lozenges of weakened footwall material (Figure 4.11).

4.5.2 A Model of Fault Zone Evolution in Different Alteration Regimes

Cycles of deformation, fluid flow, and alteration influence the evolution of fault zone architecture. In fault systems that are dominated by fault-rock-weakening reactions, fluid rock interactions promote fault localization. In the epithermal environment, focused advection, boiling, and cooling of silica-rich fluids results in mineral precipitation-strengthening and growth of the fault core. Based on our field observations of fault zone features at Dixie Comstock we propose a model of fault zone evolution by precipitation hardening that involves the following seven stages (Figure 4.14):

1. Inheritance in crystalline rock influences the early development of faults (Crider and Peacock, 2004; Crider, 2015). Inheritance may include the distribution of discontinuities (faults, fractures, fabrics) and mechanical contrast (lithology, prior alteration) (Figure 4.4).

2. Incipient fault formation through shear reactivation and linkage of inherited structures and the formation and growth of new fractures with increasing deformation (early and intermediate shear stage of Myers and Aydin, 2004).

3. Well-developed fault stage reflects slip on discrete surfaces, with thin intervals of mechanical fault breccia, cataclasite, or gouge bounded by inherited and early fault structures (Figure 4.6).

Further fluid-rock interactions may produce phyllosilicate rich cores, facilitating alteration weakening (stage 4a), or promote precipitation-strengthening of the fault core (stages 4b-5):

4b. Cementation results in fault cores ±damage zones with varying amounts of healing, from crusts and fracture-spanning crystals, to matrix supported breccia and replacement (Figure 4.7). Cycles of deformation and cementation in this phase may promote fault core growth through repeated dilation and sealing (Figure 4.13).

5. Cementation-widening occurs when slip and mechanical contrast between a strong, cemented fault core and weaker damage zone promotes distributed, outward-stepping fractures that subsequently become cemented (Figure 4.10, Figure 4.11). Repeated cycles of deformation and healing in this phase isolate and entrain damage zone material into the cemented fault core (Figure 4.5).

6. Core degradation occurs as deformation outpaces precipitation, with differential slip promoting brittle failure and the accumulation of uncemented fractures within the fault core (Figure 4.10). An increase in the density of fractures leads to fault rock-weakening.

7. Core dislocation occurs as continued deformation in an alteration-weakening environment distributes pieces of the remnant fault core through a wide matrix of fault rock and gouge (Figure 4.12). Slip may localize in the weakened material but evidence for prior precipitation-strengthening and cementation-widening is preserved in entrained clasts of cemented fault breccia.

4.5.3 Alteration-Weakening and Precipitation-Strengthening in Other Fault Systems

Hydrothermal alteration resulting in the generation of phyllosilicates, clay minerals, and serpentinite is commonly attributed with fault rock weakening and strain localization. Alteration-weakening of granitic rocks has been attributed to fault rock weakening in the southern segment of the Dixie Valley-Stillwater fault zone (Parry et al., 1991; Bruhn et al., 1994; Seront et al., 1998), where biotite, sericite, chlorite, and calcite have replaced feldspars and mafic minerals in the footwall. Notably, deformation in the footwall here grades into an “ultradamage zone” but the fault core is missing, either

because the fault core was thin or weak and susceptible to erosion. Similar alteration-weakening reactions have been documented from the Wasatch fault (Bruhn et al., 1994). Chester and Logan (1986) described reduction in rock strength and elastic properties with increasing alteration and damage in crystalline and sedimentary sequences at the Punchbowl fault of the San Andreas fault system, resulting in strain localization into relatively thin (10s of cm) clay-rich fault cores. Serpentinization of dunite is associated with decreased strength and strain localization (Escartin et al., 2001) contributing to fault-zone weakening and strain localization in the Parkfield section of the San Andreas fault (Lockner et al., 2011). Solum et al. (2010) attributed the generation of clay smear from both mechanical grain size reduction of sedimentary protolith and water-rock interaction to thin (1 cm to 1 m) continuous slip surfaces in the Moab fault. A consequence of fault-rock weakening in these different fault systems is strain localization into discrete slip surfaces, through focused deformation and increase ductility. Fault core widening in these environments is thought to occur through the gradual wear and incorporation of fault zone asperities as faults accumulate slip (Chester and Chester, 1998; Wilson et al., 2003; Brodsky et al., 2011).

Faulkner et al. (2008) speculated that wide fault cores in crystalline rock may be formed by wear and erosion of geometric irregulates, or through fault core strengthening by cementation. We argue that precipitation-strengthening is indeed an important influence on fault zone evolution, and the influence of fault-core strengthening is observed in other fault systems with wide fault damage zones and cores. The best example of fault core growth through precipitation-strengthening may be the type-example of dual conduit-barrier faults found at the Mirrors normal fault exposure 11 km NNE of Dixie Comstock on a NE-SW striking section of the Stillwater Fault Zone (Caine et al., 1996). The Mirrors fault zone is also developed in the Jurassic Humboldt Igneous Complex (Dilek and Moores, 1995) with intense, fault-related hydrothermal alteration and cementation impacting both the damage zone and thick fault core (Power and Tullis, 1989; Lutz and Moore, 1996; Caine et al., 2010). Silicification in the footwall and fault core is largely responsible for the

development of the remarkable slickensides at this site and is loosely attributed with fault zone widening (Caine et al., 2010).

Precipitation-strengthening and alteration weakening can occur at the same time in different parts of a fault system, or at different times in the same part of the fault system. In southern Dixie Valley, conditions that favored the generation of phyllosilicates promoted alteration-weakening of the fault core (Bruhn et al., 1994), whereas precipitation-dominated hydrothermal regimes at the Mirrors (Caine et al., 2010) and at Dixie Comstock (this study) promoted and preserved thick, strong fault cores. Nortje et al. (2011) related cementation and strengthening of existing faults to the development of new, weaker faults in the same part of the mineralizing Mount Gordon fault system. On a smaller scale, Laubach et al. (2014) related local changes in substrate to cementation and fault architecture in a small fault cutting the Eribol and Applecross formations in Scotland, showing that partial-quartz cementation in the Eribol contributed to fault complexity. Because the effects of hydrothermal flow are focused and ephemeral, the impact of fluid-rock interaction and precipitation-strengthening imparts additional spatial and temporal heterogeneity to fault rock properties and fault zone evolution. The impacts on fault zone architecture may be persistent, even if hydrothermal fluid flow is not.

4.5.4 Implications of Precipitation-Strengthening on Hydromechanical Properties of Faults

The model of fault evolution proposed here has distinct implications for the distribution and evolution of hydrologic and mechanical properties of fault zones, with cycles of cementation and deformation influencing fault properties differently in each stage of fault growth.

In the most cemented state, fault systems may be stronger and less hydraulically conductive than incipient faults, early faults, and mature, alteration-weakened fault systems. However, embrittlement and dilatancy of mineralized material in precipitation-dominated systems may facilitate transient upwelling of hydrothermal fluids following co-seismic deformation, and infiltration of cool, meteoric fluids during waning hydrothermal flow and core degradation. Although the episodes of deformation and cementation we

observed at Dixie Comstock record conditions in the near surface and did not form in the seismogenic zone, they may be intrinsically linked to co-seismic rupture.

Precipitation-dominated fault systems preserve better records of past deformation and paleo-flow conditions than dissolution dominated-systems. Distinct phases of deformation may be preserved as cross-cutting relationships in clasts and cements in the fault core and damage zone, and changes in composition and condition of fluids may be recorded in fluid inclusion and isotopic variations. If precipitation-strengthening faults demonstrate different mechanical and hydrological behavior than alteration-weakened faults, it follows that inferences about fault zone properties and processes based on fault cements may not apply to weak, clay-rich fault systems, and *vice versa*.

Under the influence of precipitation-strengthening, fault zones are wider and deformation is more distributed than equivalent sized faults controlled by alteration-weakening. Thus, complex fault zone architecture may not just be a control on fluid flow, but also a consequence of fluid flow and associated precipitation-strengthening.

4.6 CONCLUSIONS

Focused alteration, fluid flow, and economic mineralization at the Dixie Comstock epithermal deposit results from the colocation of early sodic and calcic alteration of the Humboldt Igneous Complex, intrusion of Cretaceous plutons and associated sulfates and sulfides, Fe and Cu minerals, recent dextral oblique reactivation of a Miocene fault in the modern stress regime and localized dilation on fault corrugations, embrittlement of the fault zone and mechanical contrast with altered footwall, allowing for dilatant fracturing. The periodic interaction between deformation, alteration, and fluid flow contributed to the development and preservation of complex fault core and damage zone features. Chlorite and calcite alteration and damage in the footwall contributed to a weaker damage zone relative to the strengthened and embrittled silicified fault core. Precipitation in the epithermal environment captured and entrained fractured footwall material. Continued deformation during waning hydrothermal flow outpaced healing and resulted in the breakup of the silicified fault core where it was backed by the weakest damage zone

material. Our observations suggest that hydrothermal fluid flow is influenced by and can contribute to along strike variations in fault zone architecture.

ACKNOWLEDGMENTS

Support for this work was provided by graduate research grants from the GDL Foundation, AAPG Foundation, and the Geothermal Resources Council. Additional support was provided by The Jackson School of Geosciences at the University of Texas at Austin and the Fracture Research and Application Consortium (FRAC) at the Bureau of Economic Geology, Austin, Texas. Sol Cooperdock, Alison MacNamee, and Adenike Tokan-Lawal assisted with fieldwork. Robin Zuza, Ormat Technologies, Inc., shared subsurface information from geothermal exploration wells. Publication authorized by the Director, Bureau of Economic Geology.

Table 4.1. Mineralogy for Common Alteration Assemblages at Dixie Comstock from X-Ray Diffraction

Alteration	Sample	Cor spike (wt%)	Cor (wt%)	Normalized wt%								
				quartz	feldspars	amphiboles and pyroxenes	calcite	epidote	chlorite	sericite	clays	oxides + sulfides
minor chl	083114-2A	10.2%	9	10	76		1	2	8	2		2
minor chl	083114-2B	10.0%	9	10	77			1	7	3		2
chl, minor cal	083114-1C	10.0%	11	2	56	16	2	3	20		1	
chl, minor cal	061214-5	10.0%	11	11	38	16	2	2	29		2	
chl, minor cal	052815-3B	10.0%	9	2	59		1	1	32	4		
chl-cal	052815-3A	10.2%	9	1	57		19		22			1
silicified, cal	090114-5C	10.1%	8	55	2		41		2			
silicified	090114-5B	10.0%	8	88	5		4		4			1
silicified	061114-4B	10.0%	7	91	5				4			1
silicified	052815-2	10.0%	6	97			1		3			1

Table 4.2. Unconfined Compressive Strength (UCS), Static Elastic, and Fracture Mechanical Properties of Altered Rock Types at Dixie Comstock

Alteration	Sample	UCS (MPa)		E (GPa)		*v*		G (GPa)		n	K_{IC} (MPa √m)		
		mean	std dev	mean	std dev	mean	std dev	mean	std dev		Mean	std dev	n
minor chl	083114-2A	-	-	-	-	-	-	-	-	-	0.68	0.20	14
chl, minor cal	052815-3B	50.7	-	22.8	-	0.20	-	9.5	-	1	0.56	0.13	8
chl-cal	052815-3A	148.0	-	48.2	-	0.22	-	19.7	-	1	2.12	0.23	7
silicified	090114-5B	301.3	38.4	58.1	0.8	0.18	0.01	24.7	0.4	3	2.40	0.16	16
silicified	061114-4B	187.8	-	51.1	-	0.13	-	22.6	-	1	2.67	0.44	10
silicified	052815-2	286.5	12.7	62.8	1.6	0.11	0.02	28.3	0.3	2	3.20	0.33	10

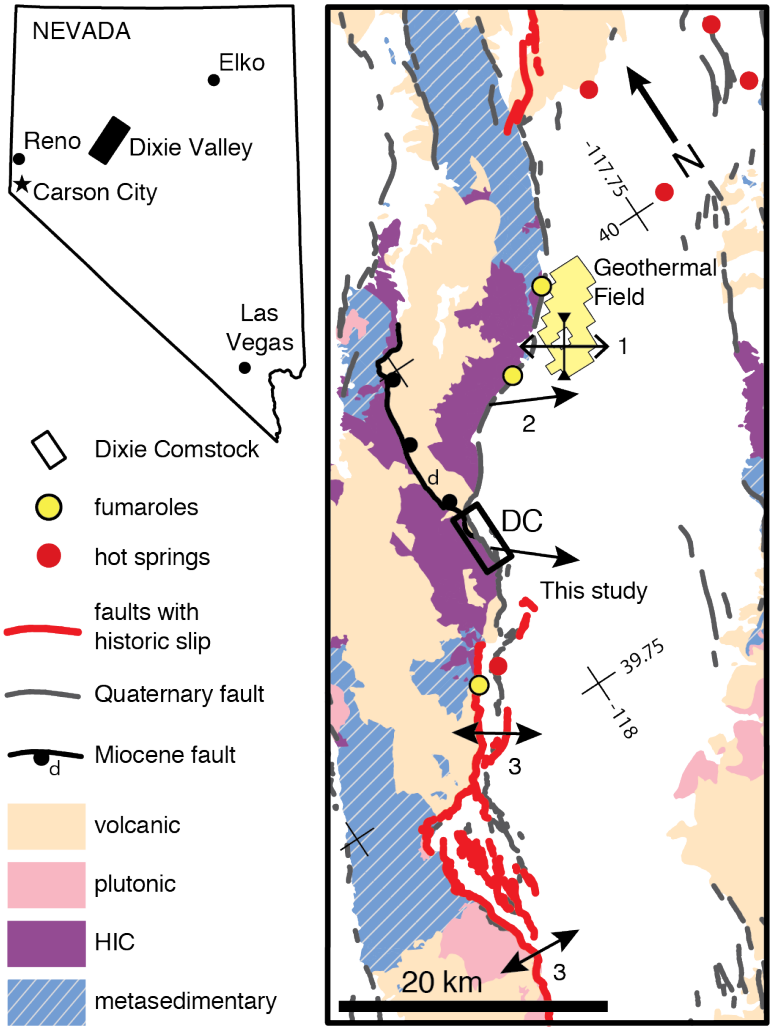

Figure 4.1. Regional map showing location of Dixie Valley (inset) and the Dixie Comstock epithermal deposit (DC). The epithermal deposit is hosted by a north-striking, east-dipping segment of the Dixie Valley - Stillwater fault zone, between fault segments with historic offset and active hydrothermal features. Fault orientation is partially controlled by the Miocene White Rock Canyon Fault, which places Oligocene volcaniclastics against the Jurassic Humboldt Igneous Complex (HIC). Modern stress orientations (1) are consistent with SE-NW extension indicated by fault striations (2) and SE-NW to E-W extension associated with the 1954 Dixie Valley earthquake (3) (Caskey et al., 1996; Caine, 1999; Hickman et al., 2007).

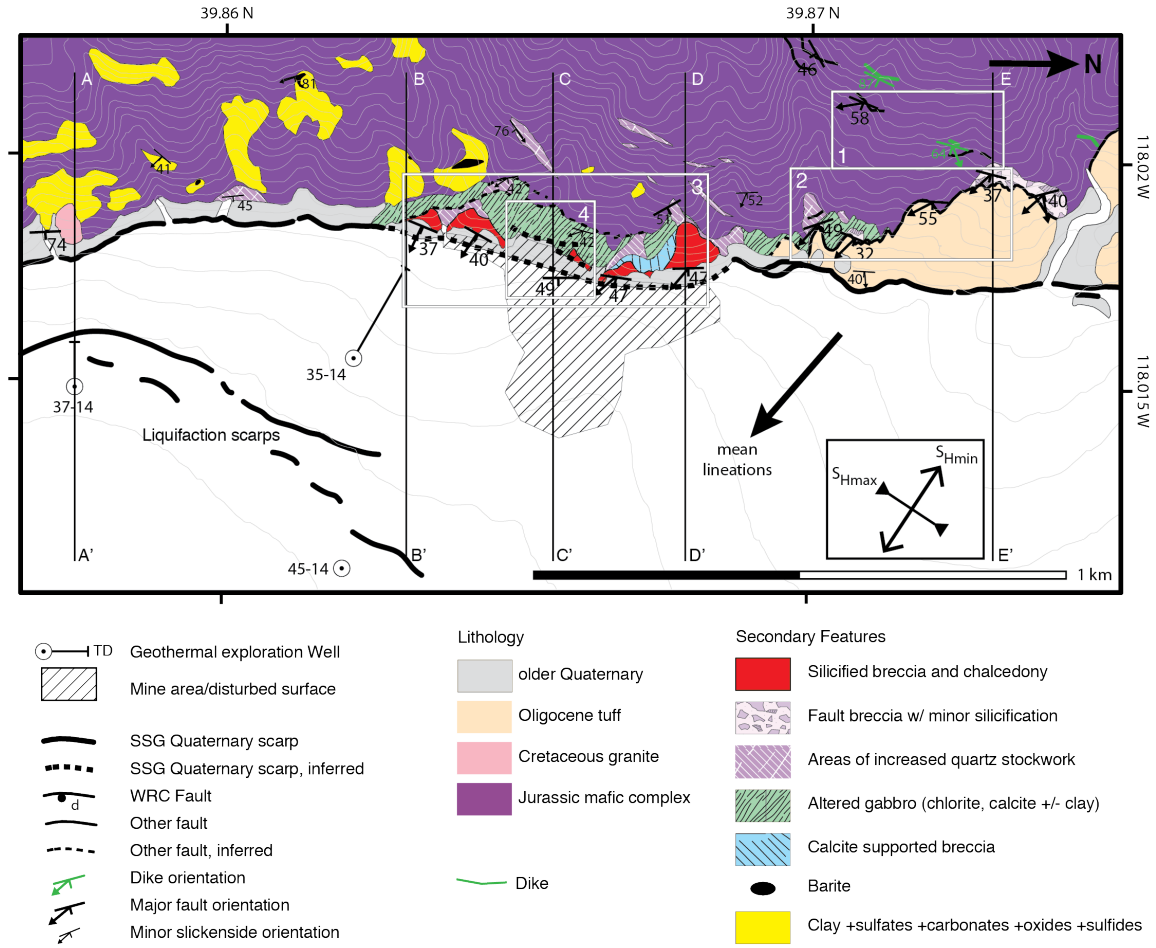

Figure 4.2. Geologic map of the Dixie Comstock epithermal deposit. Silicification and mineralization overprints a larger region of damage and chlorite, calcite ±clay altered gabbro. Lineations on silicified fault material trend ~130°, similar to average Dixie Valley extension directions and S_{hmin} from the producing geothermal field (Hickman et al., 2007). Carbonate, barite, sulfide, oxide, and clay alteration is associated with Cretaceous plutons. Background alteration in the Jurassic mafic complex is not differentiated but includes widespread chlorite + calcite alteration. Numbered boxes correspond to fault areas described in the text. Modified in part from (Vikre, 1993).

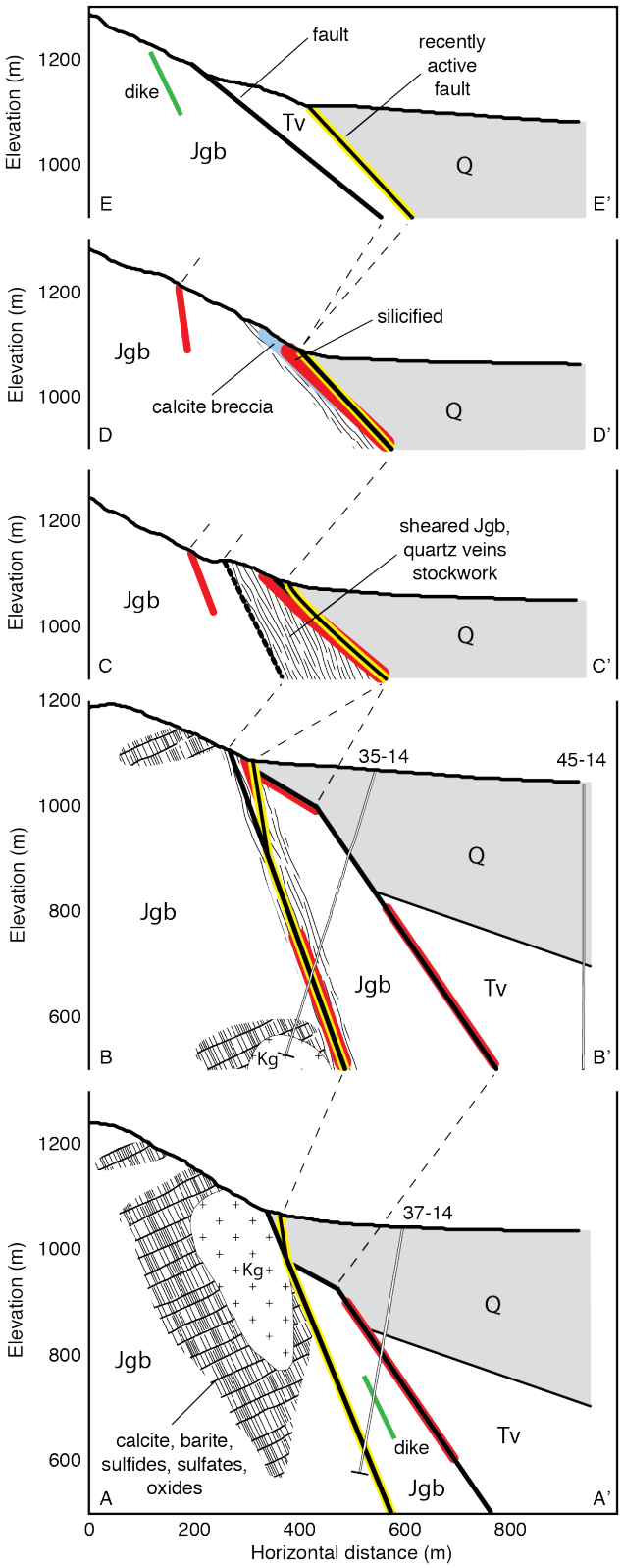

Figure 4.3. Serial cross sections from south to north, AA' to EE'. Transition of Quaternary slip (yellow) to basinward fault occurs near the southern end of the mine area (section BB'). Hydrothermal alteration and widening of fault zone damage and cemented fault core occur in the same interval. Well bore trajectories, and lithologic and fault contact interpretations for 37-14 and 35-14 provided by Robin Zuza, Ormat Technologies, Inc.

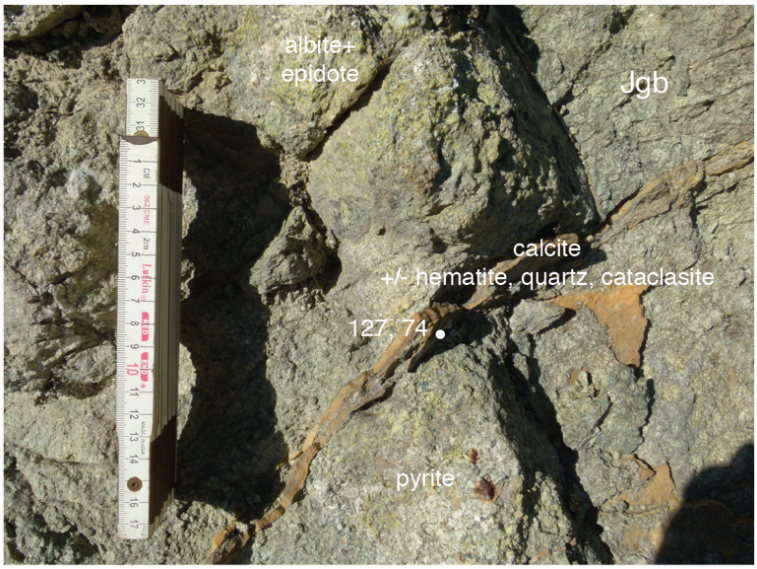

Figure 4.4. Example of inherited alteration and damage in the Jurassic Humboldt Igneous Complex (Jgb) in the footwall at Dixie Comstock.

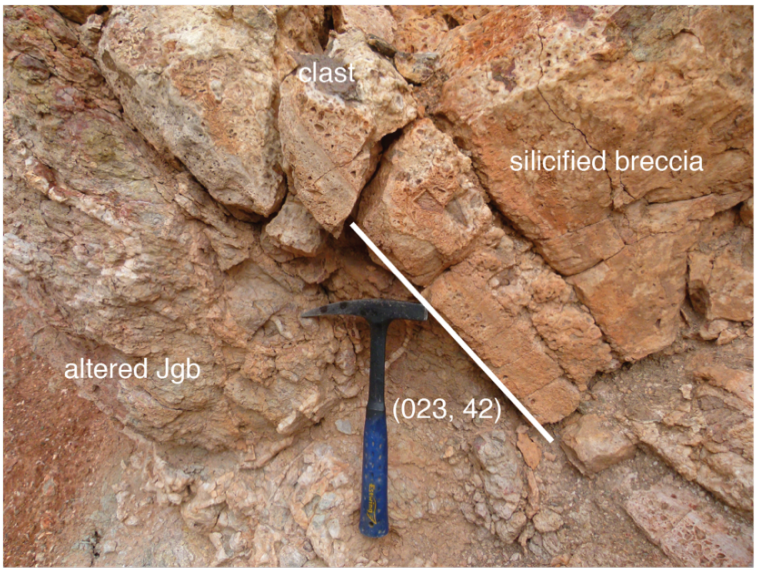

Figure 4.5. Silicified fault breccia, Dixie Comstock epithermal deposit. Clasts of altered and sheared gabbro from the footwall in matrix support, quartz cemented and silicified breccia.

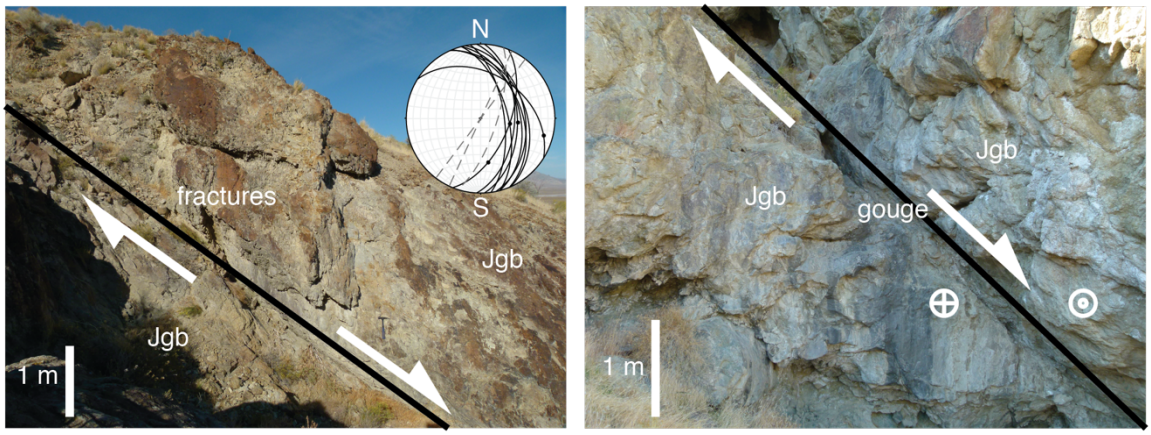

Figure 4.6. Small faults in footwall gabbro from Area 1 described in the text. Discrete slip surfaces are relatively planar, with minor (<10 cm thick) fault gouge. Stereonet shows orientations of small faults and associated open fractures in the northern part of the map area. Black lines are faults, dashed lines are open fractures.

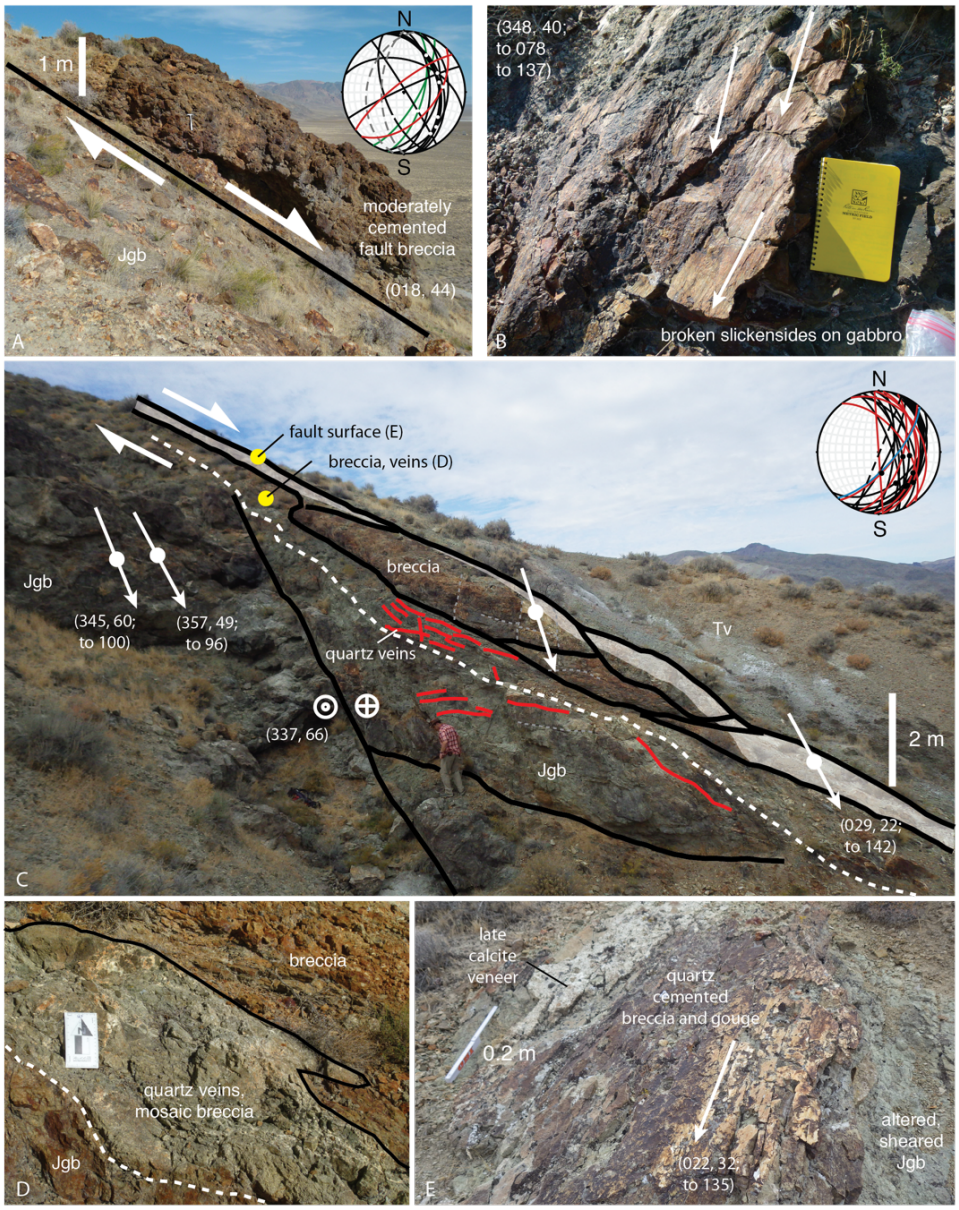

Figure 4.7. Faults in Area 2 juxtapose Oligocene volcanics against Humboldt Igneous Complex rocks (Jgb). A. Weak to moderate cementation of gabbro clasts. B. Minor silicification of fault breccia and gouge. C. Fault exposure in the southern part of Area 2. The top of Jgb contains a zone of increased shearing, fracturing, and low angle quartz veins, red (C, D) below quartz-cemented fault gouge and breccia (E). Minor quartz veins, brecciation, and normal faulting is observed in the volcanic units above. Yellow circles show locations of 4.7 D and 4.7 E. Black lines show faults. The green line in 4.7 A shows the orientation of a nearby basalt dike.

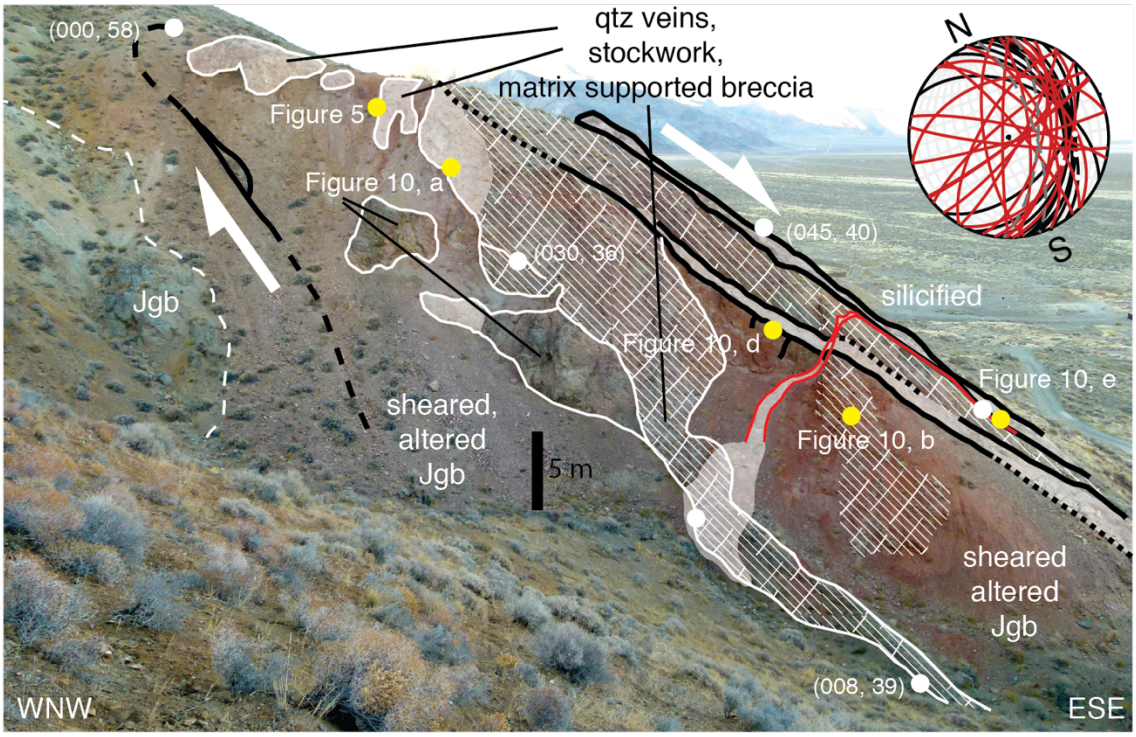

Figure 4.8. Range front fault exposure in Area 3, south of the mine. The silicified interval in this area is >3 m thick, with extensive damage and quartz cementation encountered >30 m behind the range front fault. Sections of fractured, moderately altered, quartz cemented gabbro with complex fracture networks are located between and incorporated into matrix supported graded breccia, silicified fault breccia, and quartz stockwork veins. Black lines in the photograph and stereonet depict fault orientations; red lines show quartz veins.

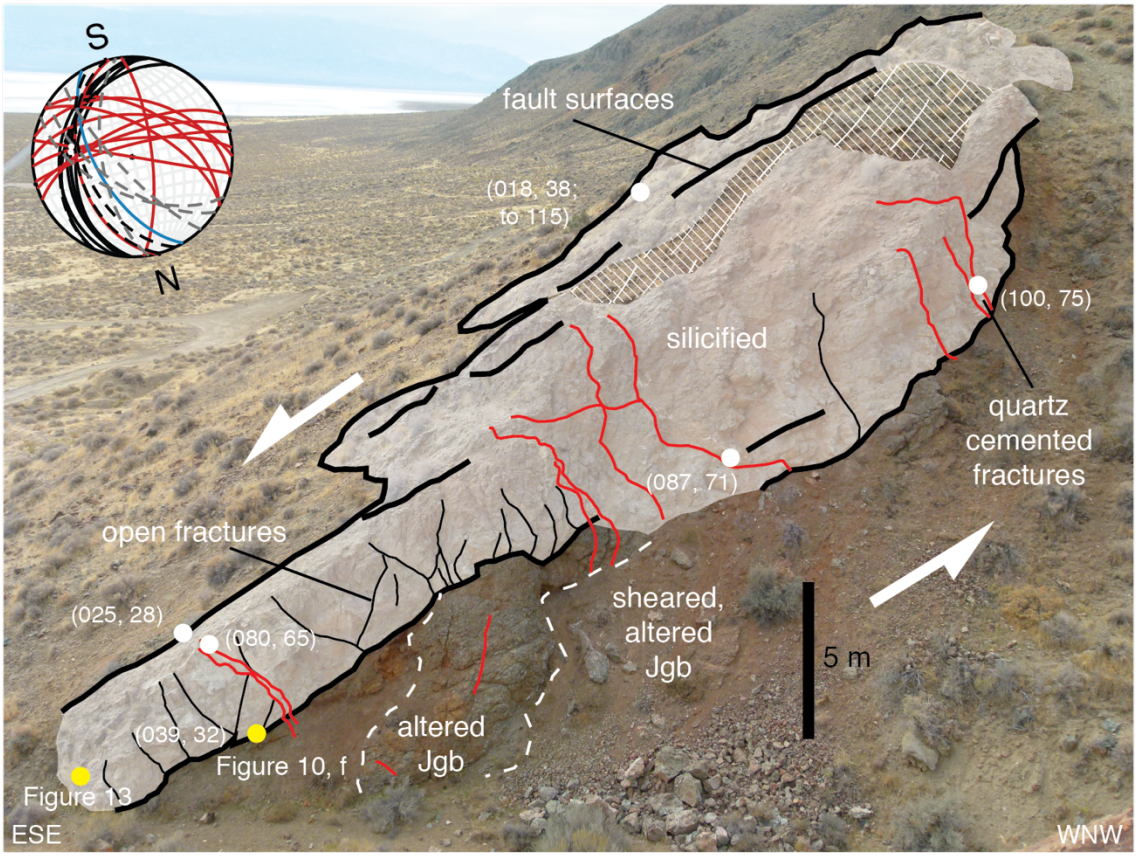

Figure 4.9. Southern end of the silicified fault interval in Area 3. Thick (>3 m) section of silicified fault breccia with incorporated gabbro clasts (boulders) with a distinct but undulatory basal shear zone above weakly altered Jgb with multiple generations of quartz veins. The silicified interval is broken by open fractures that sole into the sheared interval, and by steep ~E-W striking quartz-filled fractures that cut into the basal shear zone. Black lines in the photograph and stereonet depict fault orientations, red lines show quartz veins, blue lines are calcite veins, and dashed grey lines depict open fractures.

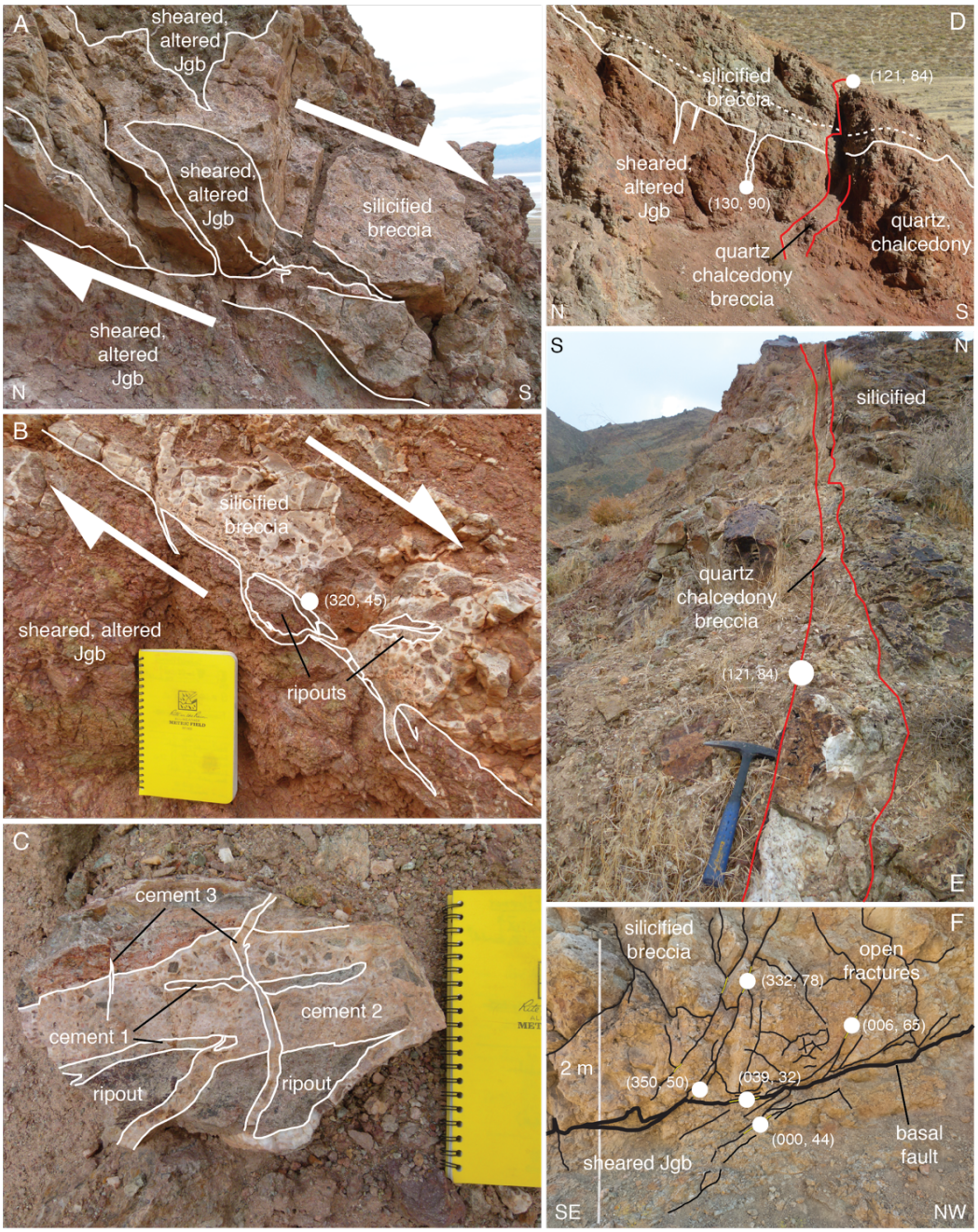

Figure 4.10. Selected fault zone elements from Area 3. A-C, incorporation of altered and sheared footwall into silicified fault breccia through (multiple generations of) fracturing and cementation. D, E, steep, ~E-W striking, quartz, chalcedony, and uncemented fractures cut the silicified breccia and penetrate into the altered footwall rocks. F. Some open fractures cutting thick silicified fault breccia sole into the basal shear zone.

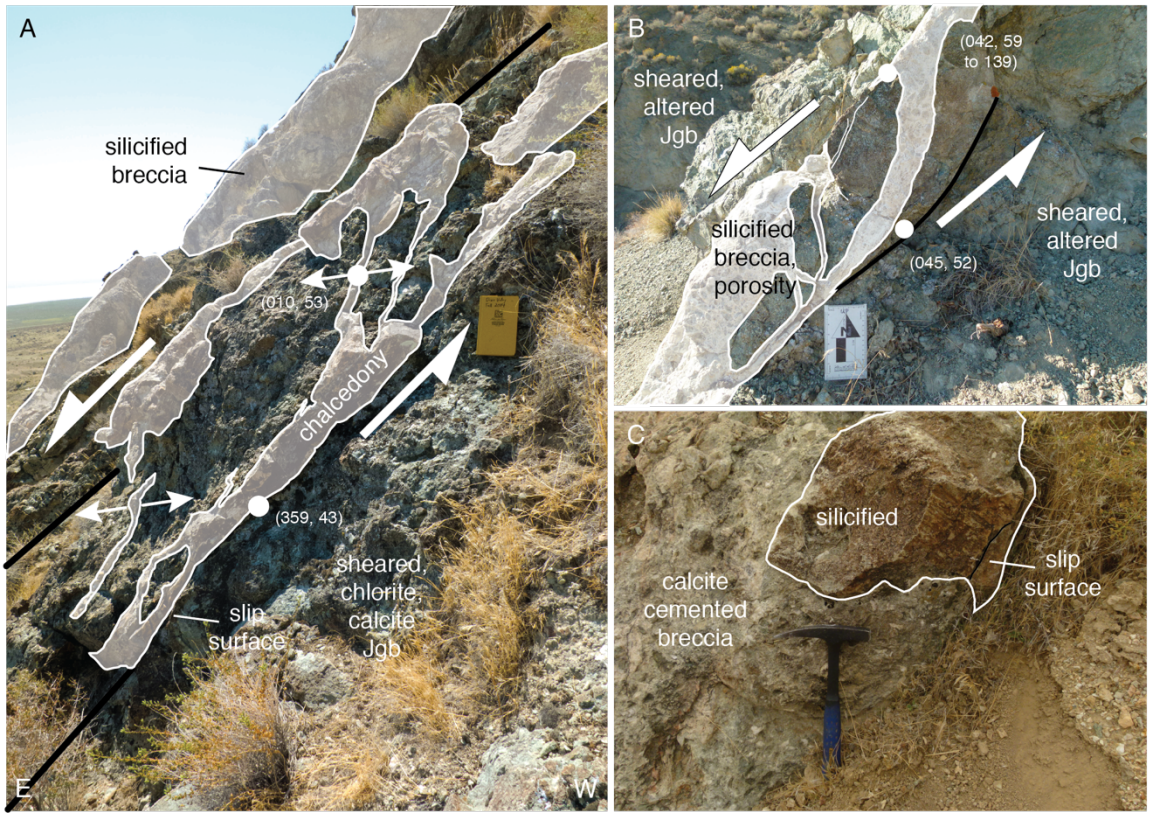

Figure 4.11. Footwall detail from northern silicified triangular facet, Area 3. A. Silicified breccia and chalcedony layers. A, B. Curved, mixed mode and dilatant pinnate fractures with chalcedony and quartz cemented graded breccia forming between slip surfaces in sheared, calcite-chlorite + quartz altered gabbro. Altered footwall material between these fractures may become isolated and incorporated into the silicified fault breccia. C. Large block of silicified fault breccia with slip surface in massive, calcite supported breccia. Calcite breccia is also incorporated into the silicified material.

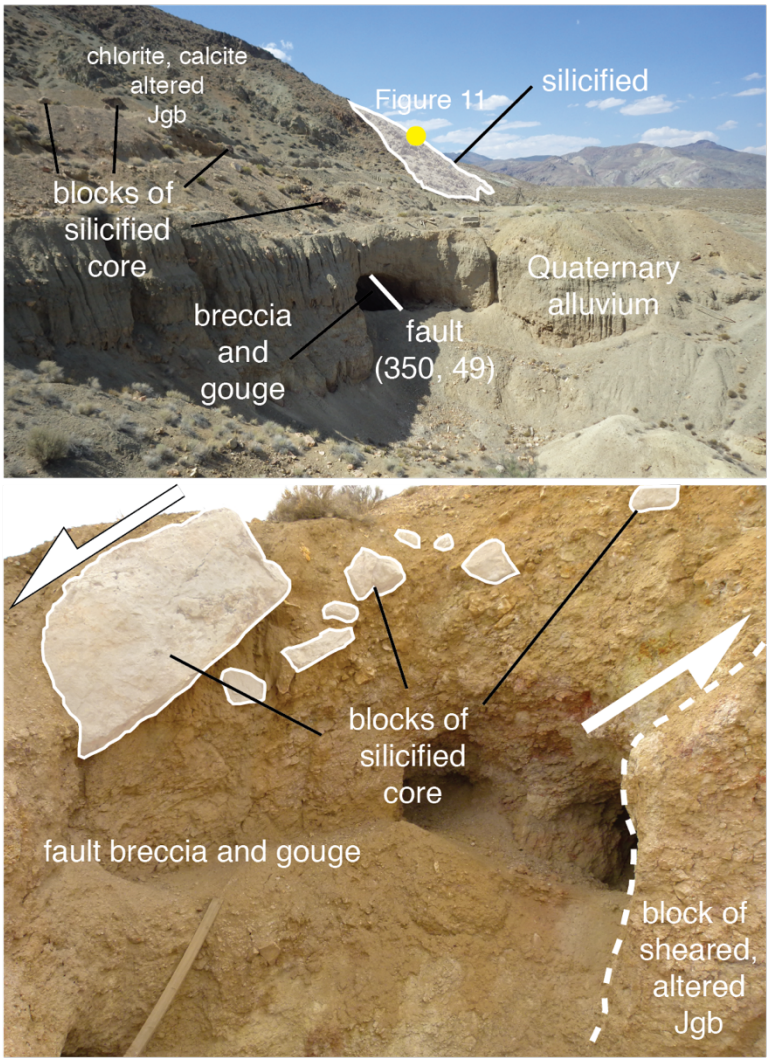

Figure 4.12. The range front fault exposed in the immediate vicinity of the mine, Area 4. Dislocated blocks of silicified fault breccia are spread out in clay-rich fault gouge and breccia. The range front steps into chlorite, calcite, and clay rich gabbro in the footwall, behind the former silicified facet.

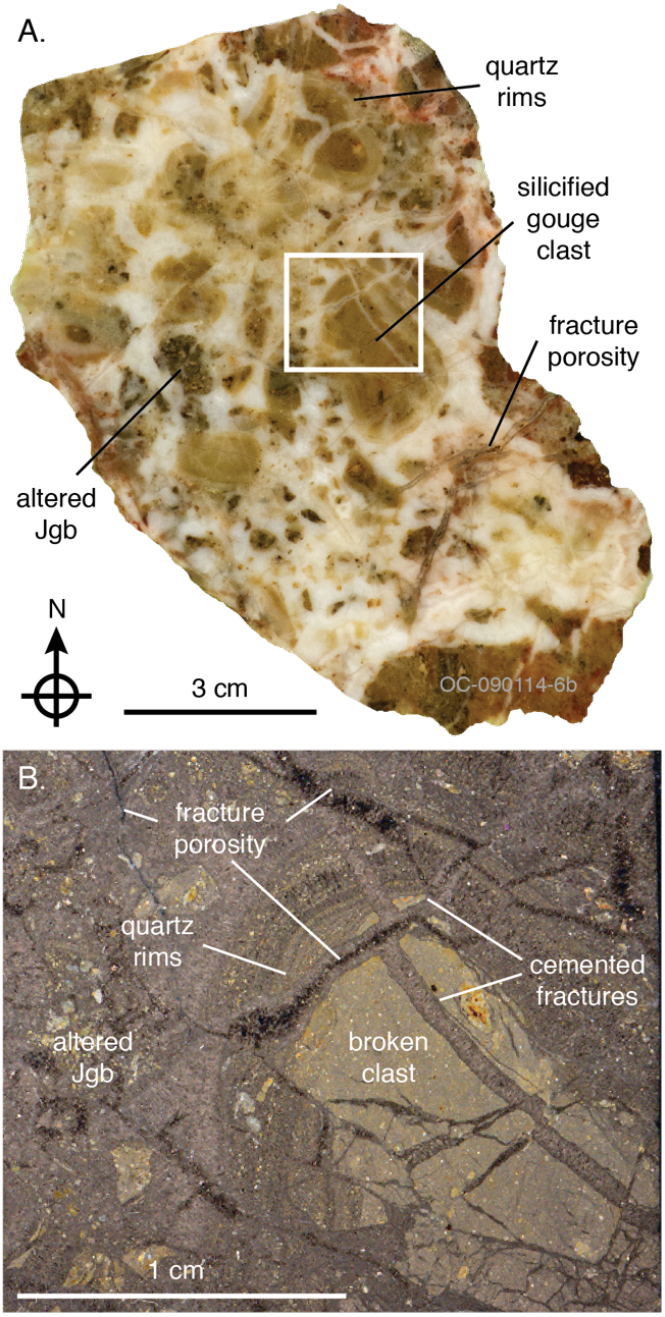

Figure 4.13. Multiple episodes of deformation, dilation, and cementation recorded in a slabbed sample (A) and associated scanned thin section (B) of silicified fault breccia from the southern part of Area 3 (Figure 4.9). Inset in upper photograph shows the location of the thin section scan, below.

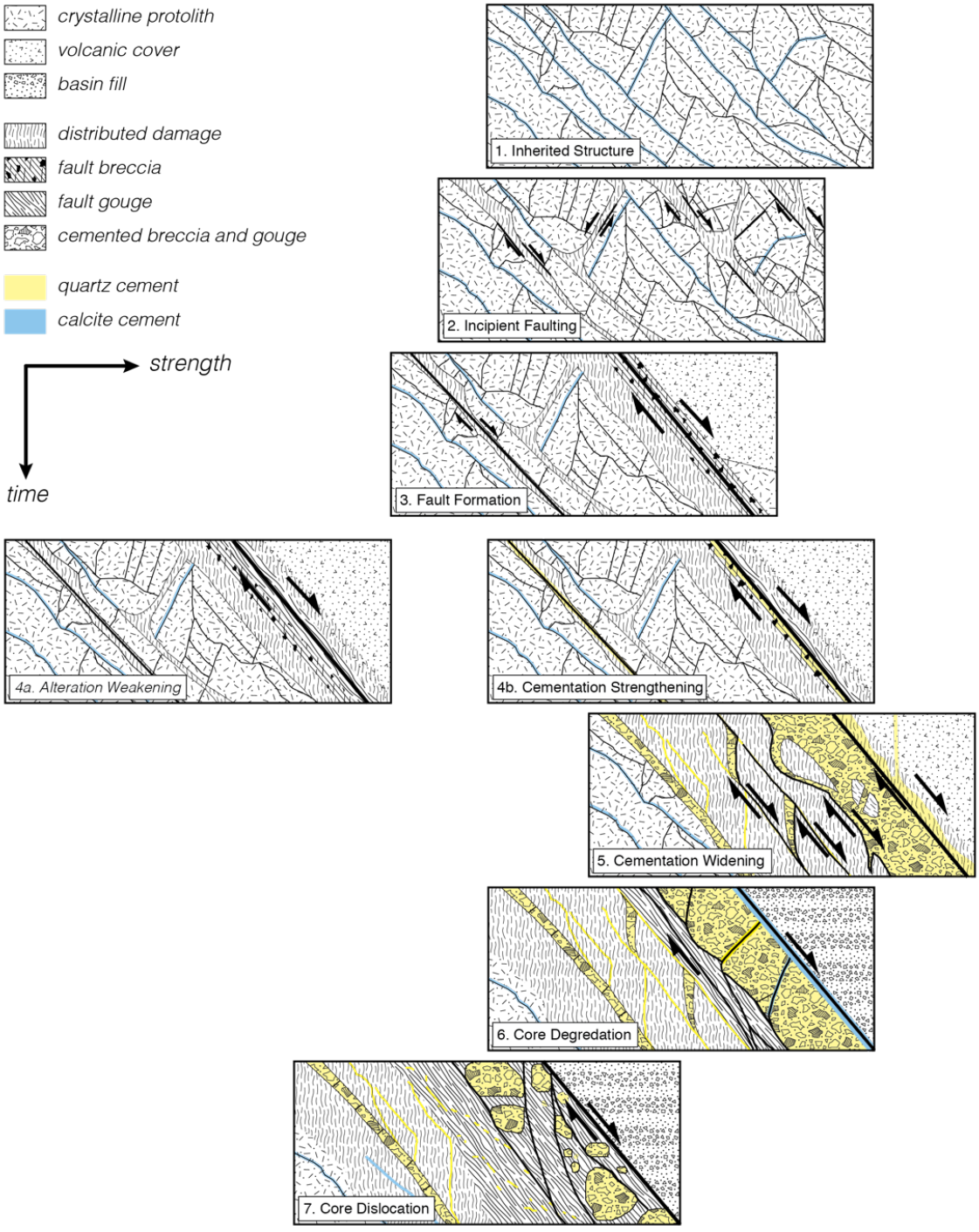

Figure 4.14. Caption on proceeding page.

Figure 4.14. Evolution of fault zone elements in alteration weakening and precipitation hardening regimes. 1 to 3) Fault formation and localization in previously altered and damaged host rock. 4) Minor cementation, healing, and strengthening of fault zone. 5) Precipitation dominated, accumulation widening of the fault zone in the epithermal environment. 6) Deformation begins to outpace cementation, and slip becomes localized at areas of high mechanical contrast, with fracturing in the more competent layers. 7) Break down of silicified core in a wide zone of previously damaged material in an alteration-weakening regime.

5. Synthesis

5.1 THE WORKS

This dissertation is composed of 3 main chapters prepared as manuscripts exploring different aspects of chemical-mechanical interactions in hydrothermal systems and the possible impact that these interactions may have on hydrothermal fluid flow in fault-fracture networks. Chapter 2, *Fracture-mechanical properties of damaged and hydrothermally altered rocks, Dixie Valley - Stillwater fault zone, Nevada, USA*, investigated rock and fracture mechanical properties of rocks exhumed from different hydrothermal environments. I demonstrated that 1) fault zone rocks contain varying degrees of alteration, damage, and healing depending on hydrothermal and deformation histories, 2) silicification increases compressive strength, fracture toughness, and subcritical index relative to chlorite-calcite altered material, and 3) sealing of microfractures by quartz and calcite is associated with strength recovery when remnant fracture porosity drops below ~15%. Chapter 3, *Experimental investigation of chemically aided fracture growth in silicified rocks*, focused on the impact of different physiochemical environments on fracture growth in silicified fault material from the Dixie Comstock epithermal deposit. Even in this end member material, with high strength and limited reactivity, 1) subcritical fracture growth depends upon chemical environment, 2) aqueous conditions increase fracture velocity by up to 2 orders of magnitude at lower stress intensities, 3) fracture velocity depends on dissolution rate at fracture tips, and 4) elevated temperature, pH, and salinity promote fracture growth in silicified rocks. Chapter 4, *The impact of hydrothermal alteration on fault zone evolution, Dixie Comstock epithermal deposit, Dixie Valley, NV,* explores the role of hydrothermal alteration in the evolution of fault-fracture networks from field observations and is informed by the petrographic and mechanical characterization completed in Chapters 2 and 3. The field relationships indicate that 1) strong, thick silicified fault breccia and wide, weak damage zones, 2) mixed mode dilatant failure within more altered footwall intervals in response to distributed shear, 3) evidence for repeated fracturing and sealing recorded in multiple breccia and cement types

and textures, 4) widening of the fault core through entrainment of damage zone material, and 5) eventual breakup of the fault core as deformation outpaces cementation. The target journal for these chapters are *Journal of Geophysical Research-Solid Earth*, *Geothermics*, and *Journal of Structural Geology*. Together these investigations form a body of work investigating chemical-mechanical interactions in materials and conditions relevant to hydrothermal systems, mineral deposits, and fault zones more generally.

5.2 Some Additional Findings

In addition to the key findings presented above, other observations, results, or relationships emerged from the work. These observations are included in the chapters, but are not explicitly highlighted due to the particular scope or focus of the works. Some pieces include important mechanical relationships described in Chapter 2 that underpinned interpretations in Chapter 3, whereas others represent side notes possibly worth revisiting in the future.

A great deal of work went into conducting and refining the fracture mechanical tests presented in Chapters 2 and 3. An early review of the double torsion testing method we used criticized the derivation of fracture toughness, K_{IC}, from slow loading tests. Experimental work has classically demonstrated a loading rate dependence on K_{IC}, but this does not apply to all materials (see discussion in Atkinson and Meredith (1987)). After retesting all of the samples, I found no consistent difference between toughness calculated from rapid or slow displacement tests (Figure 5.1). I presented and briefly discussed the linear correlation between K_{IC} and K_{IC}* in Chapter 2, and this relationship simplified our interpretation of K_{IC}* values during numerous and more labor-intensive environmental tests presented in Chapter 3. In addition, I observed a positive correlation between ambient K_{IC}, K_{IC}*, and UCS for all samples, which further enforces the assertion that results from the double torsion tests were meaningful and the change in toughness due to alteration and damage impacted other measures of rock strength.

I investigated but did not spend a great deal of time discussing the influence of mineral and structural heterogeneity in these samples on rock and fracture mechanical

properties. I initially hypothesized that fault core material would have different mechanical properties depending upon orientation. I conducted a suite UCS and DT tests from multiply oriented plugs and specimens of the Mirror fault core sample (052715-7). However, at the plug and specimen scale there was no significant difference between mechanical properties in the horizontal, down dip, or perpendicular orientations (Figure 5.2). The seemingly isotropic behavior of this material may arise from large errors associated with mechanical measurements, but could also reflect effective healing by mineral precipitation. Intense silicification of the Dixie Comstock fault core almost certainly resulted in a reduction in anisotropic behavior.

As part of Chapter 3, I conducted simple boundary element models to investigate the possible impact of changing SCI on fracture patterns in different chemical environments. Differences in SCI have been attributed to varying degrees of clustering and spacing (Olson, 1993, 2004), but changes in subcritical fracture growth also impart a time dependence on fracture accumulation and long term strength (Swanson, 1984; Fabre and Pellet, 2006; Brantut et al., 2013; Hashiba and Fukui, 2016). I use JOINTS, a pseudo-3D numerical fracture pattern simulator (Olson, 1993), to explore the impact that changing SCI under different chemical environments may have on fracture network growth. Model run times were limited to ~10,000 yrs, in an effort to capture changes in fracture patterns that might be possible in a hypothetical interseismic period, when subcritical growth is probably more important. The model results show the tendency towards fracture clusters at higher SCI and more evenly spaced fractures at lower SCI is present, but at the end of the model run the dominant effect is on fracture intensity, with lower SCI ultimately favoring more fracture growth (Figure 3.10). These models illustrate possible outcomes of changing SCI on fracture growth under different conditions, although specific subsurface strain boundary conditions, geometry, and chemical complexity will all effect the actual fracture patterns in the subsurface.

Outcrop-based work at Dixie Comstock revealed a wide variety of hydrothermal textures that were not fully explored in Chapter 4. Large bodies of calcite supported breccia, graded, matrix supported breccias, and cockade breccia with bladed calcite (Figure

5.3) may all reflect dynamic processes that were not included in the more steady-state conceptual model. Co-seismic rupture, rapid fluid flow, and boiling are clearly important factors in epithermal systems, and Dixie Comstock preserves a rich record of these processes worth further investigation.

5.3 LIMITATIONS

Throughout the dissertation, I use fracture intensity, tendency toward increased fracture intensity by reduction of K_{IC} and SCI, and type and degree of alteration or cement as proxies for fluid flow. The use of mineral cement as a record of past fluid conditions and pathways is well established (Eichhubl and Boles, 2000; Eichhubl et al., 2004; Eichhubl et al., 2009; Becker et al., 2010; Laubach et al., 2010). Massive silicification of gabbro and bladed calcite are both indications of substantial advection of high temperature fluids, but, like other proxies, these have limitations. The relationship between changing fracture mechanical properties, fracture intensity, and fluid flow is more tenuous. I did conduct preliminary investigations of fluid conditions, including fluid inclusion microthermometry and stable isotopes of calcite from veins and travertine in Dixie and Buena Vista valleys. However, the results did not add appreciably to the investigations and were not included in the text, other than to verify epithermal conditions reported by Vikre (1993).

In framing this research, I proposed a field-based approach so that results from the mechanical tests could be placed into a structural context. An unavoidable limitation of working with rocks collected in outcrop is the degree of retrograde alteration, mechanical damage, and weathering that overprints the original subsurface textures and compositions. This was particularly problematic in some fault-proximal Box Canyons materials presented in Chapter 2, where significant damage accumulated after the dominant phase of chlorite-calcite alteration. Due to the potential differences between outcrop samples and rocks in the subsurface, it was impossible to directly relate changes in mechanical properties to alteration assemblage or intensity. Instead, the impact of alteration and damage or healing had to be addressed together. Less ambiguous relationships between alteration type and

intensity and fracture mechanics may have been possible with rocks from a young magmatic or volcanically hosted system. Geomechanical testing of subsurface samples obtained from drill core is limited by availability of core and the required sample size, and samples from mines may be impacted by blasting. In the end the combination of alteration and damage observed in the Dixie Valley samples facilitated a more general discussion about the influence of damage-dominated versus healing-dominated settings on mechanical properties.

Similarly, the experimental conditions explored in Chapter 3 do not reflect the full range of physiochemical conditions found in hydrothermal systems. There was no simple way to add confining pressure, and temperatures in excess of ~65 °C resulted poor signal to noise ratios. Direct comparisons to subcritical fracture growth are therefore extrapolated and speculative. I demonstrated that physiochemical environments impact subcritical fracture growth in silicified rocks, but fluid conditions and rock types in hydrothermal systems are generally more complex. A site-specific investigation focusing on a suite of altered rocks and in situ fluid compositions may be useful if trying to characterize chemically-aided subcritical fracture growth in a specific geothermal resource.

The influence of observational scale on rock mechanics is another important topic that is not explicitly addressed. Relating laboratory measurements conducted on small samples to estimates of rock mass strength is a well know problem (Schmidt and Montgomery, 1995; Hoek and Brown, 1997; Griffith et al., 2009). As fracture networks become more connected, sliding friction and fracture interaction become increasingly important and the mechanical properties of a volume of rock deviate from those of a sample of that rock. By necessity, double torsion tests were conducted on small specimens prepared from relatively intact rock. When the propagation paths of induced fractures were clearly influenced by natural fractures, these tests were ignored because the geometric derivations of K_{IC} and SCI were violated (Figure 5.4). However, fracturing and deformation of highly damaged rock volumes is undoubtedly important in fault zones and hydrothermal systems. Outcrop-scale rock mass strength distribution around hydrothermal systems is something I would like to explore in more detail in future investigations.

5.4 CLOSING

Fault-hosted hydrothermal systems are complex. They are ephemeral, commonly superimposed on existing structures, and include temporal and spatial variation in fluid-rock interactions, geochemistry, mechanics, and permeability arising both from internal mechanism and external forces. Interactions between these processes result in positive and negative feedback mechanisms, impacting the lifecycle and productivity of geothermal resources, mineral deposits, and fault zone properties. One of the key topics that I frequently revisited in this dissertation is the different mechanical behavior in precipitation-dominated regimes versus damage-dominated regimes. The tendency toward precipitation, healing, and strengthening or toward damage, dissolution, and weakening happens in different places in hydrothermal systems and at different times. Generalizing spatial and temporal changes in the behavior of fault-fracture networks in hydrothermal systems into a strengthening vs weakening framework may serve as a useful conceptual model going forward.

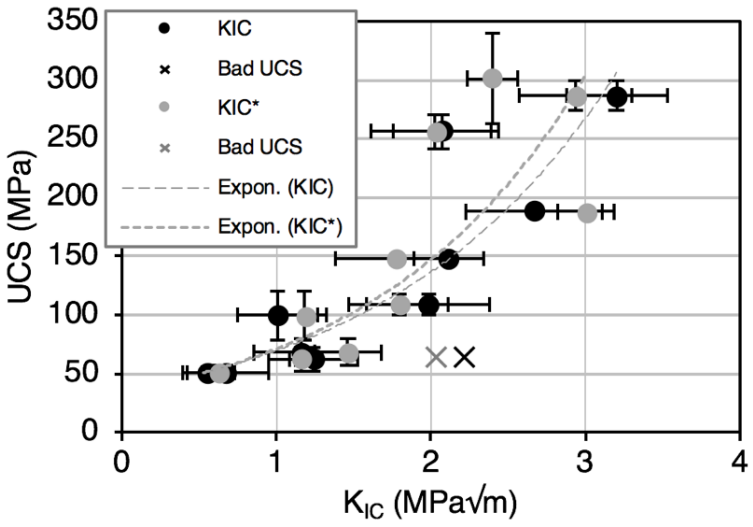

Figure 5.1. K_{IC} and K_{IC}* vs UCS for all samples tested. Similar positive correlations between K_{IC} and K_{IC}* vs UCS increase confidence that K_{IC} and K_{IC}* reflect similar approximations of fracture toughness, and that fracture toughness measured with the DT apparatus underpins bulk failure properties in these samples. Not all samples have a K_{IC}-K_{IC}* pair. The single UCS core from the sample marked "x" contained a natural fracture and failed early.

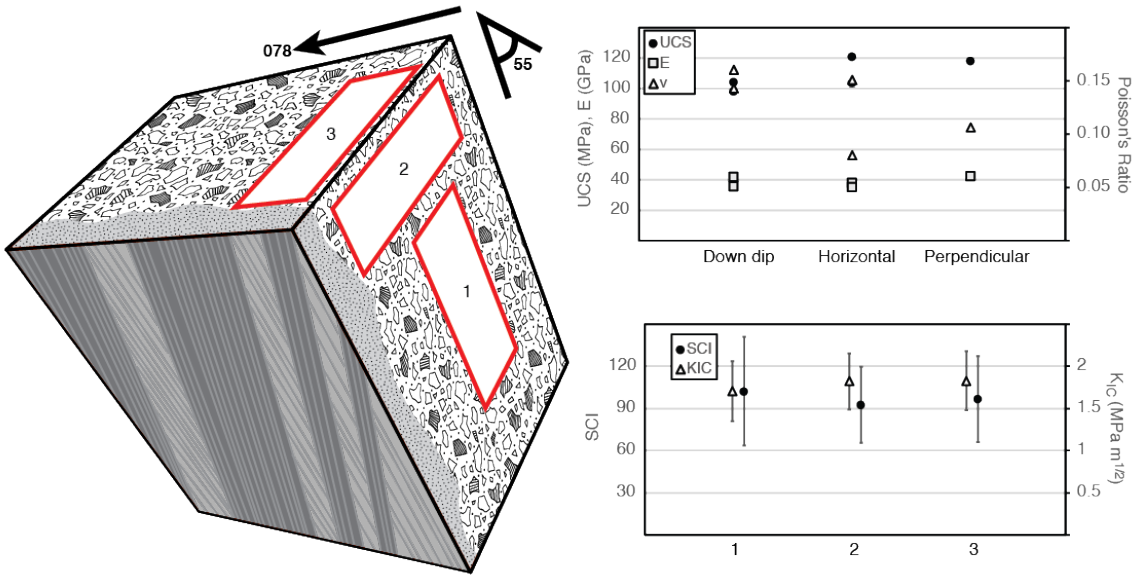

Figure 5.2. Rock and fracture mechanics results show little difference based on plug and specimen orientation for the Mirrors fault core sample.

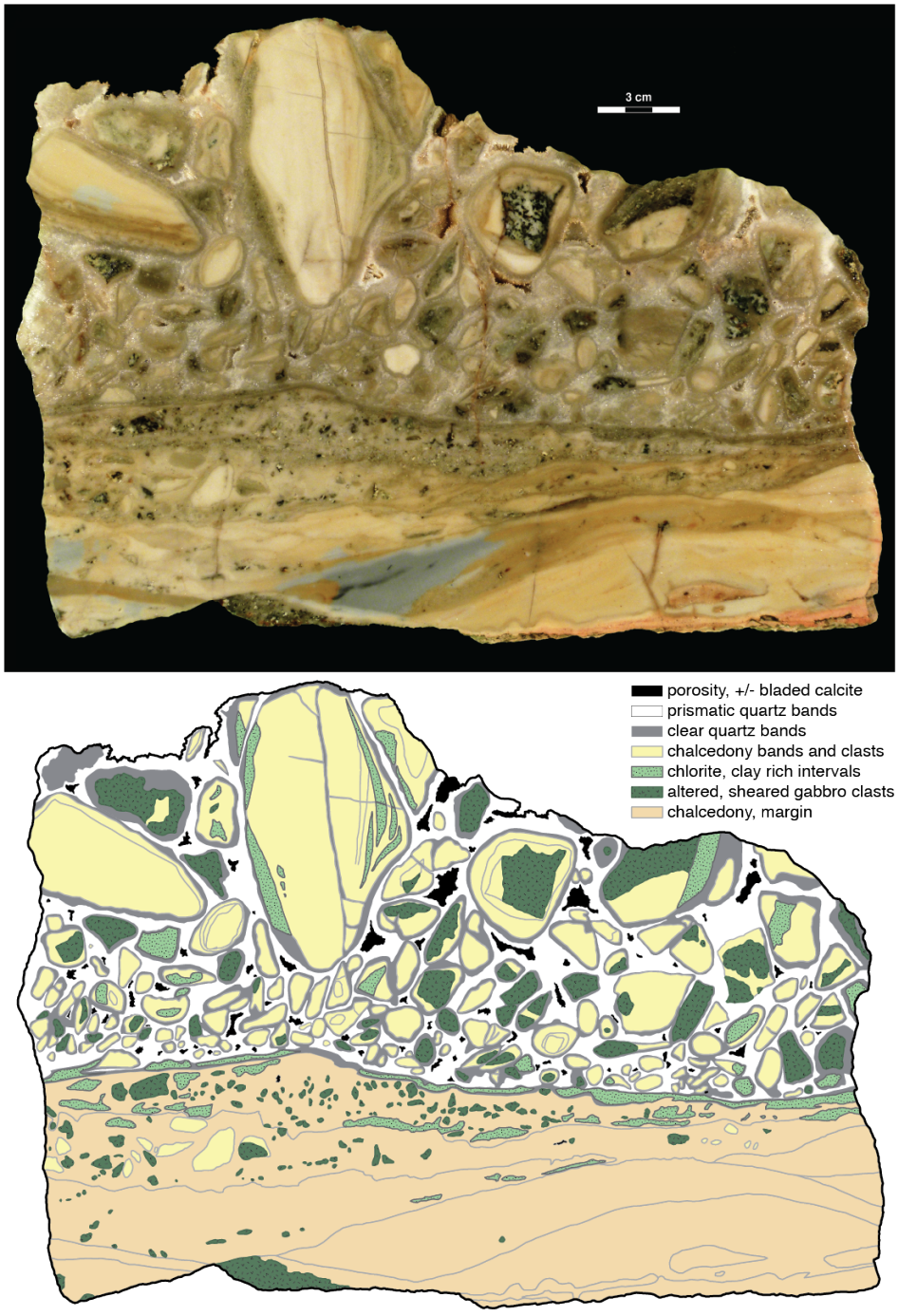

Figure 5.3. Slabbed Graded Cockade Breccia, Dixie Comstock Epithermal Deposit. Multiple clast and cement types indicate repeated cycles of deformation and cementation, and bladed calcite in partially open cavities indicates boiling conditions existed during part of the mineralization.

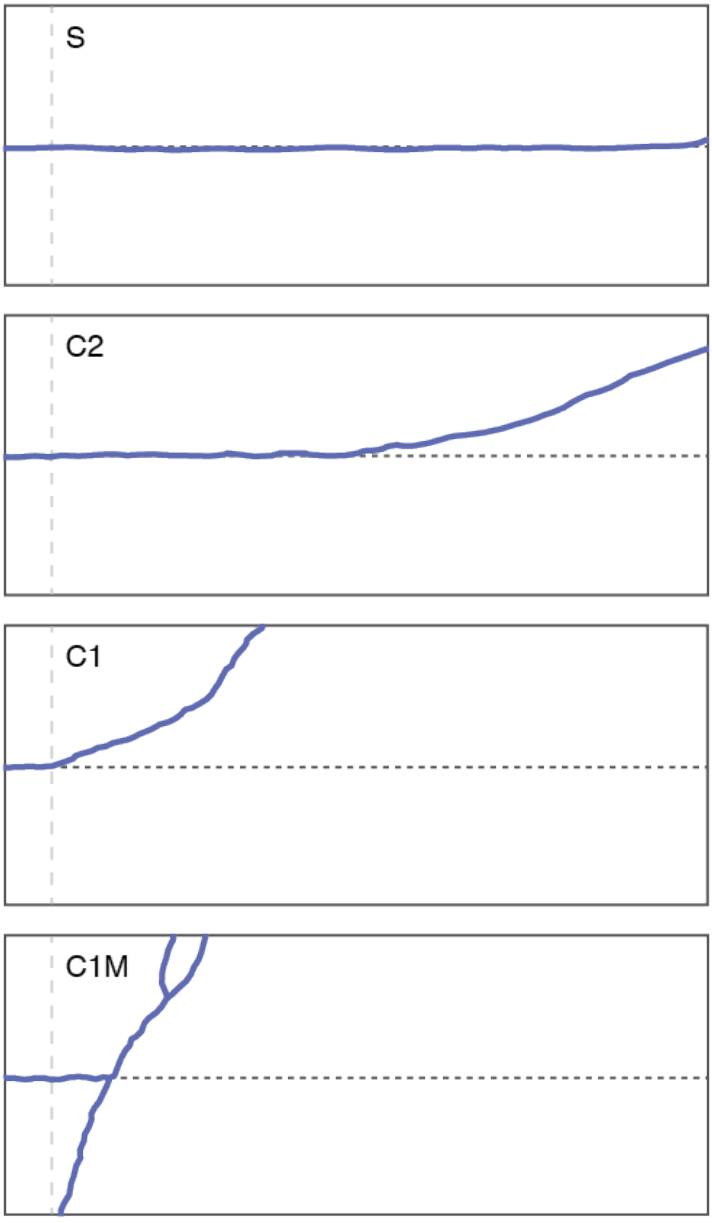

Figure 5.4. Common failure types observed during double torsion testing. S = straight fracture that propagated along the axial groove. C2 = fracture that propagated out of the axial groove at some point. C1 = fracture that propagated away from the axial groove at the loading lined (dashed). C1M = multiple strands or branching fracture. SCI and K_{IC}* were calculated from S specimens, and from early load decays in C2 specimens. C1, C2, and M specimens frequently showed interaction with natural fractures.

A. Appendix: Sample Identification and Locations

Table A.1. Sample Locations, Site Names, and Descriptions

Sample	Northing* (m)	Easting* (m)	Elevation (m)	Site	Material
052915-1A	4537136	551049	1409	Gold Strike, Betze-Post	Popovich Fm, upper mud, moderately silicified
052915-2A	4537497	551152	1442	Gold Strike, Betze-Post	Rodeo Creek Fm, lower argillite, silicified mudstone
052915-2B	4537522	551177	1447	Gold Strike, Betze-Post	Rodeo Creek Fm, fresh to more argillic material
052915-3	4537758	551426	1479	Gold Strike, Betze-Post	Rodeo Creek Fm, basal sandstone
052915-4A	4537372	551255	1290	Gold Strike, Betze-Post	Popovich Fm, Wispy Member, w/ calcite
052915-4B	4537355	551233	1290	Gold Strike, Betze-Post	Popovich Fm, Wispy Member, minor silica
052915-4C	4537337	551211	1290	Gold Strike, Betze-Post	Popovich Fm, silicified debris flow
052915-4D	4537321	551201	1290	Gold Strike, Betze-Post	dike (lamprophyre)
052915-4E	4537309	551188	1290	Gold Strike, Betze-Post	Popovich Fm, unsilicified debris flow
072213-6	4426505	426054	1164	Dixie Valley, Black Canyon	Humboldt Igneous Complex, cemented breccia
031214-1A	4383023	398126	1294	Dixie Valley, Box Canyons	granite, sericite, qtz veins
031214-2	4383023	398126	1294	Dixie Valley, Box Canyons	granite, sericite, qtz veins
052615-1A	4385629	398938	1269	Dixie Valley, Box Canyons	mafic plutonic
052615-1B	4385629	398936	1272	Dixie Valley, Box Canyons	felsic plutonic
052615-2A	4386097	399328	1194	Dixie Valley, Box Canyons	altered plutonic (chl, cal, hem)
052615-2B	4386097	399328	1194	Dixie Valley, Box Canyons	altered plutonic (chl, cal, hem)
060914-1	4386112	399210	1238	Dixie Valley, Box Canyons	Oligocene granodiorite
060914-2	4386087	399312	1200	Dixie Valley, Box Canyons	Oligocene granodiorite, chl, hem, cal
060914-3	4385343	398582	1324	Dixie Valley, Box Canyons	Oligocene granodiorite
071413-1	4384781	398364	1302	Dixie Valley, Box Canyons	quartz vein in granite

*NAD83, UTM Zone 11 N

Sample	Northing* (m)	Easting* (m)	Elevation (m)	Site	Material
071413-2	4385288	398577	1322	Dixie Valley, Box Canyons	fractured (cataclastic) granite
071813-1	4386110	399275	1233	Dixie Valley, Box Canyons	cataclasite, qtz, chl, cal, hem altered plutonic
071813-2	4386084	399334	1198	Dixie Valley, Box Canyons	chl, cal, hem altered plutonic
071813-3	4385280	398673	1282	Dixie Valley, Box Canyons	granite
083014-1	4385298	398657	1288	Dixie Valley, Box Canyons	Oligocene (Miocene?) granodiorite
083014-2	4385396	398289	1342	Dixie Valley, Box Canyons	Oligocene (Miocene?) volcanic
083014-3	4385286	398581	1315	Dixie Valley, Box Canyons	Oligocene (Miocene?) granodiorite
052715-4A	4425651	425295	1150	Dixie Valley, Cottonwood Canyon	Quaternary (?) blocky calcite
052715-4B	4425645	425303	1145	Dixie Valley, Cottonwood Canyon	travertine
052715-5	4425517	425120	1178	Dixie Valley, Cottonwood Canyon	botryoidal calcite vein in talus
060314-A1	4425276	424817	1201	Dixie Valley, Cottonwood Canyon	Boyer Formation, oxide vein
060314-A2	4425276	424817	1201	Dixie Valley, Cottonwood Canyon	oxide
061214-10	4425225	424797	1174	Dixie Valley, Cottonwood Canyon	white material around fumarole
061214-8	4425514	425120	1177	Dixie Valley, Cottonwood Canyon	Boyer Formation, near dike
061214-9	4425224	424784	1178	Dixie Valley, Cottonwood Canyon	orange porous (fumarole?) material
072013-1	4425367	424727	1184	Dixie Valley, Cottonwood Canyon	Boyer Formation, fine grained section
072013-2	4425355	424718	1175	Dixie Valley, Cottonwood Canyon	Boyer Formation, with red staining
072013-3	4425366	424716	1180	Dixie Valley, Cottonwood Canyon	Boyer Formation, open vein in float
072013-4	4425232	424817	1173	Dixie Valley, Cottonwood Canyon	altered brown/green section in quarry
072013-5	4425232	424820	1174	Dixie Valley, Cottonwood Canyon	faulted Boyer Formation section
072213-12	4425234	424818	1174	Dixie Valley, Cottonwood Canyon	quarry, green, pearly, unoriented
072213-13	4425232	424809	1176	Dixie Valley, Cottonwood Canyon	quarry, yellow section (mafic)
072213-14	4425226	424799	1174	Dixie Valley, Cottonwood Canyon	quarry, white, crumbly
072213-15	4425225	424787	1178	Dixie Valley, Cottonwood Canyon	quarry, clastic dike
072213-16	4425225	424782	1180	Dixie Valley, Cottonwood Canyon	quarry, red section
072213-17	4425223	424765	1183	Dixie Valley, Cottonwood Canyon	quarry, black + gypsum section

Sample	Northing* (m)	Easting* (m)	Elevation (m)	Site	Material
072213-3	4425362	424725	1185	Dixie Valley, Cottonwood Canyon	Boyer Formation, calcite, Liesegang banding
072213-4	4425360	424722	1186	Dixie Valley, Cottonwood Canyon	Boyer Formation, cemented breccia
072213-5	4425310	424705	1183	Dixie Valley, Cottonwood Canyon	Boyer Formation, thick vein with oblique bridges
072313-1A	4425303	424709	1186	Dixie Valley, Cottonwood Canyon	Boyer Formation
072313-1B	4425303	424709	1186	Dixie Valley, Cottonwood Canyon	Boyer Formation
072313-1C	4425303	424709	1186	Dixie Valley, Cottonwood Canyon	Boyer Formation
030814-1	4414134	412801	1115	Dixie Valley, Dixie Comstock	calcite and oxide material in gabbro
030814-2	4414080	412869	1137	Dixie Valley, Dixie Comstock	hydrothermal quartz breccia in Oligocene Tuff
031114-1	4412776	412665	1180	Dixie Valley, Dixie Comstock	calcite, barite, sulfide zone
052615-4	4413817	412898	1120	Dixie Valley, Dixie Comstock	calcite in large vein in gabbro
052615-5	4413526	412971	1095	Dixie Valley, Dixie Comstock	calcite in bladed calcite/chlorite breccia
052615-6A	4413449	412957	1093	Dixie Valley, Dixie Comstock	bladed calcite in vertical veins
052615-6B	4413448	412956	1093	Dixie Valley, Dixie Comstock	blocky calcite filling quartz lined vugs
052815-1	4413171	412764	1125	Dixie Valley, Dixie Comstock	calcite from barite, oxide zone
052815-2	4413210	412885	1115	Dixie Valley, Dixie Comstock	silicified fault zone
052815-3A	4413298	412864	1105	Dixie Valley, Dixie Comstock	fine grained cal, chl, hem, pyr gabbro
052815-3B	4413298	412864	1105	Dixie Valley, Dixie Comstock	fine grained chl gabbro
052815-4A	4413524	412981	1089	Dixie Valley, Dixie Comstock	silicified material
052815-4B	4413524	412981	1089	Dixie Valley, Dixie Comstock	silicified fault material
052815-4C	4413524	412981	1089	Dixie Valley, Dixie Comstock	calcite breccia material
061014-1A	4414172	412781	1198	Dixie Valley, Dixie Comstock	brecciated medium grained gabbro
061014-1B	4414171	412781	1198	Dixie Valley, Dixie Comstock	gabbro
061014-2A	4413880	412867	1142	Dixie Valley, Dixie Comstock	gabbro
061014-2B	4413877	412869	1142	Dixie Valley, Dixie Comstock	gabbro
061014-3	4413643	412956	1098	Dixie Valley, Dixie Comstock	calcite and Humboldt
061114-1	4412372	412805	1127	Dixie Valley, Dixie Comstock	altered around granodiorite

Sample	Northing* (m)	Easting* (m)	Elevation (m)	Site	Material
061114-2	4412372	412870	1095	Dixie Valley, Dixie Comstock	altered granodiorite
061114-3A	4412577	412815	1122	Dixie Valley, Dixie Comstock	epidote and albitized zone?
061114-3B	4412576	412816	1122	Dixie Valley, Dixie Comstock	epidote and albitized zone?
061114-4A	4413095	412874	1108	Dixie Valley, Dixie Comstock	silicified gabbro
061114-4B	4413103	412871	1110	Dixie Valley, Dixie Comstock	silicified gabbro
061214-5	4413390	412918	1103	Dixie Valley, Dixie Comstock	altered gabbro near main deposit
061214-6	4413470	412975	1092	Dixie Valley, Dixie Comstock	silicified breccia
061214-7A	4413523	412984	1088	Dixie Valley, Dixie Comstock	silicified, rounded breccia
061214-7B	4413522	412983	1088	Dixie Valley, Dixie Comstock	silicified, vuggy
061214-7C	4413524	412986	1086	Dixie Valley, Dixie Comstock	silicified (altered dike/tuff?)
061214-7D	4413522	412984	1088	Dixie Valley, Dixie Comstock	calcite breccia
072013-7	4413152	412873	1108	Dixie Valley, Dixie Comstock	silicified gabbro, qtz vein
083114-1A	4412734	412823	1106	Dixie Valley, Dixie Comstock	coarse grained gabbro
083114-1B	4412735	412822	1107	Dixie Valley, Dixie Comstock	coarse grained gabbro
083114-1C	4412733	412825	1105	Dixie Valley, Dixie Comstock	coarse grained gabbro
083114-1D	4412732	412828	1104	Dixie Valley, Dixie Comstock	coarse grained gabbro
083114-2A	4413881	412870	1141	Dixie Valley, Dixie Comstock	medium grained gabbro, below fault zone
083114-2B	4413881	412870	1140	Dixie Valley, Dixie Comstock	medium grained gabbro, below fault zone
090114-1	4413882	412922	1116	Dixie Valley, Dixie Comstock	quartz filled breccia, near southern edge of tuff
090114-2	4413647	412940	1108	Dixie Valley, Dixie Comstock	silicified gabbro breccia
090114-3	4413592	412949	1112	Dixie Valley, Dixie Comstock	chalcedony
090114-4	4413615	412953	1103	Dixie Valley, Dixie Comstock	altered fine grained gabbro
090114-5A	4413525	412981	1096	Dixie Valley, Dixie Comstock	vuggy silica
090114-5B	4413526	412980	1097	Dixie Valley, Dixie Comstock	silicified fault zone
090114-5C	4413527	412978	1090	Dixie Valley, Dixie Comstock	qtz-cal breccia in gabbro
090114-6A	4413126	412889	1099	Dixie Valley, Dixie Comstock	massive silica

Sample	Northing* (m)	Easting* (m)	Elevation (m)	Site	Material
090114-6B	4413128	412878	1102	Dixie Valley, Dixie Comstock	altered/weathered gabbro, qtz veins
090314-2B	4413440	412971	1087	Dixie Valley, Dixie Comstock	replaced calcite blades
090314-2C	4413446	412960	1091	Dixie Valley, Dixie Comstock	altered gabbro
102917-1	4413137	412858	1100	Dixie Valley, Dixie Comstock	cockade breccia in background
103017-1	4413837	412891	1120	Dixie Valley, Dixie Comstock	cemented interval
103017-2	4413837	412891	1120	Dixie Valley, Dixie Comstock	cemented interval, float
103017-3	4413899	412906	1132	Dixie Valley, Dixie Comstock	cemented breccia below slip surface
103117-1	4413822	412827	1139	Dixie Valley, Dixie Comstock	float, qtz calcite vein
110117-1a	4412380	412846	1112	Dixie Valley, Dixie Comstock	qtz vein
110117-1b	4412380	412846	1112	Dixie Valley, Dixie Comstock	highly altered rock above granite
110117-2	4412413	412870	1108	Dixie Valley, Dixie Comstock	Cretaceous granite
110117-3a	4412577	412789	1130	Dixie Valley, Dixie Comstock	qtz vein, background
110117-3b	4412577	412789	1130	Dixie Valley, Dixie Comstock	calcite vein
110117-4	4412719	412707	1138	Dixie Valley, Dixie Comstock	rhombic calcite for isotopes
110117-5	4413110	412798	1144	Dixie Valley, Dixie Comstock	weathered gabbro in gypsum area
110217-1	4413686	412901	1119	Dixie Valley, Dixie Comstock	top of shear dilatant breccia
110217-2	4413690	412773	1187	Dixie Valley, Dixie Comstock	limey sand
110217-3	4413672	412775	1183	Dixie Valley, Dixie Comstock	qtz stockwork/gabbro breccia
110217-4	4413478	412696	1248	Dixie Valley, Dixie Comstock	qtz veins in fine gabbro
110217-5	4413555	412859	1167	Dixie Valley, Dixie Comstock	large dilatant vein at slide top
110217-6	4413617	412915	1135	Dixie Valley, Dixie Comstock	gabbro sample (green clay gabbro)
110317-1	4413664	412915	1115	Dixie Valley, Dixie Comstock	rhombic calcite for isotopes
110317-2	4413283	412903	1096	Dixie Valley, Dixie Comstock	hematite and kaolinite?
110317-3	4413193	412873	1123	Dixie Valley, Dixie Comstock	silicified fault breccia
110317-4	4413238	412808	1149	Dixie Valley, Dixie Comstock	cockade breccia
110317-5a	4413281	412701	1156	Dixie Valley, Dixie Comstock	unusual morphology in float

Sample	Northing* (m)	Easting* (m)	Elevation (m)	Site	Material
110317-5b	4413281	412701	1156	Dixie Valley, Dixie Comstock	botryoidal and breccia
110317-5c	4413281	412701	1156	Dixie Valley, Dixie Comstock	botryoidal and breccia
110317-X	4413392	412772	1167	Dixie Valley, Dixie Comstock	punky gabbro
110317-6	4413309	412845	1116	Dixie Valley, Dixie Comstock	heavy black material
110317-7	4413487	412829	1162	Dixie Valley, Dixie Comstock	more silicified bright oxide zone
110317-8	4413517	412803	1189	Dixie Valley, Dixie Comstock	qtz breccia vein in coarse gabbro
110317-9	4413489	412931	1123	Dixie Valley, Dixie Comstock	veins that look like bladed calcite
110417-1	4413891	412903	1130	Dixie Valley, Dixie Comstock	late calcite breccia (surficial?)
110417-2	4413523	412986	1094	Dixie Valley, Dixie Comstock	high silica (felsic dike?)
110417-3	4413522	412974	1094	Dixie Valley, Dixie Comstock	calcite breccia
110417-4	4413190	412841	1131	Dixie Valley, Dixie Comstock	matrix supported breccia
110417-5	4413190	412841	1131	Dixie Valley, Dixie Comstock	silicified breccia
110417-6	4413146	412883	1104	Dixie Valley, Dixie Comstock	wide late quartz vein
052615-3A	4405598	406895	1115	Dixie Valley, Dixie Meadows	tuff
052615-3B	4405632	406899	1120	Dixie Valley, Dixie Meadows	silica cemented bladed calcite breccia
052615-3C	4405632	406899	1120	Dixie Valley, Dixie Meadows	silica cemented bladed calcite breccia
071313-1	4374982	395695	1478	Dixie Valley, Elevenmile Canyon	hematite, silicified, float
071313-2	4375529	396349	1437	Dixie Valley, Elevenmile Canyon	quartz and native sulfur in tuff
052715-6A	4422945	421316	1118	Dixie Valley, Frying Pan Fumaroles	opal, geyserite
053015-1	4473238	424953	1398	Buena Vista Valley, Kyle Hot Springs	sinter, travertine
030914-1	4422278	419228	1151	Dixie Valley, Mirrors	fault damage zone material
052715-7A	4422269	419198	1163	Dixie Valley, Mirrors	cemented fault core
060314-C1	4422322	419220	1188	Dixie Valley, Mirrors	quartz-kaolin vein fill
060314-C2	4422317	419221	1185	Dixie Valley, Mirrors	quartz-kaolin vein fill
071613-1	4422175	419054	1164	Dixie Valley, Mirrors	banded quartz/kaolin fracture fill material
071613-2	4422179	419064	1163	Dixie Valley, Mirrors	fault slickenside

Sample	Northing* (m)	Easting* (m)	Elevation (m)	Site	Material
053015-2A	4434403	414188	1407	Buena Vista Valley, NY Canyon	kaolinite
053015-2B	4434392	414232	1417	Buena Vista Valley, NY Canyon	sinter
053015-2C	4434392	414232	1417	Buena Vista Valley, NY Canyon	sinter
052715-1A	4427272	427024	1152	Dixie Valley, Senator Fumaroles	blocky fumarole calcite
052715-1B	4427266	427025	1151	Dixie Valley, Senator Fumaroles	blocky fumarole calcite
052715-1C	4427261	427027	1150	Dixie Valley, Senator Fumaroles	altered Boyer Formation from fumarole area
052715-2	4427518	426937	1226	Dixie Valley, Senator Fumaroles	cone calcite in fault zone above gabbro
052715-3A	4427550	427056	1193	Dixie Valley, Senator Fumaroles	altered Boyer Formation from fumarole area
052715-3B	4427550	427056	1193	Dixie Valley, Senator Fumaroles	altered Boyer Formation from fumarole area
060214-A	4427653	427124	1186	Dixie Valley, Senator Fumaroles	Boyer Formation with kaolin and qtz veins
060214-B	4427636	427083	1200	Dixie Valley, Senator Fumaroles	in fault zone, one canyon south. float?
060814-1A	4427960	427437	1184	Dixie Valley, Senator Fumaroles	Boyer Formation, breccia
060814-1B	4427962	427433	1188	Dixie Valley, Senator Fumaroles	Boyer Formation, breccia
060814-2	4427603	426972	1225	Dixie Valley, Senator Fumaroles	silicified dolomite?
060814-3A	4427583	427014	1220	Dixie Valley, Senator Fumaroles	quartz with blades
060814-3B	4427583	427015	1220	Dixie Valley, Senator Fumaroles	Boyer Formation between fumaroles
061214-1	4427897	427048	1250	Dixie Valley, Senator Fumaroles	silicified Boyer Formation
061214-2	4427679	427162	1177	Dixie Valley, Senator Fumaroles	silicified Boyer Formation at range front
061214-3A	4427630	427113	1186	Dixie Valley, Senator Fumaroles	hematite, gypsum near fumarole
061214-3B	4427631	427111	1187	Dixie Valley, Senator Fumaroles	white material around fumarole zone
061214-4	4427553	427055	1195	Dixie Valley, Senator Fumaroles	white material around fumarole zone
071713-1	4427545	427064	1190	Dixie Valley, Senator Fumaroles	Boyer Formation
071713-2	4427545	427064	1190	Dixie Valley, Senator Fumaroles	Boyer Formation
072013-6	4427545	427064	1190	Dixie Valley, Senator Fumaroles	Boyer Formation float, druzy qtz
072213-10	4427561	427064	1193	Dixie Valley, Senator Fumaroles	white material around fumarole zone
072213-11	4427348	426917	1190	Dixie Valley, Senator Fumaroles	near purple vent.

Sample	Northing* (m)	Easting* (m)	Elevation (m)	Site	Material
072213-7	4427704	427151	1184	Dixie Valley, Senator Fumaroles	Boyer Formation
072213-8	4427658	427105	1190	Dixie Valley, Senator Fumaroles	silicified Boyer Formation, druzy qtz
072213-9	4427564	427065	1192	Dixie Valley, Senator Fumaroles	red section (gypsum, hematite)
090214-1A	4427970	427424	1210	Dixie Valley, Senator Fumaroles	red material, northern fumarole zone
090214-1B	4427969	427422	1211	Dixie Valley, Senator Fumaroles	white material, northern fumarole zone
090214-1C	4427984	427431	1209	Dixie Valley, Senator Fumaroles	white breccia, northern fumarole zone
090214-2A	4427636	427102	1199	Dixie Valley, Senator Fumaroles	faulted Boyer Formation
090214-2B	4427636	427102	1199	Dixie Valley, Senator Fumaroles	faulted Boyer Formation
090214-2C	4427636	427113	1199	Dixie Valley, Senator Fumaroles	faulted Boyer Formation
090214-3A	4427390	427110	1168	Dixie Valley, Senator Fumaroles	silicified Boyer Formation (?) near main fumarole
090314-1A	4427568	427081	1192	Dixie Valley, Senator Fumaroles	silicified Boyer Formation
090314-1B	4427572	427082	1192	Dixie Valley, Senator Fumaroles	silicified, dissolved Boyer Formation
071513-1	4398101	397342	1404	Dixie Valley, The Bend	quartz vein in granite

B. Appendix: Thin Section Catalog

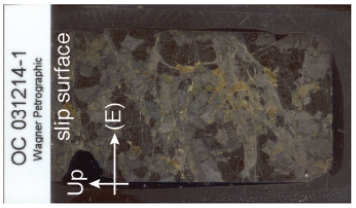

Dixie Valley
Box Canyons
031214-1

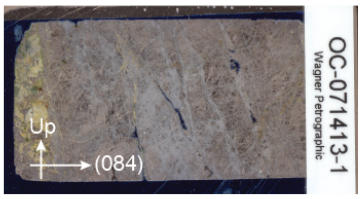

Dixie Valley
Box Canyons
071413-1

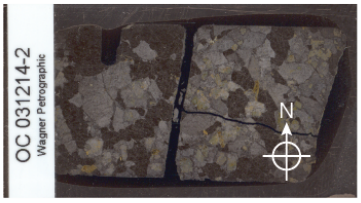

Dixie Valley
Box Canyons
031214-2

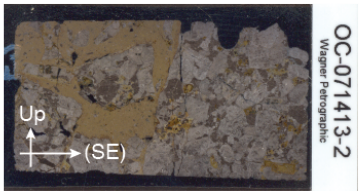

Dixie Valley
Box Canyons
071413-2

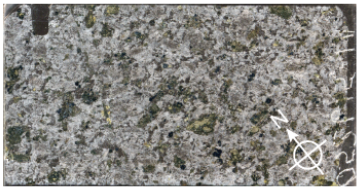

Dixie Valley
Box Canyons
052615-1A

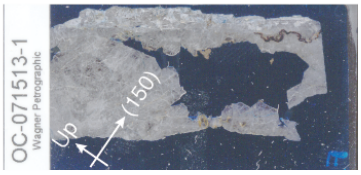

Dixie Valley
Box Canyons
071513-1

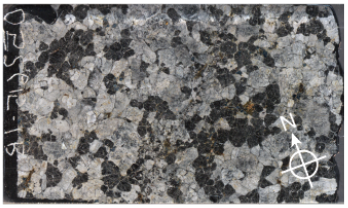

Dixie Valley
Box Canyons
052615-1B

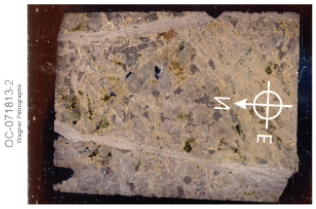

Dixie Valley
Box Canyons
071813-2

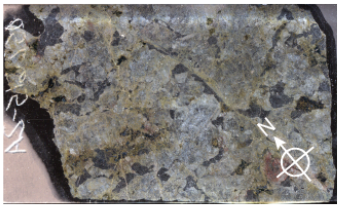

Dixie Valley
Box Canyons
052615-2A

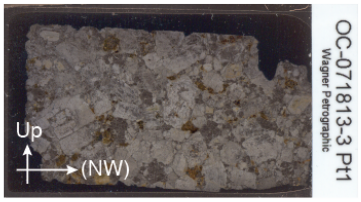

Dixie Valley
Box Canyons
071813-3 part 1

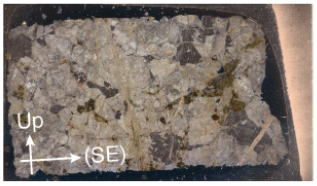

Dixie Valley
Box Canyons
060914-2 part 1

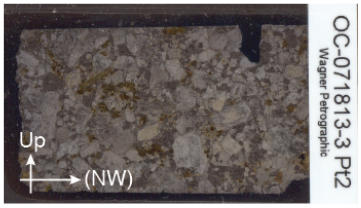

Dixie Valley
Box Canyons
071813-3 part 2

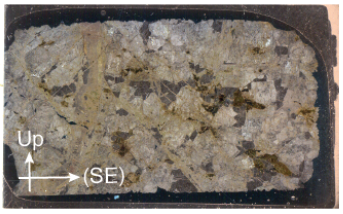

Dixie Valley
Box Canyons
060914-2 part 2

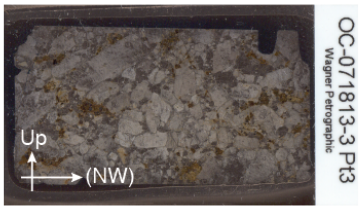

Dixie Valley
Box Canyons
071813-3 part 3

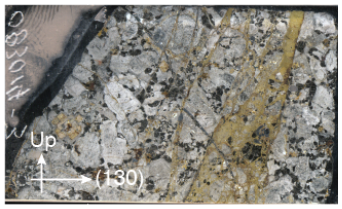

Dixie Valley
Box Canyons
083014-3

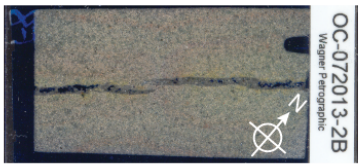

Dixie Valley
Cottonwood Canyon
072013-2B

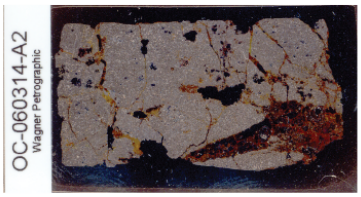

Dixie Valley
Cottonwood Canyon
060314-A2
unoriented

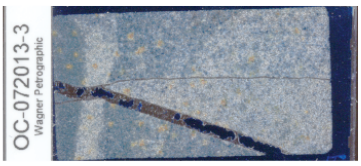

Dixie Valley
Cottonwood Canyon
072013-3
unoriented

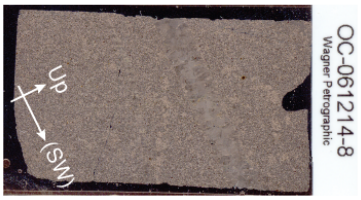

Dixie Valley
Cottonwood Canyon
061214-8

Dixie Valley
Cottonwood Canyon
072013-4
unoriented

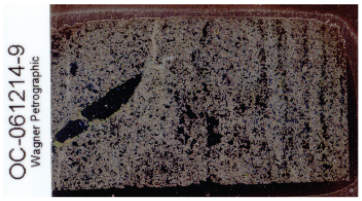

Dixie Valley
Cottonwood Canyon
061214-9
unoriented

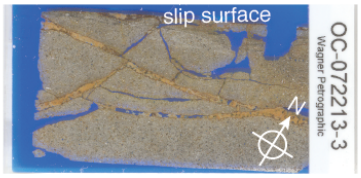

Dixie Valley
Cottonwood Canyon
072213-3

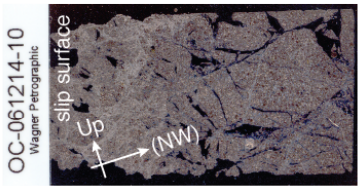

Dixie Valley
Cottonwood Canyon
061214-10

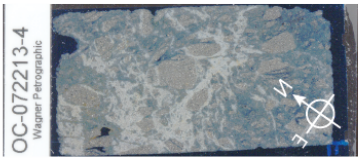

Dixie Valley
Cottonwood Canyon
072213-4

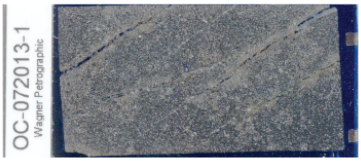

Dixie Valley
Cottonwood Canyon
072013-1
unoriented
bedding plane

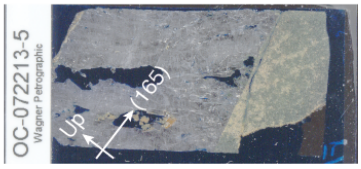

Dixie Valley
Cottonwood Canyon
072213-5

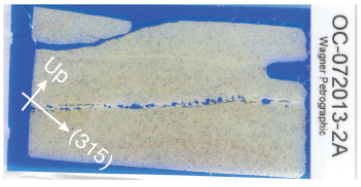

Dixie Valley
Cottonwood Canyon
072013-2A

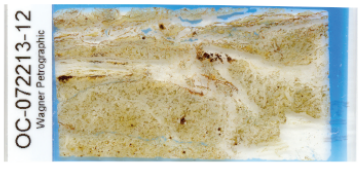

Dixie Valley
Cottonwood Canyon
072213-12
unoriented

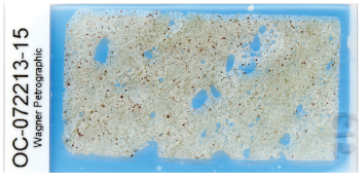

Dixie Valley
Cottonwood Canyon
072213-15
unoriented

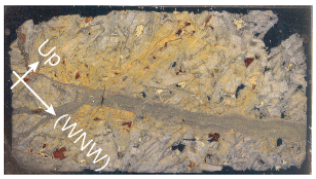

Dixie Valley
Dixie Comstock
061014-1B

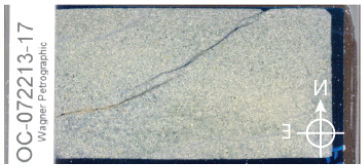

Dixie Valley
Cottonwood Canyon
072213-17

Dixie Valley
Dixie Comstock
061014-2A part 1

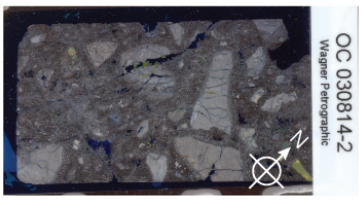

Dixie Valley
Dixie Comstock
030814-2

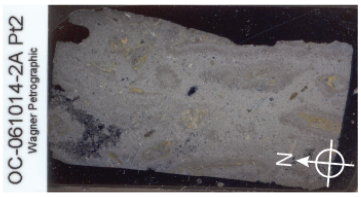

Dixie Valley
Dixie Comstock
061014-2A part 2

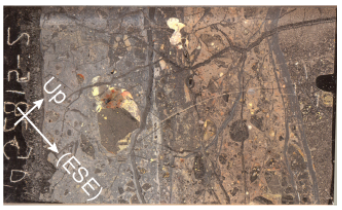

Dixie Valley
Dixie Comstock
052815-2

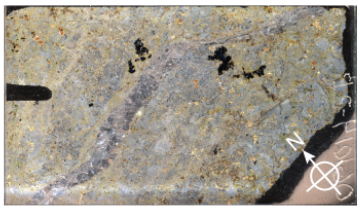

Dixie Valley
Dixie Comstock
061014-2B

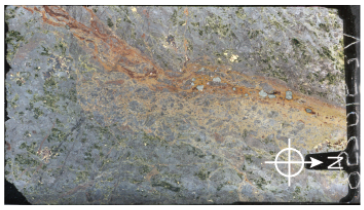

Dixie Valley
Dixie Comstock
052815-3A

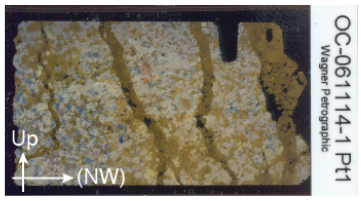

Dixie Valley
Dixie Comstock
061114-1 part 1

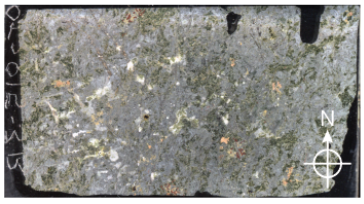

Dixie Valley
Dixie Comstock
052815-3B

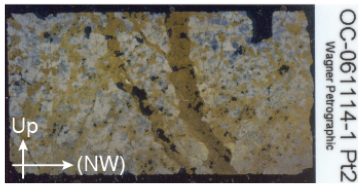

Dixie Valley
Dixie Comstock
061114-1 part 2

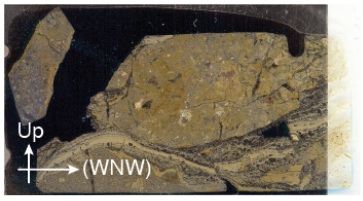

Dixie Valley
Dixie Comstock
061014-1A

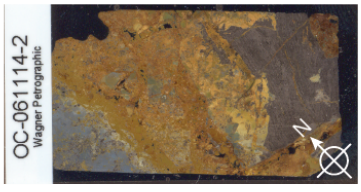

Dixie Valley
Dixie Comstock
061114-2

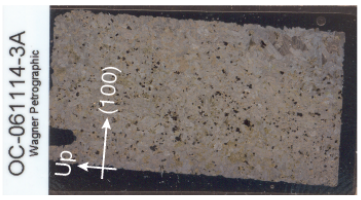

Dixie Valley
Dixie Comstock
061114-3A

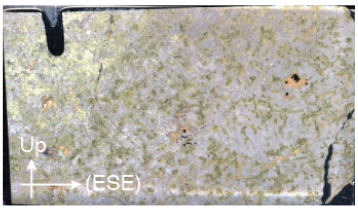

Dixie Valley
Dixie Comstock
061214-5

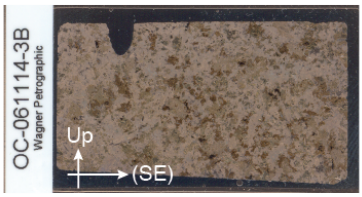

Dixie Valley
Dixie Comstock
061114-3B

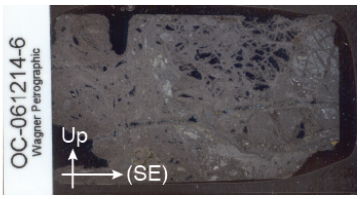

Dixie Valley
Dixie Comstock
061214-6

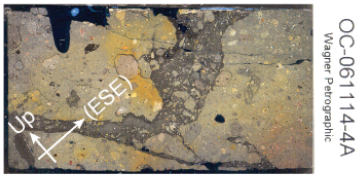

Dixie Valley
Dixie Comstock
061114-4A

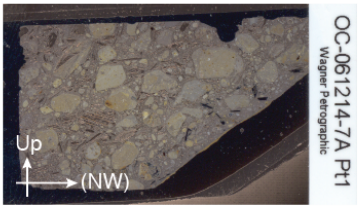

Dixie Valley
Dixie Comstock
061214-7A part 1

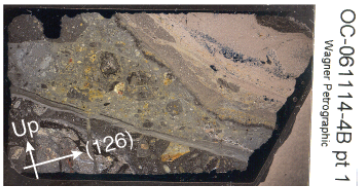

Dixie Valley
Dixie Comstock
061114-4B part 1

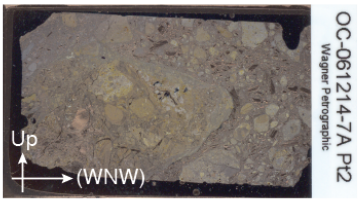

Dixie Valley
Dixie Comstock
061214-7A part 2

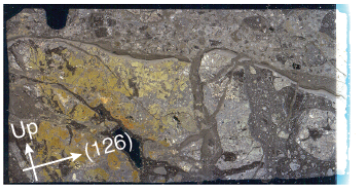

Dixie Valley
Dixie Comstock
061114-4B part 2

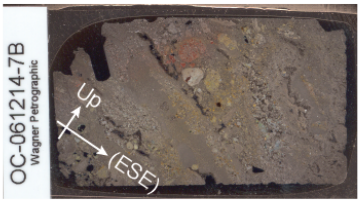

Dixie Valley
Dixie Comstock
061214-7B

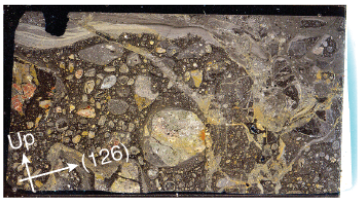

Dixie Valley
Dixie Comstock
061114-4B part 3

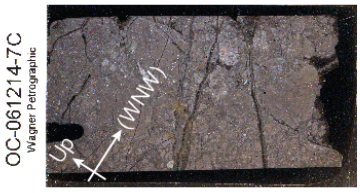

Dixie Valley
Dixie Comstock
061214-7C

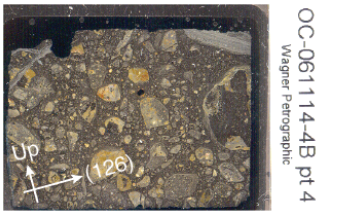

Dixie Valley
Dixie Comstock
061114-4B part 4

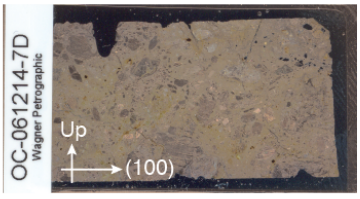

Dixie Valley
Dixie Comstock
061214-7D

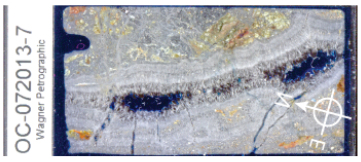

Dixie Valley
Dixie Comstock
072013-7 (PE)

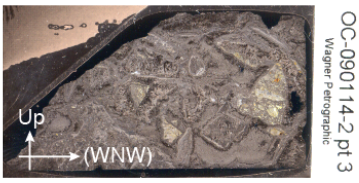

Dixie Valley
Dixie Comstock
090114-2 part 3

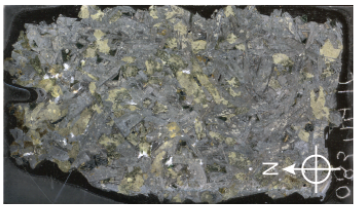

Dixie Valley
Dixie Comstock
083114-1C

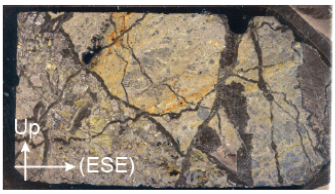

Dixie Valley
Dixie Comstock
090114-2 part 4

Dixie Valley
Dixie Comstock
083114-1D

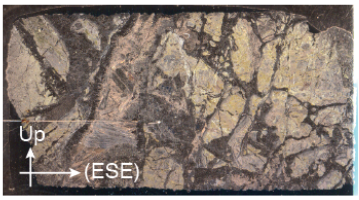

Dixie Valley
Dixie Comstock
090114-2 part 5

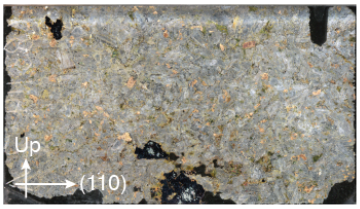

Dixie Valley
Dixie Comstock
083114-2A

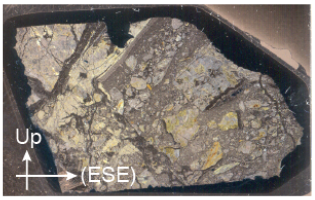

Dixie Valley
Dixie Comstock
090114-2 part 6

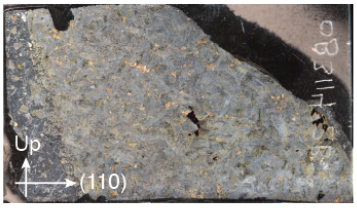

Dixie Valley
Dixie Comstock
083114-2B

Dixie Valley
Dixie Comstock
090114-3

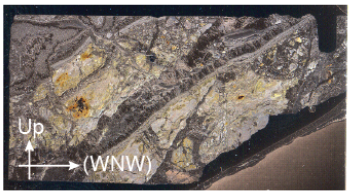

Dixie Valley
Dixie Comstock
090114-2 part 1

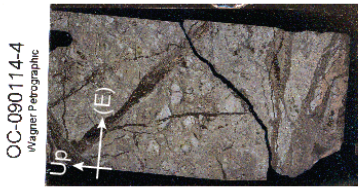

Dixie Valley
Dixie Comstock
090114-4

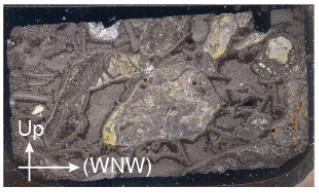

Dixie Valley
Dixie Comstock
090114-2 part 2

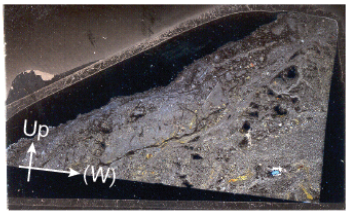

Dixie Valley
Dixie Comstock
090114-5A part 1

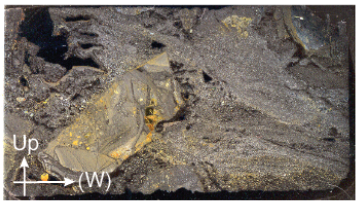

Dixie Valley
Dixie Comstock
090114-5A part 2

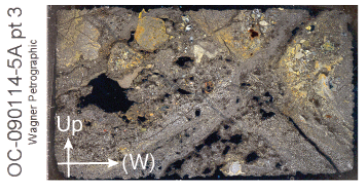

Dixie Valley
Dixie Comstock
090114-5A part 3

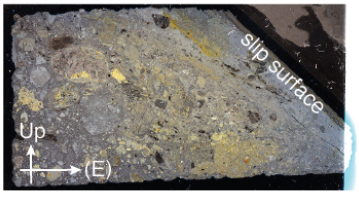

Dixie Valley
Dixie Comstock
090114-5B part 1

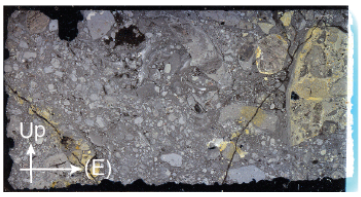

Dixie Valley
Dixie Comstock
090114-5B part 2

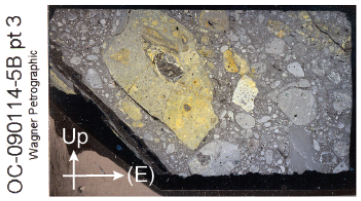

Dixie Valley
Dixie Comstock
090114-5B part 3

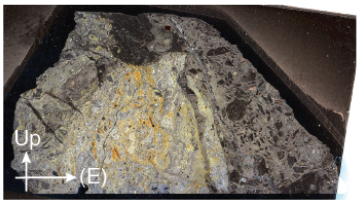

Dixie Valley
Dixie Comstock
090114-5C part 1

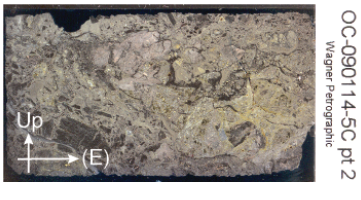

Dixie Valley
Dixie Comstock
090114-5C part 2

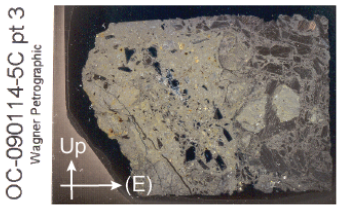

Dixie Valley
Dixie Comstock
090114-5C part 3

Dixie Valley
Dixie Comstock
090114-6A

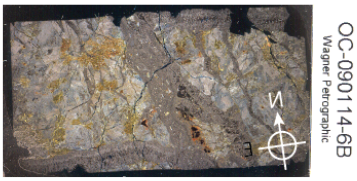

Dixie Valley
Dixie Comstock
090114-6B

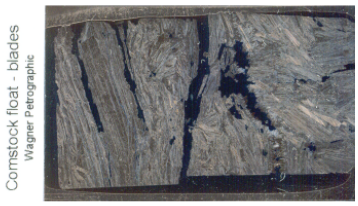

Dixie Valley
Dixie Comstock
calcite blades - float

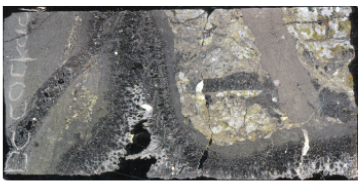

Dixie Valley
Dixie Comstock
cockade - float

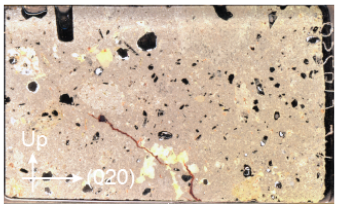

Dixie Valley
Dixie Meadows
052615-3A

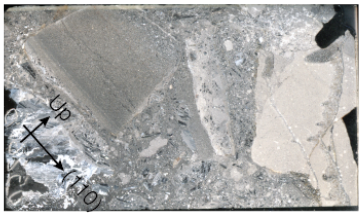

Dixie Valley
Dixie Meadows
052615-3B

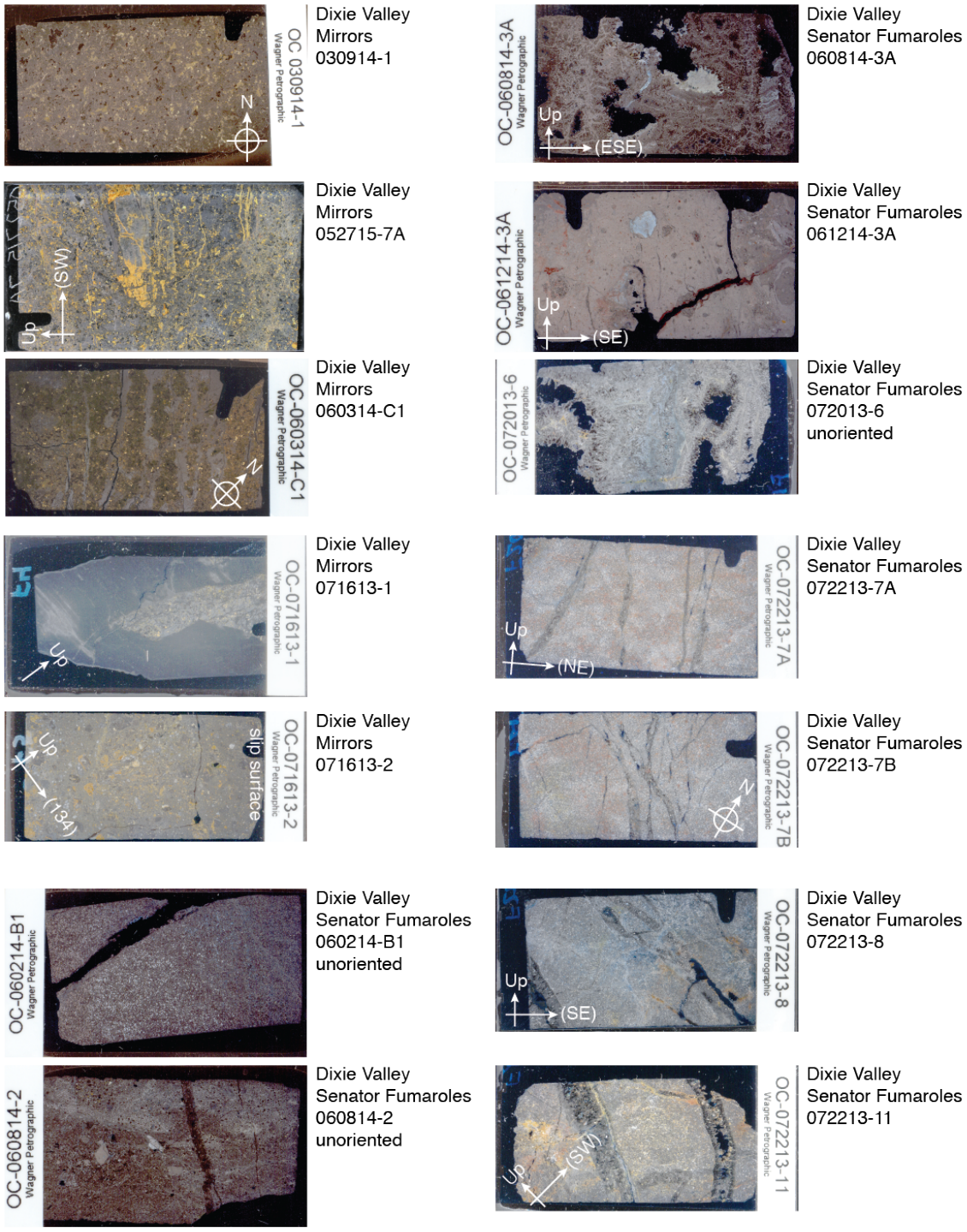

Figure B.1. Scanned thin sections. Oriented sections are noted with up and/or azimuthal directions clockwise from north.

C. Appendix: X-Ray Diffraction Patterns for Select Samples

Semi-quantitative identification of bulk rock composition of spray-dried powders was conducted using a Bruker D8 Advanced X-Ray Diffractometer with LynxEye detector at the Department of Geological Science, Jackson School of Geosciences, The University of Texas at Austin.

Sample preparation included crushing, ball-milling, and wet micronizing with 11-18 ml 0.05% PVA and 1 drop of foam-reducing octanol. Samples were spiked with ~10 wt% corundum standard prior to micronizing. The amount of PVA was increased for samples with higher clay content and decreased for more monomineralic samples to improve the consistency of the slurry. Slurries were sprayed through an oven drier at ~135 °C and collected on heat resistant paper. Sample duplicates were independently prepared.

Bruker D8 settings included a 0.2 or 0.6 mm divergence slit, 3 or 8 mm antiscatter slit, 2.5° soller slit, and a Ni filter. Most powders were scanned from ~4-66° 2-theta, with an incremental step size of ~0.0118°/step, and a 1 second/step dwell time. Total scan time per sample was approximately 1.5 hours. Several early samples were scanned over a shorter 2-theta interval and for ~20 minutes, and some later duplicates were scanned for ~2 hours. The 8 mm antiscatter slit resulted in a low, broad peak between 9.5-11.5° or 10.5-12.5° 2-theta for the mobile and solid holder, respectively, with other peaks occasionally observed at 20.5°, 22.75°, 34.45°, 40.1°, 45.5°, 48.05°, 53.8° 2-theta when using the mobile sample holders. These humps are labeled as “artifacts” on the following patterns. Patterns were improved with the 3 mm antiscatter slit.

Color code on the following patterns: short scan mobile holder = magenta; scan with mobile holder, 0.2 mm + 8 mm slits = red; scan with solid holder, 0.2 mm + 8 mm slits = orange; scan with solid holder, 0.2 mm + 3 mm slit = green; scan with solid holder, 0.6 mm + 3 mm slit = blue; final spectrum: black line. Red DIF patterns show corundum peaks associated with the sample spike. Labels for these peaks are occasionally removed to reduce clutter.

Initial analysis of XRD spectra was conducted using EVA, with final semi-quantitative analysis conducted with TOPAS 4.2 software.

Note vertical scales on the following patterns are linear, but that some low peaks were identified with non-linear scales:

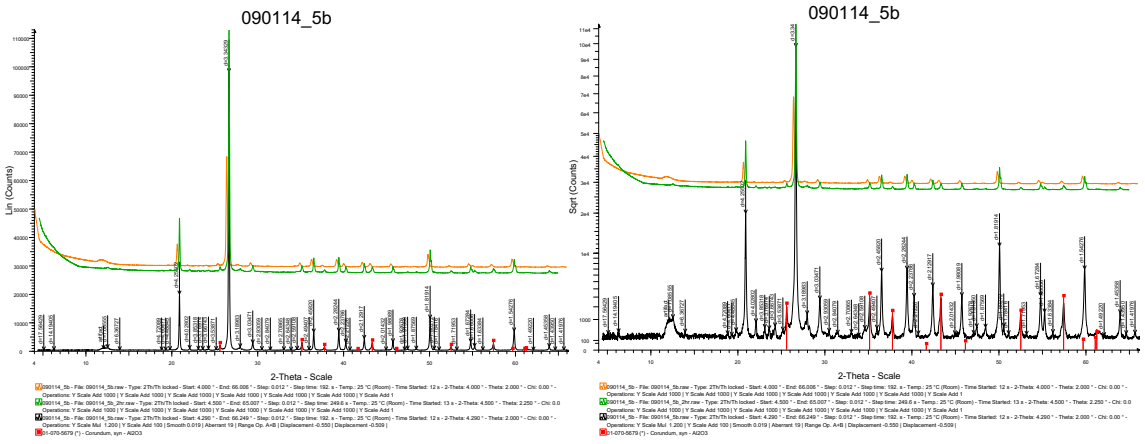

Figure C.1. Comparison of X-ray diffraction patterns with linear and non-linear scales.

030914_1

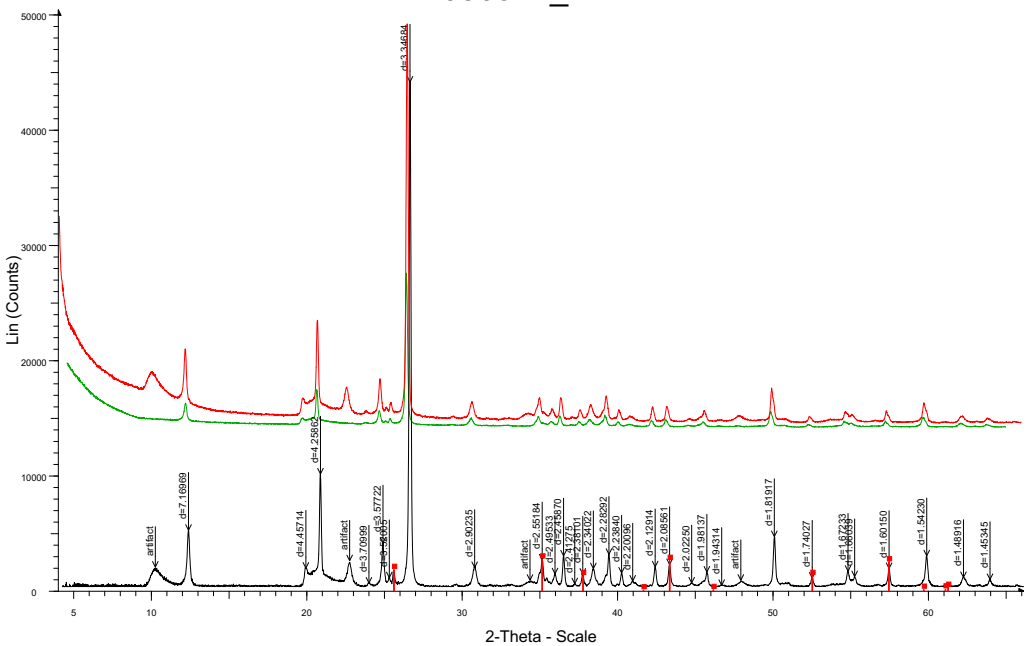

030914_1 - File: 030914_1.raw - Type: 2Th/Th locked - Start: 4.000 ° - End: 66.006 ° - Step: 0.012 ° - Step time: 192. s - Temp.: 25 °C (Room) - Time Started: 11 s - 2-Theta: 4.000 ° - Theta: 2.000 ° - Chi: 0.00 ° - Phi
Operations: Y Scale Add 1000 | Y Scale Add 1000 | Y Scale Add 1000 | Y Scale Add 1000 | Y Scale Add 1000 | Y Scale Add 1

030914_1 - File: 030914_1_2hr.raw - Type: 2Th/Th locked - Start: 4.500 ° - End: 65.007 ° - Step: 0.012 ° - Step time: 249.6 s - Temp.: 25 °C (Room) - Time Started: 15 s - 2-Theta: 4.500 ° - Theta: 2.250 ° - Chi: 0.00
Operations: Y Scale Add 1000 | Y Scale Add 1000 | Y Scale Add 1000 | Y Scale Add 1000 | Y Scale Add 1000 | Y Scale Add 1

030914_1 - File: 030914_1.raw - Type: 2Th/Th locked - Start: 4.209 ° - End: 66.181 ° - Step: 0.012 ° - Step time: 192. s - Temp.: 25 °C (Room) - Time Started: 11 s - 2-Theta: 4.209 ° - Theta: 2.000 ° - Chi: 0.00 ° - Phi
Operations: Y Scale Add 333 | Y Scale Mul 1.300 | Aberrant 28 | Range Op. A+B | Displacement -0.396 | Background 0.500,1.000 | Strip kAlph

01-070-5679 (*) - Corundum, syn - Al2O3

052615_1a

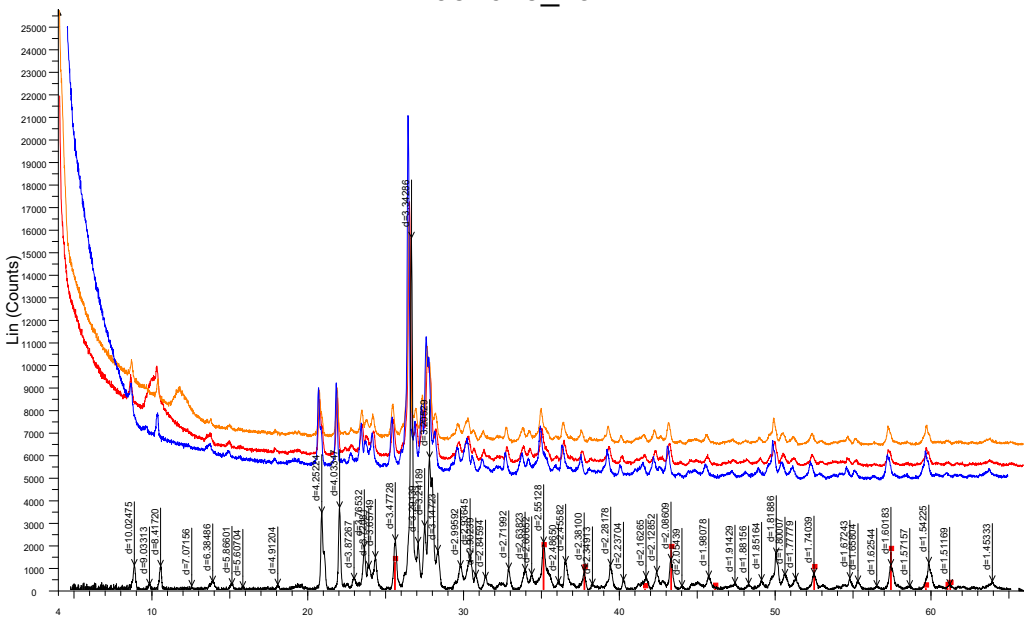

052615_1a - File: 052615_1a_clip.raw - Type: Locked Coupled - Start: 4.007 ° - End: 66.001 ° - Step: 0.
Operations: Y Scale Add 801 | Y Scale Add 1000 | Y Scale Add 1000 | Y Scale Add 1000 | Y Scale Add

052615_1a - File: 052615_1a_rerun.raw - Type: 2Th/Th locked - Start: 4.000 ° - End: 66.006 ° - Step: 0.
Operations: Y Scale Add 801 | Y Scale Add 1000 | Y Scale Add 1000 | Y Scale Add 1000 | Y Scale Add

052615_1a - File: 052615_1a_2hr.raw - Type: 2Th/Th locked - Start: 4.500 ° - End: 65.007 ° - Step: 0.01
Operations: Y Scale Add 1000 | Y Scale Add 1000 | Y Scale Add 1000 | Y Scale Add 1000 | Import

052615_1a - File: 052615_1a_2hr.raw - Type: 2Th/Th locked - Start: 4.500 ° - End: 65.007 ° - Step: 0.01
Operations: X Offset 0.208 | X Offset 0.185 | X Offset 0.118 | Background 0.457,1.000 | Import

01-070-5679 (*) - Corundum, syn - Al2O3 - Y: 7.12 % - d x by: 1. - WL: 1.5406 - Rhombo.H.axes - a 4.75

052615_1b

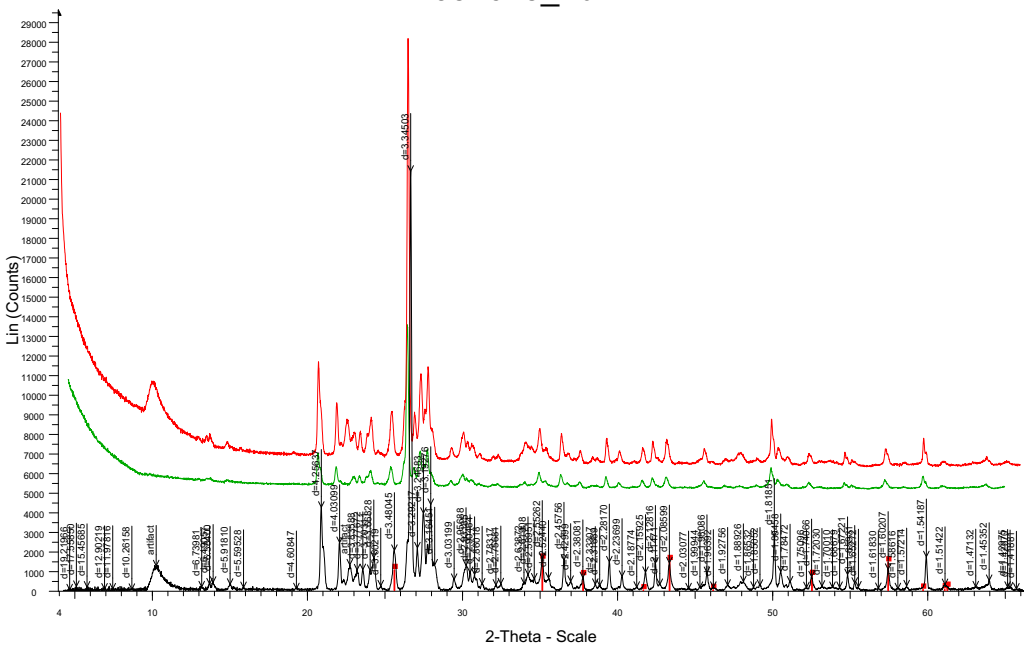

052615_1b - File: 052615_1b_2hr.raw - Type: 2Th/Th locked - Start: 4.500 ° - End: 65.007 ° - Step: 0.012 ° - Step time: 249.6 s - Temp.: 25 °C (Room) - Time Started: 12 s - 2-Theta: 4.500 ° - Theta: 2.250 ° - Chi: 0.0
Operations: Y Scale Add 1000 | Y Scale Add 1000 | Y Scale Add 1000 | Y Scale Add 1000 | Y Scale Add 1000 | Import

052615_1b - File: 052615_1b.raw - Type: 2Th/Th locked - Start: 4.191 ° - End: 66.167 ° - Step: 0.012 ° - Step time: 192. s - Temp.: 25 °C (Room) - Time Started: 12 s - 2-Theta: 4.191 ° - Theta: 2.000 ° - Chi: 0.00 ° -
Operations: Aberrant 25 | Range Op. A+B | Displacement -0.363 | Background 0.501,1.000 | Strip kAlpha2 0.500 | Import

052615_1b - File: 052615_1b.raw - Type: 2Th/Th locked - Start: 4.000 ° - End: 66.006 ° - Step: 0.012 ° - Step time: 192. s - Temp.: 25 °C (Room) - Time Started: 12 s - 2-Theta: 4.000 ° - Theta: 2.000 ° - Chi: 0.00 ° -
Operations: Y Scale Add 1000 | Y Scale Add 801 | Y Scale Add 1000 | Y Scale Add 1000 | Y Scale Add 1000 | Import

01-070-5679 (*) - Corundum, syn - Al2O3

052615_2

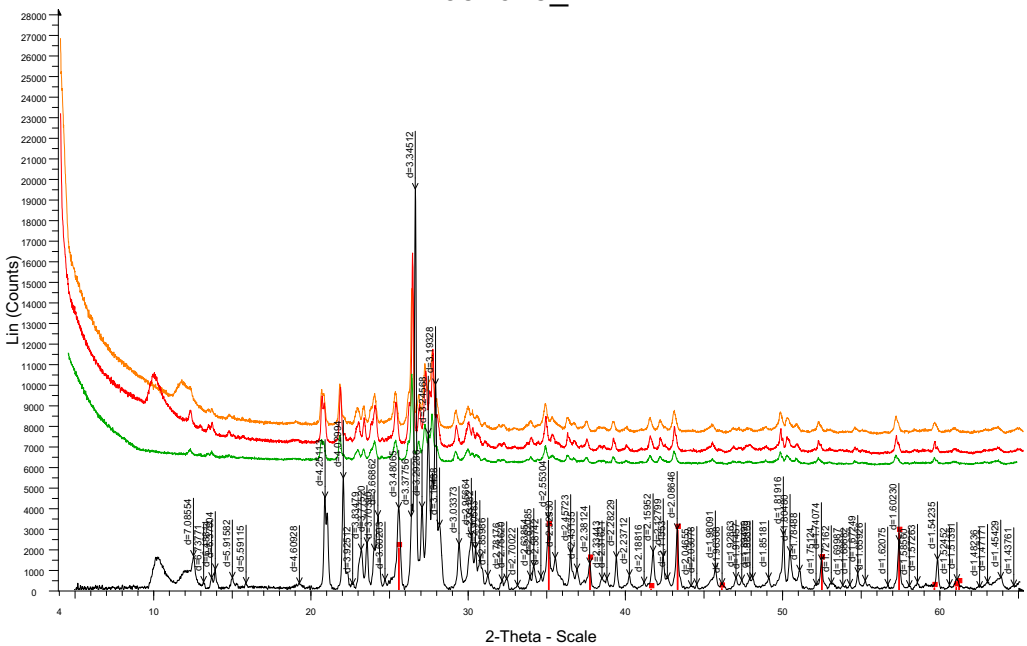

052615_2 - File: 052615_2_rerun.raw - Type: 2Th/Th locked - Start: 4.000 ° - End: 66.006 ° - Step: 0.01
Operations: Y Scale Add 1000 | Y Scale Add 1000 | Y Scale Add 1000 | Y Scale Add 1000 | Y Scale Add

052615_2_1 - File: 052615_2_clip.raw - Type: Locked Coupled - Start: 4.007 ° - End: 66.001 ° - Step: 0.
Operations: Y Scale Add 1000 | Y Scale Add 1000 | Y Scale Add 1000 | Y Scale Add 1000 | Y Scale Add

052615_2 - File: 052615_2_2hr.raw - Type: 2Th/Th locked - Start: 4.500 ° - End: 65.007 ° - Step: 0.012 °
Operations: Y Scale Add 1000 | Y Scale Add 1000 | Y Scale Add 1000 | Y Scale Add 1000 | Y Scale Add

052615_2_1 - File: 052615_2_clip.raw - Type: Locked Coupled - Start: 4.731 ° - End: 65.202 ° - Step: 0.
Operations: Smooth 0.050 | Range Op. A+B | Range Op. A+B | Displacement -0.388 | Background 0.50

01-070-5679 (*) - Corundum, syn - Al2O3 - Y: 11.32 % - d x by: 1. - WL: 1.5406 - Rhombo.H.axes - a 4.7

052615_3a_1

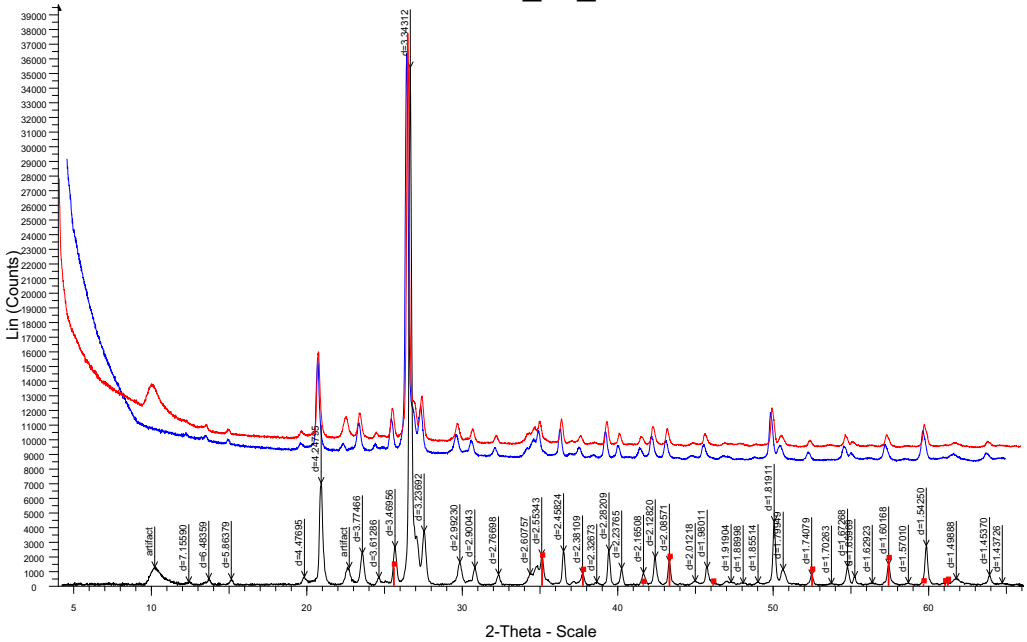

052615_3a_1 - File: 052615_3a_1.raw - Type: 2Th/Th locked - Start: 4.000 ° - End: 66.006 ° - Step: 0.012 ° - Step time: 192. s - Temp.: 25 °C (Room) - Time Started: 13 s - 2-Theta: 4.000 ° - Theta: 2.000 ° - Chi: 0.0
Operations: Y Scale Add 1000 | Y Scale Add 1000 | Y Scale Add 1000 | Y Scale Add 1000 | Y Scale Add 1000 | Y Scale Add 1

052615_3a - File: 052615_3a_2hr.raw - Type: 2Th/Th locked - Start: 4.500 ° - End: 65.007 ° - Step: 0.012 ° - Step time: 249.6 s - Temp.: 25 °C (Room) - Time Started: 15 s - 2-Theta: 4.500 ° - Theta: 2.250 ° - Chi: 0.0
Operations: Y Scale Add 1000 | Y Scale Add 1000 | Y Scale Add 1000 | Y Scale Add 1000 | Y Scale Add 1000 | Y Scale Add 1

052615_3a_1 - File: 052615_3a_1.raw - Type: 2Th/Th locked - Start: 4.171 ° - End: 66.150 ° - Step: 0.012 ° - Step time: 192. s - Temp.: 25 °C (Room) - Time Started: 13 s - 2-Theta: 4.171 ° - Theta: 2.000 ° - Chi: 0.0
Operations: Smooth 0.019 | Aberrant 21 | Range Op. A+B | Displacement -0.325 | Background 0.500,1.000 | Strip kAlpha2 0.500 | Import

01-070-5679 (*) - Corundum, syn - Al2O3

052615_3b

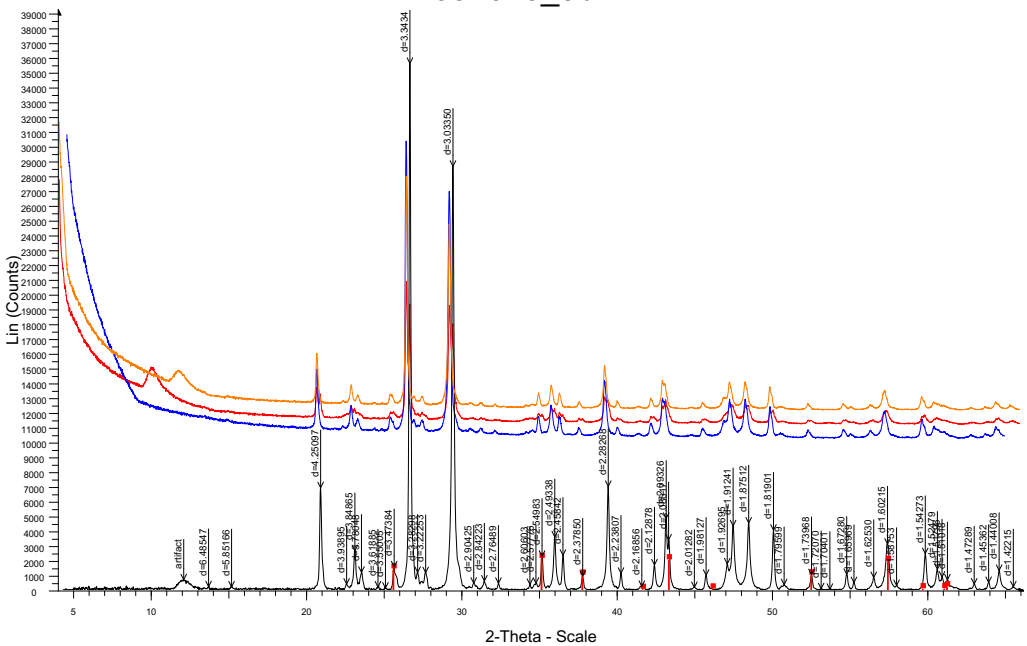

052615_3b - File: 052615_3b_clip.raw - Type: Locked Coupled - Start: 4.007 ° - End: 66.001 ° - Step: 0.
Operations: Y Scale Add -1000 | Y Scale Add 1000 | Y Scale Add 1000 | Y Scale Add 1000 | Y Scale Ad

052615_3b - File: 052615_3b_rerun.raw - Type: 2Th/Th locked - Start: 4.000 ° - End: 66.006 ° - Step: 0.
Operations: Y Scale Add -1000 | Y Scale Add -1000 | Y Scale Add 1000 | Y Scale Add 1000 | Y Scale Ad

052615_3b - File: 052615_3b_2hr.raw - Type: 2Th/Th locked - Start: 4.500 ° - End: 65.007 ° - Step: 0.01
Operations: Y Scale Add 1000 | Y Scale Add 1000 | Y Scale Add 1000 | Y Scale Add 1000 | Y Scale Add

052615_3b - File: 052615_3b_rerun.raw - Type: 2Th/Th locked - Start: 4.257 ° - End: 66.222 ° - Step: 0.
Operations: Smooth 0.033 | Aberrant 19 | Range Op. A+B | Range Op. A+B | Displacement -0.488 | Disp

01-070-5679 (*) - Corundum, syn - Al2O3

052715_3a

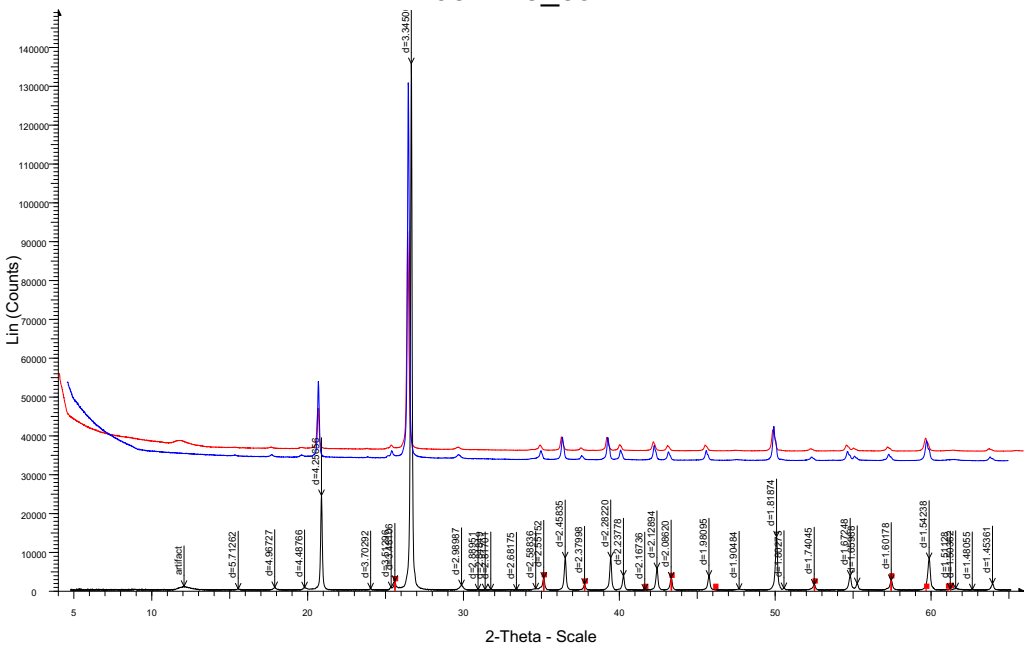

052715_3a - File: 052715_3a.raw - Type: 2Th/Th locked - Start: 4.000 ° - End: 66.006 ° - Step: 0.012 ° - Step time: 192. s - Temp.: 25 °C (Room) - Time Started: 12 s - 2-Theta: 4.000 ° - Theta: 2.000 ° - Chi: 0.00 ° - Operations: Y Scale Add 801 | Y Scale Add 801 | Y Scale Add 801 | Y Scale Add 801 | Y Scale Add 801 | Y Scale Add 801 | Y

052715_3a - File: 052715_3a_2hr.raw - Type: 2Th/Th locked - Start: 4.500 ° - End: 65.007 ° - Step: 0.012 ° - Step time: 249.6 s - Temp.: 25 °C (Room) - Time Started: 13 s - 2-Theta: 4.500 ° - Theta: 2.250 ° - Chi: 0.0 Operations: Y Scale Add 1000 | Y Scale Add 1000 | Y Scale Add 1000 | Y Scale Add 1000 | Y Scale Add 1000 | Y Scale Add 1

052715_3a - File: 052715_3a.raw - Type: 2Th/Th locked - Start: 4.711 ° - End: 65.185 ° - Step: 0.012 ° - Step time: 249.6 s - Temp.: 25 °C (Room) - Time Started: 13 s - 2-Theta: 4.711 ° - Theta: 2.250 ° - Chi: 0.00 ° - Operations: Aberrant 14 | Displacement -0.400 | Displacement -0.413 | Range Op. A+B | Displacement -0.450 | Background 0.500,1.000 | Strip

01-070-5679 (*) - Corundum, syn - Al2O3

052715_7_2

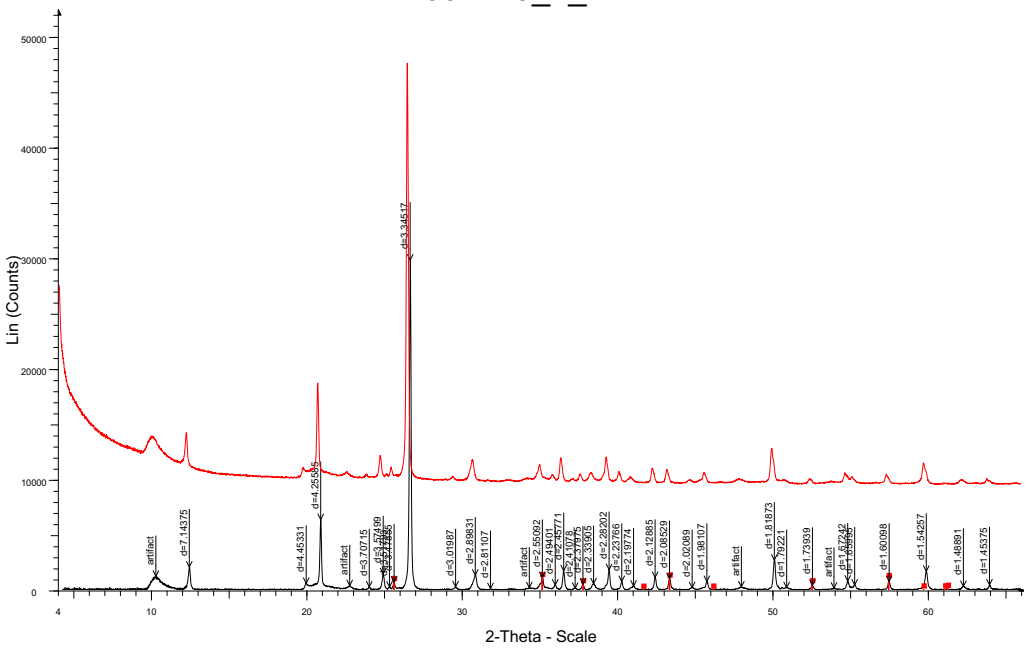

052715_7_2 - File: 052715_7_2.raw - Type: 2Th/Th locked - Start: 4.000 ° - End: 66.006 ° - Step: 0.012 ° - Step time: 192. s - Temp.: 25 °C (Room) - Time Started: 13 s - 2-Theta: 4.000 ° - Theta: 2.000 ° - Chi: 0.00 ° Operations: Y Scale Add 1000 | Y Scale Add 1000 | Y Scale Add 1000 | Y Scale Add 1000 | Y Scale Add 1000 | Y Scale Add 1

052715_7_2 - File: 052715_7_2.raw - Type: 2Th/Th locked - Start: 4.211 ° - End: 66.183 ° - Step: 0.012 ° - Step time: 192. s - Temp.: 25 °C (Room) - Time Started: 13 s - 2-Theta: 4.211 ° - Theta: 2.000 ° - Chi: 0.00 ° Operations: Aberrant 26 | Displacement -0.400 | Background 0.501,1.000 | Strip kAlpha2 0.500 | Import

01-070-5679 (*) - Corundum, syn - Al2O3

052715_7_3

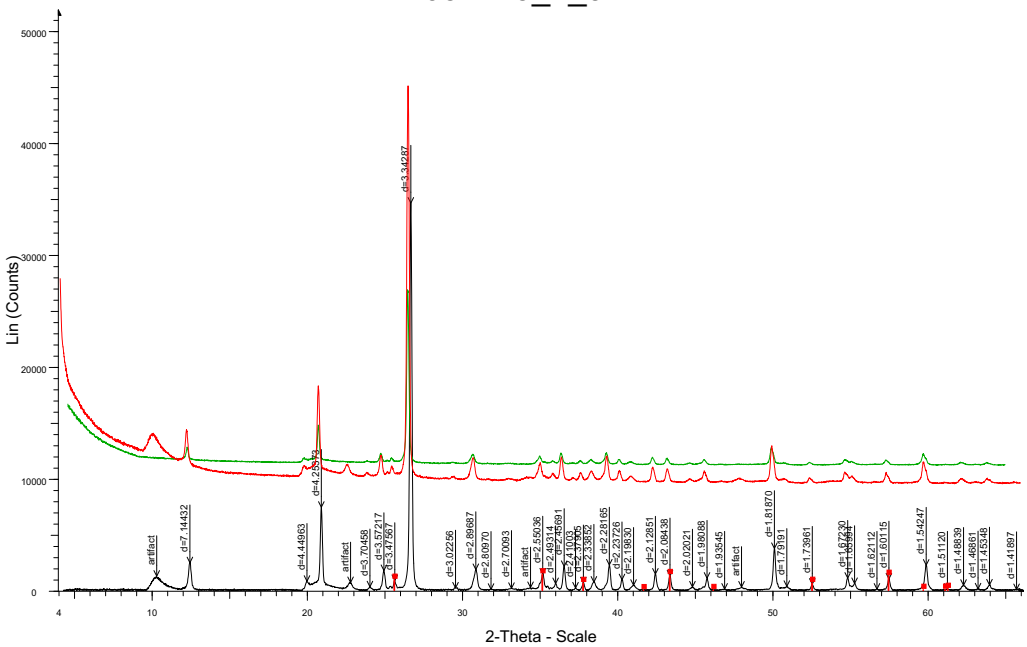

052715_7_3 - File: 052715_7_3.raw - Type: 2Th/Th locked - Start: 4.211 ° - End: 66.183 ° - Step: 0.012 ° - Step time: 192. s - Temp.: 25 °C (Room) - Time Started: 12 s - 2-Theta: 4.211 ° - Theta: 2.000 ° - Chi: 0.00 °
Operations: Smooth 0.026 | Aberrant 19 | Range Op. A+B | Displacement -0.400 | Displacement -0.350 | Displacement -0.400 | Background 0.501
052715_7_3 - File: 052715_7_3.raw - Type: 2Th/Th locked - Start: 4.000 ° - End: 66.006 ° - Step: 0.012 ° - Step time: 192. s - Temp.: 25 °C (Room) - Time Started: 12 s - 2-Theta: 4.000 ° - Theta: 2.000 ° - Chi: 0.00 °
Operations: Y Scale Add 1000 | Y Scale Add -1000 | Y Scale Add -1000 | Y Scale Add -1000 | Y Scale Add 1000 | Y Scale Add 1000 | Y Scale Ad
052715_7_3 - File: 052715_7_3_2hr.raw - Type: 2Th/Th locked - Start: 4.500 ° - End: 65.007 ° - Step: 0.012 ° - Step time: 249.6 s - Temp.: 25 °C (Room) - Time Started: 12 s - 2-Theta: 4.500 ° - Theta: 2.250 ° - Chi:
Operations: Y Scale Add 1000 | Y Scale Add 1000 | Y Scale Add -1000 | Y Scale Add 1000 | Y Scale Add 1000 | Y Scale Add
01-070-5679 (*) - Corundum, syn - Al2O3

052715_7_2

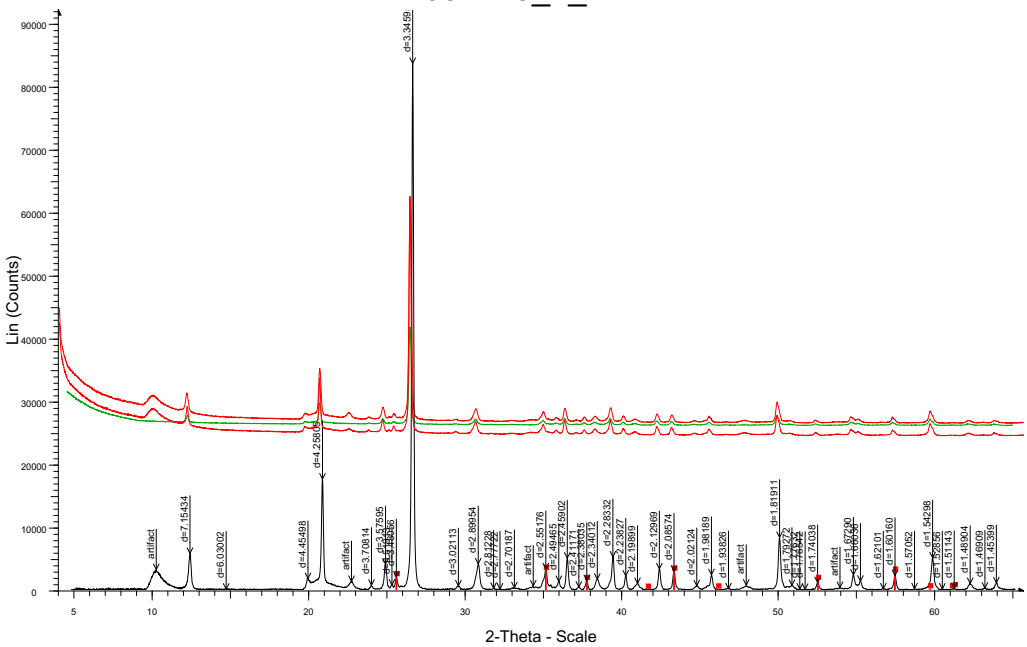

052715_7_2 - File: 052715_7_2.raw - Type: 2Th/Th locked - Start: 4.000 ° - End: 66.006 ° - Step: 0.012
Operations: Y Scale Add 1000 | Y Scale Add 1000 | Y Scale Add 1000 | Y Scale Add 1000 | Y Scale Add
052715_7_3 - File: 052715_7_3.raw - Type: 2Th/Th locked - Start: 4.000 ° - End: 66.006 ° - Step: 0.012
Operations: Y Scale Add 1000 | Y Scale Add 1000 | Y Scale Add 1000 | Y Scale Add 1000 | Y Scale Add
052715_7_3 - File: 052715_7_3_2hr.raw - Type: 2Th/Th locked - Start: 4.500 ° - End: 65.007 ° - Step: 0.
Operations: Y Scale Add 1000 | Y Scale Add 1000 | Y Scale Add 1000 | Y Scale Add 1000 | Y Scale Add
052715_7 combined - File: 052715_7_3.raw - Type: 2Th/Th locked - Start: 4.697 ° - End: 65.174 ° - Step
Operations: Range Op. A+B | Range Op. A+B | Displacement -0.338 | Displacement -0.363 | Backgroun
01-070-5679 (*) - Corundum, syn - Al2O3

052815_2_1

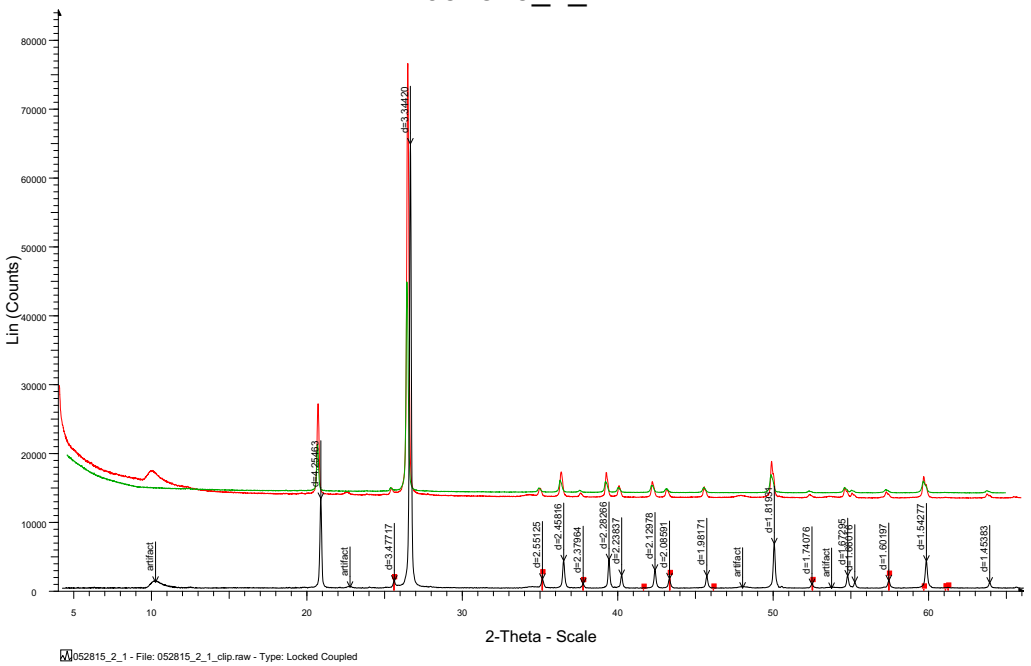

052815_2_1 - File: 052815_2_1_clip.raw - Type: Locked Coupled
Operations: Y Scale Add -750 | Y Scale Add 1000 | Smooth 0.019 | Aberrant 24 | Range Op. A+B | Displacement -0.363 | Displacement -0.325 |
052815_2_1 - File: 052815_2_1_clip.raw - Type: Locked Coupled
Operations: Y Scale Add 1000 | Y Scale Add 1000 | Y Scale Add 1000 | Y Scale Add 1000 | Y Scale Add 1000 | Y Scale Add 1000 | Y Scale Add 1
052815_2_1 - File: 052815_2_1_2hr.raw - Type: 2Th/Th locked
Operations: Y Scale Add 1000 | Y Scale Add 1000 | Y Scale Add 1000 | Y Scale Add 1000 | Y Scale Add 1000 | Y Scale Add 1000 | Y Scale Add 1
01-070-5679 (*) - Corundum, syn - Al2O3

052815_2_2

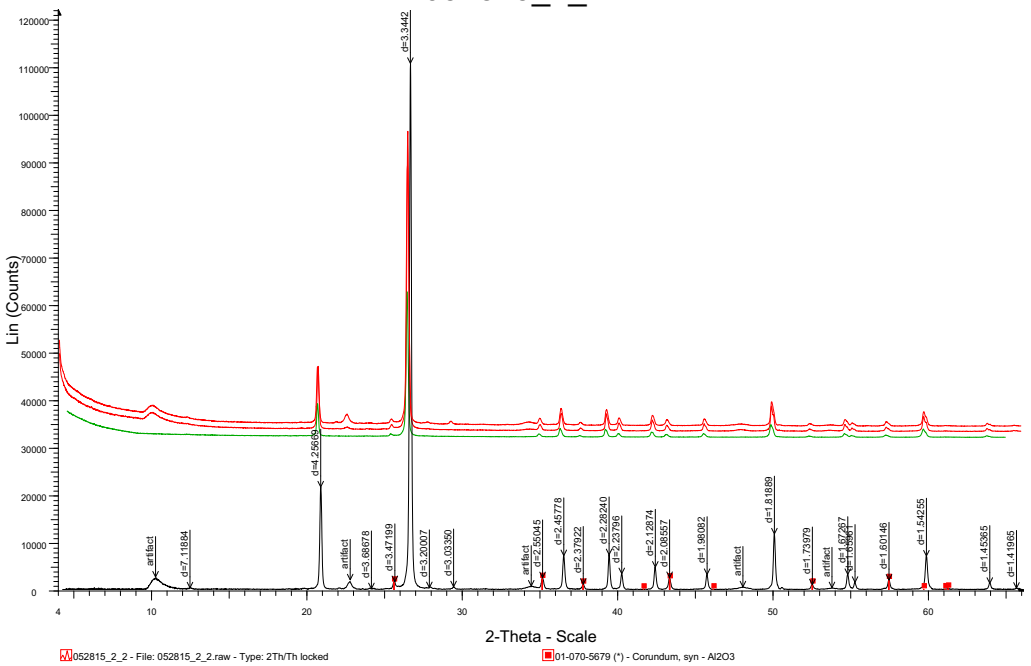

052815_2_2 - File: 052815_2_2.raw - Type: 2Th/Th locked
Operations: Y Scale Add -1000 | Y Scale Add -1000 | Y Scale Add 1000 | Y Scale Add 1000 | Y Scale Ad
052815_2_1 - File: 052815_2_1_clip.raw - Type: Locked Coupled
Operations: Y Scale Add -1000 | Y Scale Add -1000 | Y Scale Add 1000 | Y Scale Add 1000 | Y Scale Ad
052815_2_1 - File: 052815_2_1_2hr.raw - Type: 2Th/Th locked
Operations: Y Scale Add 1000 | Y Scale Add 1000 | Y Scale Add 1000 | Y Scale Add 1000 | Y Scale Add
052815_2 combined - File: 052815_2_1_clip.raw - Type: Locked Coupled
Operations: Range Op. A+B | Range Op. A+B | Displacement -0.375 | Background 0.500,1.000 | Strip k
01-070-5679 (*) - Corundum, syn - Al2O3

052815_2_2

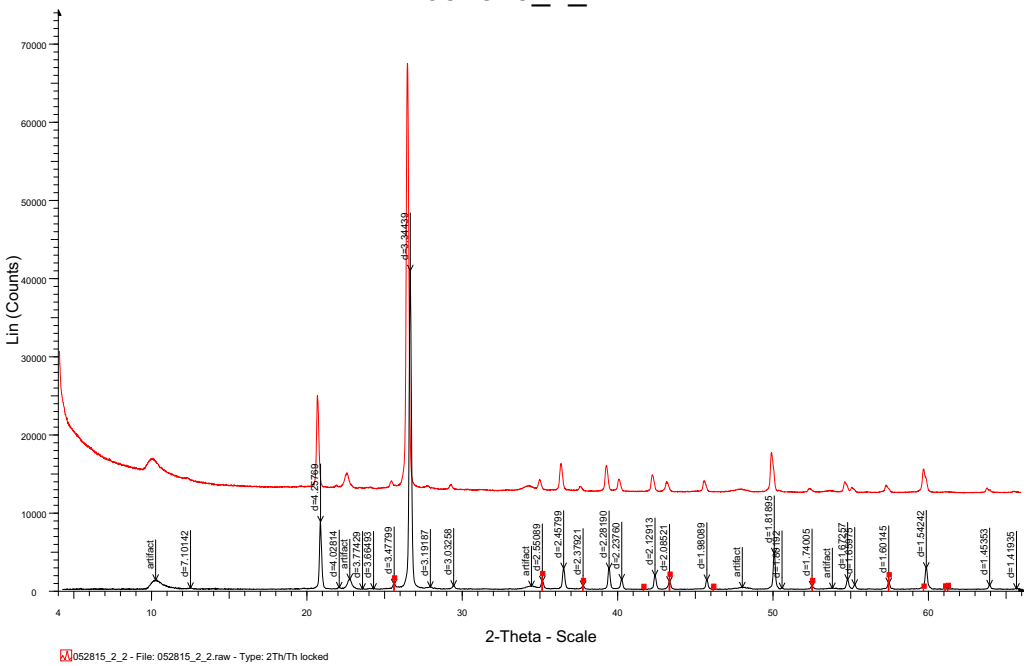

052815_2_2 - File: 052815_2_2.raw - Type: 2Th/Th locked
Operations: Y Scale Add 1000 | Y Scale Add 1000 | Y Scale Add 1000 | Y Scale Add 1000 | Y Scale Add 1000 | Y Scale Add 1000 | Y Scale Add 1
052815_2_2 - File: 052815_2_2.raw - Type: 2Th/Th locked
Operations: Y Scale Add 83 | Displacement -0.388 | Displacement -0.400 | Displacement -0.375 | Smooth 0.026 | Aberrant 56 | Background 0.00
01-070-5679 (*) - Corundum, syn - Al2O3

052815_3a

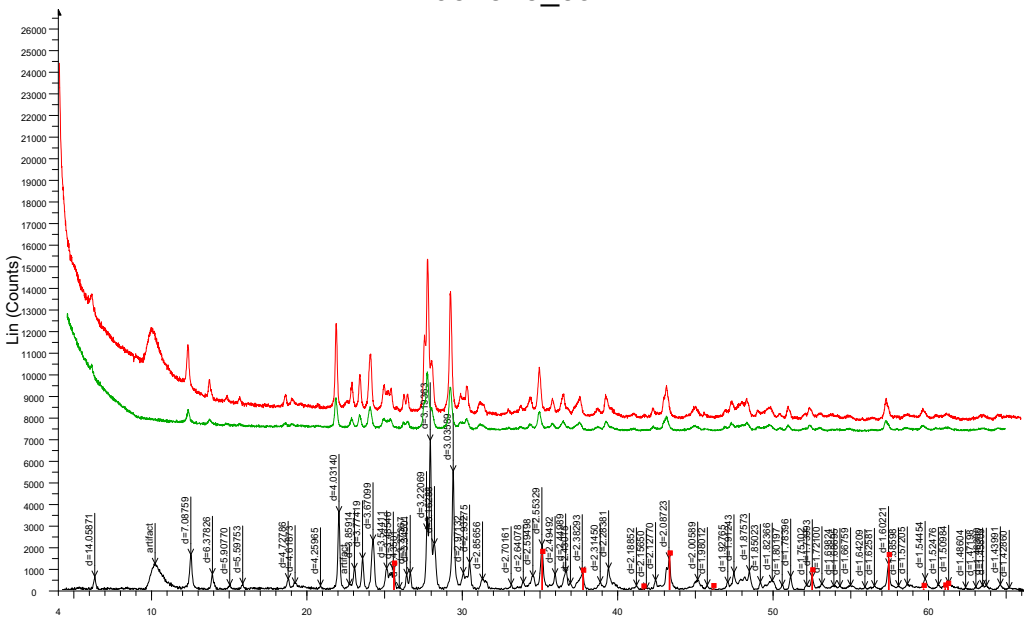

052815_3a - File: 052815_3a.raw - Type: 2Th/Th locked - Start: 4.000 ° - End: 66.006 ° - Step: 0.012 ° - Step time: 192. s - Temp.: 25 °C (Room) - Time Started: 13 s - 2-Theta: 4.000 ° - Theta: 2.000 ° - Chi: 0.00 ° -
Operations: Y Scale Add 1000 | Y Scale Add 1000 | Y Scale Add 1000 | Y Scale Add -1000 | Y Scale Add -1000 | Y Scale Add 1000 | Y Scale Add
052815_3a - File: 052815_3a_2hr.raw - Type: 2Th/Th locked - Start: 4.500 ° - End: 65.007 ° - Step: 0.012 ° - Step time: 249.6 s - Temp.: 25 °C (Room) - Time Started: 12 s - 2-Theta: 4.500 ° - Theta: 2.250 ° - Chi: 0.0
Operations: Y Scale Add -1000 | Y Scale Add 1000 | Y Scale Add 1000 | Y Scale Add 1000 | Y Scale Add 1000 | Y Scale Add -1000 | Y Scale Add
052815_3a - File: 052815_3a.raw - Type: 2Th/Th locked - Start: 4.197 ° - End: 66.172 ° - Step: 0.012 ° - Step time: 192. s - Temp.: 25 °C (Room) - Time Started: 13 s - 2-Theta: 4.197 ° - Theta: 2.000 ° - Chi: 0.00 ° -
Operations: Displacement -0.375 | Smooth 0.040 | Aberrant 19 | Range Op. A+B | Displacement -0.400 | Background 0.501,1.000 | Strip kAlpha2
01-070-5679 (*) - Corundum, syn - Al2O3

052815_3b

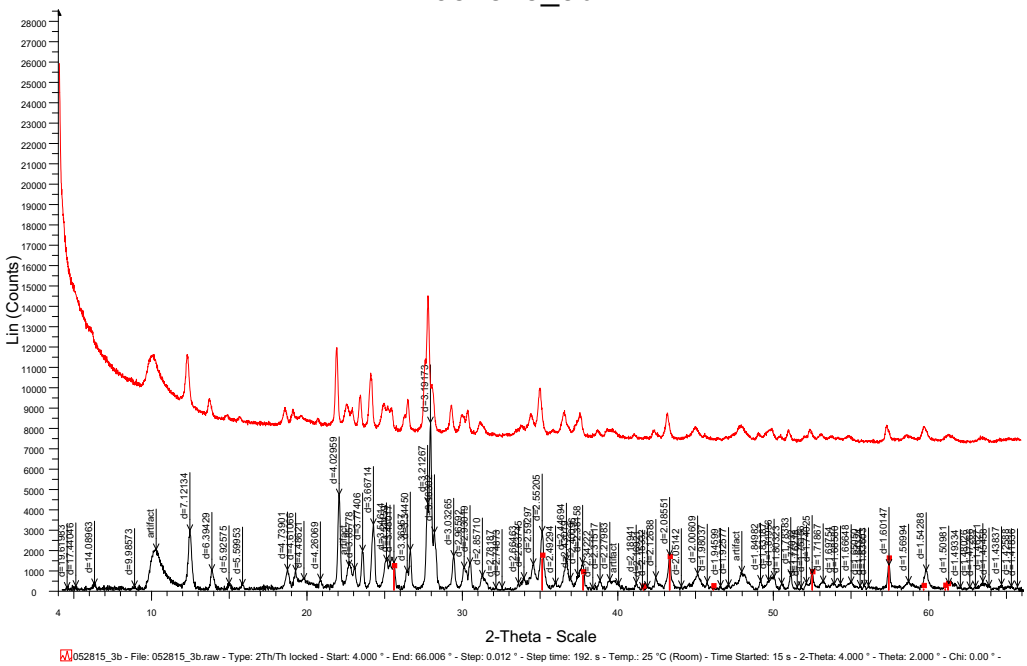

052815_3b - File: 052815_3b.raw - Type: 2Th/Th locked - Start: 4.000 ° - End: 66.006 ° - Step: 0.012 ° - Step time: 192. s - Temp.: 25 °C (Room) - Time Started: 15 s - 2-Theta: 4.000 ° - Theta: 2.000 ° - Chi: 0.00 ° - Operations: Y Scale Add 800 | Y Scale Add 800 | Y Scale Add 800 | Y Scale Add 0 | Y Scale Add 0 | Y Scale

052815_3b - File: 052815_3b.raw - Type: 2Th/Th locked - Start: 4.178 ° - End: 66.156 ° - Step: 0.012 ° - Step time: 192. s - Temp.: 25 °C (Room) - Time Started: 15 s - 2-Theta: 4.178 ° - Theta: 2.000 ° - Chi: 0.00 ° - Operations: Y Scale Mul 1.708 | Smooth 0.026 | Aberrant 18 | Displacement -0.338 | Background 0.501,1.000 | Strip kAlpha2 0.500 | Import

01-070-5679 (*) - Corundum, syn - Al2O3

053015_2a

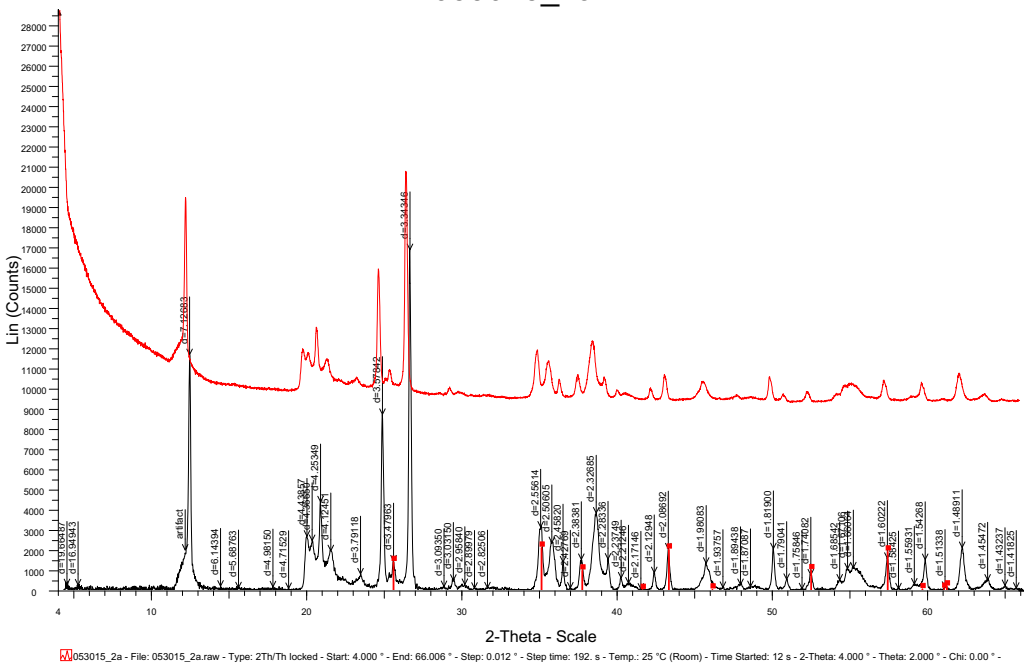

053015_2a - File: 053015_2a.raw - Type: 2Th/Th locked - Start: 4.000 ° - End: 66.006 ° - Step: 0.012 ° - Step time: 192. s - Temp.: 25 °C (Room) - Time Started: 12 s - 2-Theta: 4.000 ° - Theta: 2.000 ° - Chi: 0.00 ° - Operations: Y Scale Add -1000 | Y Scale Add -1000 | Y Scale Add 1000 | Y Scale Add 1000 | Y Scale Add 1000 | Y Scale Add 1000 | Y Scale Add

053015_2a - File: 053015_2a.raw - Type: 2Th/Th locked - Start: 4.276 ° - End: 66.238 ° - Step: 0.012 ° - Step time: 192. s - Temp.: 25 °C (Room) - Time Started: 12 s - 2-Theta: 4.276 ° - Theta: 2.000 ° - Chi: 0.00 ° - Operations: Y Scale Mul 2.000 | Smooth 0.019 | Aberrant 23 | Displacement -0.525 | Background 0.501,1.000 | Strip kAlpha2 0.500 | Import

01-070-5679 (*) - Corundum, syn - Al2O3 - Y: 6.99 % - d x by: 1. - WL: 1.5406 - Rhombo.H.axes - a 4.75970 - b 4.75970 - c 12.99350 - alpha 90.000 - beta 90.000 - gamma 120.000 - Primitive - R-3c (167) - 6 - 254.9

060914_3

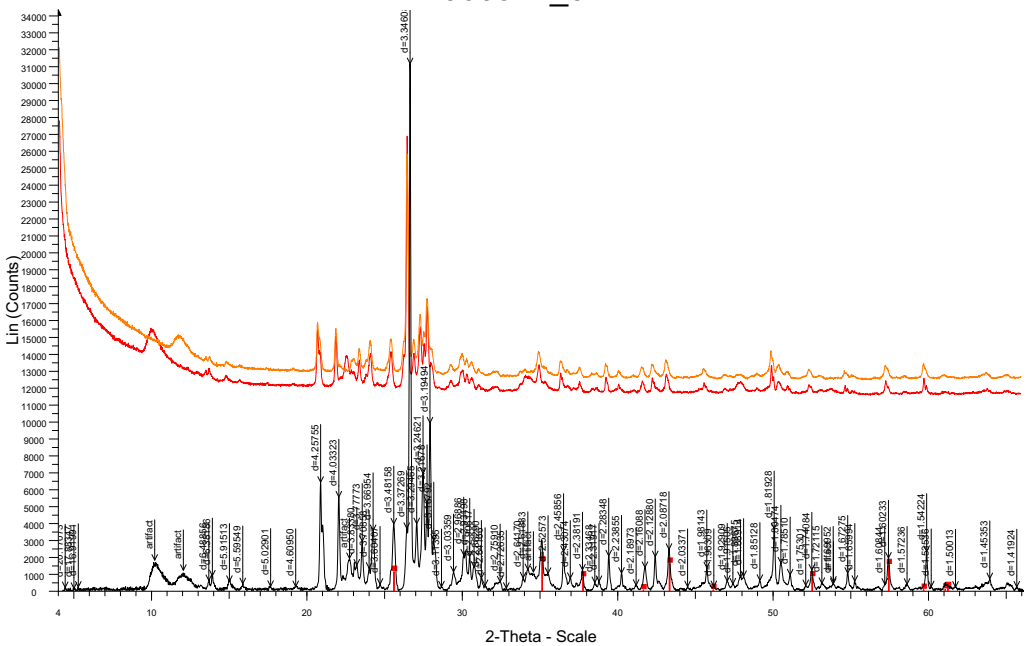

060914_3 - File: 060914_3_clip.raw - Type: Locked Coupled - Start: 4.007 ° - End: 66.001 ° - Step: 0.012 ° - Step time: 172.8 s - Temp.: 25 °C (Room) - Time Started: 12 s - 2-Theta: 4.007 ° - Theta: 2.003 ° - Chi: 0.0
Operations: Y Scale Add 1000 | Y Scale Add 1000 | Y Scale Add 1000 | Y Scale Add 1000 | Y Scale Add 1000 | Y Scale Add 1000 | Y Scale Add 1

060914_3 - File: 060914_3_rerun.raw - Type: 2Th/Th locked - Start: 4.000 ° - End: 66.006 ° - Step: 0.012 ° - Step time: 192. s - Temp.: 25 °C (Room) - Time Started: 12 s - 2-Theta: 4.000 ° - Theta: 2.000 ° - Chi: 0.00
Operations: Y Scale Add 1000 | Y Scale Add 1000 | Y Scale Add 1000 | Y Scale Add 1000 | Y Scale Add 1000 | Y Scale Add 1

060914_3 - File: 060914_3_clip.raw - Type: Locked Coupled - Start: 4.209 ° - End: 66.171 ° - Step: 0.012 ° - Step time: 172.8 s - Temp.: 25 °C (Room) - Time Started: 12 s - 2-Theta: 4.209 ° - Theta: 2.003 ° - Chi: 0.0
Operations: Y Scale Mul 1.458 | Smooth 0.019 | Aberrant 6 | Range Op. A+B | Displacement -0.385 | Displacement -0.388 | Displacement -0.42

01-070-5679 (*) - Corundum, syn - Al2O3

061014_2b

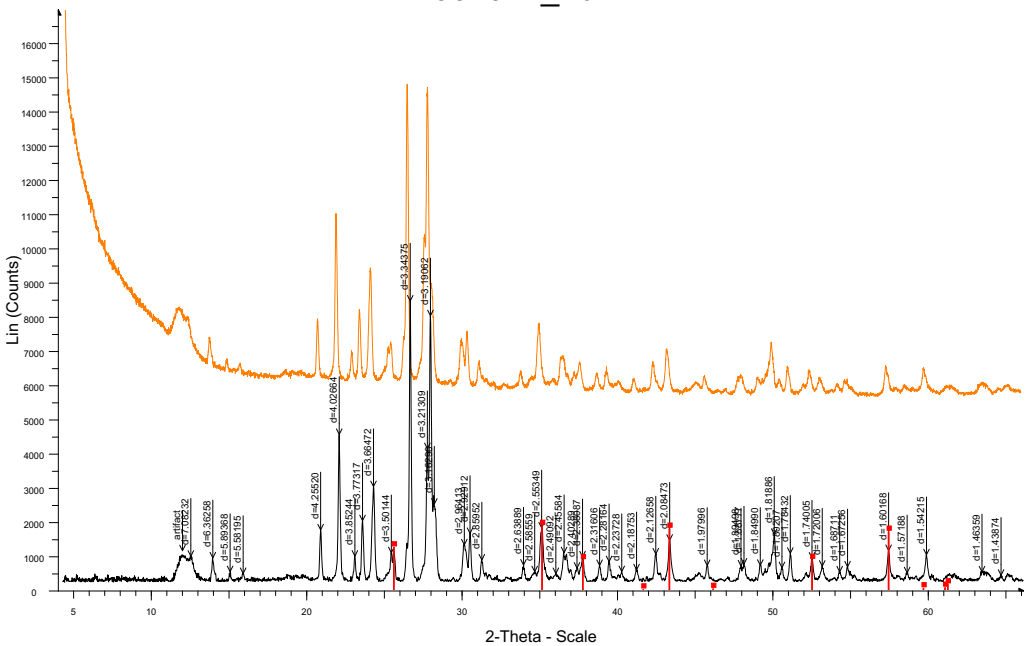

061014_2b - File: 061014_2b.raw - Type: 2Th/Th locked - Start: 4.000 ° - End: 66.006 ° - Step: 0.012 ° - Step time: 192. s - Temp.: 25 °C (Room) - Time Started: 12 s - 2-Theta: 4.000 ° - Theta: 2.000 ° - Chi: 0.00 ° -
Operations: Y Scale Add 1000 | Y Scale Add 1000 | Y Scale Add 1000 | Y Scale Add 1000 | Y Scale Add 1000 | Import

061014_2b - File: 061014_2b.raw - Type: 2Th/Th locked - Start: 4.220 ° - End: 66.191 ° - Step: 0.012 ° - Step time: 192. s - Temp.: 25 °C (Room) - Time Started: 12 s - 2-Theta: 4.220 ° - Theta: 2.000 ° - Chi: 0.00 ° -
Operations: Y Scale Mul 1.200 | Y Scale Add 208 | Smooth 0.026 | Aberrant 23 | Displacement -0.417 | Background 0.501,1.000 | Strip kAlpha

01-070-5679 (*) - Corundum, syn - Al2O3

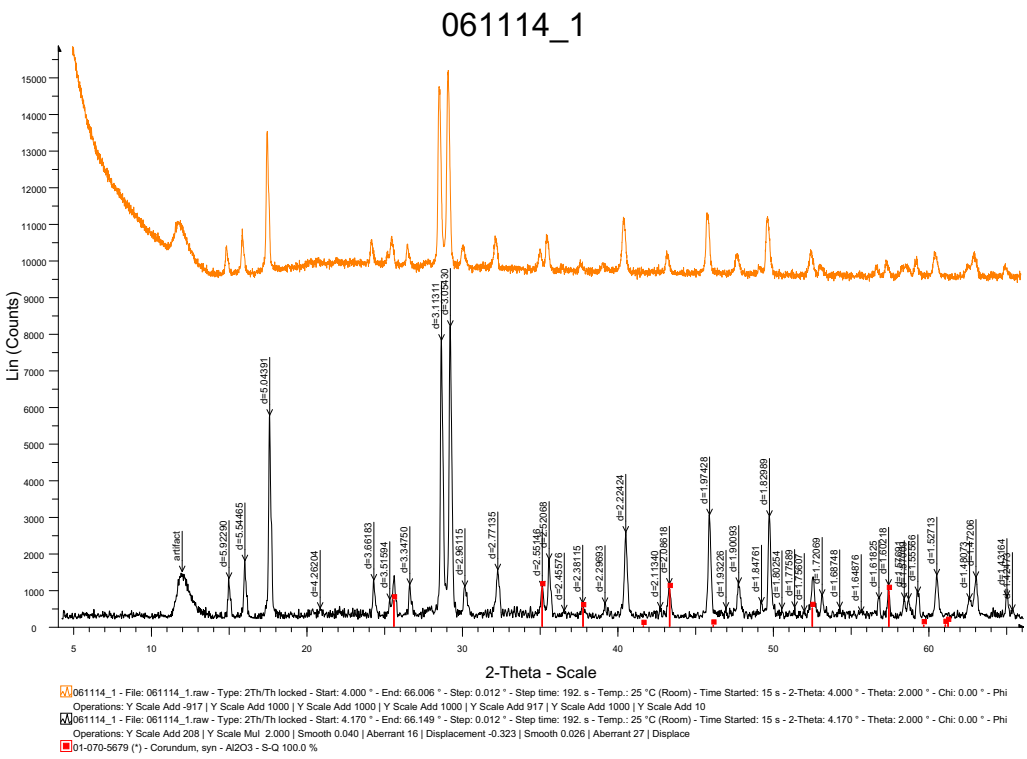
061114_1
Lin (Counts)
2-Theta - Scale
061114_1 - File: 061114_1.raw - Type: 2Th/Th locked - Start: 4.000 ° - End: 66.006 ° - Step: 0.012 ° - Step time: 192. s - Temp.: 25 °C (Room) - Time Started: 15 s - 2-Theta: 4.000 ° - Theta: 2.000 ° - Chi: 0.00 ° - Phi
Operations: Y Scale Add -917 | Y Scale Add 1000 | Y Scale Add 1000 | Y Scale Add 1000 | Y Scale Add 917 | Y Scale Add 1000 | Y Scale Add 10
061114_1 - File: 061114_1.raw - Type: 2Th/Th locked - Start: 4.170 ° - End: 66.149 ° - Step: 0.012 ° - Step time: 192. s - Temp.: 25 °C (Room) - Time Started: 15 s - 2-Theta: 4.170 ° - Theta: 2.000 ° - Chi: 0.00 ° - Phi
Operations: Y Scale Add 208 | Y Scale Mul 2.000 | Smooth 0.040 | Aberrant 16 | Displacement -0.323 | Smooth 0.026 | Aberrant 27 | Displace
01-070-5679 (*) - Corundum, syn - Al2O3 - S-Q 100.0 %

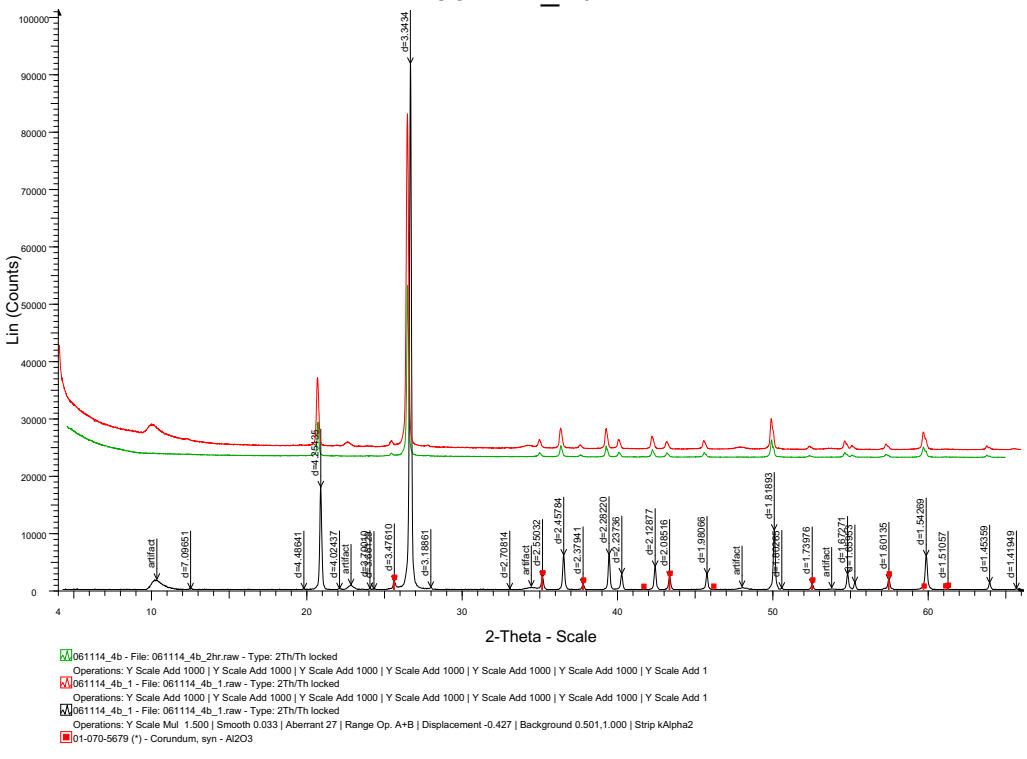
061114_4b
Lin (Counts)
2-Theta - Scale
061114_4b - File: 061114_4b_2hr.raw - Type: 2Th/Th locked
Operations: Y Scale Add 1000 | Y Scale Add 1000 | Y Scale Add 1000 | Y Scale Add 1000 | Y Scale Add 1000 | Y Scale Add 1000 | Y Scale Add 1
061114_4b_1 - File: 061114_4b_1.raw - Type: 2Th/Th locked
Operations: Y Scale Add 1000 | Y Scale Add 1000 | Y Scale Add 1000 | Y Scale Add 1000 | Y Scale Add 1000 | Y Scale Add 1000 | Y Scale Add 1
061114_4b_1 - File: 061114_4b_1.raw - Type: 2Th/Th locked
Operations: Y Scale Mul 1.500 | Smooth 0.033 | Aberrant 27 | Range Op. A+B | Displacement -0.427 | Background 0.501,1.000 | Strip kAlpha2
01-070-5679 (*) - Corundum, syn - Al2O3

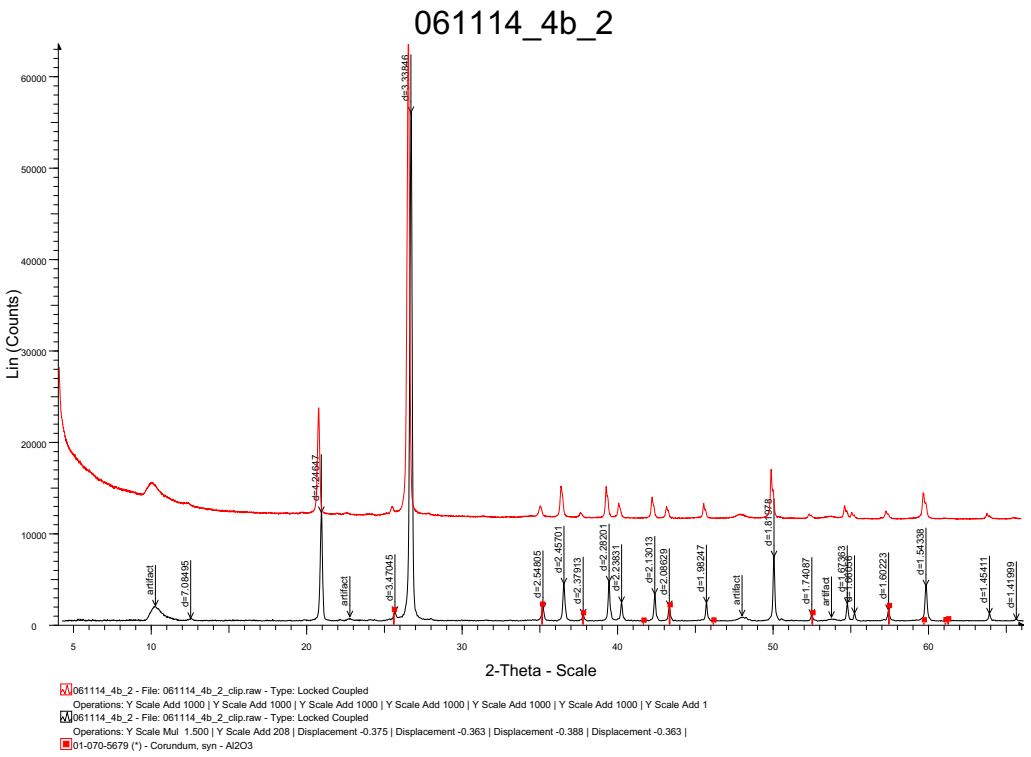
061114_4b_2
Lin (Counts)
2-Theta - Scale
d=3.33946
d=4.24647
d=3.47045
d=2.54805
d=2.45701
d=2.37913
d=2.28201
d=2.23651
d=2.13013
d=2.08629
d=1.98247
d=1.81978
d=1.74087
d=1.67683
d=1.66052
d=1.60223
d=1.54338
d=1.45411
d=1.41999
d=7.08495
artifact
061114_4b_2 - File: 061114_4b_2_clip.raw - Type: Locked Coupled
Operations: Y Scale Add 1000 | Y Scale Add 1000 | Y Scale Add 1000 | Y Scale Add 1000 | Y Scale Add 1000 | Y Scale Add 1000 | Y Scale Add 1
061114_4b_2 - File: 061114_4b_2_clip.raw - Type: Locked Coupled
Operations: Y Scale Mul 1.500 | Y Scale Add 208 | Displacement -0.375 | Displacement -0.363 | Displacement -0.388 | Displacement -0.363 |
01-070-5679 (*) - Corundum, syn - Al2O3

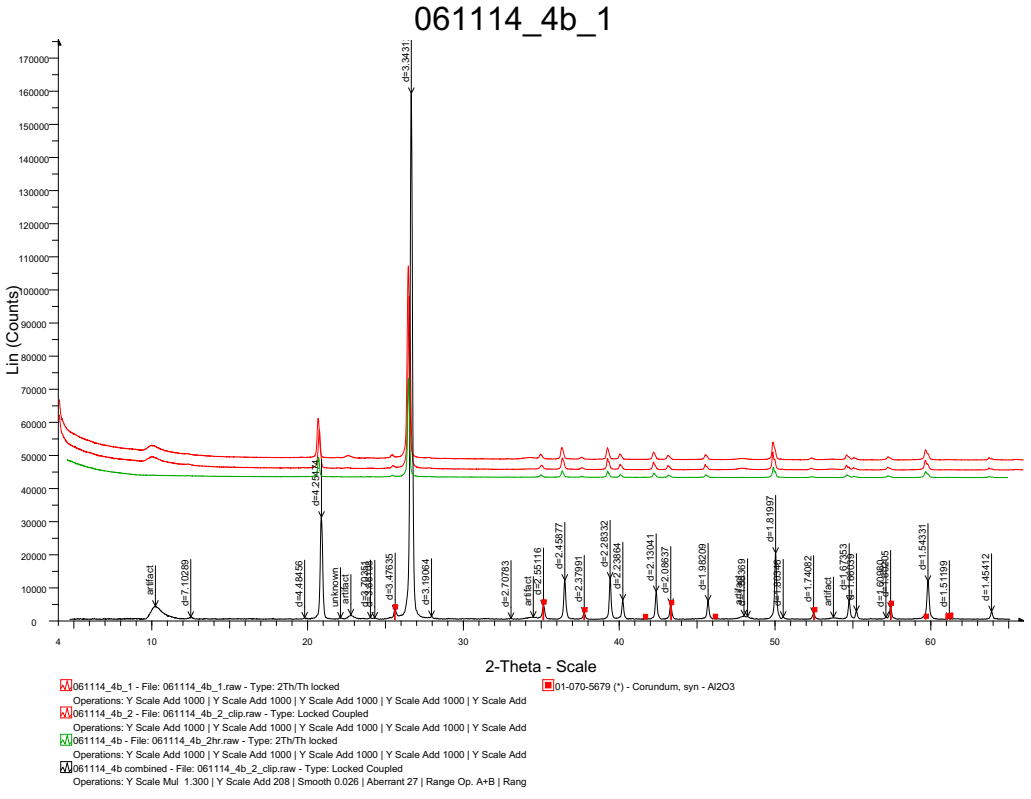
061114_4b_1
Lin (Counts)
2-Theta - Scale
d=3.34311
d=4.25434
d=3.47635
d=3.19064
d=2.70793
d=2.55116
d=2.46877
d=2.37991
d=2.28332
d=2.23864
d=2.13041
d=2.08637
d=1.98209
d=1.81997
d=1.74082
d=1.67683
d=1.66052
d=1.60980
d=1.54331
d=1.51199
d=1.45412
d=7.10289
d=4.49456
artifact
unknown
061114_4b_1 - File: 061114_4b_1.raw - Type: 2Th/Th locked
Operations: Y Scale Add 1000 | Y Scale Add 1000 | Y Scale Add 1000 | Y Scale Add 1000 | Y Scale Add
061114_4b_2 - File: 061114_4b_2_clip.raw - Type: Locked Coupled
Operations: Y Scale Add 1000 | Y Scale Add 1000 | Y Scale Add 1000 | Y Scale Add 1000 | Y Scale Add
061114_4b - File: 061114_4b_2hr.raw - Type: 2Th/Th locked
Operations: Y Scale Add 1000 | Y Scale Add 1000 | Y Scale Add 1000 | Y Scale Add 1000 | Y Scale Add
061114_4b combined - File: 061114_4b_2_clip.raw - Type: Locked Coupled
Operations: Y Scale Mul 1.300 | Y Scale Add 208 | Smooth 0.026 | Aberrant 27 | Range Op. A+B | Rang
01-070-5679 (*) - Corundum, syn - Al2O3

061214_5

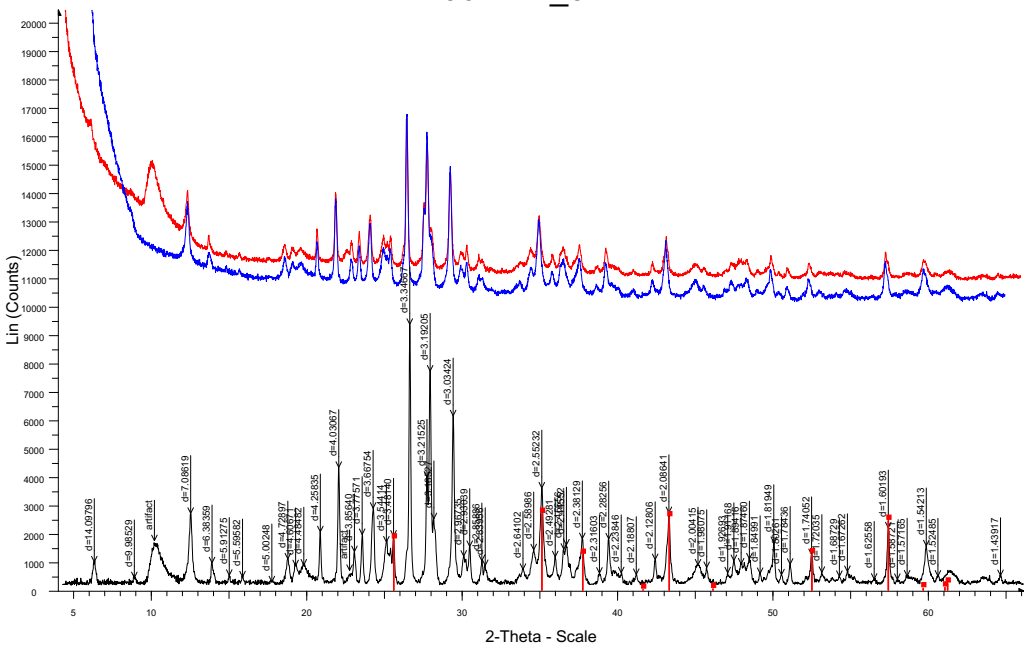

061214_5 - File: 061214_5.raw - Type: 2Th/Th locked - Start: 4.000 ° - End: 66.006 ° - Step: 0.012 ° - Step time: 192. s - Temp.: 25 °C (Room) - Time Started: 13 s - 2-Theta: 4.000 ° - Theta: 2.000 ° - Chi: 0.00 ° - Phi
Operations: Y Scale Add 1000 | Y Scale Add 1000 | Y Scale Add 1000 | Y Scale Add 1000 | Y Scale Add 1000 | Y Scale Add 1000 | Y Scale Add 1

061214_5 - File: 061214_5_2hr.raw - Type: 2Th/Th locked - Start: 4.500 ° - End: 65.007 ° - Step: 0.012 ° - Step time: 249.6 s - Temp.: 25 °C (Room) - Time Started: 12 s - 2-Theta: 4.500 ° - Theta: 2.250 ° - Chi: 0.00
Operations: Y Scale Add 958 | Y Scale Add 1000 | Y Scale Add 1000 | Y Scale Add 1000 | Y Scale Add 1000 | Y Scale Add 10

061214_5 - File: 061214_5.raw - Type: 2Th/Th locked - Start: 4.211 ° - End: 66.183 ° - Step: 0.012 ° - Step time: 192. s - Temp.: 25 °C (Room) - Time Started: 13 s - 2-Theta: 4.211 ° - Theta: 2.000 ° - Chi: 0.00 ° - Phi
Operations: Y Scale Mul 1.200 | Y Scale Add 167 | Smooth 0.019 | Aberrant 19 | Range Op. A+B | Displacement -0.400 | Background 0.501,1.00

01-070-5679 (*) - Corundum, syn - Al2O3

071613_2

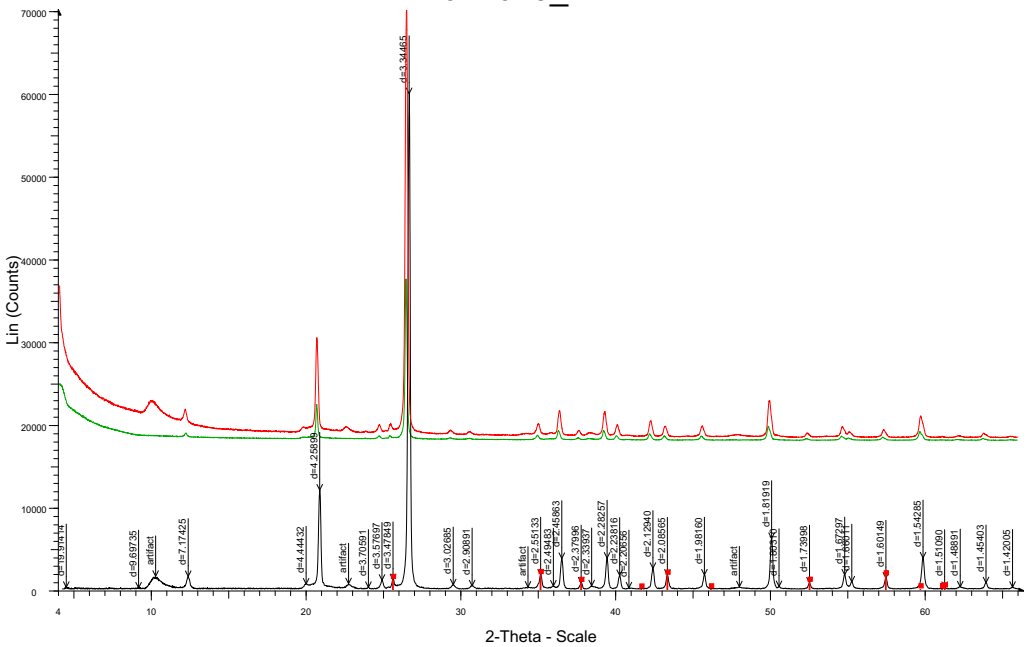

071613_2 - File: 071613_2.raw - Type: 2Th/Th locked - Start: 4.000 ° - End: 66.006 ° - Step: 0.012 ° - Step time: 192. s - Temp.: 25 °C (Room) - Time Started: 12 s - 2-Theta: 4.000 ° - Theta: 2.000 ° - Chi: 0.00 ° - Phi
Operations: Y Scale Add 1000 | Y Scale Add 1000 | Y Scale Add 1000 | Y Scale Add 1000 | Y Scale Add 1000 | Y Scale Add 1

071613_2 - File: 071613_2_std.raw - Type: 2Th/Th locked - Start: 4.000 ° - End: 66.006 ° - Step: 0.012 ° - Step time: 192. s - Temp.: 25 °C (Room) - Time Started: 15 s - 2-Theta: 4.000 ° - Theta: 2.000 ° - Chi: 0.00 ° -
Operations: Y Scale Add 1000 | Y Scale Add 1000 | Y Scale Add 1000 | Y Scale Add 1000 | Y Scale Add 1000 | Y Scale Add 1

071613_2 - File: 071613_2.raw - Type: 2Th/Th locked - Start: 4.184 ° - End: 66.161 ° - Step: 0.012 ° - Step time: 192. s - Temp.: 25 °C (Room) - Time Started: 12 s - 2-Theta: 4.184 ° - Theta: 2.000 ° - Chi: 0.00 ° - Phi
Operations: Y Scale Mul 1.200 | Y Scale Add 83 | Smooth 0.026 | Aberrant 21 | Range Op. A+B | Displacement -0.350 | Background 0.501,1.00

01-070-5679 (*) - Corundum, syn - Al2O3

071813_2_1

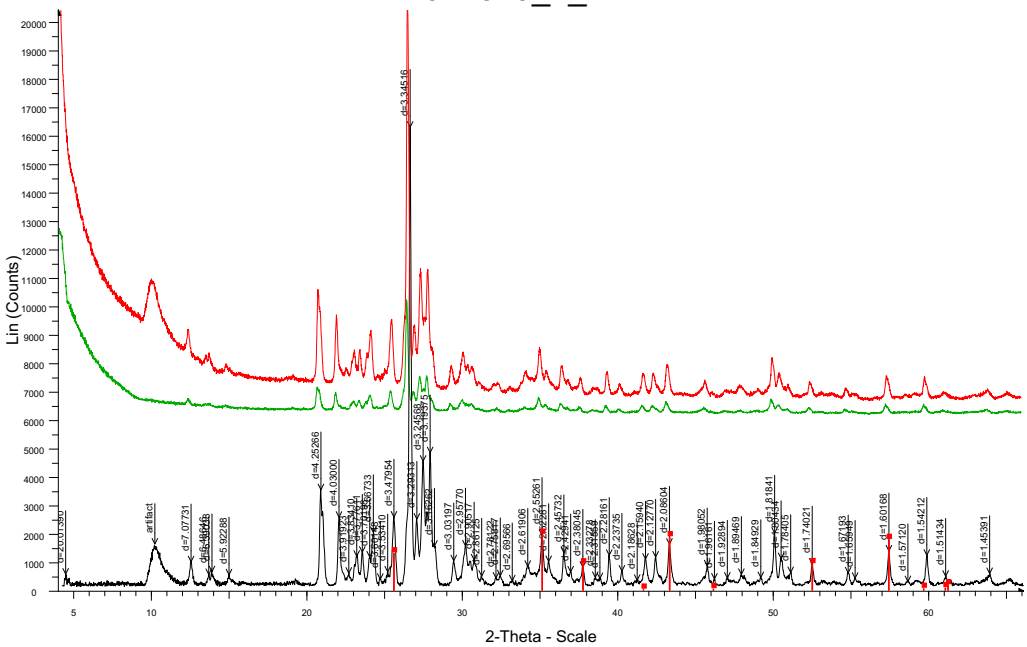

071813_2_1 - File: 071813_2_1.raw - Type: 2Th/Th locked - Start: 4.000 ° - End: 66.006 ° - Step: 0.012 ° - Step time: 192. s - Temp.: 25 °C (Room) - Time Started: 15 s - 2-Theta: 4.000 ° - Theta: 2.000 ° - Chi: 0.00 °
Operations: Y Scale Add 1000 | Y Scale Add 1000 | Y Scale Add 1000 | Y Scale Add 1000 | Y Scale Add 1000 | Y Scale Add 1000 | Import
071813_2_1 - File: 071813_2_1_std.raw - Type: 2Th/Th locked - Start: 4.000 ° - End: 66.006 ° - Step: 0.012 ° - Step time: 192. s - Temp.: 25 °C (Room) - Time Started: 12 s - 2-Theta: 4.000 ° - Theta: 2.000 ° - Chi: 0.
Operations: Y Scale Add -1000 | Y Scale Add 1000 | Y Scale Add 1000 | Y Scale Add 1000 | Y Scale Add 1000 | Y Scale Add
071813_2_1 - File: 071813_2_1.raw - Type: 2Th/Th locked - Start: 4.184 ° - End: 66.161 ° - Step: 0.012 ° - Step time: 192. s - Temp.: 25 °C (Room) - Time Started: 15 s - 2-Theta: 4.184 ° - Theta: 2.000 ° - Chi: 0.00 °
Operations: Y Scale Mul 1.200 | Y Scale Add 125 | Smooth 0.026 | Aberrant 19 | Range Op. A+B | Displacement -0.350 | Background 0.500,1.00
01-070-5679 (*) - Corundum, syn - Al2O3

071813_3

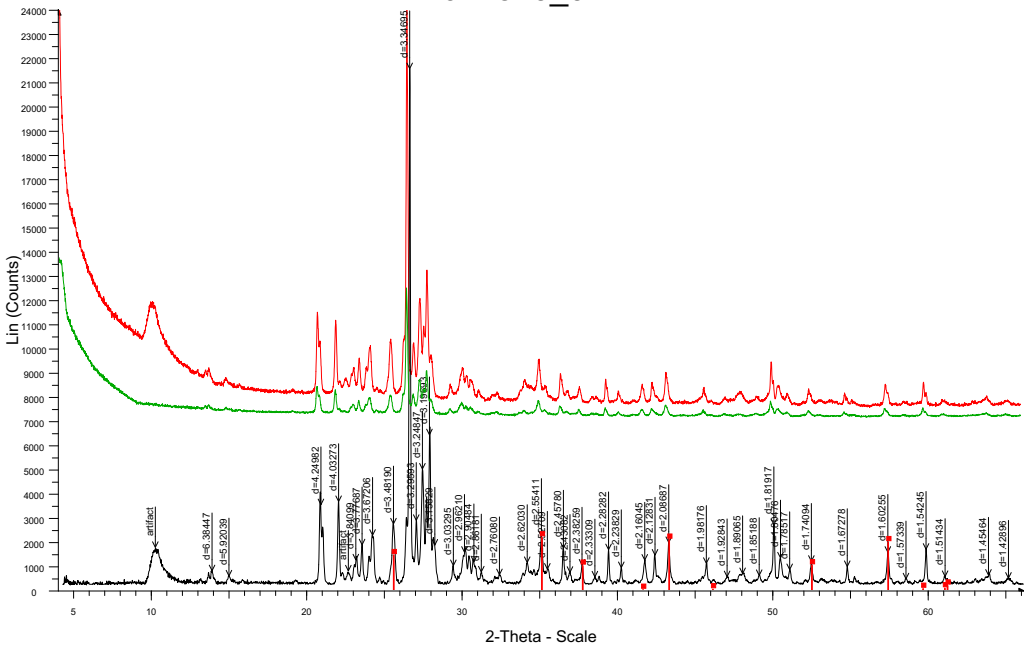

071813_3 - File: 071813_3.raw - Type: 2Th/Th locked - Start: 4.000 ° - End: 66.006 ° - Step: 0.012 ° - Step time: 192. s - Temp.: 25 °C (Room) - Time Started: 12 s - 2-Theta: 4.000 ° - Theta: 2.000 ° - Chi: 0.00 ° - Phi
Operations: Y Scale Add 1000 | Y Scale Add 1000 | Y Scale Add 1000 | Y Scale Add 1000 | Y Scale Add 1000 | Y Scale Add 1
071813_3_1 - File: 071813_3_1_std.raw - Type: 2Th/Th locked - Start: 4.000 ° - End: 66.006 ° - Step: 0.012 ° - Step time: 192. s - Temp.: 25 °C (Room) - Time Started: 12 s - 2-Theta: 4.000 ° - Theta: 2.000 ° - Chi: 0.
Operations: Y Scale Add 1000 | Y Scale Add 1000 | Y Scale Add 1000 | Y Scale Add 1000 | Y Scale Add 1000 | Y Scale Add 1
071813_3 - File: 071813_3.raw - Type: 2Th/Th locked - Start: 4.226 ° - End: 66.196 ° - Step: 0.012 ° - Step time: 192. s - Temp.: 25 °C (Room) - Time Started: 12 s - 2-Theta: 4.226 ° - Theta: 2.000 ° - Chi: 0.00 ° - Phi
Operations: Y Scale Mul 1.200 | Y Scale Add 1000 | Y Scale Add 1 | Y Scale Add 0 | Y Scale Add -1000 | Y Scale Add 200 | Smooth 0.026 | Ab
01-070-5679 (*) - Corundum, syn - Al2O3

OC072013-1

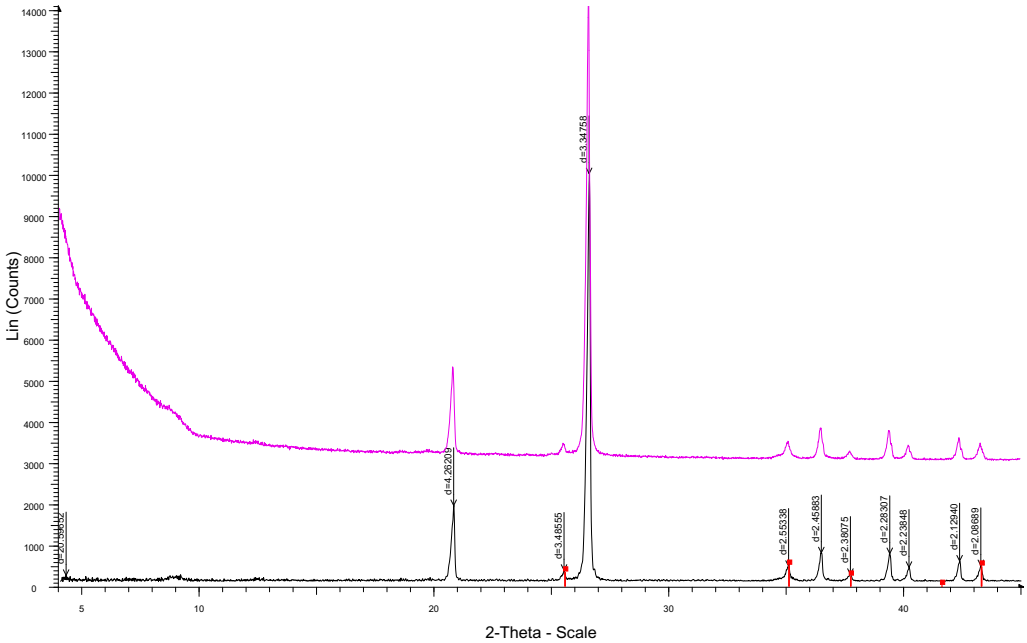

OC072013-1 - File: OC072013-1.raw - Type: 2Th/Th locked - Start: 4.000 ° - End: 44.996 ° - Step: 0.013 ° - Step time: 57.6 s - Temp.: 25 °C (Room) - Time Started: 15 s - 2-Theta: 4.000 ° - Theta: 2.000 ° - Chi: 0.00
Operations: Y Scale Add -1000 | Y Scale Add -1000 | Y Scale Add 1000 | Y Scale Add 1000 | Y Scale Add 1000 | Y Scale Add 1000 | Y Scale Add

OC072013-1 - File: OC072013-1.raw - Type: 2Th/Th locked - Start: 4.044 ° - End: 45.036 ° - Step: 0.013 ° - Step time: 57.6 s - Temp.: 25 °C (Room) - Time Started: 15 s - 2-Theta: 4.044 ° - Theta: 2.000 ° - Chi: 0.00
Operations: Y Scale Mul 1.200 | Y Scale Add 100 | Smooth 0.021 | Aberrant 24 | Displacement -0.083 | Displacement -0.083 | Background 0.50

01-070-5679 (*) - Corundum, syn - Al2O3

OC072013-2

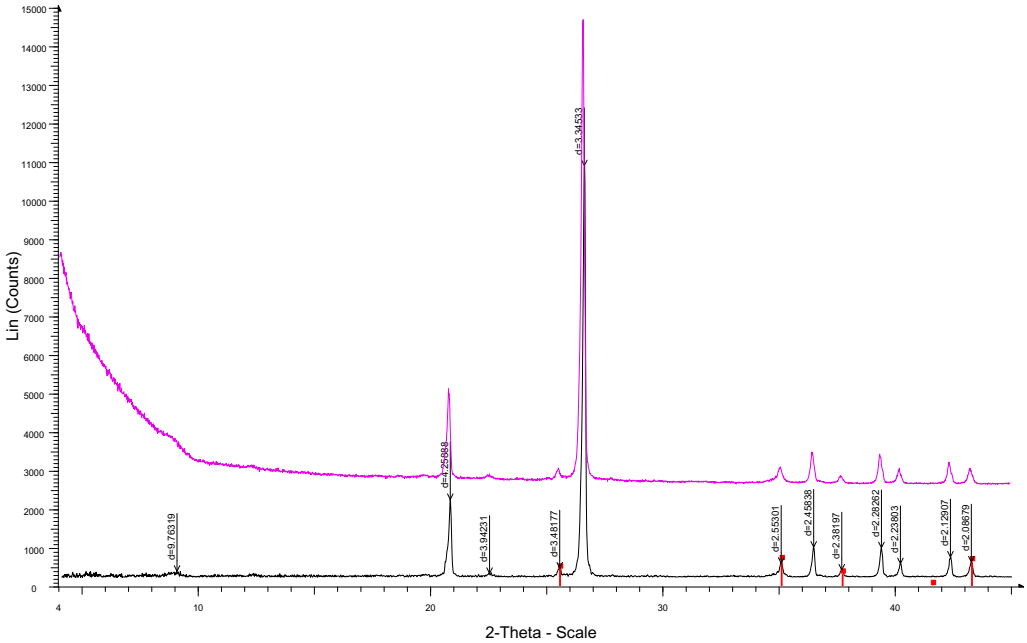

OC072013-2 - File: OC072013-2.raw - Type: 2Th/Th locked - Start: 4.000 ° - End: 44.996 ° - Step: 0.013 ° - Step time: 57.6 s - Temp.: 25 °C (Room) - Time Started: 10 s - 2-Theta: 4.000 ° - Theta: 2.000 ° - Chi: 0.00
Operations: Y Scale Add -417 | Y Scale Add 1000 | Y Scale Add 1000 | Y Scale Add 1000 | Import

OC072013-2 - File: OC072013-2.raw - Type: 2Th/Th locked - Start: 4.077 ° - End: 45.067 ° - Step: 0.013 ° - Step time: 57.6 s - Temp.: 25 °C (Room) - Time Started: 10 s - 2-Theta: 4.077 ° - Theta: 2.000 ° - Chi: 0.00
Operations: Y Scale Mul 1.200 | Y Scale Add 200 | Smooth 0.029 | Aberrant 22 | Displacement -0.146 | Background 0.501,1.000 | Strip kAlpha

01-070-5679 (*) - Corundum, syn - Al2O3

072013_7

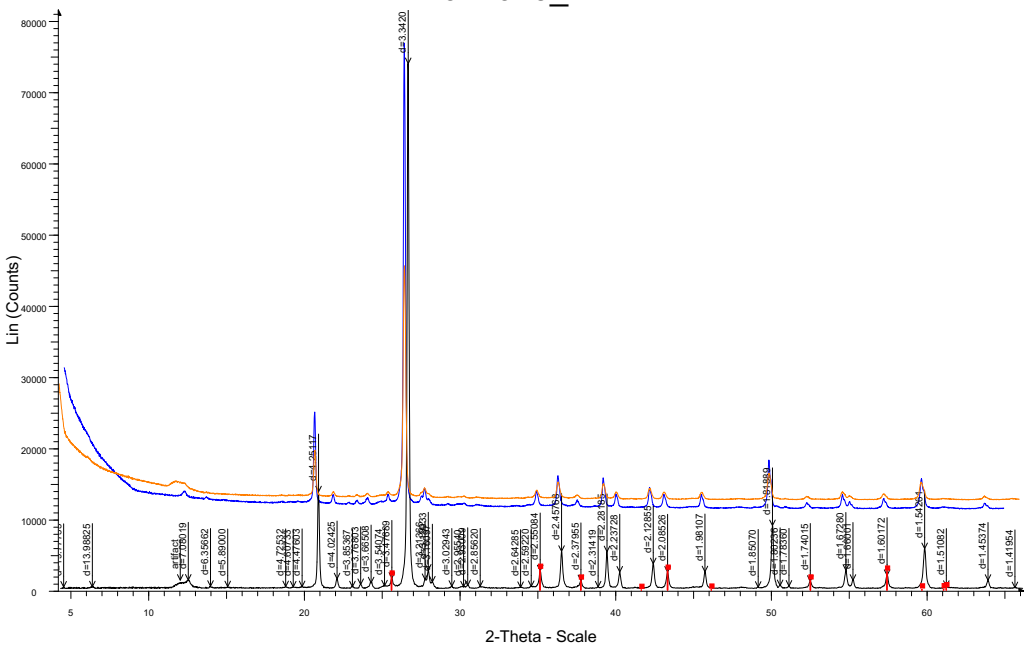

072013_7 - File: 072013_7.raw - Type: 2Th/Th locked - Start: 4.000 ° - End: 66.006 ° - Step: 0.012 ° - Step time: 192. s - Temp.: 25 °C (Room) - Time Started: 15 s - 2-Theta: 4.000 ° - Theta: 2.000 ° - Chi: 0.00 ° - Phi
Operations: Y Scale Add 801 | Y Scale Add 801 | Y Scale Add 801 | Y Scale Add 801 | Y Scale Add 1000 | Y Scale Add 1000 | Y Scale Add 1000

072013_7 - File: 072013_7_2hr.raw - Type: 2Th/Th locked - Start: 4.500 ° - End: 65.007 ° - Step: 0.012 ° - Step time: 249.6 s - Temp.: 25 °C (Room) - Time Started: 13 s - 2-Theta: 4.500 ° - Theta: 2.250 ° - Chi: 0.00
Operations: Y Scale Add 1000 | Y Scale Add 1000 | Y Scale Add 1000 | Y Scale Add 958 | Y Scale Add 958 | Y Scale Add 958

072013_7 - File: 072013_7.raw - Type: 2Th/Th locked - Start: 4.263 ° - End: 66.227 ° - Step: 0.012 ° - Step time: 192. s - Temp.: 25 °C (Room) - Time Started: 15 s - 2-Theta: 4.263 ° - Theta: 2.000 ° - Chi: 0.00 ° - Phi
Operations: Y Scale Mul 1.100 | Y Scale Mul 0.800 | Y Scale Mul 1.100 | Y Scale Mul 1.200 | Y Scale Add 200 | Smooth 0.026 | Aberrant 2

01-070-5679 (*) - Corundum, syn - Al2O3

OC072213-7

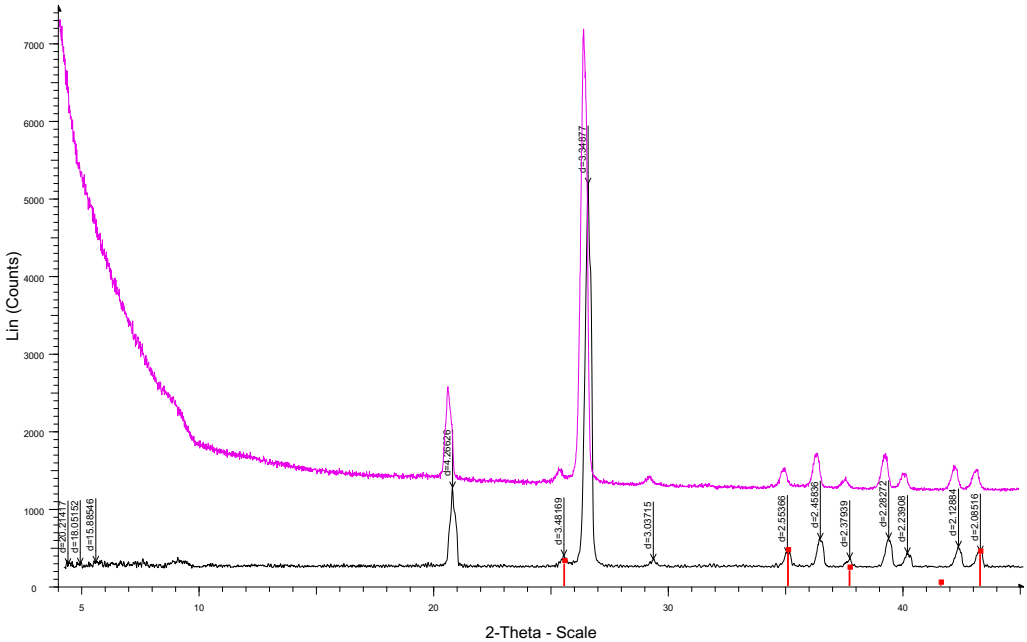

OC072213-7 - File: OC072213-7.raw - Type: 2Th/Th locked - Start: 4.000 ° - End: 44.996 ° - Step: 0.013 ° - Step time: 57.6 s - Temp.: 25 °C (Room) - Time Started: 10 s - 2-Theta: 4.000 ° - Theta: 2.000 ° - Chi: 0.00
Operations: Y Scale Mul 1.000 | Y Scale Add -833 | Y Scale Add 1000 | Y Scale Add 1000 | Import

OC072213-7 - File: OC072213-7.raw - Type: 2Th/Th locked - Start: 4.206 ° - End: 45.187 ° - Step: 0.013 ° - Step time: 57.6 s - Temp.: 25 °C (Room) - Time Started: 10 s - 2-Theta: 4.206 ° - Theta: 2.000 ° - Chi: 0.00
Operations: Y Scale Mul 1.200 | Y Scale Add 200 | Smooth 0.037 | Aberrant 13 | Displacement -0.392 | Background 0.501,1.000 | Strip kAlpha

01-070-5679 (*) - Corundum, syn - Al2O3

OC072213-9

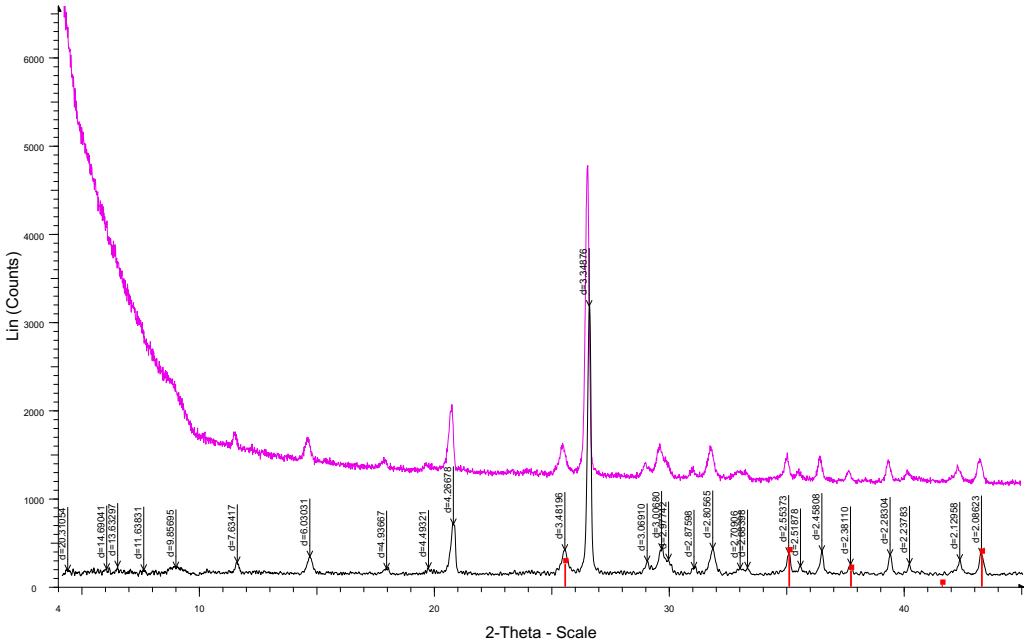

OC072213-9 - File: OC072213-9.raw - Type: 2Th/Th locked - Start: 4.000 ° - End: 44.996 ° - Step: 0.013 ° - Step time: 57.6 s - Temp.: 25 °C (Room) - Time Started: 10 s - 2-Theta: 4.000 ° - Theta: 2.000 ° - Chi: 0.00
Operations: Y Scale Add 1000 | Import
OC072213-9 - File: OC072213-9.raw - Type: 2Th/Th locked - Start: 4.110 ° - End: 45.097 ° - Step: 0.013 ° - Step time: 57.6 s - Temp.: 25 °C (Room) - Time Started: 10 s - 2-Theta: 4.110 ° - Theta: 2.000 ° - Chi: 0.00
Operations: Y Scale Mul 1.200 | Y Scale Add 100 | Smooth 0.053 | Aberrant 31 | Displacement -0.208 | Background 0.501,1.000 | Strip kAlpha
01-070-5679 (*) - Corundum, syn - Al2O3

OC072213-10

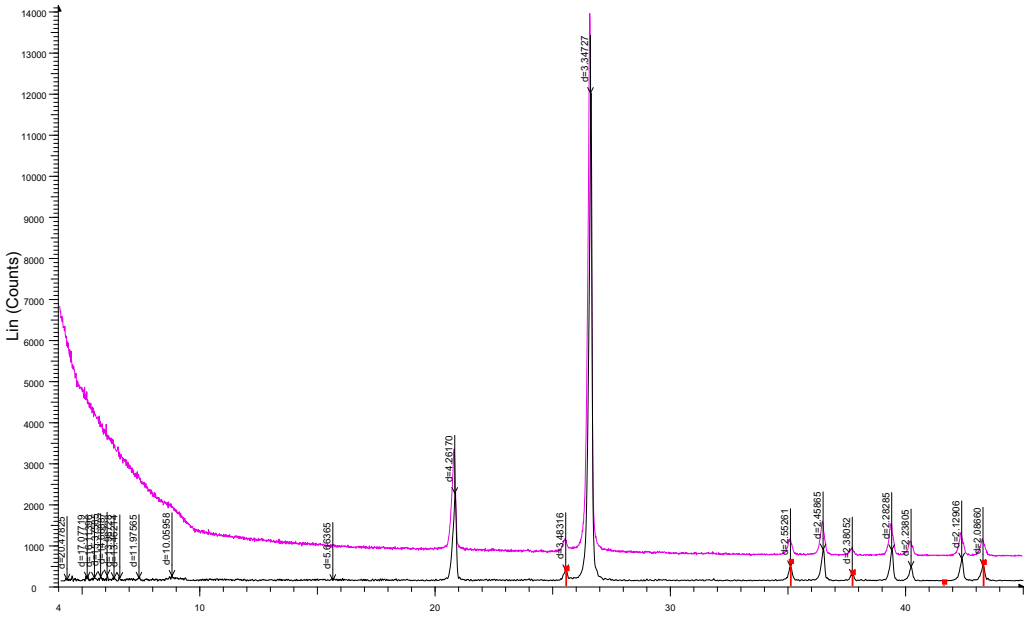

OC072213-10 - File: OC072213-10.raw - Type: 2Th/Th locked - Start: 4.000 ° - End: 44.996 ° - Step: 0.013 ° - Step time: 57.6 s - Temp.: 25 °C (Room) - Time Started: 10 s - 2-Theta: 4.000 ° - Theta: 2.000 ° - Chi: 0.0
Operations: Y Scale Add 667 | Import
OC072213-10 - File: OC072213-10.raw - Type: 2Th/Th locked - Start: 4.053 ° - End: 45.045 ° - Step: 0.013 ° - Step time: 57.6 s - Temp.: 25 °C (Room) - Time Started: 10 s - 2-Theta: 4.053 ° - Theta: 2.000 ° - Chi: 0.0
Operations: Y Scale Mul 1.200 | Y Scale Add 100 | Smooth 0.045 | Aberrant 28 | Displacement -0.100 | Background 0.501,1.000 | Strip kAlpha
01-070-5679 (*) - Corundum, syn - Al2O3

OC072213-14

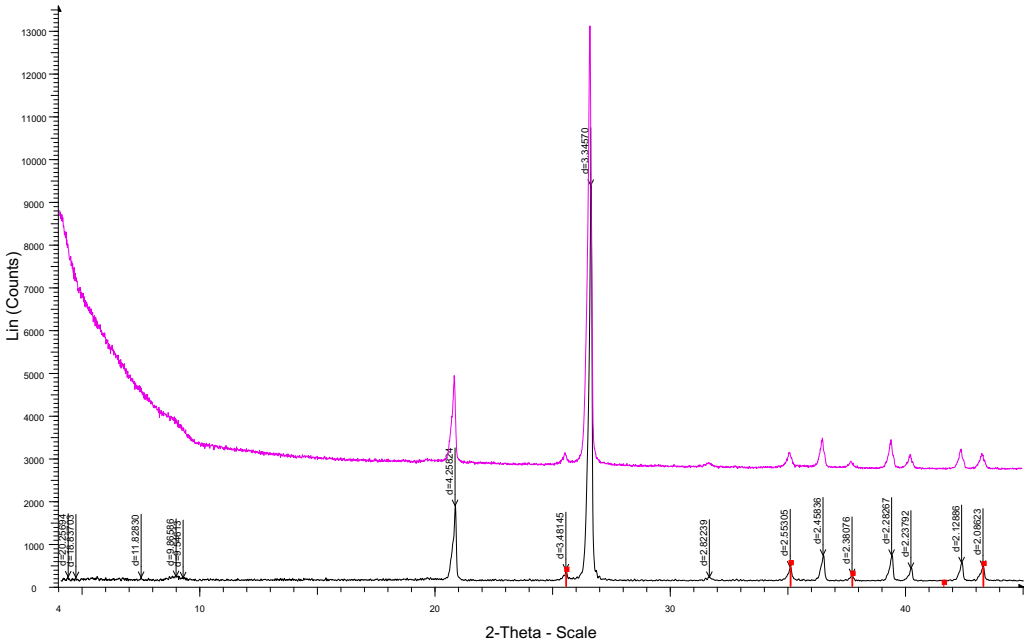

OC072213-14 - File: OC072213-14.raw - Type: 2Th/Th locked - Start: 4.000 ° - End: 44.996 ° - Step: 0.013 ° - Step time: 57.6 s - Temp.: 25 °C (Room) - Time Started: 10 s - 2-Theta: 4.000 ° - Theta: 2.000 ° - Chi: 0.0
Operations: Y Scale Add 667 | Y Scale Add 1000 | Y Scale Add 1000 | Import
OC072213-14 - File: OC072213-14.raw - Type: 2Th/Th locked - Start: 4.057 ° - End: 45.049 ° - Step: 0.013 ° - Step time: 57.6 s - Temp.: 25 °C (Room) - Time Started: 10 s - 2-Theta: 4.057 ° - Theta: 2.000 ° - Chi: 0.0
Operations: Y Scale Mul 1.200 | Y Scale Add 100 | Smooth 0.037 | Aberrant 19 | Displacement -0.108 | Background 0.501,1.000 | Strip kAlpha
01-070-5679 (*) - Corundum, syn - Al2O3

OC072213-16

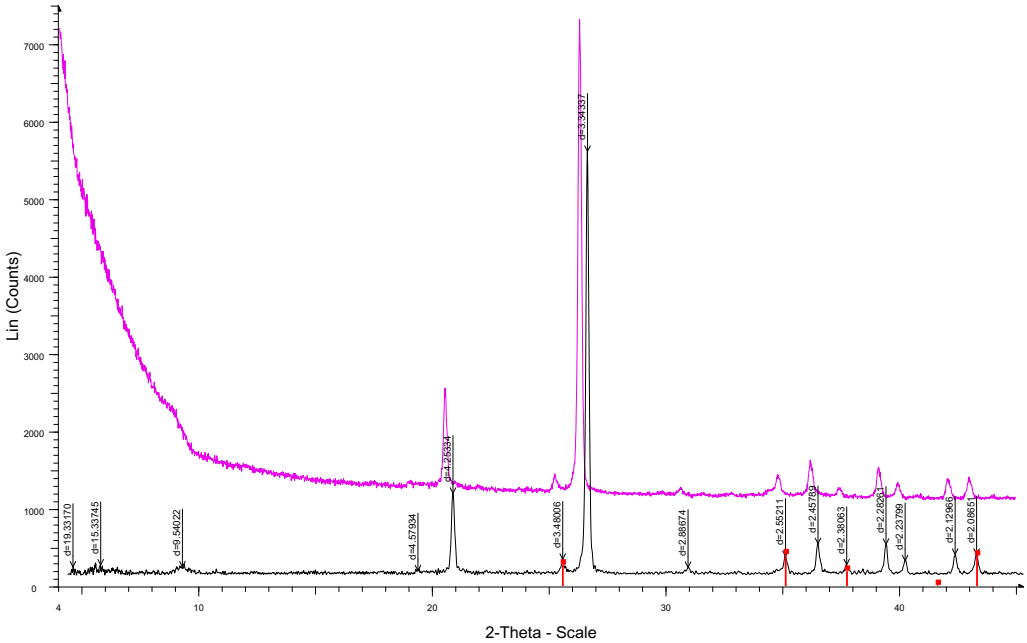

OC072213-16 - File: OC072213-16.raw - Type: 2Th/Th locked - Start: 4.000 ° - End: 44.996 ° - Step: 0.013 ° - Step time: 57.6 s - Temp.: 25 °C (Room) - Time Started: 10 s - 2-Theta: 4.000 ° - Theta: 2.000 ° - Chi: 0.0
Operations: Y Scale Add 1000 | Import
OC072213-16 - File: OC072213-16.raw - Type: 2Th/Th locked - Start: 4.358 ° - End: 45.326 ° - Step: 0.013 ° - Step time: 57.6 s - Temp.: 25 °C (Room) - Time Started: 10 s - 2-Theta: 4.358 ° - Theta: 2.000 ° - Chi: 0.0
Operations: Y Scale Mul 1.200 | Y Scale Add 125 | Smooth 0.037 | Aberrant 12 | Displacement -0.679 | Background 0.501,1.000 | Strip kAlpha
01-070-5679 (*) - Corundum, syn - Al2O3

OC072213-17

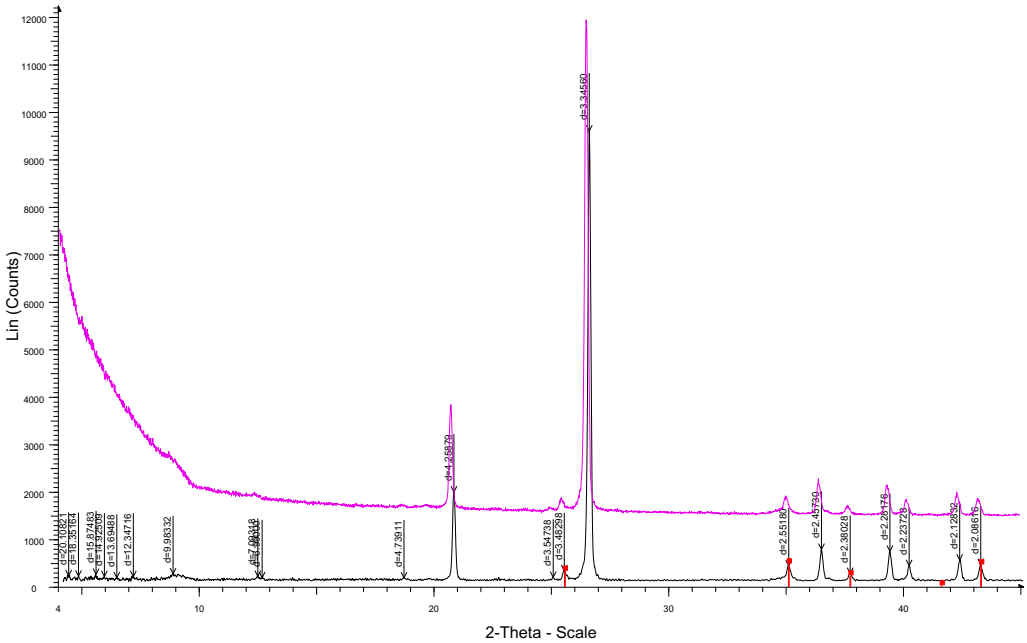

OC072213-17 - File: OC072213-17.raw - Type: 2Th/Th locked - Start: 4.000 ° - End: 44.996 ° - Step: 0.013 ° - Step time: 57.6 s - Temp.: 25 °C (Room) - Time Started: 11 s - 2-Theta: 4.000 ° - Theta: 2.000 ° - Chi: 0.0
Operations: Y Scale Add 417 | Y Scale Add 1000 | Import

OC072213-17 - File: OC072213-17.raw - Type: 2Th/Th locked - Start: 4.154 ° - End: 45.138 ° - Step: 0.013 ° - Step time: 57.6 s - Temp.: 25 °C (Room) - Time Started: 11 s - 2-Theta: 4.154 ° - Theta: 2.000 ° - Chi: 0.0
Operations: Y Scale Mul 1.200 | Y Scale Add 100 | Displacement -0.292 | Smooth 0.037 | Aberrant 26 | Background 0.501,1.000 | Strip kAlpha

01-070-5679 (*) - Corundum, syn - Al2O3

083014_3

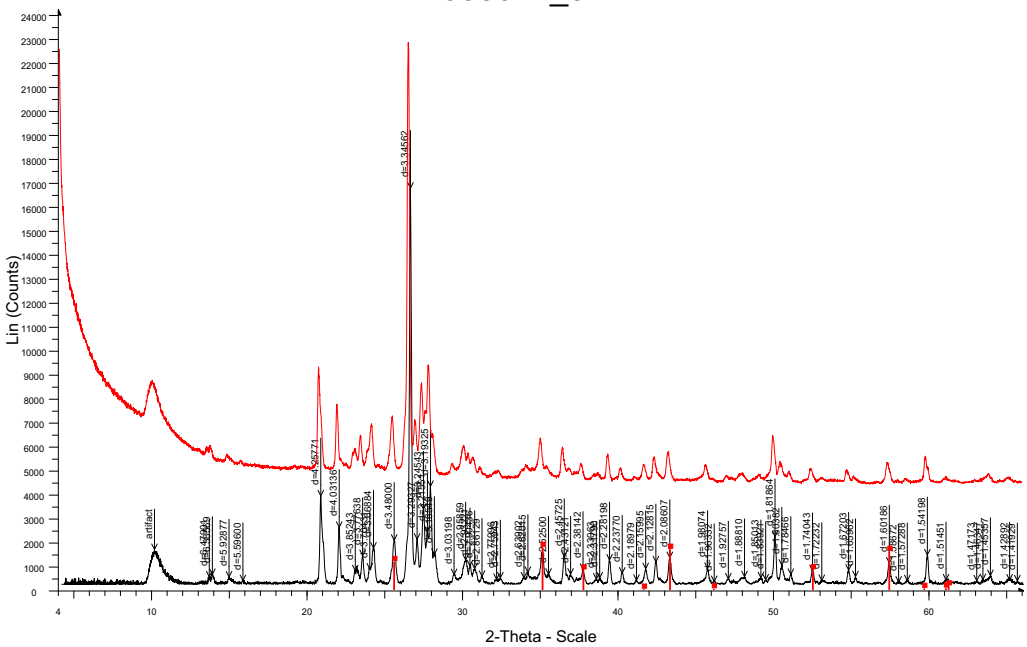

083014_3 - File: 083014_3.raw - Type: 2Th/Th locked - Start: 4.000 ° - End: 66.006 ° - Step: 0.012 ° - Step time: 192. s - Temp.: 25 °C (Room) - Time Started: 12 s - 2-Theta: 4.000 ° - Theta: 2.000 ° - Chi: 0.00 ° - Phi
Operations: Y Scale Add 875 | Y Scale Add 1000 | Y Scale Add 1000 | Y Scale Add 1000 | Import

083014_3 - File: 083014_3.raw - Type: 2Th/Th locked - Start: 4.158 ° - End: 66.139 ° - Step: 0.012 ° - Step time: 192. s - Temp.: 25 °C (Room) - Time Started: 12 s - 2-Theta: 4.158 ° - Theta: 2.000 ° - Chi: 0.00 ° - Phi
Operations: Y Scale Mul 1.200 | Y Scale Add 200 | Displacement -0.300 | Aberrant 45 | Background 0.501,1.000 | Strip kAlpha2 0.500 | Impor

01-070-5679 (*) - Corundum, syn - Al2O3

083114_1c

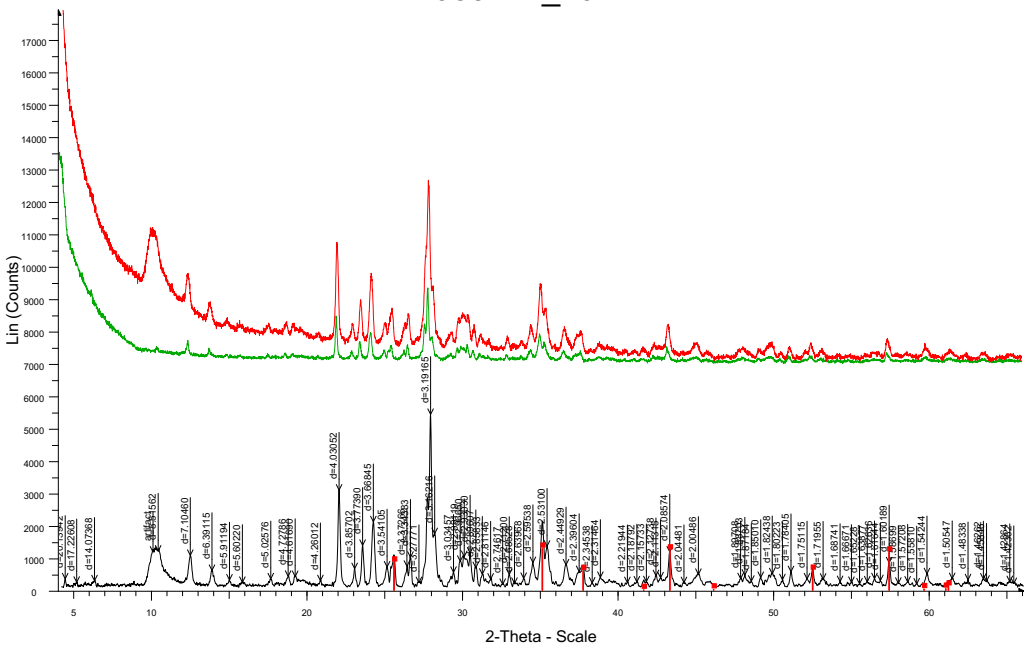

083114_1c - File: 083114_1c.raw - Type: 2Th/Th locked - Start: 4.000 ° - End: 66.006 ° - Step: 0.012 ° - Step time: 192. s - Temp.: 25 °C (Room) - Time Started: 13 s - 2-Theta: 4.000 ° - Theta: 2.000 ° - Chi: 0.00 ° - Operations: Y Scale Add 917 | Y Scale Add 1000 | Y Scale Add 1000 | Y Scale Add 1000 | Y Scale Add 1000 | Import

083114_1c - File: 083114_1c_std.raw - Type: 2Th/Th locked - Start: 4.000 ° - End: 66.006 ° - Step: 0.012 ° - Step time: 192. s - Temp.: 25 °C (Room) - Time Started: 12 s - 2-Theta: 4.000 ° - Theta: 2.000 ° - Chi: 0.00 - Operations: Y Scale Add 875 | Y Scale Add -250 | Y Scale Add 1000 | Y Scale Add 1000 | Y Scale Add 1000 | Y Scale Add 10

083114_1c - File: 083114_1c.raw - Type: 2Th/Th locked - Start: 4.152 ° - End: 66.134 ° - Step: 0.012 ° - Step time: 192. s - Temp.: 25 °C (Room) - Time Started: 13 s - 2-Theta: 4.152 ° - Theta: 2.000 ° - Chi: 0.00 ° - Operations: Y Scale Add 100 | Smooth 0.048 | Aberrant 25 | Range Op. A+B | Displacement -0.288 | Background 0.501,1.000 | Strip kAlpha2 0.5

01-070-5679 (*) - Corundum, syn - Al2O3

083114_2a

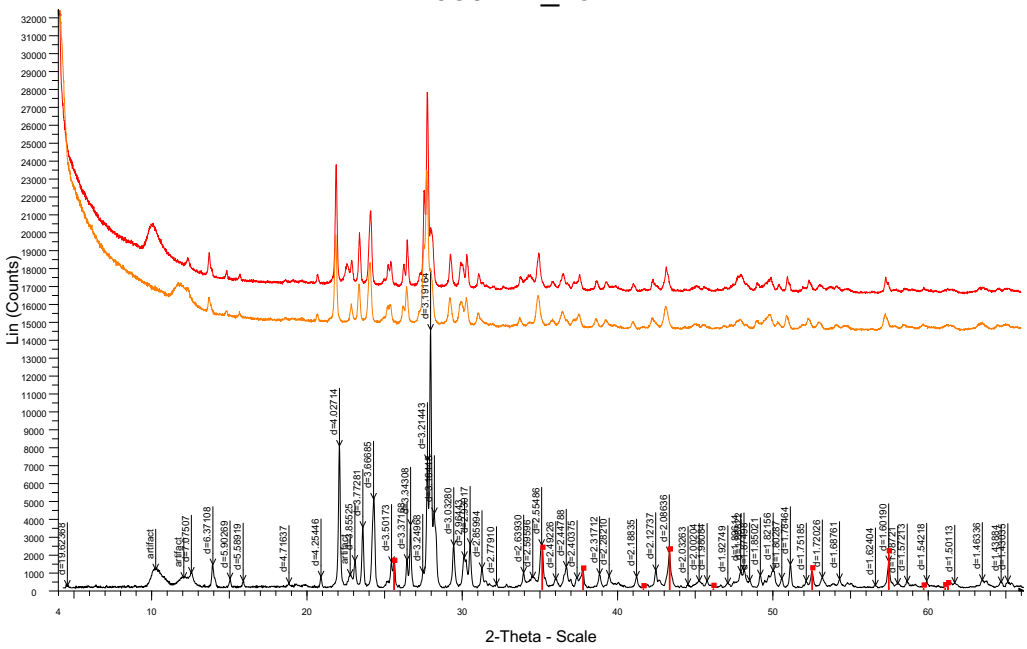

083114_2a - File: 083114_2a_clip.raw - Type: Locked Coupled - Start: 4.007 ° - End: 66.001 ° - Step: 0.012 ° - Step time: 172.8 s - Temp.: 25 °C (Room) - Time Started: 12 s - 2-Theta: 4.007 ° - Theta: 2.003 ° - Chi: - Operations: Y Scale Add 1000 | Y Scale Add 1000 | Y Scale Add 1000 | Y Scale Add 1000 | Y Scale Add 1000 | Y Scale Add 1

083114_2a - File: 083114_2a_rerun.raw - Type: 2Th/Th locked - Start: 4.000 ° - End: 66.006 ° - Step: 0.012 ° - Step time: 192. s - Temp.: 25 °C (Room) - Time Started: 13 s - 2-Theta: 4.000 ° - Theta: 2.000 ° - Chi: 0. - Operations: Y Scale Add 1000 | Y Scale Add 1000 | Y Scale Add 1000 | Y Scale Add 1000 | Y Scale Add 1000 | Y Scale Add 1

083114_2a - File: 083114_2a_clip.raw - Type: Locked Coupled - Start: 4.230 ° - End: 66.189 ° - Step: 0.012 ° - Step time: 172.8 s - Temp.: 25 °C (Room) - Time Started: 12 s - 2-Theta: 4.230 ° - Theta: 2.003 ° - Chi: - Operations: Y Scale Add 100 | Smooth 0.033 | Aberrant 21 | Range Op. A+B | Displacement -0.425 | Background 0.500,1.000 | Strip kAlpha2 0.5

01-070-5679 (*) - Corundum, syn - Al2O3

083114_2b

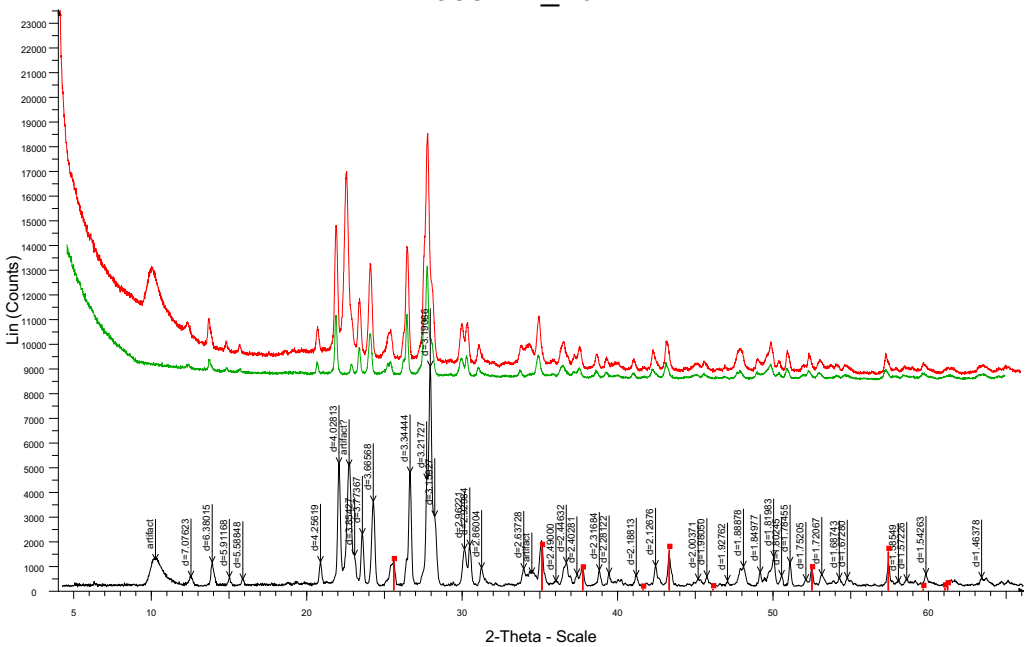

083114_2b - File: 083114_2b.raw - Type: 2Th/Th locked - Start: 4.000 ° - End: 66.006 ° - Step: 0.012 ° - Step time: 192. s - Temp.: 25 °C (Room) - Time Started: 12 s - 2-Theta: 4.000 ° - Theta: 2.000 ° - Chi: 0.00 ° - Operations: Y Scale Add 1000 | Y Scale Add 1000 | Y Scale Add 1000 | Y Scale Add 1 | Y Scale Add 1000 | Y Scale Add 1000 | Y Scale Add 1000

083114_2b - File: 083114_2b_2hr.raw - Type: 2Th/Th locked - Start: 4.500 ° - End: 65.007 ° - Step: 0.012 ° - Step time: 249.6 s - Temp.: 25 °C (Room) - Time Started: 12 s - 2-Theta: 4.500 ° - Theta: 2.250 ° - Chi: 0.0 - Operations: Y Scale Add -750 | Y Scale Add 1000 | Y Scale Add 1000 | Y Scale Add 1000 | Y Scale Add 1000 | Y Scale Add 1

083114_2b - File: 083114_2b.raw - Type: 2Th/Th locked - Start: 4.204 ° - End: 66.178 ° - Step: 0.012 ° - Step time: 192. s - Temp.: 25 °C (Room) - Time Started: 12 s - 2-Theta: 4.204 ° - Theta: 2.000 ° - Chi: 0.00 ° - Operations: Y Scale Add 150 | Smooth 0.033 | Aberrant 14 | Range Op. A+B | Displacement -0.388 | Background 0.501,1.000 | Strip kAlpha2 0.5

01-070-5679 (*) - Corundum, syn - Al2O3

090114_5a

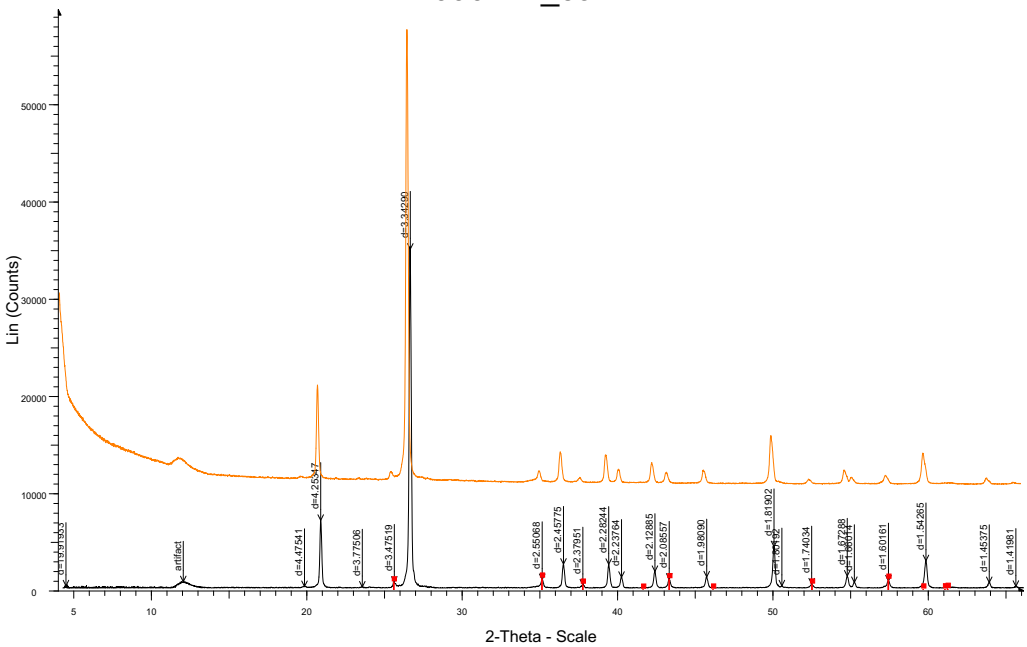

090114_5a - File: 090114_5a.raw - Type: 2Th/Th locked - Start: 4.000 ° - End: 66.006 ° - Step: 0.012 ° - Step time: 192. s - Temp.: 25 °C (Room) - Time Started: 11 s - 2-Theta: 4.000 ° - Theta: 2.000 ° - Chi: 0.00 ° - Operations: Y Scale Add -417 | Y Scale Add 1000 | Y Scale Add 1000 | Y Scale Add 1000 | Y Scale Add 1000 | Y Scale Add 1

090114_5a - File: 090114_5a.raw - Type: 2Th/Th locked - Start: 4.234 ° - End: 66.203 ° - Step: 0.012 ° - Step time: 192. s - Temp.: 25 °C (Room) - Time Started: 11 s - 2-Theta: 4.234 ° - Theta: 2.000 ° - Chi: 0.00 ° - Operations: Y Scale Add 100 | Y Scale Add 100 | Aberrant 19 | Displacement -0.444 | Displacement -0.475 | Displacement -0.463 | Background

01-070-5679 (*) - Corundum, syn - Al2O3

090114_5b

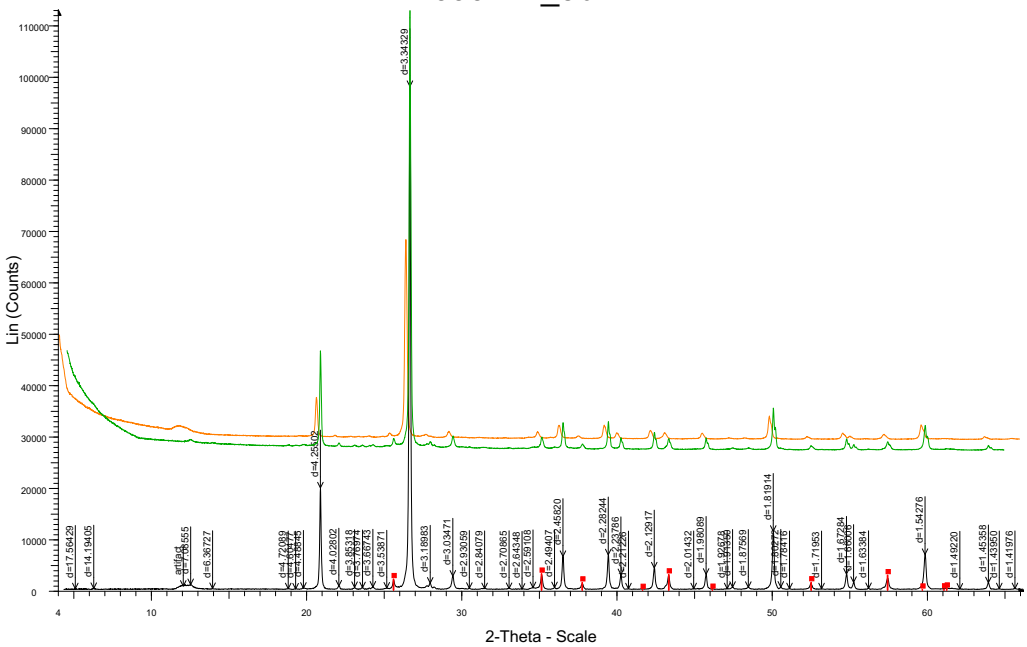

090114_5b - File: 090114_5b.raw - Type: 2Th/Th locked - Start: 4.000 ° - End: 66.006 ° - Step: 0.012 ° - Step time: 192. s - Temp.: 25 °C (Room) - Time Started: 12 s - 2-Theta: 4.000 ° - Theta: 2.000 ° - Chi: 0.00 ° - Operations: Y Scale Add 1000 | Y Scale Add 1000 | Y Scale Add 1000 | Y Scale Add 1000 | Y Scale Add 1000 | Y Scale Add 1

090114_5b - File: 090114_5b_2hr.raw - Type: 2Th/Th locked - Start: 4.500 ° - End: 65.007 ° - Step: 0.012 ° - Step time: 249.6 s - Temp.: 25 °C (Room) - Time Started: 13 s - 2-Theta: 4.500 ° - Theta: 2.250 ° - Chi: 0.0 Operations: Y Scale Add 1000 | Y Scale Add 1000 | Y Scale Add 1000 | Y Scale Add 1000 | Y Scale Add 1000 | Y Scale Add 1

090114_5b - File: 090114_5b.raw - Type: 2Th/Th locked - Start: 4.290 ° - End: 66.249 ° - Step: 0.012 ° - Step time: 192. s - Temp.: 25 °C (Room) - Time Started: 12 s - 2-Theta: 4.290 ° - Theta: 2.000 ° - Chi: 0.00 ° - Operations: Y Scale Mul 1.200 | Y Scale Add 100 | Smooth 0.019 | Aberrant 19 | Range Op. A+B | Displacement -0.550 | Displacement -0.509 |

01-070-5679 (*) - Corundum, syn - Al2O3

090114_5c

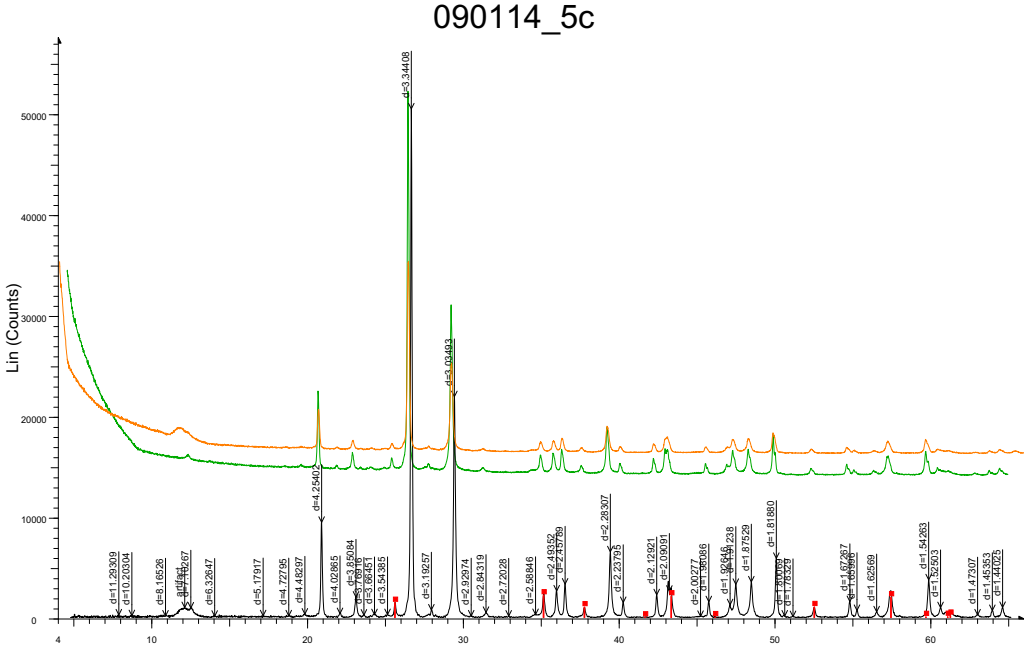

090114_5c - File: 090114_5c.raw - Type: 2Th/Th locked - Start: 4.000 ° - End: 66.006 ° - Step: 0.012 ° - Step time: 192. s - Temp.: 25 °C (Room) - Time Started: 12 s - 2-Theta: 4.000 ° - Theta: 2.000 ° - Chi: 0.00 ° - Operations: Y Scale Add 1000 | Y Scale Add 1000 | Y Scale Add 1000 | Y Scale Add 1000 | Y Scale Add 1000 | Y Scale Add 1

090114_5c - File: 090114_5c_2hr.raw - Type: 2Th/Th locked - Start: 4.500 ° - End: 65.007 ° - Step: 0.012 ° - Step time: 249.6 s - Temp.: 25 °C (Room) - Time Started: 12 s - 2-Theta: 4.500 ° - Theta: 2.250 ° - Chi: 0.0 Operations: Y Scale Add 1000 | Y Scale Add 1000 | Y Scale Add 1000 | Y Scale Add -333 | Y Scale Add 1000 | Y Scale Add 1

090114_5c - File: 090114_5c.raw - Type: 2Th/Th locked - Start: 4.727 ° - End: 65.199 ° - Step: 0.012 ° - Step time: 249.6 s - Temp.: 25 °C (Room) - Time Started: 12 s - 2-Theta: 4.727 ° - Theta: 2.250 ° - Chi: 0.00 ° - Operations: Smooth 0.019 | Aberrant 15 | Range Op. A+B | Displacement -0.442 | Displacement -0.402 | Displacement -0.463 | Displacement -0.

01-070-5679 (*) - Corundum, syn - Al2O3

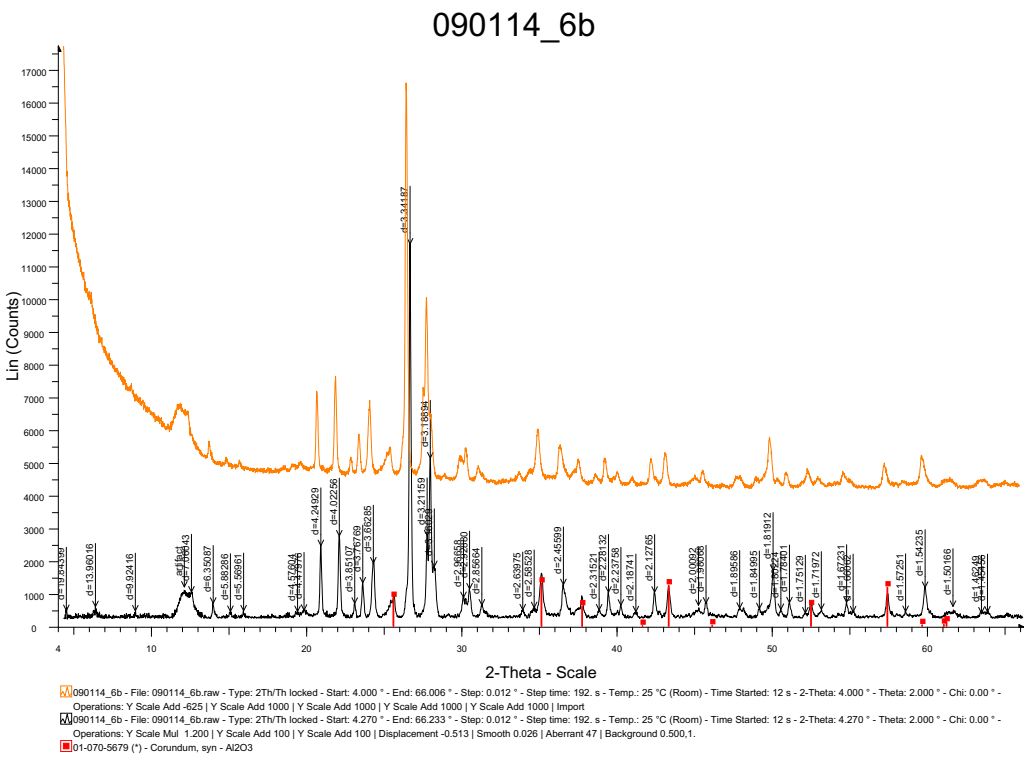

Figure C.2. X-ray diffraction patterns for selected samples, with d-spacing of selected peaks. Sample preparation, analysis methods, and color codes are described in the text.

D. Appendix: Unconfined Compressive Strength and Static Elastic Properties from UCS Tests

Table D.1. Sample Geometry, Mass, and Derived Density

Sample	Material/Alteration	Plug*	Length (cm)	error† (cm)	Diam. (cm)	error (cm)	Mass (g)	error (g)	Density (g/cm^3)	error (g/cm^3)
030914-1	silicic, argillic	v1	5.446	0.006	2.534	0.003	72.63	0.01	2.645	0.002
061114-4b	silicified	h1	5.506	0.007	2.535	0.002	73.38	0.01	2.641	0.001
052615-1a	diorite	h1	5.390	-	2.540	-	73.32	0.01	2.685	0.001
052615-1a	diorite	h2	5.490	-	2.540	-	74.40	0.01	2.675	0.001
052615-1a	diorite	v1	5.460	-	2.540	-	74.34	0.01	2.687	0.001
052615-1b	granite	h1	5.397	0.002	2.540	0.001	70.34	0.01	2.572	0.001
052615-1b	granite	h2	5.323	0.003	2.537	0.001	69.60	0.01	2.586	0.001
052615-1b	granite	v1	4.848	0.003	2.545	0.004	63.35	0.01	2.569	0.002
052615-2	chl, hem, cal granite	h1	5.390	-	2.540	-	70.66	0.01	2.587	0.001
052615-2	chl, hem, cal granite	h2	5.320	-	2.540	-	69.31	0.01	2.571	0.001
052615-2	chl, hem, cal granite	v1	4.730	0.003	2.541	0.006	61.33	0.01	2.556	0.002
052615-3a	tuff	h1	5.456	0.001	2.532	0.001	60.08	0.01	2.187	0.000
052615-3a	tuff	h2	5.455	0.006	2.542	0.001	59.60	0.01	2.153	0.001
052615-3a	tuff	v1	5.461	0.003	2.534	0.003	59.96	0.01	2.177	0.001
052615-3a	tuff	v2	4.907	0.004	2.540	0.001	54.68	0.01	2.200	0.001
052615-3b	silicified bladed calcite	h1	5.353	0.002	2.529	0.002	67.40	0.01	2.506	0.001

* v = long axis is vertical, h = long axis is parallel to strike, p = long axis is perpendicular to strike and dip, d = long axis is parallel to dip of local range front fault/body

† Error associated with length and diameter from 3 measurements.

Sample	Material/Alteration	Plug*	Length (cm)	error† (cm)	Diam. (cm)	error (cm)	Mass (g)	error (g)	Density (g/cm^3)	error (g/cm^3)
052615-3b	silicified bladed calcite	h2	5.355	0.002	2.538	0.001	67.14	0.01	2.479	0.001
052615-3b	silicified bladed calcite	p1	5.356	0.010	2.533	0.002	66.80	0.01	2.476	0.002
052615-3b	silicified bladed calcite	p2	5.227	0.003	2.534	0.001	66.33	0.01	2.516	0.001
052715-7	silicic, argillic, carbonate	d1	4.962	0.004	2.530	0.002	64.12	0.01	2.570	0.001
052715-7	silicic, argillic, carbonate	d2	5.491	0.003	2.530	0.003	71.14	0.01	2.576	0.001
052715-7	silicic, argillic, carbonate	h1	5.043	0.003	2.533	0.001	65.49	0.01	2.577	0.001
052715-7	silicic, argillic, carbonate	h2	5.404	0.005	2.531	0.003	69.23	0.01	2.546	0.002
052715-7	silicic, argillic, carbonate	p1	5.383	0.009	2.528	0.002	69.70	0.01	2.580	0.002
052715-7	silicic, argillic, carbonate	p2	5.430	0.005	2.527	0.002	70.21	0.01	2.578	0.001
052815-2	silicified	h1	5.218	0.008	2.536	0.002	69.05	0.01	2.619	0.002
052815-2	silicified	h2	5.279	0.007	2.537	0.003	69.63	0.01	2.610	0.002
052815-3a	chl, cal gabbro	v1	5.491	0.002	2.535	0.001	74.56	0.01	2.690	0.001
052815-3b	chl, cal gabbro	v1	5.309	0.005	2.534	0.003	68.58	0.01	2.562	0.002
052815-4b	silicified	A, P	5.512	0.003	2.547	0.001	73.18	0.01	2.606	0.001
052815-4b	silicified	B, P	5.620	0.002	2.546	0.002	74.72	0.01	2.611	0.001
090114-5b	silicified	C, D	5.352	0.002	2.546	0.002	69.88	0.01	2.565	0.001
090114-5b	silicified	D, D	5.028	0.001	2.547	0.001	66.59	0.01	2.599	0.001

Table D.2. Unconfined Compressive Strength and UCS Test Parameters Used to Derive Static Elastic Properties

Sample	Plug	Load 1 (MPa)	Load 2 (MPa)	ε_{A1}	ε_{A2}	ε_{R1}	ε_{R2}	E (GPa)	ν	G (GPa)	UCS (MPa)	NOTE*
030914-1	v1	9.35	15.58	0.0447	0.0677	-0.0052	-0.0139	27.0	0.38	9.8	67.1	3
061114-4b	h1	61.08	158.77	0.1632	0.3545	-0.0054	-0.0302	51.1	0.13	22.6	187.8	
052615-1a	h1	30.71	57.12	0.1018	0.1682	-0.0076	-0.0166	39.8	0.14	17.5	59.8	1, 4
052615-1a	h2	121.40	218.48	0.2556	0.4134	-0.0377	-0.0872	61.5	0.31	23.4	270.7	
052615-1a	v1	101.02	180.68	0.2422	0.3815	-0.0437	-0.0795	57.2	0.26	22.7	241.8	
052615-1b	h1	35.60	71.13	0.1763	0.2797	-0.0090	-0.0294	34.4	0.20	14.4	78.9	
052615-1b	h2	65.82	103.73	0.2117	0.2947	-0.0321	-0.0556	45.7	0.28	17.8	120.6	
052615-1b	v1	-	-	-	-	-	-	-	-	-	-	2, 5
052615-2	h1	26.32	42.57	0.2004	0.2866	-0.0132	-0.0413	18.8	0.33	7.1	55.5	3
052615-2	h2	15.29	29.75	0.1099	0.2094	0.0000	-0.0109	14.5	0.11	6.6	43.4	
052615-2	v1	24.39	45.51	0.1737	0.2826	-0.0184	-0.0512	19.4	0.30	7.5	54.5	3, 6
052615-3a	h1	23.33	55.74	0.1741	0.3780	0.0067	-0.0258	15.9	0.16	6.9	72.7	
052615-3a	h2	20.26	34.80	0.1682	0.2699	0.0111	0.0079	14.3	0.03	6.9	52.1	
052615-3a	v1	-	-	-	-	-	-	-	-	-	-	1, 7
052615-3a	v2	-	-	-	-	-	-	-	-	-	-	2, 5
052615-3b	h1	22.60	51.45	0.1245	0.2287	-0.0010	-0.0249	27.7	0.23	11.3	77.0	
052615-3b	h2	18.54	40.44	0.1057	0.1873	-0.0001	-0.0127	26.8	0.15	11.6	64.3	
052615-3b	p1	21.29	40.64	0.2376	0.3490	0.0090	-0.0003	17.4	0.08	8.0	51.3	
052615-3b	p2	20.74	49.39	0.0709	0.1481	-0.0021	-0.0170	37.1	0.19	15.5	79.7	3
052715-7	d1	35.78	84.30	0.1258	0.2604	0.0022	-0.0170	36.1	0.14	15.8	98.2	

*

Sample	Plug	Load 1 (MPa)	Load 2 (MPa)	ε_{A1}	ε_{A2}	ε_{R1}	ε_{R2}	E (GPa)	ν	G (GPa)	UCS (MPa)	NOTE*
052715-7	d2	40.85	89.06	0.1165	0.2310	-0.0060	-0.0243	42.1	0.16	18.1	104.1	
052715-7	h1	42.61	69.25	0.1559	0.2256	0.0034	-0.0022	38.2	0.08	17.7	103.7	
052715-7	h2	40.73	94.48	0.1753	0.3265	-0.0060	-0.0288	35.5	0.15	15.4	120.9	
052715-7	p1	-	-	-	-	-	-	-	-	-	-	1, 8
052715-7	p2	50.81	99.01	0.1665	0.2794	0.0052	-0.0068	42.7	0.11	19.3	118.1	
052815-2	h1	50.99	223.70	0.1328	0.4148	-0.0016	-0.0277	61.3	0.09	28.0	273.8	3
052815-2	h2	76.30	248.70	0.1480	0.4158	-0.0030	-0.0368	64.4	0.13	28.6	299.2	3
052815-3a	v1	50.91	119.05	0.1468	0.2882	-0.0111	-0.0428	48.2	0.22	19.7	148.0	
052815-3b	v1	20.53	39.51	0.1256	0.2089	-0.0018	-0.0183	22.8	0.20	9.5	50.7	
052815-4b	A, P	102.17	255.93	0.1713	0.4375	-0.0175	-0.0651	57.8	0.18	24.5	332.6	
052815-4b	B, P	101.16	242.99	0.1869	0.4274	-0.0165	-0.0578	59.0	0.17	25.2	314.2	
090114-5b	C, D	-	-	-	-	-	-	-	-	-	-	2, 6
090114-5b	D, D	100.11	200.17	0.2120	0.3857	-0.0062	-0.0366	57.6	0.18	24.5	258.8	

E. Appendix: Double Torsion – Load Relaxation Test Results (Slow Displacement)

Table E.1. Specimen Geometry and Per Cycle Load, K_{IC}*, and SCI

Sample	Wafer	Load	L (in)	W (in)	t (in)	t_n (in)	W_m (m)	ν^*	P† (N)	K_{IC}* (MPa √m)	SCI	Notes‡
030914-1	a	1	3.0420	1.2230	0.0610	0.0435	0.008225	0.15	42.96	1.90	68.6	1
030914-1	a	2	3.0420	1.2230	0.0610	0.0435	0.008225	0.15	42.36	1.87	68.7	1
030914-1	a	3	3.0420	1.2230	0.0610	0.0435	0.008225	0.15	43.67	1.93	87.2	1
030914-1	a	4	3.0420	1.2230	0.0610	0.0435	0.008225	0.15	46.30	2.04	124.8	1
030914-1	a	5	3.0420	1.2230	0.0610	0.0435	0.008225	0.15	45.95	2.03	-	1
030914-1	b	1	3.0410	1.2500	0.0685	0.0500	0.008225	0.15	63.59	-	91.3	1, PC
030914-1	b	2	3.0410	1.2500	0.0685	0.0500	0.008225	0.15	56.32	1.94	111.1	1
030914-1	b	3	3.0410	1.2500	0.0685	0.0500	0.008225	0.15	57.08	1.96	67.2	1
030914-1	b	4	3.0410	1.2500	0.0685	0.0500	0.008225	0.15	54.07	1.86	110.4	1
030914-1	b	5	3.0410	1.2500	0.0685	0.0500	0.008225	0.15	54.46	1.87	-	1
030914-1	c	1	3.0400	1.2500	0.0688	0.0560	0.008225	0.15	75.73	-	69.3	1, PC
030914-1	c	2	3.0400	1.2500	0.0688	0.0560	0.008225	0.15	68.14	2.20	47.2	1
030914-1	c	3	3.0400	1.2500	0.0688	0.0560	0.008225	0.15	67.06	2.17	146.9	1
030914-1	c	4	3.0400	1.2500	0.0688	0.0560	0.008225	0.15	67.70	2.19	135.8	1
030914-1	c	5	3.0400	1.2500	0.0688	0.0560	0.008225	0.15	68.38	2.21	57.1	1

* ***Bold*** indicates wafers where Poisson's ratio was estimated from similar material.

† Load flatlined ~153.5-153.9 N.

‡ 1. Wafer broke straight. 2. Fracture curved out of groove from load point. 3. Fracture curved out of groove mid-wafer. 4. Wafer broke on pre-fracturing. 5. Exceeded load cell capacity. LQ = low quality test based on wafer behavior or mechanical issue. K_{IC}*, SCI, or both omitted PC = pre-fracturing load.

Sample	Wafer	Load	L (in)	W (in)	t (in)	t_n (in)	W_m (m)	ν^*	P† (N)	K_{IC}* (MPa √m)	SCI	Notes‡
030914-1	c	6	3.0400	1.2500	0.0688	0.0560	0.008225	0.15	65.31	2.11	-	1
030914-1	d	1	3.0410	1.2505	0.0685	0.0520	0.008225	0.15	65.29	-	97.6	1, PC
030914-1	d	2	3.0410	1.2505	0.0685	0.0520	0.008225	0.15	72.18	2.43	41.8	1
030914-1	d	3	3.0410	1.2505	0.0685	0.0520	0.008225	0.15	59.48	2.00	-	1
030914-1	d	4	3.0410	1.2505	0.0685	0.0520	0.008225	0.15	52.20	1.76	102.7	1
030914-1	d	5	3.0410	1.2505	0.0685	0.0520	0.008225	0.15	56.27	1.90	-	1
030914-1	g	2	3.0415	1.2500	0.0680	0.0530	0.008225	0.15	69.13	-	66.7	1, LQ
030914-1	g	3	3.0415	1.2500	0.0680	0.0530	0.008225	0.15	60.45	2.04	39.7	1
030914-1	g	4	3.0415	1.2500	0.0680	0.0530	0.008225	0.15	57.59	1.94	98.9	1
030914-1	g	5	3.0415	1.2500	0.0680	0.0530	0.008225	0.15	63.59	2.15	-	1
030914-1	h	1	3.0400	1.2505	0.0695	0.0500	0.008225	0.15	55.69	1.87	83.7	1
030914-1	h	2	3.0400	1.2505	0.0695	0.0500	0.008225	0.15	56.17	1.89	80.8	1
030914-1	h	3	3.0400	1.2505	0.0695	0.0500	0.008225	0.15	68.11	2.29	-	1
030914-1	i	1	3.0410	1.2525	0.0668	0.0510	0.008225	0.15	60.93	-	67.3	1, PC
030914-1	i	2	3.0410	1.2525	0.0668	0.0510	0.008225	0.15	55.68	1.97	87.3	1
030914-1	i	3	3.0410	1.2525	0.0668	0.0510	0.008225	0.15	55.52	1.96	108.3	1
030914-1	i	4	3.0410	1.2525	0.0668	0.0510	0.008225	0.15	55.94	1.97	136.5	1
030914-1	i	5	3.0410	1.2525	0.0668	0.0510	0.008225	0.15	50.83	1.79	-	1
030914-1	j	1	3.0400	1.2500	0.0785	0.0600	0.008225	0.15	76.00	1.95	62.3	1
030914-1	j	2	3.0400	1.2500	0.0785	0.0600	0.008225	0.15	67.50	1.74	-	1
030914-1	k	1	3.0400	1.2500	0.0700	0.0570	0.008225	0.15	67.86	2.12	105.8	1
030914-1	k	2	3.0400	1.2500	0.0700	0.0570	0.008225	0.15	68.92	2.15	89.4	1
030914-1	k	3	3.0400	1.2500	0.0700	0.0570	0.008225	0.15	68.43	2.13	111.6	1
030914-1	k	4	3.0400	1.2500	0.0700	0.0570	0.008225	0.15	67.53	2.11	166.5	1

Sample	Wafer	Load	L (in)	W (in)	t (in)	t_n (in)	W_m (m)	ν^*	P† (N)	K_{IC}* (MPa √m)	SCI	Notes‡
030914-1	k	5	3.0400	1.2500	0.0700	0.0570	0.008225	0.15	66.08	2.06	129.2	1
030914-1	k	6	3.0400	1.2500	0.0700	0.0570	0.008225	0.15	65.00	2.03	-	1
030914-1	l	1	3.0400	1.2505	0.0750	0.0560	0.008225	0.15	49.87	-	-	1, 4, LQ
052615-1A	a	1	2.9900	1.2000	0.0570	0.0395	0.008225	0.29	31.93	1.75	47.6	1
052615-1A	a	2	2.9900	1.2000	0.0570	0.0395	0.008225	0.29	31.23	1.71	34.9	1
052615-1A	a	3	2.9900	1.2000	0.0570	0.0395	0.008225	0.29	29.34	1.61	-	1
052615-1A	b	1	2.9890	1.2000	0.0650	0.0410	0.008225	0.29	42.96	1.91	-	1
052615-1A	c	1	2.9890	1.1980	0.0510	0.0290	0.008225	0.29	35.91	-	-	1, PC
052615-1A	c	2	2.9890	1.1980	0.0510	0.0290	0.008225	0.29	35.55	2.68	50.0	1
052615-1A	c	3	2.9890	1.1980	0.0510	0.0290	0.008225	0.29	36.49	2.75	83.8	1
052615-1A	c	4	2.9890	1.1980	0.0510	0.0290	0.008225	0.29	40.71	3.07	-	1
052615-1A	d	1	2.9920	1.2030	0.0680	0.0440	0.008225	0.29	51.88	2.08	75.2	1
052615-1A	d	2	2.9920	1.2030	0.0680	0.0440	0.008225	0.29	50.22	2.01	65.8	1
052615-1A	d	3	2.9920	1.2030	0.0680	0.0440	0.008225	0.29	45.34	1.81	-	1
052615-1A	e	1	2.9880	1.1980	0.0595	0.0380	0.008225	0.29	34.76	1.82	56.7	1
052615-1A	e	2	2.9880	1.1980	0.0595	0.0380	0.008225	0.29	34.42	1.81	-	1
052615-1A	f	1	2.9920	1.2050	0.0795	0.0500	0.008225	0.29	31.42	-	-	1, LQ
052615-1A	g	1	2.9940	1.2050	0.0815	0.0520	0.008225	0.29	65.02	1.84	-	1
052615-1A	h	1	2.9910	1.2050	0.0865	0.0585	0.008225	0.29	79.24	1.94	52.1	1
052615-1A	h	2	2.9910	1.2050	0.0865	0.0585	0.008225	0.29	73.89	1.81	60.7	1
052615-1A	h	3	2.9910	1.2050	0.0865	0.0585	0.008225	0.29	74.42	1.82	-	1
052615-1A	i	1	2.9910	1.2040	0.0910	0.0620	0.008225	0.29	103.05	-	63.6	1, 4, PC
052615-1B	a	1	3.0290	1.3140	0.0660	0.0450	0.008225	0.24	36.27	1.40	48.8	2
052615-1B	a	2	3.0290	1.3140	0.0660	0.0450	0.008225	0.24	37.41	1.45	-	2

Sample	Wafer	Load	L (in)	W (in)	t (in)	t_n (in)	W_m (m)	ν^*	P† (N)	K_{IC}* (MPa √m)	SCI	Notes‡
052615-1B	a	3	3.0290	1.3140	0.0660	0.0450	0.008225	0.24	36.37	1.41	-	2
052615-1B	b	1	3.0280	1.3120	0.0730	0.0515	0.008225	0.24	48.03	-	61.0	2, PC
052615-1B	b	2	3.0280	1.3120	0.0730	0.0515	0.008225	0.24	43.97	1.37	46.0	2
052615-1B	b	3	3.0280	1.3120	0.0730	0.0515	0.008225	0.24	42.51	1.33	63.4	2
052615-1B	b	4	3.0280	1.3120	0.0730	0.0515	0.008225	0.24	42.61	1.33	71.2	2
052615-1B	b	5	3.0280	1.3120	0.0730	0.0515	0.008225	0.24	41.36	1.29	55.9	2
052615-1B	c	1	3.0330	1.3220	0.0700	0.0560	0.008225	0.24	41.82	-	56.1	1, PC
052615-1B	c	2	3.0330	1.3220	0.0700	0.0560	0.008225	0.24	40.53	1.28	96.1	1
052615-1B	c	3	3.0330	1.3220	0.0700	0.0560	0.008225	0.24	36.65	1.16	89.5	1
052615-1B	c	4	3.0330	1.3220	0.0700	0.0560	0.008225	0.24	35.34	1.12	109.4	1
052615-1B	c	5	3.0330	1.3220	0.0700	0.0560	0.008225	0.24	35.03	1.11	97.7	1
052615-1B	c	6	3.0330	1.3220	0.0700	0.0560	0.008225	0.24	33.97	1.08	89.9	1
052615-1B	d	1	3.0270	1.3140	0.0810	0.0600	0.008225	0.24	48.40	1.20	43.1	1
052615-1B	d	2	3.0270	1.3140	0.0810	0.0600	0.008225	0.24	43.90	1.09	-	1
052615-1B	e	1	3.0320	1.3200	0.0780	0.0520	0.008225	0.24	37.00	1.04	63.0	1
052615-1B	e	2	3.0320	1.3200	0.0780	0.0520	0.008225	0.24	41.18	1.16	-	1
052615-1B	f	1	3.0300	1.3170	0.0790	0.0600	0.008225	0.24	37.99	0.98	59.6	1
052615-1B	f	2	3.0300	1.3170	0.0790	0.0600	0.008225	0.24	37.38	0.96	61.3	1
052615-1B	f	3	3.0300	1.3170	0.0790	0.0600	0.008225	0.24	37.16	0.96	82.5	1
052615-1B	f	4	3.0300	1.3170	0.0790	0.0600	0.008225	0.24	37.58	0.97	45.7	1
052615-1B	g	1	3.0280	1.3190	0.0900	0.0670	0.008225	0.24	61.54	1.24	68.6	3
052615-1B	g	2	3.0280	1.3190	0.0900	0.0670	0.008225	0.24	59.27	1.19	73.6	3
052615-1B	g	3	3.0280	1.3190	0.0900	0.0670	0.008225	0.24	58.12	1.17	86.8	3
052615-1B	g	4	3.0280	1.3190	0.0900	0.0670	0.008225	0.24	55.20	1.11	74.9	3
052615-2A	a	1	3.2590	1.3010	0.0930	0.0780	0.008225	0.25	42.09	0.76	68.1	2

Sample	Wafer	Load	L (in)	W (in)	t (in)	t_n (in)	W_m (m)	ν^*	P† (N)	K_{IC}* (MPa √m)	SCI	Notes‡
052615-2A	a	2	3.2590	1.3010	0.0930	0.0780	0.008225	0.25	44.06	0.79	-	2, LQ
052615-2A	b	1	3.2520	1.2980	0.0800	0.0620	0.008225	0.25	23.42	0.59	-	2
052615-2A	c	1	3.2540	1.3000	0.0870	0.0620	0.008225	0.25	31.52	0.70	111.1	2
052615-2A	c	2	3.2540	1.3000	0.0870	0.0620	0.008225	0.25	35.44	0.79	105.8	2
052615-2A	c	3	3.2540	1.3000	0.0870	0.0620	0.008225	0.25	34.59	0.77	-	2, LQ
052615-2A	d	1	3.1680	1.2750	0.0930	0.0670	0.008225	0.25	31.79	0.62	110.2	2
052615-2A	d	2	3.1680	1.2750	0.0930	0.0670	0.008225	0.25	34.86	0.68	109.1	2
052615-2A	d	3	3.1680	1.2750	0.0930	0.0670	0.008225	0.25	33.11	0.65	164.2	2
052615-2A	d	4	3.1680	1.2750	0.0930	0.0670	0.008225	0.25	34.52	0.68	101.2	2
052615-2A	d	5	3.1680	1.2750	0.0930	0.0670	0.008225	0.25	31.26	0.61	113.6	2
052615-2A	d	6	3.1680	1.2750	0.0930	0.0670	0.008225	0.25	29.03	0.57	-	2
052615-2A	e	1	3.2555	1.2990	0.0800	0.0620	0.008225	0.25	17.61	0.44	-	2
052615-2A	f	1	3.1810	1.3000	0.0820	0.0600	0.008225	0.25	22.41	0.55	62.9	2
052615-2A	f	2	3.1810	1.3000	0.0820	0.0600	0.008225	0.25	20.38	0.50	73.2	2
052615-2A	g	1	3.2490	1.2980	0.0900	0.0670	0.008225	0.25	26.35	0.54	-	2
052615-2A	h	1	3.0000	1.2980	0.0890	0.0660	0.008225	0.25	25.42	0.53	22.1	2
052615-2A	i	1	1.9930	1.3010	0.0970	0.0730	0.008225	0.25	25.57	0.45	76.0	3
052615-3A	a	1	3.0890	1.3200	0.0735	0.0570	0.008225	0.10	52.27	-	15.2	1, PC
052615-3A	a	2	3.0890	1.3200	0.0735	0.0570	0.008225	0.10	38.12	1.05	104.2	1
052615-3A	a	3	3.0890	1.3200	0.0735	0.0570	0.008225	0.10	41.72	1.15	98.9	1
052615-3A	a	4	3.0890	1.3200	0.0735	0.0570	0.008225	0.10	43.08	1.19	74.1	1
052615-3A	a	5	3.0890	1.3200	0.0735	0.0570	0.008225	0.10	42.42	1.17	-	1
052615-3A	b	1	3.0740	1.3360	0.0785	0.0575	0.008225	0.10	51.61	-	66.9	1, PC
052615-3A	b	2	3.0740	1.3360	0.0785	0.0575	0.008225	0.10	43.59	1.08	69.2	1
052615-3A	b	3	3.0740	1.3360	0.0785	0.0575	0.008225	0.10	41.03	1.02	111.6	1

Sample	Wafer	Load	L (in)	W (in)	t (in)	t_n (in)	W_m (m)	ν^*	P† (N)	K_{IC}* (MPa √m)	SCI	Notes‡
052615-3A	b	4	3.0740	1.3360	0.0785	0.0575	0.008225	0.10	43.68	1.08	-	1
052615-3A	c	1	3.0720	1.3400	0.0820	0.0500	0.008225	0.10	73.97	-	34.3	1, PC
052615-3A	c	2	3.0720	1.3400	0.0820	0.0500	0.008225	0.10	48.15	1.20	69.5	1
052615-3A	c	3	3.0720	1.3400	0.0820	0.0500	0.008225	0.10	44.76	1.11	27.7	1
052615-3A	f	1	3.0740	1.3270	0.0770	0.0480	0.008225	0.10	46.06	1.29	36.8	1
052615-3A	f	2	3.0740	1.3270	0.0770	0.0480	0.008225	0.10	42.35	1.19	62.5	1
052615-3A	f	3	3.0740	1.3270	0.0770	0.0480	0.008225	0.10	46.06	1.29	56.3	1
052615-3A	f	4	3.0740	1.3270	0.0770	0.0480	0.008225	0.10	44.08	1.23	-	1
052615-3A	g	1	3.0720	1.3310	0.0750	0.0480	0.008225	0.10	48.93	-	34.0	1, PC
052615-3A	g	2	3.0720	1.3310	0.0750	0.0480	0.008225	0.10	41.43	1.20	50.6	1
052615-3A	g	3	3.0720	1.3310	0.0750	0.0480	0.008225	0.10	39.97	1.16	58.0	1
052615-3A	g	4	3.0720	1.3310	0.0750	0.0480	0.008225	0.10	37.49	1.09	58.3	1
052615-3A	g	5	3.0720	1.3310	0.0750	0.0480	0.008225	0.10	30.27	-	-	1, LQ
052615-3A	g	6	3.0720	1.3310	0.0750	0.0480	0.008225	0.10	28.09	-	-	1, LQ
052615-3A	j	1	3.0860	1.3220	0.0860	0.0660	0.008225	0.10	69.18	-	-	2, 4, PC
052615-3A	k	1	3.0860	1.3240	0.0700	0.0540	0.008225	0.10	55.13	-	63.4	1, PC
052615-3A	k	2	3.0860	1.3240	0.0700	0.0540	0.008225	0.10	42.07	1.28	68.7	1
052615-3A	k	3	3.0860	1.3240	0.0700	0.0540	0.008225	0.10	37.69	1.14	60.2	1
052615-3A	k	4	3.0860	1.3240	0.0700	0.0540	0.008225	0.10	36.35	1.10	-	1
052615-3A	l	1	3.0860	1.3190	0.0770	0.0530	0.008225	0.10	62.71	-	63.9	1, PC
052615-3A	l	2	3.0860	1.3190	0.0770	0.0530	0.008225	0.10	48.89	1.31	45.6	1
052615-3A	l	3	3.0860	1.3190	0.0770	0.0530	0.008225	0.10	43.73	1.17	37.3	1
052615-3A	l	4	3.0860	1.3190	0.0770	0.0530	0.008225	0.10	38.98	1.04	-	1
052615-3A	m	1	3.0890	1.3240	0.0720	0.0520	0.008225	0.10	51.41	-	51.6	1, PC

Sample	Wafer	Load	L (in)	W (in)	t (in)	t_n (in)	W_m (m)	ν^*	P† (N)	K_{IC}* (MPa √m)	SCI	Notes‡
052615-3A	m	2	3.0890	1.3240	0.0720	0.0520	0.008225	0.10	41.54	1.23	50.6	1
052615-3A	m	3	3.0890	1.3240	0.0720	0.0520	0.008225	0.10	38.23	1.14	76.3	1
052615-3A	m	4	3.0890	1.3240	0.0720	0.0520	0.008225	0.10	39.60	1.18	67.7	1
052615-3A	m	5	3.0890	1.3240	0.0720	0.0520	0.008225	0.10	37.37	1.11	-	1
052615-3B	a	1	3.1610	1.2750	0.0790	0.0560	0.008225	0.16	68.13	-	-	2, 4, PC
052615-3B	b	1	3.1560	1.2950	0.0730	0.0520	0.008225	0.16	43.45	1.31	114.6	1
052615-3B	b	2	3.1560	1.2950	0.0730	0.0520	0.008225	0.16	42.76	1.29	92.3	1
052615-3B	b	3	3.1560	1.2950	0.0730	0.0520	0.008225	0.16	39.21	1.19	73.8	1
052615-3B	c	1	3.1550	1.2900	0.0735	0.0500	0.008225	0.16	70.93	-	67.6	1, PC
052615-3B	c	2	3.1550	1.2900	0.0735	0.0500	0.008225	0.16	48.76	1.49	-	1
052615-3B	d	1	3.0610	1.3000	0.0790	0.0560	0.008225	0.16	62.58	1.62	112.4	2
052615-3B	d	2	3.0610	1.3000	0.0790	0.0560	0.008225	0.16	63.54	1.65	105.5	2
052615-3B	d	3	3.0610	1.3000	0.0790	0.0560	0.008225	0.16	59.77	1.55	123.8	2
052615-3B	e	1	3.1560	1.2980	0.0690	0.0465	0.008225	0.16	44.27	1.54	166.9	2
052615-3B	e	2	3.1560	1.2980	0.0690	0.0465	0.008225	0.16	42.74	1.48	161.9	2
052615-3B	e	3	3.1560	1.2980	0.0690	0.0465	0.008225	0.16	41.31	1.43	99.2	2
052615-3B	e	4	3.1560	1.2980	0.0690	0.0465	0.008225	0.16	39.30	1.36	140.0	2
052615-3B	f	1	3.1535	1.2970	0.0705	0.0490	0.008225	0.16	49.92	-	96.9	2, PC
052615-3B	f	2	3.1535	1.2970	0.0705	0.0490	0.008225	0.16	38.61	1.27	90.1	2
052615-3B	f	3	3.1535	1.2970	0.0705	0.0490	0.008225	0.16	35.26	1.16	60.2	2
052615-3B	g	1	3.1600	1.2770	0.0710	0.0460	0.008225	0.16	53.46	-	-	2, 4, PC
052615-3B	h	1	3.1590	1.2845	0.0715	0.0540	0.008225	0.16	59.93	-	74.5	2, PC
052615-3B	h	2	3.1590	1.2845	0.0715	0.0540	0.008225	0.16	54.04	1.66	-	2
052615-3B	i	1	3.1580	1.2800	0.0715	0.0510	0.008225	0.16	43.57	1.38	86.6	1
052615-3B	i	2	3.1580	1.2800	0.0715	0.0510	0.008225	0.16	64.62	2.05	122.3	1

Sample	Wafer	Load	L (in)	W (in)	t (in)	t_n (in)	W_m (m)	ν^*	P† (N)	K_{IC}* (MPa √m)	SCI	Notes‡
052715-7i	a	1	3.1840	1.3171	0.0813	0.0625	0.008225	0.13	42.48	-	-	2, LQ
052715-7i	a	2	3.1840	1.3171	0.0813	0.0625	0.008225	0.13	35.62	-	-	2, LQ
052715-7i	b	1	3.1880	1.2669	0.0651	0.0479	0.008225	0.13	17.02	-	-	2, LQ
052715-7i	c	1	3.1890	1.3130	0.0485	0.0310	0.008225	0.13	23.67	1.66	-	1, LQ
052715-7i	d	1	3.1870	1.2710	0.0465	0.0270	0.008225	0.13	24.92	2.02	102.0	1
052715-7i	d	1	3.1870	1.2710	0.0465	0.0270	0.008225	0.13	24.92	-	79.0	1
052715-7i	d	2	3.1870	1.2710	0.0465	0.0270	0.008225	0.13	22.09	1.79	-	1
052715-7i	e	1	3.1790	1.3210	0.0605	0.0430	0.008225	0.13	45.66	-	145.0	2, PC
052715-7i	e	2	3.1790	1.3210	0.0605	0.0430	0.008225	0.13	57.03	2.44	163.6	2
052715-7i	e	3	3.1790	1.3210	0.0605	0.0430	0.008225	0.13	55.54	2.38	-	2, LQ
052715-7i	f	1	3.1830	1.3190	0.0840	0.0615	0.008225	0.13	39.25	-	-	2, LQ
052715-7i	f	2	3.1830	1.3190	0.0840	0.0615	0.008225	0.13	36.01	-	-	2, LQ
052715-7i	f	3	3.1830	1.3190	0.0840	0.0615	0.008225	0.13	35.73	-	-	2, LQ
052715-7i	f	4	3.1830	1.3190	0.0840	0.0615	0.008225	0.13	34.37	-	-	2, LQ
052715-7i	g	1	3.2010	1.3120	0.0900	0.0690	0.008225	0.13	109.79	2.08	-	1
052715-7i	h	1	3.2040	1.3070	0.0875	0.0660	0.008225	0.13	81.22	-	158.9	1, PC
052715-7i	h	2	3.2040	1.3070	0.0875	0.0660	0.008225	0.13	104.04	2.11	158.1	1
052715-7i	h	3	3.2040	1.3070	0.0875	0.0660	0.008225	0.13	109.04	2.21	-	1, LQ
052715-7i	h	4	3.2040	1.3070	0.0875	0.0660	0.008225	0.13	112.93	2.29	186.5	1
052715-7i	h	5	3.2040	1.3070	0.0875	0.0660	0.008225	0.13	118.73	2.40	-	1
052715-7i	i	1	3.1990	1.3130	0.0920	0.0750	0.008225	0.13	105.86	1.86	-	1
052715-7ii	b	1	3.1740	1.3740	0.0520	0.0360	0.008225	0.13	26.62	-	56.7	1, PC
052715-7ii	b	2	3.1740	1.3740	0.0520	0.0360	0.008225	0.13	22.86	1.31	78.9	1
052715-7ii	b	3	3.1740	1.3740	0.0520	0.0360	0.008225	0.13	25.85	1.48	-	1

Sample	Wafer	Load	L (in)	W (in)	t (in)	t_n (in)	W_m (m)	ν^*	P† (N)	K_{IC}* (MPa √m)	SCI	Notes‡
052715-7ii	c	1	3.1740	1.3480	0.0570	0.0430	0.008225	0.13	30.60	1.41	79.0	2
052715-7ii	c	2	3.1740	1.3480	0.0570	0.0430	0.008225	0.13	35.16	1.62	92.1	2
052715-7ii	d	1	3.1740	1.3745	0.0640	0.0470	0.008225	0.13	40.32	-	-	1, LQ
052715-7ii	d	2	3.1740	1.3745	0.0640	0.0470	0.008225	0.13	46.97	1.73	118.1	1
052715-7ii	d	3	3.1740	1.3745	0.0640	0.0470	0.008225	0.13	53.61	1.98	-	1
052715-7ii	e	1	3.1645	1.3675	0.0600	0.0400	0.008225	0.13	43.25	1.91	57.2	1
052715-7ii	e	2	3.1645	1.3675	0.0600	0.0400	0.008225	0.13	49.42	2.18	112.9	1
052715-7ii	e	3	3.1645	1.3675	0.0600	0.0400	0.008225	0.13	40.23	1.77	53.1	1
052715-7ii	e	4	3.1645	1.3675	0.0600	0.0400	0.008225	0.13	34.60	1.53	-	1
052715-7ii	g	1	3.1660	1.3670	0.0690	0.0540	0.008225	0.13	63.13	-	97.0	2, PC
052715-7ii	g	2	3.1660	1.3670	0.0690	0.0540	0.008225	0.13	65.85	2.04	121.8	2
052715-7ii	g	3	3.1660	1.3670	0.0690	0.0540	0.008225	0.13	51.79	1.60	124.6	2
052715-7ii	g	4	3.1660	1.3670	0.0690	0.0540	0.008225	0.13	50.36	1.56	-	2
052715-7ii	h	1	3.1740	1.3430	0.0780	0.0620	0.008225	0.13	80.34	1.96	133.0	1
052715-7ii	h	2	3.1740	1.3430	0.0780	0.0620	0.008225	0.13	87.15	2.12	-	1
052715-7ii	i	1	3.1735	1.3710	0.0700	0.0505	0.008225	0.13	57.11	1.78	77.0	1
052715-7ii	i	2	3.1735	1.3710	0.0700	0.0505	0.008225	0.13	57.73	1.80	105.9	1
052715-7ii	i	3	3.1735	1.3710	0.0700	0.0505	0.008225	0.13	60.77	1.90	96.1	1
052715-7ii	i	4	3.1735	1.3710	0.0700	0.0505	0.008225	0.13	59.68	1.86	137.1	1
052715-7ii	i	5	3.1735	1.3710	0.0700	0.0505	0.008225	0.13	47.71	1.49	-	1
052715-7ii	j	1	3.1720	1.3700	0.0755	0.0605	0.008225	0.13	66.54	1.70	62.0	1
052715-7ii	j	2	3.1720	1.3700	0.0755	0.0605	0.008225	0.13	53.40	1.37	84.4	1
052715-7ii	j	3	3.1720	1.3700	0.0755	0.0605	0.008225	0.13	48.03	1.23	-	1
052715-7ii	k	1	3.1760	1.3435	0.0880	0.0705	0.008225	0.13	99.64	1.91	123.7	1
052715-7ii	k	2	3.1760	1.3435	0.0880	0.0705	0.008225	0.13	104.44	2.00	84.4	1

Sample	Wafer	Load	L (in)	W (in)	t (in)	t_n (in)	W_m (m)	ν^*	P† (N)	K_{IC}* (MPa √m)	SCI	Notes‡
052715-7ii	k	3	3.1760	1.3435	0.0880	0.0705	0.008225	0.13	127.01	2.43	47.3	1
052715-7ii	k	4	3.1760	1.3435	0.0880	0.0705	0.008225	0.13	109.63	2.10	65.6	1
052715-7ii	k	5	3.1760	1.3435	0.0880	0.0705	0.008225	0.13	107.47	2.06	-	1
052715-7ii	l	1	3.1740	1.3740	0.0830	0.0635	0.008225	0.13	79.48	1.72	-	1
052715-7ii	m	1	3.1620	1.3615	0.0890	0.0650	0.008225	0.13	95.79	1.86	122.0	1
052715-7ii	m	2	3.1620	1.3615	0.0890	0.0650	0.008225	0.13	95.44	1.86	-	1
052715-7iii	a	1	3.1720	1.3480	0.0680	0.0530	0.008225	0.13	57.44	1.84	123.4	1
052715-7iii	a	2	3.1720	1.3480	0.0680	0.0530	0.008225	0.13	73.30	2.35	107.5	1
052715-7iii	a	3	3.1720	1.3480	0.0680	0.0530	0.008225	0.13	64.78	2.08	172.2	1
052715-7iii	a	4	3.1720	1.3480	0.0680	0.0530	0.008225	0.13	55.60	1.79		1
052715-7iii	b	1	3.1680	1.3460	0.0620	0.0440	0.008225	0.13	40.27	1.63	83.3	1
052715-7iii	b	2	3.1680	1.3460	0.0620	0.0440	0.008225	0.13	38.12	1.54	93.1	1
052715-7iii	b	3	3.1680	1.3460	0.0620	0.0440	0.008225	0.13	31.33	1.27	111.1	1
052715-7iii	b	4	3.1680	1.3460	0.0620	0.0440	0.008225	0.13	30.42	1.23	98.2	1
052715-7iii	b	5	3.1680	1.3460	0.0620	0.0440	0.008225	0.13	29.09	1.17	-	1
052715-7iii	c	1	3.1630	1.2565	0.0670	0.0500	0.008225	0.13	56.20	-	80.6	1, PC
052715-7iii	c	2	3.1630	1.2565	0.0670	0.0500	0.008225	0.13	44.33	1.56	103.6	1
052715-7iii	c	3	3.1630	1.2565	0.0670	0.0500	0.008225	0.13	49.24	1.73	110.3	1
052715-7iii	c	4	3.1630	1.2565	0.0670	0.0500	0.008225	0.13	49.81	1.75	128.3	1
052715-7iii	c	5	3.1630	1.2565	0.0670	0.0500	0.008225	0.13	52.93	1.86	93.7	1
052715-7iii	c	6	3.1630	1.2565	0.0670	0.0500	0.008225	0.13	42.18	1.48	-	1
052715-7iii	d	1	3.1730	1.2564	0.0640	0.0490	0.008225	0.13	48.73	1.85	107.4	1
052715-7iii	d	2	3.1730	1.2564	0.0640	0.0490	0.008225	0.13	46.65	1.77	149.0	1
052715-7iii	d	3	3.1730	1.2564	0.0640	0.0490	0.008225	0.13	50.82	1.93	-	1, LQ

Sample	Wafer	Load	L (in)	W (in)	t (in)	t_n (in)	W_m (m)	ν^*	P† (N)	K_{IC}* (MPa √m)	SCI	Notes‡
052715-7iii	d	4	3.1730	1.2564	0.0640	0.0490	0.008225	0.13	68.74	2.61	-	1
052715-7iii	e	1	3.1700	1.2500	0.0700	0.0510	0.008225	0.13	67.73	2.21	101.3	1
052715-7iii	e	2	3.1700	1.2500	0.0700	0.0510	0.008225	0.13	65.87	2.15	111.5	1
052715-7iii	e	3	3.1700	1.2500	0.0700	0.0510	0.008225	0.13	66.69	2.18	111.4	1
052715-7iii	e	4	3.1700	1.2500	0.0700	0.0510	0.008225	0.13	82.48	2.69	-	1
052715-7iii	f	1	3.1660	1.3430	0.0635	0.0490	0.008225	0.13	50.64	1.87	109.0	1
052715-7iii	f	2	3.1660	1.3430	0.0635	0.0490	0.008225	0.13	51.42	1.90	77.5	1
052715-7iii	f	3	3.1660	1.3430	0.0635	0.0490	0.008225	0.13	46.65	1.73	103.3	1
052715-7iii	f	4	3.1660	1.3430	0.0635	0.0490	0.008225	0.13	47.86	1.77	152.8	1
052715-7iii	f	5	3.1660	1.3430	0.0635	0.0490	0.008225	0.13	48.31	1.79	-	1
052715-7iii	g	1	3.1620	1.3410	0.0515	0.0410	0.008225	0.13	-	-	101.7	1, LQ
052715-7iii	g	2	3.1620	1.3410	0.0515	0.0410	0.008225	0.13	27.17	1.50	35.8	1
052715-7iii	g	3	3.1620	1.3410	0.0515	0.0410	0.008225	0.13	27.57	1.52	65.9	1
052715-7iii	g	4	3.1620	1.3410	0.0515	0.0410	0.008225	0.13	25.65	1.41	40.0	1
052715-7iii	g	5	3.1620	1.3410	0.0515	0.0410	0.008225	0.13	25.15	1.39	64.4	1
052715-7iii	g	6	3.1620	1.3410	0.0515	0.0410	0.008225	0.13	21.83	1.20	-	1
052715-7iii	g	7	3.1620	1.3410	0.0515	0.0410	0.008225	0.13	21.18	1.17	51.6	1
052715-7iii	i	1	3.1640	1.3460	0.0495	0.0340	0.008225	0.13	22.30	-	-	1, LQ
052715-7iii	i	2	3.1640	1.3460	0.0495	0.0340	0.008225	0.13	17.14	-	-	1, LQ
052715-7iii	j	1	3.1650	1.3450	0.0840	0.0645	0.008225	0.13	86.71	1.86	68.0	1
052715-7iii	j	2	3.1650	1.3450	0.0840	0.0645	0.008225	0.13	89.88	1.92	52.2	1
052715-7iii	j	3	3.1650	1.3450	0.0840	0.0645	0.008225	0.13	86.48	1.85	86.5	1
052715-7iii	j	4	3.1650	1.3450	0.0840	0.0645	0.008225	0.13	86.25	1.85	101.9	1
052715-7iii	j	5	3.1650	1.3450	0.0840	0.0645	0.008225	0.13	93.48	2.00	63.6	1

Sample	Wafer	Load	L (in)	W (in)	t (in)	t_n (in)	W_m (m)	ν^*	P† (N)	K_{IC}* (MPa √m)	SCI	Notes‡
052715-7iii	j	6	3.1650	1.3450	0.0840	0.0645	0.008225	0.13	90.21	1.93	-	1
052715-7iii	l	1	3.1780	1.3580	0.0865	0.0660	0.008225	0.13	101.08	2.04	120.1	1
052715-7iii	l	2	3.1780	1.3580	0.0865	0.0660	0.008225	0.13	114.88	2.32	133.1	1
052715-7iii	l	3	3.1780	1.3580	0.0865	0.0660	0.008225	0.13	-	-	75.8	1
052715-7iii	l	4	3.1780	1.3580	0.0865	0.0660	0.008225	0.13	97.30	1.96	-	1
052715-7iv	a	1	3.1910	1.3275	0.0680	0.0490	0.008225	0.13	43.48	1.46	63.9	1
052715-7iv	a	2	3.1910	1.3275	0.0680	0.0490	0.008225	0.13	38.44	1.29	103.1	1
052715-7iv	a	3	3.1910	1.3275	0.0680	0.0490	0.008225	0.13	47.76	1.61	127.4	1
052715-7iv	a	4	3.1910	1.3275	0.0680	0.0490	0.008225	0.13	39.55	1.33	-	1
052715-7iv	b	1	3.1970	1.3270	0.0528	0.0380	0.008225	0.13	44.52	-	100.9	1, PC
052715-7iv	b	2	3.1970	1.3270	0.0528	0.0380	0.008225	0.13	26.32	1.46	104.6	1
052715-7iv	b	3	3.1970	1.3270	0.0528	0.0380	0.008225	0.13	26.95	1.50	-	1, LQ
052715-7iv	b	4	3.1970	1.3270	0.0528	0.0380	0.008225	0.13	28.09	1.56	-	1
052715-7iv	c	1	3.2050	1.3290	0.0653	0.0485	0.008225	0.13	59.37	-	142.0	1, PC
052715-7iv	c	2	3.2050	1.3290	0.0653	0.0485	0.008225	0.13	56.30	2.02	52.4	1
052715-7iv	c	3	3.2050	1.3290	0.0653	0.0485	0.008225	0.13	48.44	1.74	88.8	1
052715-7iv	c	4	3.2050	1.3290	0.0653	0.0485	0.008225	0.13	46.72	1.68	70.5	1
052715-7iv	c	5	3.2050	1.3290	0.0653	0.0485	0.008225	0.13	44.62	1.60	-	1
052715-7iv	c	6	3.2050	1.3290	0.0653	0.0485	0.008225	0.13	39.57	1.42	51.6	1
052715-7iv	d	1	3.1570	1.3275	0.0488	0.0350	0.008225	0.13	18.07	1.17	90.3	1
052715-7iv	d	2	3.1570	1.3275	0.0488	0.0350	0.008225	0.13	17.58	1.14	84.0	1
052715-7iv	d	3	3.1570	1.3275	0.0488	0.0350	0.008225	0.13	23.68	1.54	-	1
052715-7iv	e	1	3.0470	1.3265	0.0790	0.0590	0.008225	0.13	68.34	1.68	60.9	1
052715-7iv	e	2	3.0470	1.3265	0.0790	0.0590	0.008225	0.13	65.58	1.62	92.3	1

Sample	Wafer	Load	L (in)	W (in)	t (in)	t_n (in)	W_m (m)	ν^*	P† (N)	K_{IC}* (MPa √m)	SCI	Notes‡
052715-7iv	e	3	3.0470	1.3265	0.0790	0.0590	0.008225	0.13	76.02	1.87	-	1
052715-7iv	f	1	3.1940	1.3205	0.0800	0.0630	0.008225	0.13	50.78	-	-	2, LQ
052715-7iv	f	2	3.1940	1.3205	0.0800	0.0630	0.008225	0.13	46.40	-	-	2, LQ
052715-7iv	f	3	3.1940	1.3205	0.0800	0.0630	0.008225	0.13	39.12	-	-	2, LQ
052715-7iv	f	4	3.1940	1.3205	0.0800	0.0630	0.008225	0.13	34.93	-	-	2, LQ
052715-7iv	h	1	3.1955	1.3240	0.0880	0.0690	0.008225	0.13	70.10	1.37	64.1	2
052715-7iv	h	2	3.1955	1.3240	0.0880	0.0690	0.008225	0.13	61.76	1.20	63.8	2
052715-7iv	i	1	3.1965	1.3245	0.0900	0.0740	0.008225	0.13	58.66	-	-	2, LQ
052715-7iv	i	2	3.1965	1.3245	0.0900	0.0740	0.008225	0.13	60.40	-	-	2, LQ
052815-2	a	1	3.1810	1.3160	0.0790	0.0520	0.008225	0.11	110.58	2.89	72.4	1
052815-2	b	1	3.2140	1.3640	0.0570	0.0330	0.008225	0.11	82.12	-	128.6	3, PC
052815-2	b	2	3.2140	1.3640	0.0570	0.0330	0.008225	0.11	60.61	3.15	174.2	3
052815-2	b	3	3.2140	1.3640	0.0570	0.0330	0.008225	0.11	67.81	3.52	200.4	3
052815-2	b	4	3.2140	1.3640	0.0570	0.0330	0.008225	0.11	68.82	3.58	112.3	3
052815-2	b	5	3.2140	1.3640	0.0570	0.0330	0.008225	0.11	67.97	3.53	-	3
052815-2	c	1	3.2110	1.3150	0.0520	0.0380	0.008225	0.11	119.73	-	202.1	1, PC
052815-2	c	2	3.2110	1.3150	0.0520	0.0380	0.008225	0.11	51.25	2.90	142.9	1
052815-2	c	3	3.2110	1.3150	0.0520	0.0380	0.008225	0.11	49.87	2.82	176.6	1
052815-2	c	4	3.2110	1.3150	0.0520	0.0380	0.008225	0.11	47.61	2.69	-	1
052815-2	d	1	3.2200	1.3180	0.0850	0.0630	0.008225	0.11	136.87	2.92	115.8	1
052815-2	d	2	3.2200	1.3180	0.0850	0.0630	0.008225	0.11	130.07	2.77	-	1
052815-2	e	1	2.9950	1.3170	0.0750	0.0580	0.008225	0.11	116.28	3.10	171.7	1
052815-2	e	2	2.9950	1.3170	0.0750	0.0580	0.008225	0.11	96.68	2.58	-	1
052815-2	f	1	3.0560	1.3190	0.0570	0.0370	0.008225	0.11	90.78	-	137.8	1, PC

Sample	Wafer	Load	L (in)	W (in)	t (in)	t_n (in)	W_m (m)	ν^*	P† (N)	K_{IC}* (MPa √m)	SCI	Notes‡
052815-2	f	2	3.0560	1.3190	0.0570	0.0370	0.008225	0.11	36.43	1.82	-	1
052815-2	g	1	3.1070	1.3120	0.0830	0.0580	0.008225	0.11	119.41	2.75	177.9	1
052815-2	g	2	3.1070	1.3120	0.0830	0.0580	0.008225	0.11	126.83	2.93	-	1, LQ
052815-2	g	3	3.1070	1.3120	0.0830	0.0580	0.008225	0.11	127.85	2.95	-	1, LQ
052815-2	g	4	3.1070	1.3120	0.0830	0.0580	0.008225	0.11	129.22	2.98	-	1, LQ
052815-2	g	5	3.1070	1.3120	0.0830	0.0580	0.008225	0.11	128.40	2.96	-	1, LQ
052815-2	g	6	3.1070	1.3120	0.0830	0.0580	0.008225	0.11	**153.50**	-	-	1, 5
052815-2	h	1	3.2040	1.3090	0.0450	0.0340	0.008225	0.11	52.45	-	99.6	1, PC
052815-2	h	2	3.2040	1.3090	0.0450	0.0340	0.008225	0.11	42.62	3.16	95.7	1
052815-2	h	3	3.2040	1.3090	0.0450	0.0340	0.008225	0.11	37.63	2.79	161.8	1
052815-2	h	4	3.2040	1.3090	0.0450	0.0340	0.008225	0.11	39.70	2.94	-	1
052815-2	i	1	2.9410	1.3050	0.0560	0.0370	0.008225	0.11	94.54	-	-	1, 4, PC
052815-3A	a	1	2.9770	1.2120	0.0705	0.0420	0.008225	0.22	85.65	-	73.9	1, PC
052815-3A	a	2	2.9770	1.2120	0.0705	0.0420	0.008225	0.22	61.04	2.30	80.7	1
052815-3A	a	3	2.9770	1.2120	0.0705	0.0420	0.008225	0.22	59.10	2.22	68.6	1
052815-3A	a	4	2.9770	1.2120	0.0705	0.0420	0.008225	0.22	60.50	2.28	-	1
052815-3A	b	1	3.0370	1.2215	0.0815	0.0610	0.008225	0.22	103.05	-	86.7	1, PC
052815-3A	b	2	3.0370	1.2215	0.0815	0.0610	0.008225	0.22	80.73	2.03	141.7	1
052815-3A	b	3	3.0370	1.2215	0.0815	0.0610	0.008225	0.22	79.26	2.00	-	1
052815-3A	c	1	3.2020	1.2070	0.0445	0.0345	0.008225	0.22	39.06	-	68.4	1, PC
052815-3A	c	2	3.2020	1.2070	0.0445	0.0345	0.008225	0.22	28.06	2.30	46.8	1
052815-3A	c	3	3.2020	1.2070	0.0445	0.0345	0.008225	0.22	23.55	1.93	81.1	1
052815-3A	c	4	3.2020	1.2070	0.0445	0.0345	0.008225	0.22	22.37	1.83	-	1, LQ
052815-3A	d	1	2.9660	1.1750	0.0755	0.0535	0.008225	0.22	111.42	-	40.5	3, PC
052815-3A	d	2	2.9660	1.1750	0.0755	0.0535	0.008225	0.22	44.03	1.35	63.6	3

Sample	Wafer	Load	L (in)	W (in)	t (in)	t_n (in)	W_m (m)	ν^*	P† (N)	K_{IC}* (MPa √m)	SCI	Notes‡
052815-3A	d	3	2.9660	1.1750	0.0755	0.0535	0.008225	0.22	42.42	1.30	75.5	3
052815-3A	d	4	2.9660	1.1750	0.0755	0.0535	0.008225	0.22	33.76	1.04	-	3, LQ
052815-3A	e	1	3.0060	1.2240	0.0870	0.0545	0.008225	0.22	53.90	1.30	-	3, LQ
052815-3A	e	2	3.0060	1.2240	0.0870	0.0545	0.008225	0.22	14.94	-	-	3, LQ
052815-3A	e	3	3.0060	1.2240	0.0870	0.0545	0.008225	0.22	12.86	-	-	3, LQ
052815-3A	f	1	3.2000	1.1700	0.0670	0.0440	0.008225	0.22	78.21	-	89.7	3, PC
052815-3A	f	2	3.2000	1.1700	0.0670	0.0440	0.008225	0.22	34.51	1.39	107.3	3
052815-3A	f	3	3.2000	1.1700	0.0670	0.0440	0.008225	0.22	32.39	1.31	-	3
052815-3A	g	1	2.9420	1.2090	0.0730	0.0480	0.008225	0.22	79.76	-	90.5	1, PC
052815-3A	g	2	2.9420	1.2090	0.0730	0.0480	0.008225	0.22	59.93	2.01	31.8	1
052815-3A	g	3	2.9420	1.2090	0.0730	0.0480	0.008225	0.22	54.98	1.84	76.2	1
052815-3A	g	4	2.9420	1.2090	0.0730	0.0480	0.008225	0.22	55.71	1.87	-	1
052815-3A	h	1	3.0040	1.2020	0.0725	0.0490	0.008225	0.22	90.68	-	46.8	1, PC
052815-3A	h	2	3.0040	1.2020	0.0725	0.0490	0.008225	0.22	53.53	1.80	66.6	1
052815-3A	h	3	3.0040	1.2020	0.0725	0.0490	0.008225	0.22	58.89	1.98	-	1
052815-3A	i	1	2.9880	1.2170	0.0745	0.0435	0.008225	0.22	39.30	1.34	-	1, LQ
061114-4B	a	1	2.9700	1.3770	0.0560	0.0390	0.008225	0.13	94.29	-	126.0	1, PC
061114-4B	a	2	2.9700	1.3770	0.0560	0.0390	0.008225	0.13	58.09	2.86	58.2	1
061114-4B	a	3	2.9700	1.3770	0.0560	0.0390	0.008225	0.13	57.36	2.82	54.9	1
061114-4B	a	4	2.9700	1.3770	0.0560	0.0390	0.008225	0.13	56.13	2.76	158.7	1
061114-4B	a	5	2.9700	1.3770	0.0560	0.0390	0.008225	0.13	57.98	2.85	-	1
061114-4B	b	1	2.9800	1.3760	0.0520	0.0290	0.008225	0.13	67.63	-	113.9	1, PC
061114-4B	b	2	2.9800	1.3760	0.0520	0.0290	0.008225	0.13	46.78	2.98	87.2	1
061114-4B	b	3	2.9800	1.3760	0.0520	0.0290	0.008225	0.13	45.56	2.90	121.4	1
061114-4B	b	4	2.9800	1.3760	0.0520	0.0290	0.008225	0.13	49.46	3.15	-	1

Sample	Wafer	Load	L (in)	W (in)	t (in)	t_n (in)	W_m (m)	ν^*	P† (N)	K_{IC}* (MPa √m)	SCI	Notes‡
061114-4B	c	1	2.9830	1.3780	0.0570	0.0350	0.008225	0.13	87.30	-	110.1	1, PC
061114-4B	c	2	2.9830	1.3780	0.0570	0.0350	0.008225	0.13	63.25	3.20	131.5	1
061114-4B	c	3	2.9830	1.3780	0.0570	0.0350	0.008225	0.13	62.71	3.17	96.2	1
061114-4B	c	4	2.9830	1.3780	0.0570	0.0350	0.008225	0.13	59.10	2.99	-	1
061114-4B	d	1	2.9470	1.3710	0.0550	0.0390	0.008225	0.13	109.86	-	159.7	1, PC
061114-4B	d	2	2.9470	1.3710	0.0550	0.0390	0.008225	0.13	64.50	3.27	90.4	1
061114-4B	d	3	2.9470	1.3710	0.0550	0.0390	0.008225	0.13	60.83	3.08	137.1	1
061114-4B	d	4	2.9470	1.3710	0.0550	0.0390	0.008225	0.13	57.97	2.94	158.8	1
061114-4B	d	5	2.9470	1.3710	0.0550	0.0390	0.008225	0.13	54.18	2.75	-	1
061114-4B	e	1	2.9750	1.3760	0.0405	0.0270	0.008225	0.13	56.92	-	97.5	1, PC
061114-4B	e	2	2.9750	1.3760	0.0405	0.0270	0.008225	0.13	30.32	2.90	112.7	1
061114-4B	e	3	2.9750	1.3760	0.0405	0.0270	0.008225	0.13	27.23	2.60	115.9	1
061114-4B	e	4	2.9750	1.3760	0.0405	0.0270	0.008225	0.13	32.19	3.08	-	1
061114-4B	f	1	2.9610	1.3710	0.0610	0.0420	0.008225	0.13	135.59	-	149.0	1, PC
061114-4B	f	2	2.9610	1.3710	0.0610	0.0420	0.008225	0.13	73.38	3.08	182.9	1
061114-4B	f	3	2.9610	1.3710	0.0610	0.0420	0.008225	0.13	83.14	3.49	-	1
061114-4B	g	1	2.9550	1.3720	0.0650	0.0450	0.008225	0.13	129.87	-	-	1, PC
061114-4B	g	2	2.9550	1.3720	0.0650	0.0450	0.008225	0.13	82.89	3.06	143.1	1
061114-4B	g	3	2.9550	1.3720	0.0650	0.0450	0.008225	0.13	84.84	3.13	144.2	1
061114-4B	g	4	2.9550	1.3720	0.0650	0.0450	0.008225	0.13	83.31	3.07	120.2	1
061114-4B	g	5	2.9550	1.3720	0.0650	0.0450	0.008225	0.13	83.45	3.08	169.1	1
061114-4B	g	6	2.9550	1.3720	0.0650	0.0450	0.008225	0.13	79.60	2.94	-	1
061114-4B	h	1	2.9670	1.3730	0.0760	0.0540	0.008225	0.13	**153.85**	-	130.2	1, 5, PC
061114-4B	h	2	2.9670	1.3730	0.0760	0.0540	0.008225	0.13	112.05	3.00	-	1

Sample	Wafer	Load	L (in)	W (in)	t (in)	t_n (in)	W_m (m)	ν^*	P† (N)	K_{IC}* (MPa √m)	SCI	Notes‡
071813-2	1	1	3.1120	1.2400	0.0950	0.0850	0.008225	***0.20***	34.80	0.58	63.2	
071813-2	1	2	3.1120	1.2400	0.0950	0.0850	0.008225	***0.20***	33.81	0.57	54.3	
071813-2	1	3	3.1120	1.2400	0.0950	0.0850	0.008225	***0.20***	32.31	0.54	66.4	
071813-2	2	1	3.1140	1.2350	0.1180	0.1000	0.008225	***0.20***	54.80	-	36.5	PC
071813-2	2	2	3.1140	1.2350	0.1180	0.1000	0.008225	***0.20***	41.88	0.48	88.2	
071813-2	2	3	3.1140	1.2350	0.1180	0.1000	0.008225	***0.20***	43.99	0.50	62.4	
071813-2	2	4	3.1140	1.2350	0.1180	0.1000	0.008225	***0.20***	45.02	0.51	82.4	
071813-2	2	5	3.1140	1.2350	0.1180	0.1000	0.008225	***0.20***	45.23	0.51	63.1	
071813-2	3	1	3.1150	1.2420	0.1430	0.1240	0.008225	***0.20***	25.72	-	-	LQ
071813-2	4	1	3.1130	1.2320	0.0920	0.0820	0.008225	***0.20***	16.91	-	94.8	LQ
071813-2	4	2	3.1130	1.2320	0.0920	0.0820	0.008225	***0.20***	19.44	0.35	93.0	
071813-2	4	3	3.1130	1.2320	0.0920	0.0820	0.008225	***0.20***	20.07	0.36	107.0	
071813-2	4	4	3.1130	1.2320	0.0920	0.0820	0.008225	***0.20***	20.26	0.36	-	
071813-2	5	1	2.7520	1.4450	0.1270	0.1170	0.008225	***0.20***	100.69	-	-	4, PC
071813-2	6	1	2.8810	1.3980	0.1270	0.1170	0.008225	***0.20***	78.88	0.70	93.1	
071813-2	6	2	2.8810	1.3980	0.1270	0.1170	0.008225	***0.20***	84.47	0.74	70.0	
071813-2	6	3	2.8810	1.3980	0.1270	0.1170	0.008225	***0.20***	80.69	0.71	-	LQ
071813-2	7	1	2.3990	1.4400	0.1120	0.0950	0.008225	***0.20***	86.62	-	-	LQ
071813-2	7	2	2.3990	1.4400	0.1120	0.0950	0.008225	***0.20***	101.89	-	-	LQ
071813-3	1	1	3.0450	1.2450	0.0540	0.0410	0.008225	***0.20***	25.55	-	59.8	PC
071813-3	1	2	3.0450	1.2450	0.0540	0.0410	0.008225	***0.20***	24.01	1.32	68.4	
071813-3	1	3	3.0450	1.2450	0.0540	0.0410	0.008225	***0.20***	22.30	1.23	-	LQ
071813-3	2	1	3.0540	1.2380	0.0760	0.0680	0.008225	***0.20***	71.70	-	42.0	PC
071813-3	2	2	3.0540	1.2380	0.0760	0.0680	0.008225	***0.20***	65.65	1.71	54.4	
071813-3	2	3	3.0540	1.2380	0.0760	0.0680	0.008225	***0.20***	60.42	1.57	81.5	

Sample	Wafer	Load	L (in)	W (in)	t (in)	t_n (in)	W_m (m)	ν^*	P† (N)	K_{IC}* (MPa √m)	SCI	Notes‡
071813-3	2	4	3.0540	1.2380	0.0760	0.0680	0.008225	***0.20***	58.21	1.51	68.9	
071813-3	3	1	3.0600	1.2400	0.0860	0.0720	0.008225	***0.20***	68.35	-	78.2	PC
071813-3	3	2	3.0600	1.2400	0.0860	0.0720	0.008225	***0.20***	67.21	1.42	29.1	
083114-2B	a	1	3.0610	1.3670	0.0800	0.0620	0.008225	***0.20***	25.80	0.62	83.3	3
083114-2B	b	1	3.1030	1.3720	0.0870	0.0500	0.008225	***0.20***	22.94	0.54	43.3	2
083114-2B	c	1	3.1340	1.3660	0.0830	0.0530	0.008225	***0.20***	9.43	0.23	50.9	1
083114-2B	c	2	3.1340	1.3660	0.0830	0.0530	0.008225	***0.20***	9.10	0.22	50.0	1
083114-2B	d	1	2.9520	1.3670	0.0810	0.0450	0.008225	***0.20***	17.77	0.49	36.8	1
083114-2B	e	1	3.1370	1.3580	0.0880	0.0550	0.008225	***0.20***	46.31	-	54.6	2, PC
083114-2B	e	2	3.1370	1.3580	0.0880	0.0550	0.008225	***0.20***	41.80	0.93	56.9	2
083114-2B	e	3	3.1370	1.3580	0.0880	0.0550	0.008225	***0.20***	40.02	0.89	70.7	2
083114-2B	e	4	3.1370	1.3580	0.0880	0.0550	0.008225	***0.20***	38.76	0.86	69.7	2
083114-2B	f	1	3.0000	1.3700	0.0815	0.0500	0.008225	***0.20***	29.48	0.76	39.6	2
083114-2B	g	1	2.9910	1.3690	0.0825	0.0545	0.008225	***0.20***	28.42	0.69	37.0	1
083114-2B	h	1	3.1290	1.3600	0.0820	0.0540	0.008225	***0.20***	45.02	-	50.4	2, PC
083114-2B	h	2	3.1290	1.3600	0.0820	0.0540	0.008225	***0.20***	43.58	1.08	44.7	2
083114-2B	h	3	3.1290	1.3600	0.0820	0.0540	0.008225	***0.20***	41.18	1.02	58.7	2

F. Appendix: Fracture Toughness from Double Torsion Tests (Rapid Displacement)

Table F.1. Specimen (Wafer) Geometry, Peak Load, Derived K_{IC}, and Ambient Conditions

Sample	Wafer	L (in)	W (in)	t (in)	t_n (in)	W_m (m)	ν^*	Load† (N)	K_{IC} (MPa √m)	T (°C)	RH (%)	Notes‡
030914-1	A1	2.0515	0.6215	0.0640	0.0520	0.002692	***0.15***	103.84	1.86	23.0	-	1
030914-1	A2	3.0475	0.6375	0.0600	0.0480	0.002692	***0.15***	131.82	2.66	23.3	-	2
030914-1	A3	0.9835	0.5880	0.0600	0.0445	n.t.	n.t.	n.t.	n.t.	n.t.	n.t.	n.t.
030914-1	B1	3.0335	0.6175	0.0680	0.0530	0.002756	***0.15***	**151.73**	-	23.3	73.5	1, 5
030914-1	B2	3.0475	0.6375	0.0675	0.0475	0.002692	***0.15***	**151.68**	-	23.2	-	1, 5
030914-1	C1	3.0440	0.6330	0.0685	0.0500	0.002692	***0.15***	136.04	2.23	23.1	-	1
030914-1	e	3.0395	1.2505	0.0745	0.0540	0.007899	***0.15***	84.25	2.37	23.5	73.0	1
030914-1	f	3.0410	1.2500	0.0640	0.0480	0.007899	***0.15***	52.05	1.94	23.5	73.0	1
030914-1	G1	3.0470	0.6360	0.0675	0.0515	0.002756	***0.15***	**151.68**	-	23.5	73.5	1, 5
030914-1	G2	3.0350	0.6175	0.0660	0.0495	0.002692	***0.15***	**151.68**	-	23.3	46.5	1, 5
030914-1	i1	3.0500	0.6230	0.0660	0.0505	0.002756	***0.15***	121.77	2.17	23.5	73.0	1
030914-1	i2	2.0060	0.6400	0.0650	0.0500	n.t.	n.t.	n.t.	n.t.	n.t.	n.t.	n.t.
030914-1	i3	1.0510	0.5990	0.0650	0.0570	n.t.	n.t.	n.t.	n.t.	n.t.	n.t.	n.t.
030914-1	K1	3.0495	0.6450	0.0690	0.0515	0.002692	***0.15***	**151.68**	-	23.2	46.5	1, 5
052615-1a	1	2.9650	1.1860	0.0530	0.0310	0.007899	0.29	14.05	-	23.6	72.5	1, LQ

* ***Bold*** indicates wafers where Poisson's ratio was estimated from similar material.

† Load flatlined ~151.7 N.

‡ 1. Wafer broke straight. 2. Fracture curved out of groove from load point. 3. Fracture curved out of groove mid-wafer. 4. Wafer broke on pre-fracturing. 5. Exceeded load cell capacity. LQ = low quality test based on wafer behavior, mechanical issue, etc., omitted; n.t. = not tested

Sample	Wafer	L (in)	W (in)	t (in)	t_n (in)	W_m (m)	ν^*	Load† (N)	K_{IC} (MPa √m)	T (°C)	RH (%)	Notes‡
052615-1a	2	2.9840	1.1930	0.0530	0.0300	0.007899	0.29	29.99	2.02	23.6	72.5	1
052615-1a	3	2.8825	1.1860	0.0600	0.0340	0.007899	0.29	41.70	2.21	23.2	76.0	1
052615-1a	4	2.9630	1.1835	0.0635	0.0370	0.007899	0.29	41.72	1.95	23.3	76.0	1
052615-1a	5	2.9650	1.1865	0.0680	0.0420	0.007899	0.29	46.97	1.86	23.3	76.0	1
052615-1a	6	2.9400	1.1880	0.0680	0.0400	0.007899	0.29	47.11	1.91	23.4	76.0	1
052615-1a	7	2.9880	1.2030	0.0760	0.0465	0.007899	0.29	72.34	2.30	23.5	72.5	1
052615-1a	8	2.9685	1.1870	0.0795	0.0520	0.007899	0.29	79.87	2.27	23.5	72.0	1
052615-1a	9	2.9845	1.1915	0.0865	0.0520	-	0.29	-	-	-	-	4
052615-1a	10	2.0800	1.1880	0.0635	0.0390	0.007899	0.29	10.02	-	23.8	72.5	1, LQ
052615-1a	A2	2.9920	0.6050	0.0565	0.0400	0.002692	0.29	83.75	2.20	-	-	3
052615-1a	B1	2.9940	0.6090	0.0550	0.0300	0.002692	0.29	88.77	2.79	-	-	2
052615-1a	B2	2.9850	0.6090	0.0565	0.0415	0.002692	0.29	69.39	1.78	-	-	2
052615-1a	C1B	2.9855	0.6040	0.0495	0.0300	0.002692	0.29	45.97	1.69	-	-	2
052615-1a	C2	2.9910	0.6110	0.0660	0.0480	0.002692	0.29	95.48	1.82	-	-	2
052615-1a	D1	2.9870	0.6075	0.0640	0.0440	0.002692	0.29	123.20	2.57	-	-	2
052615-1a	D2	2.9980	0.6100	0.0630	0.0410	0.002692	0.29	90.47	2.00	-	-	2
052615-1a	E1	2.9910	0.6000	0.0660	0.0440	0.002692	0.29	75.81	1.53	-	-	2
052615-1a	E2	2.9840	0.6125	0.0590	0.0400	0.002692	0.29	94.25	2.31	-	-	1
052615-1b	C1	3.0245	0.6585	0.0695	0.0535	0.002692	0.24	46.64	0.74	-	-	2
052615-1b	C2	3.0300	0.6740	0.0705	0.0530	0.002692	0.24	21.65	0.33	-	-	3
052615-1b	D1	3.0345	0.6300	0.0780	0.0710	n.t.	n.t.	n.t.	n.t.	n.t.	n.t.	n.t.
052615-1b	D2	3.0250	0.6715	0.0805	0.0670	0.002692	0.24	69.71	0.79	-	-	3

Sample	Wafer	L (in)	W (in)	t (in)	t_n (in)	W_m (m)	ν^*	Load† (N)	K_{IC} (MPa √m)	T (°C)	RH (%)	Notes‡
052615-1b	E1	3.0235	0.6450	0.0775	0.0670	n.t.	n.t.	n.t.	n.t.	n.t.	n.t.	n.t.
052615-1b	E2	3.0330	0.6720	0.0745	0.0640	0.002692	0.24	63.95	0.83	-	-	2
052615-1b	F1	3.0225	0.6415	0.0790	0.0655	n.t.	n.t.	n.t.	n.t.	n.t.	n.t.	n.t.
052615-1b	F2	3.0345	0.6770	0.0840	0.0690	0.002692	0.24	95.05	0.99	-	-	3
052615-1b	H	3.0240	1.2970	0.0840	0.0575	0.007895	0.24	39.63	0.92	22.9	59.0	1
052615-1b	I	3.0260	1.2950	0.0885	0.0635	0.007895	0.24	47.94	0.98	23.2	59.0	1
052615-1b	J	3.0220	1.2780	0.0595	0.0330	0.007895	0.24	14.35	0.73	23.3	59.0	1
052615-1b	K	3.0240	1.2950	0.0710	0.0485	0.007895	0.24	10.07	-	23.5	58.0	1, LQ
052615-1b	L	3.0250	1.2830	0.0635	0.0370	0.007895	0.24	21.05	0.92	23.5	58.0	2
052615-1b	M	3.0260	1.3010	0.0820	0.0555	0.007895	0.24	49.92	1.22	23.7	59.0	1
052615-1b	N	3.0180	1.3050	0.1000	0.0710	0.007895	0.24	75.66	1.22	23.7	59.0	2
052615-1b	O	2.7700	1.3100	0.0870	0.0610	0.007895	0.24	39.53	0.84	23.6	60.0	1
052615-1b	P	3.0030	1.1360	0.0770	0.0515	0.007895	0.24	40.73	1.22	24.0	59.0	1
052615-1b	Q	2.9990	1.1615	0.0650	0.0410	0.007895	0.24	26.70	1.13	24.0	59.0	2
052615-1b	R	2.9245	1.1385	0.0740	0.0420	0.007895	0.24	28.32	0.99	24.0	59.5	1
052615-1b	S	2.8755	1.1360	0.0860	0.0525	0.007895	0.24	55.18	1.39	24.0	60.0	1
052615-1b	T	3.0030	1.1370	0.0600	0.0460	0.007895	0.24	26.78	1.22	24.1	60.0	2
052615-1b	U	3.0010	1.1580	0.0770	0.0510	0.007895	0.24	41.74	1.24	24.1	60.0	1
052615-1b	V	2.6200	1.1620	0.0890	0.0620	0.007895	0.24	64.34	1.41	23.8	60.0	2
052615-2	J	3.2255	1.2730	0.1115	0.0840	0.007895	0.25	48.26	0.62	23.5	57.0	3
052615-2	K	3.2270	1.2720	0.1150	0.0875	0.007895	0.25	102.25	1.24	23.5	57.0	3
052615-2	L	3.2355	1.2700	0.1125	0.0870	0.007895	0.25	57.69	0.73	23.6	57.0	2

Sample	Wafer	L (in)	W (in)	t (in)	t_n (in)	W_m (m)	ν^*	Load† (N)	K_{IC} (MPa √m)	T (°C)	RH (%)	Notes‡
052615-2	M	3.2340	1.2985	0.0960	0.0710	0.007895	0.25	26.41	0.46	23.6	57.0	2
052615-2	N	3.2215	1.2740	0.0965	0.0750	0.007895	0.25	53.09	0.90	23.5	57.0	2
052615-2	O	2.7155	1.3195	0.1135	0.0920	0.007895	0.25	25.81	0.31	23.6	56.5	2
052615-2	P	3.1210	1.3230	0.1265	0.0950	0.007895	0.25	35.42	0.35	23.8	56.5	2
052615-2	Q	3.1395	1.2685	0.0790	0.0540	0.007895	0.25	15.29	0.41	23.6	56.5	2
052615-2	R	2.7880	1.2625	0.1080	0.0830	0.007895	0.25	71.87	0.98	23.6	56.5	2
052615-2	S	2.6365	1.2665	0.0905	0.0670	0.007895	0.25	31.18	0.61	23.7	56.5	2
052615-2	T	3.2405	1.2670	0.1700	0.1220	0.007895	0.25	135.14	0.80	23.8	56.5	3
052615-3a	1	3.0730	1.2985	0.0455	0.0215	0.007899	0.10	13.45	1.18	23.8	75.5	1
052615-3a	2	3.0710	1.3585	0.0630	0.0395	0.007899	0.10	21.95	0.86	23.6	75.5	1
052615-3a	3	3.0720	1.3450	0.0800	0.0495	0.007899	0.10	42.48	1.06	23.6	75.0	1
052615-3a	4	3.0750	1.3365	0.0850	0.0560	0.007899	0.10	20.87	0.45	23.7	75.5	3
052615-3a	5	3.0720	1.3500	0.0730	0.0450	-	0.10	-	-	-	-	4
052615-3a	6	3.0740	1.3550	0.0750	0.0470	0.007899	0.10	41.25	1.15	23.8	75.5	1
052615-3a	7	3.0730	1.3460	0.0575	0.0310	0.007899	0.10	25.46	1.30	23.9	75.5	1
052615-3a	8	3.0730	1.3590	0.0643	0.0400	0.007899	0.10	24.00	0.91	23.6	75.5	1
052615-3a	A1	3.0940	0.6475	0.0730	0.0535	0.002692	0.10	84.19	1.18	-	-	2
052615-3a	A2	3.0820	0.6920	0.0745	0.0565	0.002692	0.10	116.06	1.48	-	-	3
052615-3a	B1	3.0780	0.6600	0.0775	0.0565	0.002692	0.10	121.68	1.51	-	-	2
052615-3a	B1V2	3.0780	0.6600	0.0775	0.0565	0.002692	0.10	84.18	1.04	-	-	2
052615-3a	B2	3.0650	0.6830	0.0800	0.0565	0.002692	0.10	134.14	1.55	-	-	3
052615-3a	C2	3.0820	0.6850	0.0755	0.0545	0.002692	0.10	146.37	1.87	-	-	1

Sample	Wafer	L (in)	W (in)	t (in)	t_n (in)	W_m (m)	ν^*	Load† (N)	K_{IC} (MPa √m)	T (°C)	RH (%)	Notes‡
052615-3a	D	3.0850	1.3140	0.0500	0.0360	0.007899	0.10	25.00	1.47	23.8	75.0	1
052615-3a	E	3.0730	1.3360	0.0730	0.0520	0.007899	0.10	44.95	1.25	23.7	75.0	1
052615-3a	G2	3.0700	0.6940	0.0700	0.0543	0.002692	0.10	102.37	1.45	-	-	3
052615-3a	i	3.0900	1.3250	0.0800	0.0610	0.007899	0.10	51.26	1.16	23.7	75.5	1
052615-3a	L1	3.0960	0.6520	0.0760	0.0560	0.002756	0.10	101.48	1.34	-	-	3
052615-3a	L2	3.0820	0.6715	0.0800	0.0615	0.002756	0.10	121.31	1.39	-	-	1
052615-3a	M1	3.0960	0.6545	0.0710	0.0505	0.002692	0.10	86.83	1.29	-	-	2
052615-3a	M2	3.0610	0.6630	0.0755	0.0520	0.002756	0.10	84.70	1.16	-	-	2
052615-3B	1	3.2045	1.3490	0.0770	0.0555	0.007899	0.16	58.23	1.48	23.7	73.5	1
052615-3B	2	3.1520	1.2645	0.0585	0.0420	0.007899	0.16	30.74	1.39	23.7	73.5	3
052615-3B	3	3.2030	1.4220	0.0600	0.0360	0.007899	0.16	20.74	0.92	23.6	75.0	3
052615-3B	4	3.2105	1.3485	0.0735	0.0505	0.007899	0.16	53.42	1.53	23.7	74.0	1
052615-3B	5	3.1515	1.2560	0.0800	0.0610	0.007899	0.16	58.80	1.40	23.9	74.0	1
052615-3B	6	3.1520	1.2615	0.0855	0.0600	0.007899	0.16	34.27	0.75	23.7	74.0	2
052615-3B	7	3.2090	1.3750	0.0820	0.0565	0.007899	0.16	64.47	1.47	23.6	74.5	1
052615-3B	8	3.2035	1.3470	0.0625	0.0450	0.007899	0.16	40.04	1.54	23.9	74.5	1
052615-3B	9	3.2080	1.3590	0.0830	0.0590	0.007899	0.16	42.59	0.94	23.7	75.0	2
052615-3B	B1	3.1440	0.6445	0.0730	0.0555	n.t.	n.t.	n.t.	n.t.	n.t.	n.t.	n.t.
052615-3B	B2	1.1240	0.6765	0.0720	0.0590	n.t.	n.t.	n.t.	n.t.	n.t.	n.t.	n.t.
052615-3B	C1	2.8620	0.6250	0.0715	0.0460	n.t.	n.t.	n.t.	n.t.	n.t.	n.t.	n.t.
052615-3B	C2	3.1725	0.6835	0.0745	0.0520	0.002692	0.16	61.22	0.84	-	-	3
052615-3B	i1	3.1450	0.6070	0.0715	0.0540	n.t.	n.t.	n.t.	n.t.	n.t.	n.t.	n.t.

Sample	Wafer	L (in)	W (in)	t (in)	t_n (in)	W_m (m)	v^*	Load† (N)	K_{IC} (MPa √m)	T (°C)	RH (%)	Notes‡
052615-3B	i2	3.1770	0.6430	0.0720	0.0475	0.002692	0.16	61.18	0.96	-	-	3
052615-3B	J	2.3000	1.3025	0.0740	0.0520	0.007836	0.16	27.42	0.77	-	-	2
052715-7	iBdyn	3.1900	1.3170	0.0665	0.0480	0.007895	0.13	45.11	1.53	24.0	55.0	1
052715-7	iC2	3.1930	0.6530	0.0485	0.0380	0.002692	0.13	58.10	1.75	-	-	2
052715-7	iD1	2.8270	0.6730	0.0485	0.0435	0.002692	0.13	42.40	1.17	-	-	3
052715-7	iE2	3.1770	0.6595	0.0600	0.0415	0.002692	0.13	76.24	1.61	-	-	2
052715-7	iiA	3.1605	1.3570	0.0380	0.0285	0.007895	0.13	25.05	2.47	23.6	60.0	3
052715-7	iiB2	3.1780	0.6660	0.0520	0.0390	0.002692	0.13	41.67	1.11	-	-	2
052715-7	iiF	3.1600	1.3570	0.0510	0.0380	0.007895	0.13	39.29	2.18	23.7	60.5	1
052715-7	iiI1	3.1755	0.7190	0.0700	0.0500	0.002692	0.13	98.44	1.44	-	-	3
052715-7	iiI2	3.1570	0.6640	0.0720	0.0500	0.002692	0.13	141.52	2.09	-	-	3
052715-7	iiiB2	3.1620	0.6610	0.0575	0.0375	0.002692	0.13	82.48	1.94	-	-	3
052715-7	iiiC1	3.1570	0.6630	0.0700	0.0480	0.002692	0.13	131.13	2.06	-	-	2
052715-7	iiiD1	3.1850	0.6485	0.0630	0.0475	0.002692	0.13	66.82	1.24	-	-	2
052715-7	iiiM	3.1330	1.3370	0.0930	0.0750	0.007895	0.13	**151.68**	-	23.7	60.5	1, 5
052715-7	iiiN	3.1760	1.2770	0.0920	0.0715	0.007895	0.13	126.07	2.22	23.7	61.0	2
052715-7	iiiO	3.1760	1.2705	0.0940	0.0730	0.007895	0.13	111.71	1.89	23.7	61.0	2
052715-7	iiiP	3.1580	1.3385	0.0945	0.0765	0.007895	0.13	142.14	2.26	23.8	61.5	3
052715-7	iiiQ	3.1820	1.3650	0.0910	0.0760	0.007895	0.13	124.14	2.07	23.6	62.0	3
052715-7	iiiS	3.1820	1.3615	0.0885	0.0660	0.007895	0.13	112.02	2.09	23.5	63.0	1
052715-7	iiN	3.1605	1.3590	0.0900	0.0715	0.007895	0.13	130.56	2.29	23.7	60.5	1
052715-7	iiO	3.1635	1.3650	0.0940	0.0760	0.007895	0.13	151.42	2.41	23.7	60.0	1

Sample	Wafer	L (in)	W (in)	t (in)	t_n (in)	W_m (m)	ν^*	Load† (N)	K_{IC} (MPa √m)	T (°C)	RH (%)	Notes‡
052715-7	ivFdyn	3.1940	1.2290	0.0790	0.0580	0.007895	0.13	77.54	1.93	24.1	55.0	1
052815-2	B1	3.1885	0.7180	0.0590	0.0445	0.002692	0.11	147.80	2.91	23.3	62.5	2
052815-2	B2	2.7750	0.6600	0.0570	0.0400	0.002692	0.11	**151.68**	-	23.3	63.0	2, 5
052815-2	C1	3.2120	0.6320	0.0515	0.0400	0.002692	0.11	108.82	2.95	23.0	63.5	1
052815-2	C2	1.5970	0.6660	0.0530	0.0390	n.t.	n.t.	n.t.	n.t.	n.t.	n.t.	n.t.
052815-2	C3	1.5985	0.6610	0.0520	0.0390	n.t.	n.t.	n.t.	n.t.	n.t.	n.t.	n.t.
052815-2	F1	2.7600	0.7140	0.0580	0.0460	0.002692	0.11	**151.68**	-	23.2	63.0	2, 5
052815-2	F2	3.0520	0.6630	0.0565	0.0430	0.002692	0.11	144.55	3.22	23.4	63.5	1
052815-2	H1	3.1970	0.6630	0.0450	0.0325	0.002692	0.11	88.71	3.16	23.2	63	1
052815-2	H2	2.0085	0.6415	0.0440	0.0330	n.t.	n.t.	n.t.	n.t.	n.t.	n.t.	n.t.
052815-2	i1	2.9680	0.6650	0.0560	0.0430	0.002692	0.11	129.46	2.92	22.9	63.0	1
052815-2	L1	3.1925	0.6660	0.0520	0.0440	0.002692	0.11	141.99	3.52	23.3	63.0	1
052815-2	N2	3.0835	0.7140	0.0390	0.0320	0.002692	0.11	90.34	3.84	23.3	64.0	1
052815-2	P	3.2035	1.3080	0.0795	0.0530	0.007899	0.11	120.53	2.98	23.9	68.0	1
052815-2	Q	2.9750	1.3755	0.0805	0.0630	0.007899	0.11	133.07	2.88	23.8	69.0	1
052815-2	R	2.9000	1.2870	0.0790	0.0570	0.007899	0.11	149.16	3.62	23.8	70.0	1
052815-3a	A2	2.9730	0.5990	0.0705	0.0555	0.002692	0.22	**151.69**	-	-	-	1, 5
052815-3a	B1	3.0330	0.6070	0.0810	0.0600	0.002692	0.22	149.63	1.87	-	-	1
052815-3a	C2	3.2130	0.5960	0.0460	0.0310	0.002692	0.22	29.67	-	-	-	2, LQ
052815-3a	G1	2.9380	0.6330	0.0730	0.0560	0.002692	0.22	**151.68**	-	-	-	1, 5
052815-3a	G2	2.9430	0.5845	0.0730	0.0540	-	0.22	-	-	-	-	4
052815-3a	H1	3.0160	0.6345	0.0725	0.0580	0.002692	0.22	**151.68**	-	-	-	1, 5

Sample	Wafer	L (in)	W (in)	t (in)	t_n (in)	W_m (m)	ν^*	Load† (N)	K_{IC} (MPa √m)	T (°C)	RH (%)	Notes‡
052815-3a	i1	2.9920	0.6550	0.0720	0.0580	-	0.22	-	-	-	-	4
052815-3a	J	3.0250	1.1970	0.0770	0.0455	0.007899	0.22	80.73	2.48	24.0	78.0	1
052815-3a	K	3.0050	1.1990	0.0790	0.0500	0.007899	0.22	75.33	2.13	24.2	70.0	1
052815-3a	L	3.0295	1.1660	0.0690	0.0440	-	0.22	-	-	-	-	4
052815-3a	m	3.2020	1.2080	0.0525	0.0350	0.007895	0.22	32.97	2.01	24.1	56.0	1
052815-3a	n	3.1960	1.1620	0.0570	0.0400	0.007895	0.22	41.22	2.13	24.0	56.0	1
052815-3a	o	2.2980	1.1900	0.0730	0.0610	0.007899	0.22	82.53	2.38	23.5	74.0	1
052815-3a	p	1.9980	1.1780	0.0640	0.0450	0.007899	0.22	44.40	1.81	23.4	74.0	1
052815-3b	1	2.4730	1.0365	0.0730	0.0620	0.007899	0.20	20.57	0.63	23.3	76.0	2
052815-3b	2	2.4770	1.0135	0.0820	0.0610	0.007899	0.20	26.75	0.70	23.5	75.5	1
052815-3b	3	2.4770	1.0155	0.0670	0.0505	0.007899	0.20	17.70	0.69	23.5	75.5	1
052815-3b	4	2.4760	1.0365	0.0885	0.0700	0.007899	0.20	30.05	0.65	23.7	75.5	1
052815-3b	5	2.4540	1.0295	0.0980	0.0770	0.007899	0.20	23.43	0.42	23.4	75.0	2
052815-3b	6	2.3395	1.0370	0.0560	0.0350	-	0.20	-	-	23.6	75.0	4
052815-3b	7	2.4580	1.0165	0.0840	0.0685	0.007899	0.20	12.58	0.30	23.8	74.5	1
052815-3b	8	2.4755	1.0160	0.0650	0.0480	0.007899	0.20	13.99	0.58	23.5	74.5	1
052815-3b	9	2.5645	1.0215	0.1040	0.0850	0.007899	0.20	29.78	0.47	23.5	74.5	2
061114-4B	A1	2.9790	0.6975	0.0565	0.0370	0.002756	0.13	115.93	2.80	23.5	74.0	1
061114-4B	A2	2.9665	0.6790	0.0645	0.0415	0.002756	0.13	111.01	2.12	23.7	74.0	1
061114-4B	B1	2.9730	0.6980	0.0650	0.0485	0.002756	0.13	106.88	1.84	23.6	74.5	1
061114-4B	B2	2.9860	0.6540	0.0540	0.0410	0.002756	0.13	107.77	2.73	23.5	74.5	1
061114-4B	C1	2.9775	0.6895	0.0635	0.0500	0.002756	0.13	128.41	2.27	23.5	74.5	1

Sample	Wafer	L (in)	W (in)	t (in)	t_n (in)	W_m (m)	v^*	Load† (N)	K_{IC} (MPa √m)	T (°C)	RH (%)	Notes‡
061114-4B	C2	2.9910	0.6965	0.0570	0.0420	n.t.	n.t.	n.t.	n.t.	n.t.	n.t.	n.t.
061114-4B	D1	2.9580	0.6575	0.0565	0.0365	0.002756	0.13	107.43	2.70	23.6	74.5	1
061114-4B	D2	2.9420	0.6885	0.0573	0.0450	0.002756	0.13	**151.68**	-	23.5	74.0	2, 5
061114-4B	E1	2.9690	0.6965	0.0410	0.0290	0.002756	0.13	66.52	2.89	23.5	74.0	1
061114-4B	E2	2.9830	0.6840	0.0410	0.0270	n.t.	n.t.	n.t.	n.t.	n.t.	n.t.	n.t.
061114-4B	F1	2.9690	0.6920	0.0618	0.0460	0.002756	0.13	**151.68**	-	23.4	74.0	1, 5
061114-4B	F2	2.9535	0.6540	0.0620	0.0450	0.002756	0.13	148.22	2.94	23.3	74.0	1
061114-4B	J	2.9650	1.3760	0.0860	0.0600	0.007899	0.13	**151.66**	-	23.9	70.0	1, 5
061114-4B	K	2.9835	1.3510	0.0780	0.0480	0.007899	0.13	128.00	3.39	24.0	70.0	1
061114-4B	L	2.9505	1.3480	0.0790	0.0610	0.007899	0.13	130.54	3.01	24.0	71.0	1
071813-3	1	3.0620	1.2290	0.0840	0.0560	0.007895	***0.20***	50.77	1.21	24.0	57.0	1
071813-3	2	3.0655	1.2285	0.0900	0.0680	0.007895	***0.20***	58.66	1.15	24.1	57.0	1
071813-3	3	3.0640	1.2320	0.1030	0.0780	0.007895	***0.20***	89.01	1.34	24.1	57.0	1
071813-3	4	3.0360	1.2430	0.0970	0.0690	0.007895	***0.20***	63.72	1.11	24.0	57.5	2
071813-3	5	3.0610	1.2365	0.0955	0.0690	0.007895	***0.20***	69.66	1.24	24.1	57.5	1
071813-3	6	3.0570	1.2400	0.1000	0.0670	0.007895	***0.20***	43.78	0.74	24.0	57.5	1
071813-3	7	3.0665	1.2270	0.0925	0.0655	0.007895	***0.20***	48.30	0.93	24.0	58.0	1
071813-3	8	2.3100	1.2415	0.1070	0.0695	0.007895	***0.20***	74.28	1.11	24.1	58.0	1
071813-3	9	2.7315	1.2270	0.0830	0.0575	0.007895	***0.20***	46.73	1.12	24.0	58.0	1
071813-3	o5	3.0420	1.2510	0.1110	0.0910	0.007899	***0.20***	64.87	0.80	-	-	2
071813-3	w1	2.6920	1.2040	0.1170	0.1020	n.t.	n.t.	n.t.	n.t.	n.t.	n.t.	n.t.
083114-2b	1	3.1440	1.3095	0.0990	0.0730	0.007899	***0.20***	53.58	0.85	23.7	80.0	2

Sample	Wafer	L (in)	W (in)	t (in)	t_n (in)	W_m (m)	ν^*	Load† (N)	K_{IC} (MPa √m)	T (°C)	RH (%)	Notes‡
083114-2b	2	3.1470	1.3055	0.0780	0.0505	0.007899	***0.20***	29.70	0.80	23.9	80.0	2
083114-2b	3	3.1405	1.3280	0.0965	0.0745	0.007899	***0.20***	39.43	0.64	24.1	79.5	3
083114-2b	4	3.1545	1.2600	0.0960	0.0780	0.007899	***0.20***	54.09	0.89	23.7	79.5	2
083114-2b	5	3.1585	1.3035	0.1020	0.0795	0.007899	***0.20***	49.27	0.72	23.8	80.5	2
083114-2b	6	3.1510	1.2920	0.1105	0.0885	0.007899	***0.20***	60.14	0.75	24.0	81.0	2
083114-2b	7	3.1635	1.2750	0.1200	0.0965	0.007899	***0.20***	88.88	0.95	24.3	82.0	3
083114-2b	c1	3.0050	0.6850	0.0820	0.0670	0.002692	***0.20***	82.16	0.88	23.9	56.0	2
083114-2b	d1	2.5000	0.6625	0.0795	0.0670	0.002692	***0.20***	48.91	0.56	23.9	56.0	2
083114-2b	g1	2.8350	0.7050	0.0825	0.0625	0.002692	***0.20***	23.43	0.25	23.9	56.0	2
083114-2b	i	3.1230	1.3700	0.0875	0.0655	0.007836	***0.20***	28.16	0.55	23.8	56.0	3
083114-2b	j	3.1210	1.3200	0.0860	0.0540	0.007836	***0.20***	35.26	0.79	23.8	56.0	3
083114-2b	x1	2.0000	0.6670	0.0840	0.0630	0.002692	***0.20***	45.78	0.50	24.0	56.0	2
083114-2b	x2	1.8750	0.7070	0.0845	0.0740	0.002692	***0.20***	41.77	0.40	23.9	56.5	2

G. Appendix: Double Torsion – Load Relaxation Tests (Environmental Conditions)

Table G.1. Sample, Environment, Specimen, Geometry, Load-Decay Details, and Derived Fracture Mechanical Properties

Sample	Envir.	Wafer	L (in.)	W (in.)	t (in.)	t_n (in.)	a_0 (in.)	W_m (m)	ν	#	Load (N)	K_{IC}* (MPa $m^{1/2}$)	SCI	Detail	Temp. (°C)	Notes†	Date
052815-2	amb.	c03	2.9600	1.2565	0.0550	0.0390	0.4910	0.00776	0.11	1	55.75	2.77	146.8	79% RH	23.8	1	5/19/17
052815-2	amb.	c03	2.9600	1.2565	0.0550	0.0390	0.9910	0.00776	0.11	2	63.81	3.17	-	79% RH	23.8	1	5/19/17
052815-2	amb.	c10	3.2045	1.3725	0.0800	0.0470	0.5980	0.00776	0.11	1	87.11	2.17	100.3	75% RH	23.4	1	5/19/17
052815-2	amb.	c10	3.2045	1.3725	0.0800	0.0470	1.0980	0.00776	0.11	2	100.48	2.50	-	75% RH	23.4	1	5/19/17
052815-2	amb.	c13	2.9275	1.3900	0.0760	0.0560	1.1730	0.00776	0.11	1	104.43	LQ	LQ	75% RH	23.5	1	5/19/17
052815-2	amb.	c13	2.9275	1.3900	0.0760	0.0560	1.6730	0.00776	0.11	2	108.80	LQ	LQ	75% RH	23.5	1	5/19/17
052815-2	amb.	c13	2.9275	1.3900	0.0760	0.0560	2.1730	0.00776	0.11	3	142.77	3.49	-	75% RH	23.5	1	5/19/17
052815-2	brine	c02	2.9230	1.2700	0.0570	0.0400	0.5000	0.00776	0.11	1	52.98	2.45	44.8	0.1% NaCl	RT	1	6/29/17
052815-2	brine	c02	2.9230	1.2700	0.0570	0.0400	1.0000	0.00776	0.11	2	49.25	2.28	64.0	0.1% NaCl	RT	1	6/29/17
052815-2	brine	c02	2.9230	1.2700	0.0570	0.0400	1.5000	0.00776	0.11	3	58.00	2.68	-	0.1% NaCl	RT	1	6/29/17
052815-2	brine	c02	2.9230	1.2700	0.0570	0.0400	0.5000	0.00776	0.11	1b	52.98	2.45	39.2	0.1% NaCl	RT	1	6/29/17
052815-2	brine	c02	2.9230	1.2700	0.0570	0.0400	0.5000	0.00776	0.11	1c	52.98	2.45	45.3	0.1% NaCl	RT	1	6/29/17
052815-2	brine	c11	2.9310	1.3890	0.0845	0.0660	0.7080	0.00776	0.11	1	152.84	2.95	-	0.1% NaCl	RT	1	6/29/17
052815-2	brine	c16	3.1725	1.3100	0.0750	0.0475	0.2040	0.00776	0.11	1	92.01	2.57	57.9	0.1% NaCl	RT	2	6/29/17
052815-2	brine	c16	3.1725	1.3100	0.0750	0.0475	0.7040	0.00776	0.11	2	94.98	2.65	LQ	0.1% NaCl	RT	2	6/29/17
052815-2	brine	c16	3.1725	1.3100	0.0750	0.0475	1.2040	0.00776	0.11	3	110.90	LQ	-	0.1% NaCl	RT	2	6/29/17
052815-2	brine	c18	2.8690	1.3695	0.0670	0.0465	1.0740	0.00776	0.11	2	71.43	2.32	24.5	0.1% NaCl	RT	1	6/29/17
052815-2	brine	c18	2.8690	1.3695	0.0670	0.0465	1.5740	0.00776	0.11	3	60.26	1.96	44.4	0.1% NaCl	RT	1	6/29/17
052815-2	brine	c18	2.8690	1.3695	0.0670	0.0465	2.0740	0.00776	0.11	4	54.92	1.78	69.1	0.1% NaCl	RT	1	6/29/17
052815-2	brine	c18	2.8690	1.3695	0.0670	0.0465	2.5740	0.00776	0.11	5	57.45	1.87	-	0.1% NaCl	RT	1	6/29/17
052815-2	brine	c18	2.8690	1.3695	0.0670	0.0465	0.5740	0.00776	0.11	1a	69.03	2.24	48.8	0.1% NaCl	RT	1	6/29/17
052815-2	brine	c18	2.8690	1.3695	0.0670	0.0465	0.5740	0.00776	0.11	1b	69.03	2.24	51.5	0.1% NaCl	RT	1	6/29/17
052815-2	brine	c21	2.9095	1.2770	0.0890	0.0640	0.4180	0.00756	0.11	1	113.77	2.11	-	0.1% NaCl	76.0	1, 6	7/20/17

* LQ = low quality, omitted from analysis.

† 1. Straight crack 2. Early curved crack 3. Late curved crack 4. Broke on pre-fracture 5. Exceeded load cell capacity 6. Tested while flowing, large load and temperature fluctuations.

Sample	Envir.	Wafer	L (in.)	W (in.)	t (in.)	t_n (in.)	a_0 (in.)	W_m (m)	ν	#	Load (N)	K_{IC}* (MPa $m^{1/2}$)	SCI	Detail	Temp. (°C)	Notes†	Date
052815-2	brine	c21	2.9095	1.2770	0.0890	0.0640	0.9180	0.00756	0.11	2	147.73	2.74	-	0.1% NaCl	57.0	1, 6	7/20/17
052815-2	brine	c29	2.9495	1.2595	0.0800	0.0590	0.5310	0.00776	0.11	1	118.92	2.77	104.2	0.1% NaCl	RT	1	6/29/17
052815-2	brine	c29	2.9495	1.2595	0.0800	0.0590	1.5310	0.00776	0.11	3	125.68	2.93	-	0.1% NaCl	RT	1	6/29/17
052815-2	brine	c29	2.9495	1.2595	0.0800	0.0590	1.0310	0.00776	0.11	2w	119.47	2.78	53.6	0.1% NaCl	RT	1	6/29/17
052815-2	brine	c30	2.9505	1.2570	0.0520	0.0365	0.8250	0.00756	0.11	1	39.56	2.15	-	0.1% NaCl	~55	1, 6	7/20/17
052815-2	brine	c36	3.1735	1.2700	0.0885	0.0535	1.8980	0.00756	0.11	3	127.26	2.61	-	0.1% NaCl	~51	1, 6	7/20/17
052815-2	brine	c36	3.1735	1.2700	0.0885	0.0535	0.8980	0.00756	0.11	1a	109.74	2.25	83.7	0.1% NaCl	~51	1, 6	7/20/17
052815-2	brine	c36	3.1735	1.2700	0.0885	0.0535	0.8980	0.00756	0.11	1w	109.74	2.25	69.3	0.1% NaCl	~51	1, 6	7/20/17
052815-2	brine	c36	3.1735	1.2700	0.0885	0.0535	1.3980	0.00756	0.11	2a	131.45	2.69	38.9	0.1% NaCl	~51	1, 6	7/20/17
052815-2	brine	c36	3.1735	1.2700	0.0885	0.0535	1.3980	0.00756	0.11	2b	131.45	2.69	105.5	0.1% NaCl	~51	1, 6	7/20/17
052815-2	brine	c36	3.1735	1.2700	0.0885	0.0535	1.3980	0.00756	0.11	2c	131.45	2.69	103.3	0.1% NaCl	~51	1, 6	7/20/17
052815-2	DI	c06	2.9420	1.2615	0.0690	0.0480	1.1850	0.00776	0.11	1	79.44	2.54	76.1	pH 7.1-6.4	22.8	1	5/20/17
052815-2	DI	c06	2.9420	1.2615	0.0690	0.0480	1.6850	0.00776	0.11	2	81.80	2.62	-	pH 7.1-6.4	22.8	1	5/20/17
052815-2	DI	c07	2.9180	1.2720	0.0720	0.0455	0.8330	0.00776	0.11	1	74.57	LQ	LQ	pH 7.4-6.9	23.2	1	5/20/17
052815-2	DI	c07	2.9180	1.2720	0.0720	0.0455	1.3330	0.00776	0.11	2	90.81	2.79	69.7	pH 7.4-6.9	23.2	1	5/20/17
052815-2	DI	c07	2.9180	1.2720	0.0720	0.0455	1.8330	0.00776	0.11	3	89.35	2.75	-	pH 7.4-6.9	23.2	1	5/20/17
052815-2	DI	c08	3.0705	1.3740	0.0840	0.0510	0.8790	0.00776	0.11	2	120.83	2.69	92.2	pH 7.0-7.1	23.6	1	5/20/17
052815-2	DI	c08	3.0705	1.3740	0.0840	0.0510	1.3790	0.00776	0.11	3	145.52	3.24	-	pH 7.0-7.1	23.6	1	5/20/17
052815-2	DI	c08	3.0705	1.3740	0.0840	0.0510	0.3790	0.00776	0.11	1a	112.36	2.50	38.6	pH 7.0-7.1	23.6	1	5/20/17
052815-2	DI	c08	3.0705	1.3740	0.0840	0.0510	0.6290	0.00776	0.11	1b	112.36	2.50	90.2	pH 7.0-7.2	22.7	1	5/21/17
052815-2	DI	c09	2.9345	1.3870	0.0505	0.0345	0.6625	0.00776	0.11	1	36.52	2.07	46.1	pH 6.8-6.5	24.1	1, 6	5/19/17
052815-2	DI	c09	2.9345	1.3870	0.0505	0.0345	1.1625	0.00776	0.11	2	42.78	2.43	-	pH 6.8-6.5	24.1	1, 6	5/19/17
052815-2	DI	c12	2.9390	1.3885	0.0830	0.0640	0.6885	0.00776	0.11	1	82.30	LQ	LQ	pH 7.2-6.3	23.8	1	5/19/17
052815-2	DI	c12	2.9390	1.3885	0.0830	0.0640	1.1885	0.00776	0.11	2	133.30	2.68	64.8	pH 7.2-6.3	23.8	1	5/19/17
052815-2	DI	c12	2.9390	1.3885	0.0830	0.0640	1.6885	0.00776	0.11	3	119.98	2.41	-	pH 7.2-6.3	23.8	1	5/19/17
052815-2	DI	c41	2.9480	1.2575	0.0475	0.0430	1.5875	0.00814	0.11	3	36.77	LQ	-		66.5	3	12/15/17
052815-2	DI	c41	2.9480	1.2575	0.0475	0.0430	0.5875	0.00814	0.11	1b	35.59	2.19	37.3		66.5	3	12/15/17
052815-2	DI	c41	2.9480	1.2575	0.0475	0.0430	0.5875	0.00814	0.11	1w	35.59	2.19	66.1		66.5	3	12/15/17
052815-2	DI	c41	2.9480	1.2575	0.0475	0.0430	1.0875	0.00814	0.11	2a	44.77	2.75	31.7		66.5	3	12/15/17
052815-2	DI	c43	3.1120	1.3800	0.0910	0.0575	1.5130	0.00814	0.11	1	114.02	2.22	-		60.8	1	12/15/17
052815-2	DI	c45	3.1110	1.2965	0.0620	0.0490	1.6525	0.00814	0.11	2	60.98	2.34	-		63.6	1	12/15/17
052815-2	DI	c45	3.1110	1.2965	0.0620	0.0490	1.1525	0.00814	0.11	1a	59.86	2.29	49.5		63.6	1	12/15/17
052815-2	DI	c45	3.1110	1.2965	0.0620	0.0490	1.1525	0.00814	0.11	1b	59.86	2.29	51.1		63.6	1	12/15/17

Sample	Envir.	Wafer	L (in.)	W (in.)	t (in.)	t_n (in.)	a_0 (in.)	W_m (m)	ν	#	Load (N)	K_{IC}* (MPa $m^{1/2}$)	SCI	Detail	Temp. (°C)	Notes†	Date
052815-2	DI	c47	3.1100	1.2980	0.0730	0.0560	0.1310	0.00814	0.11	1	97.02	2.73	78.0		62.4	1	12/15/17
052815-2	DI	c47	3.1100	1.2980	0.0730	0.0560	0.1310	0.00814	0.11	2	93.28	2.63	-		62.4	1	12/15/17
052815-2	DI	c48	3.1075	1.2750	0.0720	0.0500	1.3380	0.00814	0.11	2	68.45	2.10	-		59.3	1	12/15/17
052815-2	DI	c48	3.1075	1.2750	0.0720	0.0500	0.8380	0.00814	0.11	1ap	71.72	2.20	59.2		59.3	1	12/15/17
052815-2	DI	c48	3.1075	1.2750	0.0720	0.0500	0.8380	0.00814	0.11	1as	71.72	2.20	80.8		59.3	1	12/15/17
052815-2	DI	c48	3.1075	1.2750	0.0720	0.0500	0.8380	0.00814	0.11	1b	71.72	2.20	56.3		59.3	1	12/15/17
052815-2	DI	c48	3.1075	1.2750	0.0720	0.0500	0.8380	0.00814	0.11	1p	71.72	2.20	45.8		59.3	1	12/15/17
052815-2	DI	c48	3.1075	1.2750	0.0720	0.0500	0.8380	0.00814	0.11	1ws	71.72	2.20	45.5		59.3	1	12/15/17
052815-2	DI	c51	3.1150	1.2940	0.0740	0.0510	0.7970	0.00814	0.11	1p	88.55	2.57	57.6		62.1	1	12/15/17
052815-2	DI	c51	3.1150	1.2940	0.0740	0.0510	1.2970	0.00814	0.11	2	90.76	2.63	-		62.1	1	12/15/17
052815-2	DI	c51	3.1150	1.2940	0.0740	0.0510	0.7970	0.00814	0.11	1 s	88.55	2.57	52.0		62.1	1	12/15/17
052815-2	DI	c52	3.1170	1.2890	0.0740	0.0485	1.3275	0.00814	0.11	2	103.72	3.09	-		61.1	1	12/15/17
052815-2	DI	c52	3.1170	1.2890	0.0740	0.0485	0.8275	0.00814	0.11	1ap	104.28	3.11	74.5		61.1	1	12/15/17
052815-2	DI	c52	3.1170	1.2890	0.0740	0.0485	0.8275	0.00814	0.11	1as	104.28	3.11	65.8		61.1	1	12/15/17
052815-2	DI	c52	3.1170	1.2890	0.0740	0.0485	0.8275	0.00814	0.11	1p	104.28	3.11	82.4		61.1	1	12/15/17
052815-2	DI	c52	3.1170	1.2890	0.0740	0.0485	0.8275	0.00814	0.11	1ws	104.28	3.11	61.9		61.1	1	12/15/17
052815-2	DI	k	3.0700	1.3640	0.0835	0.0625	0.3000	0.00823	0.11	1	152.97	3.30	-		23.3	1	2/2/16
052815-2	DI	l	3.2020	1.3080	0.0520	0.0310	1.2170	0.00823	0.11	1	48.42	3.04	48.6		22.6	1	2/2/16
052815-2	DI	l	3.2020	1.3080	0.0520	0.0310	1.7170	0.00823	0.11	2	56.60	3.55	-		22.6	1	2/2/16
052815-2	DI	m	3.2030	1.3460	0.0700	0.0490	0.4180	0.00823	0.11	1	100.48	3.19	80.9		22.4	1	2/2/16
052815-2	DI	m	3.2030	1.3460	0.0700	0.0490	0.9418	0.00823	0.11	2	116.06	3.68	-		22.4	1	2/2/16
052815-2	DI	n	3.0950	1.3660	0.0385	0.0280	1.4750	0.00823	0.11	1a	28.44	2.86	LQ		22.1	1	2/2/16
052815-2	DI	o	3.2010	1.3445	0.0850	0.0530	0.7450	0.00823	0.11	1	118.46	2.72	115.8		21.7		2/2/16
052815-2	DI	o	3.2010	1.3445	0.0850	0.0530	1.2450	0.00823	0.11	2	130.41	3.00	-		21.7		2/2/16
052815-2	HCl	c04	2.9150	1.2810	0.0490	0.0340	1.7520	0.00776	0.11	2	38.13	2.38	-	pH 3.0	23.0	1	5/26/17
052815-2	HCl	c04	2.9150	1.2810	0.0490	0.0340	0.7520	0.00776	0.11	1a	37.12	2.31	66.9	pH 3.0	23.0	1	5/26/17
052815-2	HCl	c04	2.9150	1.2810	0.0490	0.0340	1.2520	0.00776	0.11	1b	37.12	2.31	84.4	pH 3.0	23.0	1	5/26/17
052815-2	HCl	c14	2.8750	1.2820	0.0895	0.0530	0.9160	0.00776	0.11	1	96.61	2.00	50.7	pH 3.0	22.2	1	5/26/17
052815-2	HCl	c14	2.8750	1.2820	0.0895	0.0530	1.4160	0.00776	0.11	2	98.52	2.04	29.2	pH 3.0	22.2	1	5/26/17
052815-2	HCl	c14	2.8750	1.2820	0.0895	0.0530	1.9160	0.00776	0.11	3	97.65	2.02	-	pH 3.0	22.2	1	5/26/17
052815-2	HCl	c15	2.9055	1.2780	0.0860	0.0860	-	0.00776	0.11	-	-	-	-	pH 3.0	RT	5	5/26/17
052815-2	HCl	c19	2.9450	1.2585	0.0550	0.0420	0.5240	0.00776	0.11	1	60.83	2.91	70.2	pH 3.0	22.1	1	5/26/17
052815-2	HCl	c19	2.9450	1.2585	0.0550	0.0420	1.0240	0.00776	0.11	2	42.01	2.01	-	pH 3.0	22.1	1	5/26/17

Sample	Envir.	Wafer	L (in.)	W (in.)	t (in.)	t_n (in.)	a_0 (in.)	W_m (m)	ν	#	Load (N)	K_{IC}* (MPa $m^{1/2}$)	SCI	Detail	Temp. (°C)	Notes†	Date
052815-2	HCl	c20	2.9430	1.2600	0.0695	0.0565	0.2030	0.00776	0.11	1	99.44	2.90	81.5	pH 3.0	22.8	1	5/26/17
052815-2	HCl	c20	2.9430	1.2600	0.0695	0.0565	0.7030	0.00776	0.11	2	82.06	2.40	-	pH 3.0	22.8	1	5/26/17
052815-2	NaOH	c17	3.2060	1.3025	0.0790	0.0630	0.6250	0.00776	0.11	1	104.88	2.36	64.0	pH 12.0	22.8	1	5/29/17
052815-2	NaOH	c17	3.2060	1.3025	0.0790	0.0630	1.1250	0.00776	0.11	2	106.99	2.41	35.7	pH 12.0	22.8	1	5/29/17
052815-2	NaOH	c17	3.2060	1.3025	0.0790	0.0630	1.6250	0.00776	0.11	3	122.68	2.76	-	pH 12.0	22.8	1	5/29/17
052815-2	NaOH	c22	2.9590	1.2425	0.0680	0.0440	0.5865	0.00776	0.11	1a	77.24	2.66	31.8	pH 12.0	22.1	1	5/29/17
052815-2	NaOH	c22	2.9590	1.2425	0.0680	0.0440	1.0865	0.00776	0.11	1b	77.24	2.66	25.3	pH 12.0	22.1	1	5/29/17
052815-2	NaOH	c23	2.9010	1.2895	0.0720	0.0530	0.6100	0.00776	0.11	1	77.90	2.20	78.0	pH 12.0	22.3	1	5/29/17
052815-2	NaOH	c23	2.9010	1.2895	0.0720	0.0530	1.1100	0.00776	0.11	2	80.70	2.28	16.5	pH 12.0	22.3	1	5/29/17
052815-2	NaOH	c23	2.9010	1.2895	0.0720	0.0530	1.6100	0.00776	0.11	3	70.29	1.99	32.1	pH 12.0	22.3	1	5/29/17
052815-2	NaOH	c23	2.9010	1.2895	0.0720	0.0530	2.1100	0.00776	0.11	4	83.80	2.37	-	pH 12.0	22.3	1	5/29/17
052815-2	NaOH	c24	2.9030	1.2785	0.0545	0.0390	0.6715	0.00776	0.11	1	42.32	2.11	48.6	pH 12.0	22.3	1	5/29/17
052815-2	NaOH	c24	2.9030	1.2785	0.0545	0.0390	1.1715	0.00776	0.11	2	45.18	2.25	60.1	pH 12.0	22.3	1	5/29/17
052815-2	NaOH	c24	2.9030	1.2785	0.0545	0.0390	1.6715	0.00776	0.11	3	46.22	2.30	-	pH 12.0	22.3	1	5/29/17
052815-2	NaOH	c25	2.9250	1.3895	0.0550	0.0380	1.0025	0.00776	0.11	2	60.52	2.89	61.4	pH 12.0	22.4	1	5/29/17
052815-2	NaOH	c25	2.9250	1.3895	0.0550	0.0380	1.5025	0.00776	0.11	3	62.84	3.00	56.0	pH 12.0	22.4	1	5/29/17
052815-2	NaOH	c25	2.9250	1.3895	0.0550	0.0380	2.0025	0.00776	0.11	4	52.75	2.51	-	pH 12.0	22.4	1	5/29/17
052815-2	NaOH	c25	2.9250	1.3895	0.0550	0.0380	0.5025	0.00776	0.11	1a	55.44	2.64	54.8	pH 12.0	22.4	1	5/29/17
052815-2	NaOH	c25	2.9250	1.3895	0.0550	0.0380	0.7525	0.00776	0.11	1b	55.44	2.64	63.5	pH 12.0	22.4	1	5/29/17
052815-2	NaOH	c25	2.9250	1.3895	0.0550	0.0380	0.5025	0.00776	0.11	1w	55.44	2.64	31.9	pH 12.0	22.4	1	5/29/17
052815-4b	amb.	24	3.0770	1.2550	0.0640	0.0450	0.6900	0.00763	0.18	1	62.90	2.36	133.2	69% RH	23.6	1	9/8/17
052815-4b	amb.	24	3.0770	1.2550	0.0640	0.0450	0.6900	0.00763	0.18	2	64.30	2.41	91.3	69% RH	23.6	1	9/8/17
052815-4b	amb.	26	3.0730	1.2230	0.0635	0.0475	1.4465	0.00763	0.18	1	61.20	2.29	135.6	69% RH	23.6	1	9/8/17
052815-4b	amb.	26	3.0730	1.2230	0.0635	0.0475	1.4465	0.00763	0.18	3	55.11	2.06	-	69% RH	23.6	1	9/8/17
052815-4b	amb.	26	3.0730	1.2230	0.0635	0.0475	1.4465	0.00763	0.18	2b	62.36	2.34	84.7	69% RH	23.6	1	9/8/17
052815-4b	amb.	27	3.0780	1.2580	0.0690	0.0530	0.6000	0.00763	0.18	1	74.29	2.30	96.8	69% RH	23.5	1	9/8/17
052815-4b	amb.	27	3.0780	1.2580	0.0690	0.0530	0.6000	0.00763	0.18	2	78.99	2.44	122.8	69% RH	23.5	1	9/8/17
052815-4b	amb.	27	3.0780	1.2580	0.0690	0.0530	0.6000	0.00763	0.18	3	81.64	2.52	-	69% RH	23.5	1	9/8/17
052815-4b	amb.	28	3.0775	1.2400	0.0855	0.0575	0.6550	0.00763	0.18	1	104.11	2.28	78.8	69% RH	23.4	1	9/8/17
052815-4b	amb.	28	3.0775	1.2400	0.0855	0.0575	0.6550	0.00763	0.18	2	102.01	2.23	-	69% RH	23.4	1	9/8/17
052815-4b	amb.	29	3.0770	1.2370	0.0950	0.0625	0.8080	0.00763	0.18	1	132.08	2.38	79.1	69% RH	23.4	1	9/8/17
052815-4b	amb.	29	3.0770	1.2370	0.0950	0.0625	0.8080	0.00763	0.18	2	153.05	2.76	-	69% RH	23.4	1	9/8/17
052815-4b	amb.	30	3.0760	1.2180	0.0925	0.0640	1.0395	0.00763	0.18	2	124.08	2.32	-	69% RH	23.6	1	9/8/17

Sample	Envir.	Wafer	L (in.)	W (in.)	t (in.)	t_n (in.)	a_0 (in.)	W_m (m)	ν	#	Load (N)	K_{IC}* (MPa $m^{1/2}$)	SCI	Detail	Temp. (°C)	Notes†	Date
052815-4b	amb.	30	3.0760	1.2180	0.0925	0.0640	1.0395	0.00763	0.18	1a	112.58	2.10	137.3	69% RH	23.6	1	9/8/17
052815-4b	amb.	30	3.0760	1.2180	0.0925	0.0640	1.0395	0.00763	0.18	1b	112.58	2.10	99.8	69% RH	23.6	1	9/8/17
052815-4b	amb.	31	3.0770	1.2250	0.0985	0.0650	0.3085	0.00763	0.18	1	142.40	2.40	118.9	69% RH	23.8	1	9/8/17
052815-4b	amb.	31	3.0770	1.2250	0.0985	0.0650	0.3085	0.00763	0.18	2	150.62	2.54	180.7	69% RH	23.8	1	9/8/17
052815-4b	amb.	31	3.0770	1.2250	0.0985	0.0650	0.3085	0.00763	0.18	3	156.42	2.64	-	69% RH	23.8	1	9/8/17
052815-4b	brine	12	2.9980	1.0800	0.0620	0.0475	0.3815	0.00767	0.18	1	60.24	2.51	46.5	0.1% NaCl	RT	1	8/28/17
052815-4b	brine	12	2.9980	1.0800	0.0620	0.0475	0.8815	0.00767	0.18	2	65.37	2.72	51.4	0.1% NaCl	RT	1	8/28/17
052815-4b	brine	12	2.9980	1.0800	0.0620	0.0475	1.3815	0.00767	0.18	3	63.46	2.64	51.7	0.1% NaCl	RT	1	8/28/17
052815-4b	brine	12	2.9980	1.0800	0.0620	0.0475	2.3815	0.00767	0.18	5	49.89	2.08	-	0.1% NaCl	RT	1	8/28/17
052815-4b	brine	12	2.9980	1.0800	0.0620	0.0475	1.8815	0.00767	0.18	4a	59.39	2.48	39.3	0.1% NaCl	RT	1	8/28/17
052815-4b	brine	12	2.9980	1.0800	0.0620	0.0475	1.8815	0.00767	0.18	4b	59.39	2.48	55.8	0.1% NaCl	RT	1	8/28/17
052815-4b	brine	15	3.0020	1.0800	0.0600	0.0440	0.6990	0.00767	0.18	1	51.69	2.35	70.0	0.1% NaCl	RT	1	8/28/17
052815-4b	brine	15	3.0020	1.0800	0.0600	0.0440	1.1990	0.00767	0.18	2	47.75	2.17	36.0	0.1% NaCl	RT	1	8/28/17
052815-4b	brine	15	3.0020	1.0800	0.0600	0.0440	1.6990	0.00767	0.18	3	32.45	LQ	-	0.1% NaCl	RT	1	8/28/17
052815-4b	brine	19	2.9850	1.0825	0.0620	0.0410	0.5000	0.00767	0.18	1	52.15	2.34	72.5	0.1% NaCl	RT	3	8/28/17
052815-4b	brine	19	2.9850	1.0825	0.0620	0.0410	1.0000	0.00767	0.18	2	58.96	2.64	89.8	0.1% NaCl	RT	3	8/28/17
052815-4b	brine	19	2.9850	1.0825	0.0620	0.0410	1.5000	0.00767	0.18	3	68.07	3.05	-	0.1% NaCl	RT	3	8/28/17
052815-4b	brine	21	2.9830	1.0805	0.0760	0.0560	0.3020	0.00767	0.18	1	78.78	2.25	69.5	0.1% NaCl	RT	1	8/28/17
052815-4b	brine	21	2.9830	1.0805	0.0760	0.0560	0.8020	0.00767	0.18	2	75.13	2.14	89.1	0.1% NaCl	RT	1	8/28/17
052815-4b	brine	21	2.9830	1.0805	0.0760	0.0560	1.3020	0.00767	0.18	3	93.11	2.66	58.5	0.1% NaCl	RT	1	8/28/17
052815-4b	brine	21	2.9830	1.0805	0.0760	0.0560	1.8020	0.00767	0.18	4	96.36	2.75	96.5	0.1% NaCl	RT	1	8/28/17
052815-4b	brine	21	2.9830	1.0805	0.0760	0.0560	2.3020	0.00767	0.18	5	102.99	2.94	-	0.1% NaCl	RT	1	8/28/17
052815-4b	DI	1	2.9940	1.0790	0.0720	0.0480	0.2040	0.00756	0.18	1	89.22	2.93	LQ	pH 7.0-6.9	23.1	1	8/23/17
052815-4b	DI	1	2.9940	1.0790	0.0720	0.0480	0.7040	0.00756	0.18	2	94.44	3.11	LQ	pH 7.0-6.9	23.1	1	8/23/17
052815-4b	DI	1	2.9940	1.0790	0.0720	0.0480	1.2040	0.00756	0.18	3	83.33	2.74	LQ	pH 7.0-6.9	23.1	1	8/23/17
052815-4b	DI	1	2.9940	1.0790	0.0720	0.0480	1.7040	0.00756	0.18	4	76.64	2.52	-	pH 7.0-6.9	23.1	1	8/23/17
052815-4b	DI	2	3.0060	1.0790	0.0640	0.0500	0.1870	0.00756	0.18	1	59.62	2.28	127.5	pH 7.2	23.5	1	8/23/17
052815-4b	DI	2	3.0060	1.0790	0.0640	0.0500	0.6870	0.00756	0.18	2	70.99	2.72	118.5	pH 7.2	23.5	1	8/23/17
052815-4b	DI	2	3.0060	1.0790	0.0640	0.0500	1.1870	0.00756	0.18	3	70.07	2.68	-	pH 7.2	23.5	1	8/23/17
052815-4b	DI	3	3.0030	1.0790	0.0910	0.0670	0.6325	0.00756	0.18	1	131.40	2.61	99.4	pH 7.1	23.0	1	8/23/17
052815-4b	DI	3	3.0030	1.0790	0.0910	0.0670	1.1325	0.00756	0.18	2	145.94	2.89	LQ	pH 7.1	23.0	1	8/23/17
052815-4b	DI	3	3.0030	1.0790	0.0910	0.0670	1.6325	0.00756	0.18	3	145.11	2.88	-	pH 7.1	23.0	1	8/23/17
052815-4b	DI	4	2.9900	1.0790	0.0650	0.0450	0.4660	0.00756	0.18	1	65.47	2.58	-	pH 7.1	23.5	2	8/23/17

Sample	Envir.	Wafer	L (in.)	W (in.)	t (in.)	t_n (in.)	a_0 (in.)	W_m (m)	ν	#	Load (N)	K_{IC}* (MPa $m^{1/2}$)	SCI	Detail	Temp. (°C)	Notes†	Date
052815-4b	DI	5	2.9870	1.0780	0.0730	0.0580	0.9400	0.00756	0.18	2	74.00	LQ	LQ	pH 7.1	23.4	1	8/23/17
052815-4b	DI	5	2.9870	1.0780	0.0730	0.0580	1.4400	0.00756	0.18	3	73.96	2.17	121.3	pH 7.1	23.4	1	8/23/17
052815-4b	DI	5	2.9870	1.0780	0.0730	0.0580	1.9400	0.00756	0.18	4	80.87	2.37	118.2	pH 7.1	23.4	1	8/23/17
052815-4b	DI	5	2.9870	1.0780	0.0730	0.0580	2.4400	0.00756	0.18	5	75.82	2.22	-	pH 7.1	23.4	1	8/23/17
052815-4b	DI	5	2.9870	1.0780	0.0730	0.0580	0.4400	0.00756	0.18	1a	80.66	2.37	94.5	pH 7.1	23.4	1	8/23/17
052815-4b	DI	5	2.9870	1.0780	0.0730	0.0580	0.4400	0.00756	0.18	1b	80.66	2.37	64.9	pH 7.1	23.4	1	8/23/17
052815-4b	HCl	6	3.0080	1.0790	0.0590	0.0460	0.9940	0.00756	0.18	1	47.35	LQ	LQ	pH 3.0	23.4	1	8/24/17
052815-4b	HCl	6	3.0080	1.0790	0.0590	0.0460	1.4940	0.00756	0.18	2	58.18	2.61	-	pH 3.0	23.4	1	8/24/17
052815-4b	HCl	7	3.0780	1.2495	0.0740	0.0540	1.1080	0.00756	0.18	1	71.75	1.97	110.7	pH 3.0	22.2	1	8/24/17
052815-4b	HCl	7	3.0780	1.2495	0.0740	0.0540	1.6080	0.00756	0.18	2	72.51	1.99	-	pH 3.0	22.2	1	8/24/17
052815-4b	HCl	8	3.0760	1.2480	0.0890	0.0650	0.5420	0.00756	0.18	1	91.39	LQ	LQ	pH 3.0	22.4	1	8/24/17
052815-4b	HCl	8	3.0760	1.2480	0.0890	0.0650	1.0420	0.00756	0.18	2	107.88	2.07	70.2	pH 3.0	22.4	1	8/24/17
052815-4b	HCl	8	3.0760	1.2480	0.0890	0.0650	0.5420	0.00756	0.18	3	112.70	2.16	-	pH 3.0	22.4	1	8/24/17
052815-4b	HCl	9	3.0755	1.2530	0.0745	0.0550	1.2070	0.00756	0.18	1	63.04	1.70	-	pH 3.0	22.2	1	8/24/17
052815-4b	HCl	10	3.0740	1.2250	0.0655	0.0520	0.3500	0.00756	0.18	1	54.24	1.84	89.0	pH 3.0	22.1	1	8/24/17
052815-4b	HCl	10	3.0740	1.2250	0.0655	0.0520	0.8500	0.00756	0.18	2	52.96	1.79	-	pH 3.0	22.1	1	8/24/17
052815-4b	HCl	16	3.0150	1.0795	0.0530	0.0360	0.2700	0.00756	0.18	2	44.95	2.67	141.4	pH 3.0	22.0	1	8/24/17
052815-4b	HCl	16	3.0150	1.0795	0.0530	0.0360	0.2700	0.00756	0.18	3	47.50	2.82	-	pH 3.0	22.0	1	8/24/17
052815-4b	HCl	16	3.0150	1.0795	0.0530	0.0360	0.2700	0.00756	0.18	1a	47.44	2.82	LQ	pH 3.0	22.0	1	8/24/17
052815-4b	HCl	16	3.0150	1.0795	0.0530	0.0360	0.2700	0.00756	0.18	1b	47.44	2.82	67.3	pH 3.0	22.0	1	8/24/17
052815-4b	HCl	22	3.0740	1.2220	0.0745	0.0460	0.5000	0.00756	0.18	1	84.46	2.52	75.1	pH 3.0	22.7	1	8/24/17
052815-4b	HCl	22	3.0740	1.2220	0.0745	0.0460	0.5000	0.00756	0.18	2	88.27	2.64	75.1	pH 3.0	22.7	1	8/24/17
052815-4b	HCl	22	3.0740	1.2220	0.0745	0.0460	0.5000	0.00756	0.18	3	81.89	2.45	-	pH 3.0	22.7	1	8/24/17
052815-4b	NaOH	13	2.9980	1.0800	0.0640	0.0495	1.2920	0.00756	0.18	1	64.80	2.49	62.9	pH 12.0	22.6	1	8/25/17
052815-4b	NaOH	14	3.0095	1.0810	0.0910	0.0660	0.5110	0.00756	0.18	1	139.89	2.79	-	pH 12.0	22.6	2	8/25/17
052815-4b	NaOH	17	2.9860	1.0780	0.0635	0.0395	0.4325	0.00756	0.18	1	64.81	2.82	-	pH 12.0	22.3	2	8/25/17
052815-4b	NaOH	18	3.0045	1.0800	0.0685	0.0450	0.7920	0.00756	0.18	1	71.33	2.60	-	pH 12.0	22.6	1	8/25/17
052815-4b	NaOH	20	2.9850	1.0820	0.0585	0.0400	1.2850	0.00756	0.18	1	49.01	2.39	82.5	pH 12.0	22.2	1	8/25/17
052815-4b	NaOH	20	2.9850	1.0820	0.0585	0.0400	1.7850	0.00756	0.18	2	53.04	2.58	-	pH 12.0	22.2	1	8/25/17
052815-4b	NaOH	23	3.0765	1.2455	0.0870	0.0575	0.9460	0.00756	0.18	2	103.81	2.19	86.0	pH 12.0	22.1	2	8/25/17
052815-4b	NaOH	23	3.0765	1.2455	0.0870	0.0575	1.4460	0.00756	0.18	3	115.43	2.44	56.2	pH 12.0	22.1	2	8/25/17
052815-4b	NaOH	23	3.0765	1.2455	0.0870	0.0575	0.4460	0.00756	0.18	1a	112.72	2.38	37.6	pH 12.0	22.1	2	8/25/17
052815-4b	NaOH	23	3.0765	1.2455	0.0870	0.0575	0.4460	0.00756	0.18	1b	112.72	2.38	68.8	pH 12.0	22.1	2	8/25/17

Sample	Envir.	Wafer	L (in.)	W (in.)	t (in.)	t_n (in.)	a_0 (in.)	W_m (m)	ν	#	Load (N)	K_{IC}* (MPa $m^{1/2}$)	SCI	Detail	Temp. (°C)	Notes†	Date
052815-4b	NaOH	25	3.0750	1.2210	0.0890	0.0605	0.7930	0.00756	0.18	2	119.30	2.40	-	pH 12.0	22.2	1	8/25/17
052815-4b	NaOH	25	3.0750	1.2210	0.0890	0.0605	0.2930	0.00756	0.18	1a	129.12	2.60	55.8	pH 12.0	22.2	1	8/25/17
052815-4b	NaOH	25	3.0750	1.2210	0.0890	0.0605	0.2930	0.00756	0.18	1b	129.12	2.60	41.6	pH 12.0	22.2	1	8/25/17
061114-4b	DI	i	2.9580	1.3750	0.0775	0.0530	-	0.00823	0.13	-	-	-	-		RT	5	11/28/17
061114-4b	DI	m	2.9735	1.3770	0.0845	0.0600	0.3670	0.00772	0.13	1	147.11	3.00	110.9		21.7	1	11/28/17
061114-4b	DI	m	2.9735	1.3770	0.0845	0.0600	0.8670	0.00772	0.13	2	153.50	3.13	181.9		21.7	1	11/28/17
061114-4b	DI	m	2.9735	1.3770	0.0845	0.0600	1.3670	0.00772	0.13	3	156.90	3.20	162.1		21.7	1	11/28/17
061114-4b	DI	m	2.9735	1.3770	0.0845	0.0600	1.8670	0.00772	0.13	4	161.66	3.30	-		21.7	1	11/28/17
061114-4b	DI	o	2.9890	1.3485	0.0800	0.0510	0.4585	0.00772	0.13	1	101.91	2.47	79.5	pH 7.2	21.7	1	11/28/17
061114-4b	DI	o	2.9890	1.3485	0.0800	0.0510	0.9585	0.00772	0.13	2	109.15	2.65	-	pH 7.2	21.7	1	11/28/17
061114-4b	DI	p	2.9350	1.3780	0.0675	0.0470	0.4585	0.00772	0.13	1	82.12	2.63	152.1	pH 7.5	21.7	1	11/28/17
061114-4b	DI	p	2.9350	1.3780	0.0675	0.0470	0.9585	0.00772	0.13	2	82.18	2.63	-	pH 7.5	21.7	1	11/28/17
061114-4b	DI	q	2.9840	1.3485	0.0840	0.0480	0.8350	0.00772	0.13	1	96.82	2.25	-	pH 6.7	22.0	1	11/29/17
061114-4b	DI	t	2.9000	1.3500	0.0860	0.0510	0.9310	0.00772	0.13	1	84.68	1.85	41.4	pH 7.2	21.4	1	11/29/17
061114-4b	DI	t	2.9000	1.3500	0.0860	0.0510	1.4310	0.00772	0.13	2	95.49	2.08	-	pH 7.2	21.4	1	11/29/17
061114-4b	DI	y	2.9540	1.2760	0.0355	0.0320	0.2015	0.00772	0.13	1	23.62	2.46	42.5	pH 7.4	21.6	1	11/29/17
061114-4b	DI	y	2.9540	1.2760	0.0355	0.0320	0.7015	0.00772	0.13	2	23.84	2.48	33.2	pH 7.4	21.6	1	11/29/17
061114-4b	DI	y	2.9540	1.2760	0.0355	0.0320	1.2015	0.00772	0.13	3	23.11	2.41	50.0	pH 7.4	21.6	1	11/29/17
061114-4b	DI	y	2.9540	1.2760	0.0355	0.0320	1.7015	0.00772	0.13	4	24.80	2.58	59.3	pH 7.4	21.6	1	11/29/17
061114-4b	DI	y	2.9540	1.2760	0.0355	0.0320	2.2015	0.00772	0.13	5	26.43	2.75	51.5	pH 7.4	21.6	1	11/29/17
061114-4b	DI	y	2.9540	1.2760	0.0355	0.0320	2.7015	0.00772	0.13	6	23.42	2.44	75.1	pH 7.4	21.6	1	11/29/17
061114-4b	NaOH	aa	2.9360	1.2735	0.0660	0.0510	0.6260	0.00772	0.13	1	55.01	1.82	46.3	pH 11.7	21.3	1	12/1/17
061114-4b	NaOH	aa	2.9360	1.2735	0.0660	0.0510	1.1260	0.00772	0.13	2	41.34	LQ	55.3	pH 11.7	21.3	1	12/1/17
061114-4b	NaOH	aa	2.9360	1.2735	0.0660	0.0510	1.6260	0.00772	0.13	3	33.41	LQ	-	pH 11.7	21.3	1	12/1/17
061114-4b	NaOH	ab	2.9500	1.2760	0.0690	0.0345	0.6705	0.00772	0.13	1	40.75	1.54	34.6	pH 12.0	21.2	1	12/1/17
061114-4b	NaOH	ab	2.9500	1.2760	0.0690	0.0345	1.1705	0.00772	0.13	2	29.94	LQ	-	pH 12.0	21.2	1	12/1/17
061114-4b	NaOH	ac	2.9670	1.2780	0.0660	0.0450	0.3880	0.00772	0.13	1	67.19	2.36	34.8	pH 12.1	21.2	3	12/1/17
061114-4b	NaOH	ac	2.9670	1.2780	0.0660	0.0450	0.8880	0.00772	0.13	2	49.80	LQ	LQ	pH 12.1	21.2	3	12/1/17
061114-4b	NaOH	ac	2.9670	1.2780	0.0660	0.0450	1.3880	0.00772	0.13	3	41.12	LQ	-	pH 12.1	21.2	3	12/1/17
061114-4b	NaOH	n	2.9770	1.3790	0.0890	0.0655	0.6505	0.00772	0.13	1	179.96	3.25	-	pH 12.0	21.2	1	12/1/17
061114-4b	NaOH	r	2.9580	1.2785	0.0870	0.0560	1.5310	0.00772	0.13	2	53.20	LQ	-	pH 12.0	21.2	1	12/1/17
061114-4b	NaOH	r	2.9580	1.2785	0.0870	0.0560	0.5310	0.00772	0.13	1a	90.48	1.91	21.2	pH 12.0	21.2	1	12/1/17
061114-4b	NaOH	r	2.9580	1.2785	0.0870	0.0560	1.0310	0.00772	0.13	1b	-	-	10.1	pH 12.0	21.2	1	12/1/17

Sample	Envir.	Wafer	L (in.)	W (in.)	t (in.)	t_n (in.)	a_0 (in.)	W_m (m)	ν	#	Load (N)	K_{IC}* (MPa $m^{1/2}$)	SCI	Detail	Temp. (°C)	Notes†	Date
061114-4b	NaOH	x	2.9390	1.2730	0.0695	0.0410	0.2760	0.00772	0.13	1	68.77	2.35	70.8	pH 12.1	22.0	3	11/29/17
061114-4b	NaOH	x	2.9390	1.2730	0.0695	0.0410	0.7760	0.00772	0.13	2	68.82	2.36	40.4	pH 12.1	22.0	3	11/29/17
061114-4b	NaOH	x	2.9390	1.2730	0.0695	0.0410	1.2760	0.00772	0.13	3	62.52	2.14	92.7	pH 12.1	22.0	3	11/29/17
061114-4b	NaOH	x	2.9390	1.2730	0.0695	0.0410	1.7760	0.00772	0.13	4	55.24	LQ	-	pH 12.1	22.0	3	11/29/17
061114-4b	NaOH	z	2.9650	1.2770	0.0670	0.0530	0.4440	0.00772	0.13	1	68.91	2.19	33.9	pH 11.8	22.0	1	11/29/17
061114-4b	NaOH	z	2.9650	1.2770	0.0670	0.0530	0.9440	0.00772	0.13	2	54.06	1.71	43.8	pH 11.8	22.0	1	11/29/17
061114-4b	NaOH	z	2.9650	1.2770	0.0670	0.0530	1.4440	0.00772	0.13	3	55.24	1.75	-	pH 11.8	22.0	1	11/29/17
090114-5b	amb.	A	3.1110	1.3715	0.0695	0.0380	0.7030	0.00756	0.18	1	74.74	2.55	-	81% RH	23.5	1	8/16/17
090114-5b	amb.	B	3.1070	1.3650	0.0690	0.0470	0.4200	0.00756	0.18	1	77.23	2.40	-	79.5% RH	23.5	3	8/16/17
090114-5b	amb.	C	3.1150	1.3795	0.0820	0.0590	1.1450	0.00756	0.18	1	76.31	1.64	-	79% RH	23.3	1	8/16/17
090114-5b	amb.	D	3.1190	1.3850	0.0840	0.0580	0.7710	0.00756	0.18	1	104.18	2.17	87.6	79% RH	23.5	1	8/16/17
090114-5b	amb.	E	3.0990	1.3540	0.0820	0.0580	0.5635	0.00756	0.18	1	87.74	1.92	54.3	79% RH	23.5	1	8/16/17
090114-5b	amb.	E	3.0990	1.3540	0.0820	0.0580	1.0635	0.00756	0.18	2	84.21	1.84	-	79% RH	23.5	1	8/16/17
090114-5b	amb.	F	3.1020	1.3600	0.0690	0.0470	0.5240	0.00756	0.18	1	69.63	2.17	91.2	79% RH	23.5	1	8/16/17
090114-5b	-	G	3.1380	1.4340	0.0820	0.0470	-	0.00756	0.18	-	-	-	-	-	RT	4	8/16/17

H. Appendix: Structural Measurements from Dixie Comstock Epithermal Deposit

Table H.1. Measurement Identification, Location, Orientation, and Classification

ID	Date	Northing (m)	Easting (m)	Elevation (m)	Strike	Dip	Plunge	Trend	Classification	GIS ID
1	3/8/14	4414078	412867	1141	232	77			qtz - breccia/stockwork	Q
2	3/8/14	4414134	412801	1181	245	85			fault - unclassified	P
3	3/8/14	4414230	412812	1184	287	46	37	060	fault - with minor mineralized slickensides	O
4	3/8/14	4414308	412720	1167	030	71			dikes - basalt	N2
5	3/8/14	4414339	412726	1164	288	84			fracture - with minor oxide/sulfide	N1
6	3/11/14	4412715	412731	1139	198	90	65	198	fault - silicified breccias and gouge	T
7	3/11/14	4412731	412827	1101	347	35			qtz - breccia/stockwork	80
8	3/11/14	4412781	412653	1183	015	74			fracture - unmineralized, partially open	S
9	3/11/14	4412852	412618	1199	342	74	15	158	fault - with minor mineralized slickensides	R
10	3/11/14	4412852	412618	1199	345	88	35	164	fault - with minor mineralized slickensides	R
11	6/10/14	4413845	412881	1132	340	52	27	136	fault - with minor mineralized slickensides	AB
12	6/10/14	4413881	412869	1144	039	69	62	172	qtz vein - unclassified	79
13	6/10/14	4413881	412869	1144	018	58			qtz vein - unclassified	79
14	6/10/14	4413891	412903	1130	027	26	25	132	fault - silicified breccias and gouge	77
15	6/10/14	4413891	412903	1130	341	72			fault - with minor mineralized slickensides	77
16	6/10/14	4413893	412835	1161	345	46			fault - silicified breccias and gouge	9
17	6/10/14	4413893	412835	1161	025	90			fracture - unmineralized, partially open	9
18	6/10/14	4413893	412835	1161	037	90			fracture - unmineralized, partially open	9
19	6/10/14	4413893	412835	1161	018	72			fracture - unmineralized, partially open	9
20	6/10/14	4414078	412867	1141	328	87	59	143	fault - with minor mineralized slickensides	Q
21	6/10/14	4414170	412784	1193	010	29	24	137	fault - silicified breccias and gouge	3

ID	Date	Northing (m)	Easting (m)	Elevation (m)	Strike	Dip	Plunge	Trend	Classification	GIS ID
22	6/10/14	4414170	412784	1193	044	50			qtz - druzy/prismatic	3
23	6/11/14	4412367	412879	1095	354	84			fault - unmineralized (loose gouge)	U
24	6/11/14	4412367	412879	1095	000	63			fault - unmineralized (loose gouge)	U
26	6/11/14	4412367	412879	1095	326	62			fracture - with sulfate (gypsum, jarosite)	U
25	6/11/14	4412367	412879	1095	246	38			qtz vein - unclassified	U
27	6/11/14	4412367	412879	1095	218	66			qtz vein - unclassified	U
28	6/11/14	4412370	412807	1130	023	78			fracture - with sulfate (gypsum, jarosite)	AC
29	6/11/14	4412370	412807	1130	205	49			fracture - with sulfate (gypsum, jarosite)	AC
35	6/11/14	4412583	412828	1102	322	67			cal w/hematite, gouge	V
30	6/11/14	4412583	412828	1102	323	70			calcite - unclassified	V
31	6/11/14	4412583	412828	1102	045	58			calcite - unclassified	V
32	6/11/14	4412583	412828	1102	108	67			calcite - unclassified	V
33	6/11/14	4412583	412828	1102	322	67			calcite - unclassified	V
36	6/11/14	4412583	412828	1102	010	83			calcite - unclassified	V
34	6/11/14	4412583	412828	1102	354	62			qtz vein - unclassified	V
37	6/11/14	4412662	412806	1127	010	48			fracture - with minor oxide/sulfide	AD
38	6/11/14	4412662	412806	1127	035	90			qtz - breccia/stockwork	AD
39	6/11/14	4412731	412827	1101	016	72			qtz - breccia/stockwork	80
40	6/11/14	4412731	412827	1101	040	60			qtz - breccia/stockwork	80
41	6/11/14	4412731	412827	1101	156	90	63	156	qtz - breccia/stockwork	80
43	6/11/14	4412731	412827	1101	170	80			qtz - breccia/stockwork	80
44	6/11/14	4412731	412827	1101	350	75			qtz - breccia/stockwork	80
42	6/11/14	4412731	412827	1101	198	90			qtz w/calcite	80
45	6/11/14	4413017	412827	1109	355	75			qtz - druzy/prismatic	AAA
46	6/11/14	4413062	412877	1101	002	44			qtz - chalcedony	AE

ID	Date	Northing (m)	Easting (m)	Elevation (m)	Strike	Dip	Plunge	Trend	Classification	GIS ID
47	6/11/14	4413099	412872	1111	018	38	38	115	fault - silicified breccias and gouge	AF
48	6/11/14	4413099	412872	1111	022	43			fault - silicified breccias and gouge	AF
49	6/11/14	4413099	412872	1111	038	33			fault - silicified breccias and gouge	AF
50	6/11/14	4413344	412987	1081	359	49			fault - silicified breccias and gouge	AG
51	6/12/14	4413213	412827	1139	027	55			qtz - breccia/stockwork	AAB
52	6/12/14	4413371	412880	1132	020	28	23	146	fault - with minor mineralized slickensides	AAC
53	6/12/14	4413371	412880	1132	337	71			qtz vein - unclassified	AAC
54	6/12/14	4413371	412880	1132	084	74			qtz vein - unclassified	AAC
55	6/12/14	4413393	412920	1111	010	56	24	173	fault - with minor mineralized slickensides	AAD
56	6/12/14	4413393	412920	1111	014	87			qtz - chalcedony	AAD
57	6/12/14	4413470	412974	1098	012	39			fault - silicified breccias and gouge	AAE
58	6/12/14	4413470	412974	1098	000	52	45	128	fault - silicified breccias and gouge	AAE
59	6/12/14	4413523	412983	1094	008	44	39	131	fault - silicified breccias and gouge	Y
60	6/12/14	4413523	412983	1094	006	45			fault - silicified breccias and gouge	Y
61	6/12/14	4413523	412983	1094	350	45			fault - silicified breccias and gouge	Y
62	6/12/14	4413523	412983	1094	345	55			fault - silicified breccias and gouge	Y
78	8/31/14	4412731	412827	1101	171	65			cal w/hematite, gouge	80
79	8/31/14	4412731	412827	1101	345	90			cal w/hematite, gouge	80
87	8/31/14	4412731	412827	1101	335	88			cal w/hematite, gouge	80
106	8/31/14	4412731	412827	1101	315	57			cal w/hematite, gouge	80
70	8/31/14	4412731	412827	1101	267	16			calcite - unclassified	80
72	8/31/14	4412731	412827	1101	234	53			calcite - unclassified	80
81	8/31/14	4412731	412827	1101	225	70			calcite - unclassified	80
82	8/31/14	4412731	412827	1101	230	82			calcite - unclassified	80
84	8/31/14	4412731	412827	1101	024	40			calcite - unclassified	80

ID	Date	Northing (m)	Easting (m)	Elevation (m)	Strike	Dip	Plunge	Trend	Classification	GIS ID
85	8/31/14	4412731	412827	1101	236	74			calcite - unclassified	80
86	8/31/14	4412731	412827	1101	005	87			calcite - unclassified	80
88	8/31/14	4412731	412827	1101	242	55			calcite - unclassified	80
89	8/31/14	4412731	412827	1101	046	79			calcite - unclassified	80
91	8/31/14	4412731	412827	1101	140	74			calcite - unclassified	80
92	8/31/14	4412731	412827	1101	195	78			calcite - unclassified	80
93	8/31/14	4412731	412827	1101	148	70			calcite - unclassified	80
94	8/31/14	4412731	412827	1101	165	64			calcite - unclassified	80
105	8/31/14	4412731	412827	1101	000	54			calcite - unclassified	80
110	8/31/14	4412731	412827	1101	081	72			calcite - unclassified	80
111	8/31/14	4412731	412827	1101	359	53			calcite - unclassified	80
112	8/31/14	4412731	412827	1101	007	78			calcite - unclassified	80
113	8/31/14	4412731	412827	1101	000	90			calcite - unclassified	80
114	8/31/14	4412731	412827	1101	323	77			calcite - unclassified	80
80	8/31/14	4412731	412827	1101	042	43			fault - unmineralized (loose gouge)	80
115	8/31/14	4412731	412827	1101	141	50			fault - unmineralized (loose gouge)	80
63	8/31/14	4412731	412827	1101	328	69			qtz - breccia/stockwork	80
64	8/31/14	4412731	412827	1101	160	72	70	220	qtz - breccia/stockwork	80
95	8/31/14	4412731	412827	1101	168	65			qtz - breccia/stockwork	80
109	8/31/14	4412731	412827	1101	019	53			qtz - breccia/stockwork	80
116	8/31/14	4412731	412827	1101	028	79			qtz - breccia/stockwork	80
66	8/31/14	4412731	412827	1101	357	52			qtz - druzy/prismatic	80
71	8/31/14	4412731	412827	1101	328	39			qtz - druzy/prismatic	80
77	8/31/14	4412731	412827	1101	006	44			qtz - druzy/prismatic	80
90	8/31/14	4412731	412827	1101	004	62			qtz - druzy/prismatic	80

ID	Date	Northing (m)	Easting (m)	Elevation (m)	Strike	Dip	Plunge	Trend	Classification	GIS ID
97	8/31/14	4412731	412827	1101	156	60			qtz - druzy/prismatic	80
99	8/31/14	4412731	412827	1101	149	72			qtz - druzy/prismatic	80
108	8/31/14	4412731	412827	1101	337	68			qtz - druzy/prismatic	80
65	8/31/14	4412731	412827	1101	355	50			qtz vein - unclassified	80
96	8/31/14	4412731	412827	1101	050	55			qtz vein - unclassified	80
98	8/31/14	4412731	412827	1101	010	52			qtz vein - unclassified	80
100	8/31/14	4412731	412827	1101	015	58			qtz vein - unclassified	80
101	8/31/14	4412731	412827	1101	190	54			qtz vein - unclassified	80
102	8/31/14	4412731	412827	1101	180	36			qtz vein - unclassified	80
103	8/31/14	4412731	412827	1101	025	66			qtz vein - unclassified	80
104	8/31/14	4412731	412827	1101	021	81			qtz vein - unclassified	80
107	8/31/14	4412731	412827	1101	002	72			qtz vein - unclassified	80
67	8/31/14	4412731	412827	1101	168	82			qtz w/calcite	80
68	8/31/14	4412731	412827	1101	231	51			qtz w/calcite	80
69	8/31/14	4412731	412827	1101	344	87			qtz w/calcite	80
73	8/31/14	4412731	412827	1101	138	87			qtz w/calcite	80
74	8/31/14	4412731	412827	1101	224	59			qtz w/calcite	80
75	8/31/14	4412731	412827	1101	213	57			qtz w/calcite	80
76	8/31/14	4412731	412827	1101	218	67			qtz w/calcite	80
83	8/31/14	4412731	412827	1101	043	87			qtz w/calcite	80
130	8/31/14	4413881	412869	1144	042	70			calcite - unclassified	79
117	8/31/14	4413881	412869	1144	022	89			fault - unmineralized (loose gouge)	79
129	8/31/14	4413881	412869	1144	026	77			fault - with minor mineralized slickensides	79
132	8/31/14	4413881	412869	1144	005	70			fault - with minor mineralized slickensides	79
121	8/31/14	4413881	412869	1144	012	82			qtz - breccia/stockwork	79

ID	Date	Northing (m)	Easting (m)	Elevation (m)	Strike	Dip	Plunge	Trend	Classification	GIS ID
125	8/31/14	4413881	412869	1144	037	86			qtz - breccia/stockwork	79
151	8/31/14	4413881	412869	1144	023	59			qtz - breccia/stockwork	79
119	8/31/14	4413881	412869	1144	012	77			qtz - druzy/prismatic	79
120	8/31/14	4413881	412869	1144	024	75			qtz - druzy/prismatic	79
126	8/31/14	4413881	412869	1144	356	82			qtz - druzy/prismatic	79
131	8/31/14	4413881	412869	1144	015	78			qtz - druzy/prismatic	79
134	8/31/14	4413881	412869	1144	004	39			qtz - druzy/prismatic	79
135	8/31/14	4413881	412869	1144	008	40			qtz - druzy/prismatic	79
136	8/31/14	4413881	412869	1144	008	39			qtz - druzy/prismatic	79
138	8/31/14	4413881	412869	1144	002	59			qtz - druzy/prismatic	79
140	8/31/14	4413881	412869	1144	209	81			qtz - druzy/prismatic	79
141	8/31/14	4413881	412869	1144	004	59			qtz - druzy/prismatic	79
142	8/31/14	4413881	412869	1144	024	82			qtz - druzy/prismatic	79
143	8/31/14	4413881	412869	1144	045	78			qtz - druzy/prismatic	79
144	8/31/14	4413881	412869	1144	060	58			qtz - druzy/prismatic	79
145	8/31/14	4413881	412869	1144	214	84			qtz - druzy/prismatic	79
146	8/31/14	4413881	412869	1144	222	90			qtz - druzy/prismatic	79
149	8/31/14	4413881	412869	1144	182	87			qtz - druzy/prismatic	79
150	8/31/14	4413881	412869	1144	033	65			qtz - druzy/prismatic	79
153	8/31/14	4413881	412869	1144	019	85			qtz - druzy/prismatic	79
154	8/31/14	4413881	412869	1144	068	78			qtz - druzy/prismatic	79
155	8/31/14	4413881	412869	1144	033	51			qtz - druzy/prismatic	79
158	8/31/14	4413881	412869	1144	011	53			qtz - druzy/prismatic	79
118	8/31/14	4413881	412869	1144	036	72			qtz vein - unclassified	79
122	8/31/14	4413881	412869	1144	350	80			qtz vein - unclassified	79

ID	Date	Northing (m)	Easting (m)	Elevation (m)	Strike	Dip	Plunge	Trend	Classification	GIS ID
123	8/31/14	4413881	412869	1144	177	82			qtz vein - unclassified	79
124	8/31/14	4413881	412869	1144	053	80			qtz vein - unclassified	79
127	8/31/14	4413881	412869	1144	229	71			qtz vein - unclassified	79
128	8/31/14	4413881	412869	1144	042	69			qtz vein - unclassified	79
147	8/31/14	4413881	412869	1144	015	78			qtz vein - unclassified	79
148	8/31/14	4413881	412869	1144	059	65			qtz vein - unclassified	79
152	8/31/14	4413881	412869	1144	018	78			qtz vein - unclassified	79
133	8/31/14	4413881	412869	1144	346	32			qtz w/calcite	79
137	8/31/14	4413881	412869	1144	352	46			qtz w/calcite	79
139	8/31/14	4413881	412869	1144	042	80			qtz w/calcite	79
156	8/31/14	4413881	412869	1144	024	42			qtz w/calcite	79
157	8/31/14	4413881	412869	1144	023	47			qtz w/calcite	79
163	9/1/14	4413123	412884	1100	350	50			fault - unmineralized (loose gouge)	X
164	9/1/14	4413123	412884	1100	039	32			fault - unmineralized (loose gouge)	X
165	9/1/14	4413123	412884	1100	000	44			fault - unmineralized (loose gouge)	X
159	9/1/14	4413123	412884	1100	309	59			fracture - unmineralized, partially open	X
160	9/1/14	4413123	412884	1100	319	65			fracture - unmineralized, partially open	X
161	9/1/14	4413123	412884	1100	332	78			fracture - unmineralized, partially open	X
162	9/1/14	4413123	412884	1100	006	65			fracture - unmineralized, partially open	X
166	9/1/14	4413123	412884	1100	135	50			qtz - druzy/prismatic	X
167	9/1/14	4413123	412884	1100	134	64			qtz - druzy/prismatic	X
168	9/1/14	4413123	412884	1100	117	42			qtz - druzy/prismatic	X
169	9/1/14	4413123	412884	1100	189	74			qtz - druzy/prismatic	X
170	9/1/14	4413523	412983	1094	356	40			fault - silicified breccias and gouge	Y
171	9/1/14	4413523	412983	1094	357	54			fault - silicified breccias and gouge	Y

ID	Date	Northing (m)	Easting (m)	Elevation (m)	Strike	Dip	Plunge	Trend	Classification	GIS ID
172	9/1/14	4413614	412959	1108	270	75			qtz - druzy/prismatic	AA
173	9/1/14	4413815	412902	1118	197	84			calcite - breccia	Z
174	9/1/14	4413831	412897	1120	015	41	38	130	fault - unmineralized (loose gouge)	K
185	9/4/14	4413644	412937	1116	012	79			qtz - breccia/stockwork	78
213	9/4/14	4413644	412937	1116	170	61			qtz - breccia/stockwork	78
216	9/4/14	4413644	412937	1116	010	68			qtz - breccia/stockwork	78
217	9/4/14	4413644	412937	1116	032	50			qtz - breccia/stockwork	78
219	9/4/14	4413644	412937	1116	163	74			qtz - breccia/stockwork	78
214	9/4/14	4413644	412937	1116	041	90			qtz - druzy/prismatic	78
218	9/4/14	4413644	412937	1116	177	71			qtz - druzy/prismatic	78
175	9/4/14	4413644	412937	1116	001	29			qtz vein - unclassified	78
176	9/4/14	4413644	412937	1116	015	84			qtz vein - unclassified	78
177	9/4/14	4413644	412937	1116	336	77			qtz vein - unclassified	78
178	9/4/14	4413644	412937	1116	023	74			qtz vein - unclassified	78
179	9/4/14	4413644	412937	1116	329	90			qtz vein - unclassified	78
180	9/4/14	4413644	412937	1116	354	59			qtz vein - unclassified	78
181	9/4/14	4413644	412937	1116	168	59			qtz vein - unclassified	78
182	9/4/14	4413644	412937	1116	200	30			qtz vein - unclassified	78
183	9/4/14	4413644	412937	1116	213	67			qtz vein - unclassified	78
184	9/4/14	4413644	412937	1116	028	82			qtz vein - unclassified	78
186	9/4/14	4413644	412937	1116	166	72			qtz vein - unclassified	78
187	9/4/14	4413644	412937	1116	194	61			qtz vein - unclassified	78
188	9/4/14	4413644	412937	1116	217	65			qtz vein - unclassified	78
189	9/4/14	4413644	412937	1116	077	13			qtz vein - unclassified	78
190	9/4/14	4413644	412937	1116	250	24			qtz vein - unclassified	78

ID	Date	Northing (m)	Easting (m)	Elevation (m)	Strike	Dip	Plunge	Trend	Classification	GIS ID
191	9/4/14	4413644	412937	1116	022	80			qtz vein - unclassified	78
192	9/4/14	4413644	412937	1116	275	81			qtz vein - unclassified	78
193	9/4/14	4413644	412937	1116	336	78			qtz vein - unclassified	78
194	9/4/14	4413644	412937	1116	199	50			qtz vein - unclassified	78
195	9/4/14	4413644	412937	1116	349	50			qtz vein - unclassified	78
196	9/4/14	4413644	412937	1116	25	81			qtz vein - unclassified	78
197	9/4/14	4413644	412937	1116	55	88			qtz vein - unclassified	78
198	9/4/14	4413644	412937	1116	236	65			qtz vein - unclassified	78
199	9/4/14	4413644	412937	1116	179	63			qtz vein - unclassified	78
200	9/4/14	4413644	412937	1116	030	05			qtz vein - unclassified	78
201	9/4/14	4413644	412937	1116	129	60			qtz vein - unclassified	78
202	9/4/14	4413644	412937	1116	034	79			qtz vein - unclassified	78
203	9/4/14	4413644	412937	1116	035	81			qtz vein - unclassified	78
204	9/4/14	4413644	412937	1116	013	90			qtz vein - unclassified	78
205	9/4/14	4413644	412937	1116	179	83			qtz vein - unclassified	78
206	9/4/14	4413644	412937	1116	48	64			qtz vein - unclassified	78
207	9/4/14	4413644	412937	1116	201	68			qtz vein - unclassified	78
208	9/4/14	4413644	412937	1116	011	81			qtz vein - unclassified	78
209	9/4/14	4413644	412937	1116	185	75			qtz vein - unclassified	78
210	9/4/14	4413644	412937	1116	020	60			qtz vein - unclassified	78
211	9/4/14	4413644	412937	1116	019	64			qtz vein - unclassified	78
212	9/4/14	4413644	412937	1116	230	63			qtz vein - unclassified	78
215	9/4/14	4413644	412937	1116	011	90			qtz vein - unclassified	78
220	5/28/15	4413196	412875	1123	000	42			fault - silicified breccias and gouge	57
221	5/28/15	4413295	412867	1107	028	66			fracture - with minor oxide/sulfide	W

ID	Date	Northing (m)	Easting (m)	Elevation (m)	Strike	Dip	Plunge	Trend	Classification	GIS ID
222	5/28/15	4413295	412867	1107	007	68			fracture - with minor oxide/sulfide	W
223	5/28/15	4413523	412983	1094	007	48			fault - silicified breccias and gouge	Y
224	5/28/15	4413523	412983	1094	357	50			fault - silicified breccias and gouge	Y
225	5/28/15	4413523	412983	1094	356	50			fault - silicified breccias and gouge	Y
226	10/29/17	4413078	412588	1167	020	35			fault - unmineralized (loose gouge)	C
227	10/29/17	4413092	412841	1122	345	60			cal w/hematite, gouge	A
228	10/29/17	4413117	412878	1104	018	35			fault - silicified breccias and gouge	D
229	10/29/17	4413117	412878	1104	025	28			fault - silicified breccias and gouge	D
230	10/29/17	4413117	412878	1104	080	65			qtz - druzy/prismatic	D
231	10/29/17	4413117	412878	1104	091	80			qtz - druzy/prismatic	D
232	10/29/17	4413117	412878	1104	087	71			qtz - druzy/prismatic	D
233	10/29/17	4413117	412878	1104	100	75			qtz - druzy/prismatic	D
234	10/29/17	4413117	412878	1104	115	90			qtz - druzy/prismatic	D
235	10/29/17	4413117	412878	1104	105	55			qtz - druzy/prismatic	D
239	10/29/17	4413128	412651	1155	058	81			calcite + barite + sulfide	F
236	10/29/17	4413128	412651	1155	320	82			fracture - unmineralized, partially open	F
237	10/29/17	4413128	412651	1155	340	86			fracture - unmineralized, partially open	F
238	10/29/17	4413128	412651	1155	325	74			fracture - unmineralized, partially open	F
240	10/29/17	4413163	412851	1115	100	86			qtz vein - unclassified	I
241	10/29/17	4413167	412754	1127	035	67			calcite - unclassified	E
242	10/29/17	4413167	412754	1127	051	39			calcite - unclassified	E
243	10/29/17	4413171	412758	1125	005	76			qtz vein - unclassified	H
244	10/29/17	4413174	412747	1130	186	75			calcite - unclassified	G
246	10/29/17	4413249	412804	1150	350	42	21	145	fault - silicified breccias and gouge	B
245	10/29/17	4413249	412804	1150	000	58			qtz - breccia/stockwork	B

ID	Date	Northing (m)	Easting (m)	Elevation (m)	Strike	Dip	Plunge	Trend	Classification	GIS ID
247	10/29/17	4413574	412936	1127	295	54			qtz - chalcedony	J2
248	10/30/17	4413831	412897	1120	341	46	29	128	fault - silicified breccias and gouge	K
249	10/30/17	4413831	412897	1120	030	42			fault - unmineralized (loose gouge)	K
250	10/30/17	4413831	412897	1120	083	90			qtz vein - unclassified	K
251	10/30/17	4413831	412897	1120	345	38			qtz vein - unclassified	K
252	10/30/17	4413899	412906	1132	022	32	29	139	fault - silicified breccias and gouge	M
253	10/30/17	4413899	412906	1132	012	29	26	131	fault - silicified breccias and gouge	M
254	10/30/17	4413899	412906	1132	034	35	35	129	fault - silicified breccias and gouge	M
255	10/30/17	4413899	412906	1132	020	35	30	142	fault - silicified breccias and gouge	M
256	10/30/17	4413899	412906	1132	024	30			fault - silicified breccias and gouge	M
257	10/31/17	4413681	412898	1121	045	53	53	135	qtz - breccia/stockwork	17
258	10/31/17	4413820	412869	1131	036	69	08	039	qtz - breccia/stockwork	15
259	10/31/17	4413820	412869	1131	032	70			qtz - breccia/stockwork	15
260	10/31/17	4413820	412869	1131	045	67			qtz - breccia/stockwork	15
261	10/31/17	4413822	412827	1139	350	70			qtz w/calcite	14
262	10/31/17	4413823	412541	1255	060	46			fault - w/calcite	13
263	10/31/17	4413823	412541	1255	316	18			geopetal	14
264	10/31/17	4413823	412541	1255	249	16			geopetal	14
265	10/31/17	4413823	412541	1255	350	89			qtz w/calcite	14
266	10/31/17	4413823	412541	1255	010	60			qtz w/calcite	14
267	10/31/17	4413893	412835	1161	003	52			fault - unmineralized (loose gouge)	9
268	10/31/17	4413899	412803	1170	336	39			fault - with minor mineralized slickensides	9.5
269	10/31/17	4413933	412677	1218	302	39	13	107	fault - with minor mineralized slickensides	10
270	10/31/17	4413934	412662	1230	022	58	40	170	fault - w/calcite	11
271	10/31/17	4413961	412611	1251	015	90			dikes - basalt	12

ID	Date	Northing (m)	Easting (m)	Elevation (m)	Strike	Dip	Plunge	Trend	Classification	GIS ID
272	10/31/17	4413961	412611	1251	035	84			dikes - basalt	12
273	10/31/17	4413978	412856	1149	021	49	44	141	fault - with minor mineralized slickensides	8
274	10/31/17	4413978	412856	1149	029	21	16	166	fault - with minor mineralized slickensides	8
275	10/31/17	4414043	412837	1164	004	54	37	152	fault - with minor mineralized slickensides	7
276	10/31/17	4414087	412847	1150	002	55			fault - unclassified	6
277	10/31/17	4414098	412757	1191	160	64	54	204	fault - with minor mineralized slickensides	5
278	10/31/17	4414098	412757	1191	180	60			fracture - with minor oxide/sulfide	5
279	10/31/17	4414098	412757	1191	190	39			fracture - with minor oxide/sulfide	5
280	10/31/17	4414099	412735	1211	015	64	30	031	dikes - basalt	4
281	10/31/17	4414099	412735	1211	015	64	64	105	dikes - basalt	4
282	10/31/17	4414170	412784	1193	018	44			fault - unclassified	3
283	10/31/17	4414254	412810	1184	347	43	32	126	fault - silicified breccias and gouge	2
284	10/31/17	4414306	412842	1151	343	36	36	082	fault - silicified breccias and gouge	1
285	10/31/17	4414306	412842	1151	348	40	40	074	fault - silicified breccias and gouge	1
286	10/31/17	4414306	412842	1151	352	42	21	147	fault - silicified breccias and gouge	1
287	11/1/17	4412380	412846	1112	010	90			calcite - unclassified	19
288	11/1/17	4412526	412874	1100	166	65			calcite - unclassified	21
289	11/1/17	4412526	412874	1100	127	74			calcite - unclassified	21
290	11/1/17	4412526	412874	1100	227	44			calcite - unclassified	21
291	11/1/17	4412526	412874	1100	124	75			calcite - unclassified	21
292	11/1/17	4412526	412874	1100	190	66			calcite - unclassified	21
293	11/1/17	4412526	412874	1100	215	52			calcite - unclassified	21
297	11/1/17	4412577	412789	1130	343	90			cal w/hematite, gouge	23
298	11/1/17	4412577	412789	1130	058	62			cal w/hematite, gouge	23
299	11/1/17	4412577	412789	1130	034	38	37	125	cal w/hematite, gouge	23

ID	Date	Northing (m)	Easting (m)	Elevation (m)	Strike	Dip	Plunge	Trend	Classification	GIS ID
294	11/1/17	4412577	412789	1130	010	58	30	168	qtz vein - unclassified	23
295	11/1/17	4412577	412789	1130	027	34			qtz vein - unclassified	23
296	11/1/17	4412577	412789	1130	028	74			qtz vein - unclassified	23
301	11/1/17	4412578	412822	1107	334	78			calcite - unclassified	28
300	11/1/17	4412578	412822	1107	028	74	74	118	fault - unmineralized (loose gouge)	28
302	11/1/17	4412607	412756	1154	040	41	41	135	fault - with minor mineralized slickensides	24
303	11/1/17	4412675	412749	1149	210	64			lithologic trends	25
304	11/1/17	4412725	412835	1101	354	45			qtz - breccia/stockwork	27
305	11/1/17	4412851	412770	1124	315	53			fracture - with minor oxide/sulfide	29
306	11/1/17	4412851	412770	1124	325	63			fracture - with minor oxide/sulfide	29
307	11/1/17	4412851	412770	1124	354	39			fracture - with minor oxide/sulfide	29
308	11/1/17	4412851	412770	1124	157	60			fracture - with minor oxide/sulfide	29
309	11/1/17	4412851	412770	1124	175	49			fracture - with minor oxide/sulfide	29
310	11/1/17	4412851	412770	1124	202	31			fracture - with minor oxide/sulfide	29
311	11/1/17	4412851	412770	1124	163	67			fracture - with minor oxide/sulfide	29
314	11/1/17	4412997	412824	1120	088	74			calcite - unclassified	31
312	11/1/17	4412997	412824	1120	115	58			calcite + barite + sulfide	31
313	11/1/17	4412997	412824	1120	090	73			fracture - with minor oxide/sulfide	31
315	11/1/17	4413052	412652	1192	168	39	00	168	fault - with minor mineralized slickensides	34
316	11/1/17	4413064	412762	1156	308	88			calcite - unclassified	32
317	11/1/17	4413095	412871	1112	016	38	38	110	fault - silicified breccias and gouge	36
318	11/1/17	4413110	412798	1144	047	73			fracture - with sulfate (gypsum, jarosite)	35
319	11/1/17	4413110	412798	1144	092	29			fracture - with sulfate (gypsum, jarosite)	35
320	11/1/17	4413110	412798	1144	175	81			fracture - with sulfate (gypsum, jarosite)	35
321	11/1/17	4413110	412798	1144	215	64			fracture - with sulfate (gypsum, jarosite)	35

ID	Date	Northing (m)	Easting (m)	Elevation (m)	Strike	Dip	Plunge	Trend	Classification	GIS ID
322	11/1/17	4413177	412874	1121	015	44			fault - silicified breccias and gouge	30
323	11/2/17	4413478	412696	1248	056	60			qtz - breccia/stockwork	43
324	11/2/17	4413478	412696	1248	020	75			qtz - breccia/stockwork	43
325	11/2/17	4413478	412696	1248	035	79			qtz - breccia/stockwork	43
326	11/2/17	4413481	412737	1224	015	52			qtz - breccia/stockwork	44
327	11/2/17	4413537	412731	1234	029	53	50	146	fault - with minor mineralized slickensides	42
328	11/2/17	4413537	412731	1234	072	64	64	165	fault - with minor mineralized slickensides	42
329	11/2/17	4413537	412731	1234	207	46	45	285	fault - with minor mineralized slickensides	42
330	11/2/17	4413537	412731	1234	045	59			qtz - breccia/stockwork	42
334	11/2/17	4413555	412859	1167	330	51			fault - unmineralized (loose gouge)	45
331	11/2/17	4413555	412859	1167	192	75			qtz - druzy/prismatic	45
332	11/2/17	4413555	412859	1167	208	76			qtz - druzy/prismatic	45
333	11/2/17	4413555	412859	1167	028	66			qtz - druzy/prismatic	45
335	11/2/17	4413559	412955	1113	358	46	36	134	fault - silicified breccias and gouge	51
336	11/2/17	4413559	412955	1113	359	46	40	124	fault - silicified breccias and gouge	51
337	11/2/17	4413564	412863	1166	018	62			qtz - breccia/stockwork	45.5
338	11/2/17	4413564	412863	1166	039	47			qtz - breccia/stockwork	45.5
339	11/2/17	4413564	412863	1166	032	68			qtz - breccia/stockwork	45.5
340	11/2/17	4413596	412771	1208	197	80			qtz - breccia/stockwork	41
341	11/2/17	4413596	412771	1208	352	90			qtz - breccia/stockwork	41
342	11/2/17	4413596	412771	1208	030	80			qtz - breccia/stockwork	41
343	11/2/17	4413605	412952	1112	359	43			fault - silicified breccias and gouge	52
344	11/2/17	4413605	412952	1112	010	53			qtz - breccia/stockwork	52
345	11/2/17	4413605	412952	1112	325	51			qtz - chalcedony	52
346	11/2/17	4413605	412952	1112	059	90			qtz - druzy/prismatic	52

ID	Date	Northing (m)	Easting (m)	Elevation (m)	Strike	Dip	Plunge	Trend	Classification	GIS ID
347	11/2/17	4413605	412952	1112	051	86			qtz - druzy/prismatic	52
348	11/2/17	4413606	412898	1143	092	72			qtz - breccia/stockwork	47
349	11/2/17	4413617	412915	1135	350	58	22	155	fault - silicified breccias and gouge	49
350	11/2/17	4413617	412915	1135	017	51	39	155	fault - silicified breccias and gouge	49
351	11/2/17	4413617	412915	1135	044	52	46	170	fault - silicified breccias and gouge	49
352	11/2/17	4413631	412845	1153	035				lithologic trends	46
354	11/2/17	4413632	412922	1127	058	59			fault - silicified breccias and gouge	48
353	11/2/17	4413632	412922	1127	032	36	25	72	qtz vein - unclassified	48
355	11/2/17	4413672	412775	1183	037	36			qtz - breccia/stockwork	40
356	11/2/17	4413672	412775	1183	183	33			qtz - breccia/stockwork	40
357	11/2/17	4413672	412775	1183	084	44			qtz - breccia/stockwork	40
358	11/2/17	4413672	412775	1183	112	58			qtz - breccia/stockwork	40
359	11/2/17	4413672	412775	1183	355	52	36	140	qtz - breccia/stockwork	40
360	11/2/17	4413672	412775	1183	035	34			qtz - breccia/stockwork	40
364	11/2/17	4413686	412901	1119	021	63	61	129	fault - silicified breccias and gouge	37
365	11/2/17	4413686	412901	1119	015	51	34	161	fault - with minor mineralized slickensides	37
361	11/2/17	4413686	412901	1119	031	55			qtz - breccia/stockwork	37
362	11/2/17	4413686	412901	1119	042	59	59	139	qtz - breccia/stockwork	37
363	11/2/17	4413686	412901	1119	045	52			qtz - breccia/stockwork	37
366	11/2/17	4413690	412773	1187	244	72			qtz w/calcite	39
367	11/2/17	4413703	412829	1166	357	52	49	112	fault - with minor mineralized slickensides	38
368	11/3/17	4413158	412879	1113	014	34	34	112	fault - silicified breccias and gouge	56
369	11/3/17	4413158	412879	1113	014	34	31	129	fault - silicified breccias and gouge	56
370	11/3/17	4413158	412879	1113	052	40			qtz vein - unclassified	56
371	11/3/17	4413158	412879	1113	307	80			qtz vein - unclassified	56

ID	Date	Northing (m)	Easting (m)	Elevation (m)	Strike	Dip	Plunge	Trend	Classification	GIS ID
372	11/3/17	4413193	412873	1123	045	40	40	140	fault - silicified breccias and gouge	58
373	11/3/17	4413196	412875	1123	066	50			fault - silicified breccias and gouge	57
374	11/3/17	4413196	412875	1123	031	40			fault - silicified breccias and gouge	57
375	11/3/17	4413196	412875	1123	021	40			fault - silicified breccias and gouge	57
376	11/3/17	4413221	412754	1156	334	75	01	154	qtz - breccia/stockwork	61
381	11/3/17	4413238	412808	1149	078	85			qtz - breccia/stockwork	59
377	11/3/17	4413238	412808	1149	079	85			qtz - druzy/prismatic	59
378	11/3/17	4413238	412808	1149	280	41			qtz - druzy/prismatic	59
379	11/3/17	4413238	412808	1149	205	85			qtz - druzy/prismatic	59
380	11/3/17	4413238	412808	1149	235	67			qtz - druzy/prismatic	59
382	11/3/17	4413258	412824	1142	040	63			qtz - breccia/stockwork	66
383	11/3/17	4413258	412824	1142	196	70			qtz - breccia/stockwork	66
384	11/3/17	4413258	412824	1142	054	81			qtz - breccia/stockwork	66
385	11/3/17	4413258	412824	1142	066	80			qtz - breccia/stockwork	66
386	11/3/17	4413281	412701	1156	286	24	18	058	fault - silicified breccias and gouge	62
387	11/3/17	4413281	412701	1156	053	76	06	054	fault - silicified breccias and gouge	62
388	11/3/17	4413281	412701	1156	312	67			qtz - breccia/stockwork	62
389	11/3/17	4413281	412701	1156	002	82			qtz - druzy/prismatic	62
390	11/3/17	4413281	412701	1195	350	69			qtz - druzy/prismatic	62
391	11/3/17	4413360	412742	1156	158	79			qtz w/calcite	63
392	11/3/17	4413392	412772	1167	114	76	61	141	fault - unmineralized (loose gouge)	64
393	11/3/17	4413392	412772	1167	114	76	31	123	fault - unmineralized (loose gouge)	64
394	11/3/17	4413392	412772	1167	114	76	00	114	fault - unmineralized (loose gouge)	64
395	11/3/17	4413392	412772	1167	000	72			qtz vein - unclassified	64
396	11/3/17	4413444	412984	1086	014	42			fault - with minor mineralized slickensides	54

ID	Date	Northing (m)	Easting (m)	Elevation (m)	Strike	Dip	Plunge	Trend	Classification	GIS ID
397	11/3/17	4413444	412984	1086	014	44			fault - with minor mineralized slickensides	54
398	11/3/17	4413444	412984	1086	356	54			fault - with minor mineralized slickensides	54
399	11/3/17	4413444	412984	1086	022	50	46	140	fault - with minor mineralized slickensides	54
400	11/3/17	4413452	412935	1106	178	90			calcite - unclassified	68
401	11/3/17	4413452	412935	1106	150	73			calcite - unclassified	68
403	11/3/17	4413452	412935	1106	326	52			fault - unmineralized (loose gouge)	68
402	11/3/17	4413452	412935	1106	350	77			qtz vein - unclassified	68
404	11/3/17	4413481	412964	1104	356	52	42	132	fault - silicified breccias and gouge	74
405	11/3/17	4413481	412964	1104	018	42	32	155	fault - silicified breccias and gouge	74
406	11/3/17	4413481	412964	1104	359	49	36	139	fault - silicified breccias and gouge	74
410	11/3/17	4413481	412964	1104	010	45			fault - silicified breccias and gouge	74
407	11/3/17	4413481	412964	1104	068	60			qtz vein - unclassified	74
408	11/3/17	4413481	412964	1104	215	59			qtz vein - unclassified	74
409	11/3/17	4413481	412964	1104	015	79			qtz vein - unclassified	74
411	11/3/17	4413487	412829	1162	323	64			fracture - unmineralized, partially open	69
413	11/3/17	4413489	412931	1123	004	59	59	94	fault - with minor mineralized slickensides	72
412	11/3/17	4413489	412931	1123	341	55			qtz w/calcite	72
414	11/3/17	4413517	412803	1189	062	60			qtz - breccia/stockwork	70
415	11/3/17	4413632	412922	1127	032	36	25	72	fault - with minor mineralized slickensides	48
416	11/3/17	4413663	412862	1135	035				lithologic trends	52.5
421	11/3/17	4413664	412915	1115	039	65			calcite - unclassified	53
426	11/3/17	4413664	412915	1115	034	40	39	135	fault - silicified breccias and gouge	53
427	11/3/17	4413664	412915	1115	006	24	17	140	fault - silicified breccias and gouge	53
419	11/3/17	4413664	412915	1115	030	56	55	106	fault - with minor mineralized slickensides	53
423	11/3/17	4413664	412915	1115	163	65			qtz - breccia/stockwork	53

ID	Date	Northing (m)	Easting (m)	Elevation (m)	Strike	Dip	Plunge	Trend	Classification	GIS ID
424	11/3/17	4413664	412915	1115	008	90			qtz - breccia/stockwork	53
430	11/3/17	4413664	412915	1115	230	80			qtz - breccia/stockwork	53
420	11/3/17	4413664	412915	1115	043	81			qtz - druzy/prismatic	53
422	11/3/17	4413664	412915	1115	065	67			qtz - druzy/prismatic	53
425	11/3/17	4413664	412915	1115	064	56			qtz - druzy/prismatic	53
418	11/3/17	4413664	412915	1115	019	89			qtz vein - unclassified	53
428	11/3/17	4413664	412915	1115	230	74			qtz vein - unclassified	53
429	11/3/17	4413664	412915	1115	215	71			qtz vein - unclassified	53
417	11/3/17	4413664	412915	1115	295	35			qtz w/calcite	53
432	11/4/17	4413167	412861	1121	008	39			fault - silicified breccias and gouge	L
433	11/4/17	4413167	412861	1121	320	45			fault - silicified breccias and gouge	L
434	11/4/17	4413167	412861	1121	020	73			qtz - chalcedony	L
435	11/4/17	4413167	412861	1121	339	40			qtz - druzy/prismatic	L
437	11/4/17	4413167	412861	1121	033	51			qtz - druzy/prismatic	L
438	11/4/17	4413167	412861	1121	345	80			qtz - druzy/prismatic	L
439	11/4/17	4413167	412861	1121	340	62			qtz - druzy/prismatic	L
440	11/4/17	4413167	412861	1121	023	42			qtz - druzy/prismatic	L
431	11/4/17	4413167	412861	1121	121	84			qtz vein - unclassified	L
436	11/4/17	4413167	412861	1121	254	78			qtz vein - unclassified	L
442	11/4/17	4413815	412902	1118	140	90			calcite - breccia	Z
444	11/4/17	4413815	412902	1118	040	90			calcite - unclassified	Z
445	11/4/17	4413815	412902	1118	000	68			calcite - unclassified	Z
441	11/4/17	4413815	412902	1118	200	15			dikes - aplite	Z
443	11/4/17	4413815	412902	1118	063	44			dikes - aplite	Z
446	11/4/17	4413815	412902	1118	343	56			qtz - breccia/stockwork	Z

ID	Date	Northing (m)	Easting (m)	Elevation (m)	Strike	Dip	Plunge	Trend	Classification	GIS ID
447	11/4/17	4413831	412897	1120	017	40			fault - unmineralized (loose gouge)	K
448	11/4/17	4413831	412897	1120	000	40			fault - unmineralized (loose gouge)	K
449	11/4/17	4413831	412897	1120	317	47			fault - unmineralized (loose gouge)	K
450	11/4/17	4413831	412897	1120	326	34			fault - unmineralized (loose gouge)	K
451	11/4/17	4413831	412897	1120	089	40	39	160	fault - with minor mineralized slickensides	K
452	11/4/17	4413831	412897	1120	340	17	08	132	fault - with minor mineralized slickensides	K
453	11/4/17	4413831	412897	1120	339	13	08	125	fault - with minor mineralized slickensides	K
454	11/4/17	4413891	412903	1130	337	44			fault - with minor mineralized slickensides	77
455	11/4/17	4413891	412903	1130	357	49	48	96	fault - with minor mineralized slickensides	77
456	11/4/17	4413891	412903	1130	345	60	57	100	fault - with minor mineralized slickensides	77
457	11/4/17	4413891	412903	1130	352	64			fault - with minor mineralized slickensides	77
458	11/4/17	4413891	412903	1130	049	43	42	151	fault - with minor mineralized slickensides	77
459	11/4/17	4413891	412903	1130	357	35			qtz vein - unclassified	77
460	11/4/17	4413891	412903	1130	333	27			qtz vein - unclassified	77
461	11/4/17	4413891	412903	1130	176	90			qtz vein - unclassified	77
462	11/4/17	4413891	412903	1130	323	55			qtz vein - unclassified	77
463	11/4/17	4413924	412973	1110	003	40	40	85	fault - with minor mineralized slickensides	75
464	11/4/17	4413953	412921	1125	306	49			fault - with minor mineralized slickensides	76
468	11/4/17	4413953	412921	1125	344	40			fault - with minor mineralized slickensides	76
465	11/4/17	4413953	412921	1125	355	67			fracture - unmineralized, partially open	76
466	11/4/17	4413953	412921	1125	008	76			fracture - unmineralized, partially open	76
467	11/4/17	4413953	412921	1125	273	32			fracture - unmineralized, partially open	76

I. Appendix: Scan Line Data, Box Canyons and Dixie Comstock

Site: Upper Big Box Canyon
Date: June 7, 2014
Coordinates: 398550 m E, 4385363 m N
Orientation: (03, 118)
Host Rock: Oligocene granodiorite
Dominant Fracture Sets: Set 1 = (222, 58), Set 2 = (034, 31), Set 3 = (270, 70), Set 4 = (183, 67)
Other Structures: deep footwall
Comparator: Peter, 1999
Notes: Eye level, south wall. Scanline runs east to west. Sheared aplite dike at 7 m.

Site: Lower Big Box Canyon
Date: August 30, 2014
Coordinates: 398667 m E, 4385280 m N
Orientation: (02, 110)
Host Rock: Oligocene granodiorite
Dominant Fracture Sets: Set 1 = (NE, ~43), Set 2 = (S, ~81), Set 3 = (302, 45), Set 4 = (210, 60)
Other Structures: footwall, near range front
Comparator: Peter, 1999
Notes: Eye level, north wall. Scanline runs east to west.

Site: Upper Little Box Canyon
Date: June 9, 2014
Coordinates: 399251 m E, 4386105 m N
Orientation: (01, 098)
Host Rock: Oligocene granodiorite
Dominant Fracture Sets: Set 1 = (018, 90), Set 2 = (NE, ~37), Set 3 = (350, 48), Set 4 = (290, 38)
Other Structures: deep footwall
Comparator: Peter, 1999
Notes: Eye level, south wall, penultimate plunge pool. Scanline runs east to west.

Site: Middle Little Box Canyon
Date: August 30, 2014
Coordinates: 399303 m E, 4386094 m N
Orientation: (04, 302)
Host Rock: Oligocene granodiorite
Dominant Fracture Sets: Set 1 = (NE, 75-90)
Alteration: chlorite, calcite, hematite
Other Structures: halos around subvertical fractures
Comparator: Peter, 1999
Notes: Knee level, north wall, around fractures with halos. Scanline runs east to west.

Site: Lower Little Box Canyon
Date: June 4 and June 7, 2014
Coordinates: 399336 m E, 4386093 m N
Orientation: (35, 098)
Host Rock: Oligocene granodiorite
Dominant Fracture Sets: -
Alteration: chlorite, calcite, hematite
Other Structures: dike at western end of scanline
Comparator: Peter, 1999
Notes: In main wash at range front. Scanline runs east to west.

Site: Dixie Comstock, South
Date: August 31, 2014
Coordinates: 412823 m E, 4412734 m N
Orientation: (15, 110)
Host Rock: Jurassic Humboldt Igneous Complex (coarse gabbro)
Dominant Fracture Sets: -
Alteration: chlorite, calcite, hematite; quartz veins
Other Structures: stockwork quartz veins
Comparator: ruler
Notes: Northern wall above range front plunge pool. Scan line starts at 1 m. Scanline runs east to west. Lower observations limit is 0.1 cm. Footwall below range front fault.

Site: Dixie Comstock, Middle
Date: September 4, 2014
Coordinates: 412935 m E, 4413646 m N
Orientation: (24, 093)
Host Rock: Jurassic Humboldt Igneous Complex, silicified fault breccia
Dominant Fracture Sets: -
Alteration: chlorite, calcite, hematite; silicification; quartz veins
Other Structures: -
Comparator: ruler
Notes: Scanline starts at 10 cm. Scanline runs east to west. Lower observations limit is 0.1 cm. In range front fault breccia.

Site: Dixie Comstock, North
Date: August 31, 2014
Coordinates: 412868 m E, 4413882 m N
Orientation: (26, 118)
Host Rock: Jurassic Humboldt Igneous Complex, medium grained gabbro
Dominant Fracture Sets: -
Alteration: chlorite, calcite, hematite; quartz veins
Other Structures: -
Comparator: ruler
Notes: Scanline starts at 19 cm. Scanline runs east to west. Lower observations limit is 0.1 cm.

Table I.1. Scanline Data

Site	Fracture (#)	Distance (mm)	App. Width (mm)*	Orientation (RHR)†	Fill	Notes
Upper Big Box Canyon	1	0		018, 70	black	
Upper Big Box Canyon	2	4	0.215	034, 31	black	
Upper Big Box Canyon	3	17	0.265	034, 31	black	
Upper Big Box Canyon	4	63	0.500	222, 58	black	
Upper Big Box Canyon	5	69	0.140	Set 1	black	
Upper Big Box Canyon	6	73	0.095	Set 1	black	
Upper Big Box Canyon	7	77	0.095	-	black	
Upper Big Box Canyon	8	80	0.330	-	black	
Upper Big Box Canyon	9	85	1.400	Set 1	black	
Upper Big Box Canyon	10	90	0.095	Set 1	black	
Upper Big Box Canyon	11	108	0.050	Set 2	-	short
Upper Big Box Canyon	12	109	0.140	Set 1	black	
Upper Big Box Canyon	13	111	0.050	Set 2	-	
Upper Big Box Canyon	14	112	0.095	Set 1	black	
Upper Big Box Canyon	15	131	1.150	Set 2	black	
Upper Big Box Canyon	16	154		Set 1	black	
Upper Big Box Canyon	17	158	0.950	Set 1	black	
Upper Big Box Canyon	18	190	0.215	-	black	
Upper Big Box Canyon	19	222	0.050	-	-	
Upper Big Box Canyon	20	252	0.620	Set 2	black	
Upper Big Box Canyon	21	255	0.095	Set 2	black	
Upper Big Box Canyon	22	270	0.500	Set 3	black	north side down shear

* Apparent width along scanline.

† Fracture orientation, using right hand rule.

Site	Fracture (#)	Distance (mm)	App. Width (mm)*	Orientation (RHR)†	Fill	Notes
Upper Big Box Canyon	23	282	0.095	Set 3	black	
Upper Big Box Canyon	24	331	0.950	150, 67	black	
Upper Big Box Canyon	25	368	0.140	-	black	
Upper Big Box Canyon	26	384	0.095	Set 2	black	
Upper Big Box Canyon	27	405	0.500	Set 1	black	
Upper Big Box Canyon	28	420	0.050	Set 2	-	
Upper Big Box Canyon	29	430	0.500	175, 77	black	
Upper Big Box Canyon	30	540	0.620	Set 4	black	
Upper Big Box Canyon	31	603	0.140	Set 1	black	
Upper Big Box Canyon	32	689	0.175	Set 1	black	
Upper Big Box Canyon	33	690	0.050	Set 1	black	
Upper Big Box Canyon	34	691	0.050	Set 1	black	
Upper Big Box Canyon	35	692	0.500	Set 2	black	
Upper Big Box Canyon	36	694	0.950	Set 2	black	
Upper Big Box Canyon	37	696	0.050	Set 2	-	
Upper Big Box Canyon	38	712		Set 4	open	
Upper Big Box Canyon	39	830	0.750	Set 3	-	eroded
Upper Big Box Canyon	40	833	0.400	-	black with white core	probably qtz
Upper Big Box Canyon	41	862	0.330	Set 4	black	
Upper Big Box Canyon	42	865	0.140	Set 4	black	
Upper Big Box Canyon	43	868	0.140	Set 4	black	
Upper Big Box Canyon	44	899	0.620	Set 4	black	eroded
Upper Big Box Canyon	45	908	0.500	Set 2	black	
Upper Big Box Canyon	46	922	0.500	Set 4	black	eroded
Upper Big Box Canyon	47	926	0.620	Set 2	black	
Upper Big Box Canyon	48	946	0.050	Set 4	-	
Upper Big Box Canyon	49	956	0.050	Set 4	-	short
Upper Big Box Canyon	50	957	0.050	Set 4	-	short

Site	Fracture (#)	Distance (mm)	App. Width (mm)*	Orientation (RHR)†	Fill	Notes
Upper Big Box Canyon	51	961	0.620	Set 2	black	
Upper Big Box Canyon	52	964	0.175	Set 2	black	
Upper Big Box Canyon	53	985	0.330	Set 3	black	
Upper Big Box Canyon	54	991	0.265	Set 4	black	short
Upper Big Box Canyon	55	995	0.330	Set 4	black	short
Upper Big Box Canyon	56	1005	0.400	Set 4	black	
Upper Big Box Canyon	57	1010	0.750	Set 2	black	cataclastic with some quartz
Upper Big Box Canyon	58	1032	0.140	Set 4	black	
Upper Big Box Canyon	59	1034	0.095	Set 4	black	
Upper Big Box Canyon	60	1045		-	black	
Upper Big Box Canyon	61	1046		-	black	
Upper Big Box Canyon	62	1048		-	black	
Upper Big Box Canyon	63	1049		-	black	
Upper Big Box Canyon	64	1054	0.950	Set 4	black	
Upper Big Box Canyon	65	1055	5.000	Set 3	black/cataclasite	cataclasite
Upper Big Box Canyon	66	1066	0.500	336, 62	open	cm scale corrugations
Upper Big Box Canyon	67	1086	0.500	Set 2	open/black	
Upper Big Box Canyon	68	1142	0.050	-	-	
Upper Big Box Canyon	69	1155	0.095	Set 4	black	
Upper Big Box Canyon	70	1160	0.500	Set 4	-	eroded
Upper Big Box Canyon	71	1213	0.215	Set 4	black	
Upper Big Box Canyon	72	1276	0.400	Set 3	black	
Upper Big Box Canyon	73	1293	0.175	Set 4	black	
Upper Big Box Canyon	74	1295	0.400	Set 2	black	
Upper Big Box Canyon	75	1299	0.115	Set 4	black	short
Upper Big Box Canyon	76	1304	0.115	Set 4	black	short
Upper Big Box Canyon	77	1312		Set 2	black	eroded
Upper Big Box Canyon	78	1329	0.050	Set 4	-	

Site	Fracture (#)	Distance (mm)	App. Width (mm)*	Orientation (RHR)†	Fill	Notes
Upper Big Box Canyon	79	1340	0.050	-	-	
Upper Big Box Canyon	80	1343	0.330	Set 4	black	eroded
Upper Big Box Canyon	81	1374	0.330	Set 3	black	
Upper Big Box Canyon	82	1380	0.265	Set 3	black	eroded
Upper Big Box Canyon	83	1394	0.265	Set 4	black	
Upper Big Box Canyon	84	1406	0.175	Set 3	black	
Upper Big Box Canyon	85	1408	0.050	Set 3	black	
Upper Big Box Canyon	86	1414	0.050	Set 4	black	
Upper Big Box Canyon	87	1429		Set 4	black	eroded
Upper Big Box Canyon	88	1461	0.620	-	black + brown qtz	
Upper Big Box Canyon	89	1510	0.140	Set 3	black	
Upper Big Box Canyon	90	1575	2.650	Set 4	cataclasite	eroded
Upper Big Box Canyon	91	1601	0.095	158, 76	-	
Upper Big Box Canyon	92	1635		Set 4	black	eroded
Upper Big Box Canyon	93	1698	0.095	Set 4	black	
Upper Big Box Canyon	94	1710	0.400	Set 4	black	eroded
Upper Big Box Canyon	95	1724	0.950	Set 4	black	eroded
Upper Big Box Canyon	96	1744	0.175	-	black	
Upper Big Box Canyon	97	1749	0.500	Set 4	black	
Upper Big Box Canyon	98	1756	0.500	Set 4	black	
Upper Big Box Canyon	99	1782	0.050	Set 3	black	
Upper Big Box Canyon	100	1784	0.050	Set 4	-	
Upper Big Box Canyon	101	1795		Set 4	black + brown qtz	eroded
Upper Big Box Canyon	102	1820	0.095	190, 81	black	
Upper Big Box Canyon	103	1825	0.050	190, 81	black	
Upper Big Box Canyon	104	1834		Set 4	open	eroded
Upper Big Box Canyon	105	1857	0.400	-	black	
Upper Big Box Canyon	106	1885	0.095	-	black	

Site	Fracture (#)	Distance (mm)	App. Width (mm)*	Orientation (RHR)†	Fill	Notes
Upper Big Box Canyon	107	1908	0.265	Set 4	black	
Upper Big Box Canyon	108	1911	0.265	Set 4	black	
Upper Big Box Canyon	109	1914	0.330	Set 4	black	
Upper Big Box Canyon	110	1916	0.095	-	black	
Upper Big Box Canyon	111	1927	0.265	Set 4	black	
Upper Big Box Canyon	112	1938	0.265	Set 2	black	
Upper Big Box Canyon	113	1940	0.095	Set 4	black	
Upper Big Box Canyon	114	1942	0.095	Set 4	black	
Upper Big Box Canyon	115	1976		Set 4	eroded	
Upper Big Box Canyon	116	1988	0.330	Set 4	black	
Upper Big Box Canyon	117	1999	0.750	Set 4	black	
Upper Big Box Canyon	118	2004	3.300	Set 2	cataclasite	
Upper Big Box Canyon	119	2013		Set 4	-	eroded
Upper Big Box Canyon	120	2025	0.500	Set 4	open	
Upper Big Box Canyon	121	2062		Set 1	-	eroded
Upper Big Box Canyon	122	2072		Set 4	-	eroded
Upper Big Box Canyon	123	2074		Set 4	-	eroded
Upper Big Box Canyon	124	2087	0.400	Set 1	black	
Upper Big Box Canyon	125	2124	0.400	Set 4	black	
Upper Big Box Canyon	126	2144	0.215	Set 4	black	
Upper Big Box Canyon	127	2145	0.175	Set 4	black	
Upper Big Box Canyon	128	2195	0.400	Set 4	black	
Upper Big Box Canyon	129	2222	0.050	Set 3	-	
Upper Big Box Canyon	130	2228	0.620	Set 4	black	
Upper Big Box Canyon	131	2244		155, 66	black	eroded. Seems related to set 4
Upper Big Box Canyon	132	2250	0.500	Set 4	black	
Upper Big Box Canyon	133	2290	0.050	Set 2	black	
Upper Big Box Canyon	134	2297	0.050	Set 3	black	

Site	Fracture (#)	Distance (mm)	App. Width (mm)*	Orientation (RHR)†	Fill	Notes
Upper Big Box Canyon	135	2308	0.400	Set 2	black	
Upper Big Box Canyon	136	2332	0.050	Set 3	-	
Upper Big Box Canyon	137	2357	0.050	Set 2	black	
Upper Big Box Canyon	138	2359	0.050	Set 2	black	
Upper Big Box Canyon	139	2364	1.150	Set 2	cataclasite	
Upper Big Box Canyon	140	2410		Set 3	-	eroded
Upper Big Box Canyon	141	2426	2.650	Set 2	cataclasite	
Upper Big Box Canyon	142	2440	0.140	Set 2	black	
Upper Big Box Canyon	143	2466	0.175	Set 2	black	
Upper Big Box Canyon	144	2468	0.050	Set 2	-	
Upper Big Box Canyon	145	2492	0.050	Set 4	-	
Upper Big Box Canyon	146	2513	0.215	Set 4	black	
Upper Big Box Canyon	147	2531		Set 4	-	eroded
Upper Big Box Canyon	148	2541	0.950	Set 4	black	
Upper Big Box Canyon	149	2551		Set 4	black	eroded
Upper Big Box Canyon	150	2580		Set 3? (278, 80)	black	eroded
Upper Big Box Canyon	151	2591	0.400	Set 3	black	
Upper Big Box Canyon	152	2592	0.050	Set 3	black	
Upper Big Box Canyon	153	2602	0.050	Set 4	black	
Upper Big Box Canyon	154	2648		Set 4	black	eroded
Upper Big Box Canyon	155	2652		Set 4	black	eroded
Upper Big Box Canyon	156	2657	0.400	Set 4	black	
Upper Big Box Canyon	157	2659		Set 3 (240, 84)	black/cataclasite	eroded
Upper Big Box Canyon	158	2670		Set 4 (352, 80)	black	eroded
Upper Big Box Canyon	159	2676	0.215	Set 4	black	
Upper Big Box Canyon	160	2692	0.400	-	black	
Upper Big Box Canyon	161	2701	0.400	Set 3	black	
Upper Big Box Canyon	162	2716	0.050	Set 4	-	

Site	Fracture (#)	Distance (mm)	App. Width (mm)*	Orientation (RHR)†	Fill	Notes
Upper Big Box Canyon	163	2730	0.050	Set 3	black	
Upper Big Box Canyon	164	2732	1.150	Set 3	cataclasite	
Upper Big Box Canyon	165	2735	0.330	Set 3	black/cataclasite	
Upper Big Box Canyon	166	2737	0.500	Set 3	cataclasite	
Upper Big Box Canyon	167	2739	0.175	Set 3	black	
Upper Big Box Canyon	168	2743		Set 4	-	
Upper Big Box Canyon	169	2746	0.050	Set 4	-	
Upper Big Box Canyon	170	2784	0.500	Set 4	black	
Upper Big Box Canyon	171	2793	1.400	Set 3	cataclasite	
Upper Big Box Canyon	172	2816	0.330	Set 2	black	
Upper Big Box Canyon	173	2839	0.050	Set 4	-	
Upper Big Box Canyon	174	2854	0.175	Set 3	black	
Upper Big Box Canyon	175	2885		Set 1	-	eroded
Upper Big Box Canyon	176	2887	0.050	Set 3	-	
Upper Big Box Canyon	177	2931	0.400	Set 4	black	
Upper Big Box Canyon	178	2940	0.400	-	black	
Upper Big Box Canyon	179	2944		Set 3	black	eroded
Upper Big Box Canyon	180	2962	0.050	Set 4	black	
Upper Big Box Canyon	181	2965	0.215	Set 3	black	
Upper Big Box Canyon	182	2976	0.050	Set 3	-	
Upper Big Box Canyon	183	2981	0.050	Set 3	-	
Upper Big Box Canyon	184	2987	0.050	Set 3	-	
Upper Big Box Canyon	185	2990		Set 4	-	eroded
Upper Big Box Canyon	186	2994	0.400	Set 4	black	
Upper Big Box Canyon	187	3022	3.300	Set 2	cataclasite, green and black	
Upper Big Box Canyon	188	3038	0.265	Set 4	black	
Upper Big Box Canyon	189	3044	0.330	Set 4	black/cataclasite	set 4 cut set 2
Upper Big Box Canyon	190	3046	0.215	-	black	

Site	Fracture (#)	Distance (mm)	App. Width (mm)*	Orientation (RHR)†	Fill	Notes
Upper Big Box Canyon	191	3073	0.500	Set 4	black	cuts set 2
Upper Big Box Canyon	192	3075	0.750	Set 2	cataclasite	
Upper Big Box Canyon	193	3077	0.400	Set 2	black	
Upper Big Box Canyon	194	3104	0.140	Set 4	black	
Upper Big Box Canyon	195	3111		Set 4	-	eroded
Upper Big Box Canyon	196	3140	0.750	Set 2	cataclasite	
Upper Big Box Canyon	197	3148		Set 4	-	eroded
Upper Big Box Canyon	198	3156	0.050	Set 3	-	
Upper Big Box Canyon	199	3176		Set 4 (353, 85)	-	eroded
Lower Big Box Canyon	1	114	0.400	Set 1	dark	
Lower Big Box Canyon	2	116	0.175	058, 86	dark	
Lower Big Box Canyon	3	120	0.140	Set 1	dark	
Lower Big Box Canyon	4	127	0.140	Set 1 (004, 36)	dark	
Lower Big Box Canyon	5	132	5.000	Set 1 (004, 36)	cataclasite	caliche cover
Lower Big Box Canyon	6	144	0.050	Set 1	dark	
Lower Big Box Canyon	7	154	0.050	Set 1	dark	
Lower Big Box Canyon	8	160	0.050	Set 1	dark	
Lower Big Box Canyon	9	161	0.215	Set 2	orange	
Lower Big Box Canyon	10	175	0.140	Set 2	dark	
Lower Big Box Canyon	11	176	0.095	Set 2	dark	
Lower Big Box Canyon	12	188	0.075	Set 2	dark	
Lower Big Box Canyon	13	190	0.095	Set 1	dark	
Lower Big Box Canyon	14	192	0.265	Set 2 (174, 75)	cataclasite (tan)	
Lower Big Box Canyon	15	196	0.062	Set 4	dark	
Lower Big Box Canyon	16	210	0.400	Set 2	open/eroded	
Lower Big Box Canyon	17	232	0.175	Set 2	open/eroded	1 mm, down to the east, offsets set 1
Lower Big Box Canyon	18	234	0.175	Set 2	open/eroded	

Site	Fracture (#)	Distance (mm)	App. Width (mm)*	Orientation (RHR)†	Fill	Notes
Lower Big Box Canyon	19	239	0.075	Set 2	open/eroded	
Lower Big Box Canyon	20	246	0.095	Set 2	open/eroded	
Lower Big Box Canyon	21	248	0.175	Set 2	open/eroded	
Lower Big Box Canyon	22	253	0.265	Set 2 (233, 90)	open/eroded	
Lower Big Box Canyon	23	267	0.620	Set 2	dark	
Lower Big Box Canyon	24	296	0.265	Set 1	dark	
Lower Big Box Canyon	25	309	0.115	Set 4	dark	
Lower Big Box Canyon	26	320	0.050	Set 2	dark	
Lower Big Box Canyon	27	321	0.050	Set 1	dark	
Lower Big Box Canyon	28	328	0.062	Set 2	dark	
Lower Big Box Canyon	29	334	0.330	Set 1 (009, 30)	dark	
Lower Big Box Canyon	30	339	0.140	Set 2	cataclasite (tan)	
Lower Big Box Canyon	31	341	0.095	Set 1	dark	
Lower Big Box Canyon	32	342	0.115	Set 1	dark	
Lower Big Box Canyon	33	344	0.115	Set 2	dark	
Lower Big Box Canyon	34	346	0.175	Set 2	dark	
Lower Big Box Canyon	35	348	0.140	Set 1	dark	
Lower Big Box Canyon	36	350	0.095	Set 1	dark	
Lower Big Box Canyon	37	351	0.140	Set 1	dark	
Lower Big Box Canyon	38	352	0.115	Set 1	dark	
Lower Big Box Canyon	39	359	0.175	Set 2 (182, 72)	open/eroded	
Lower Big Box Canyon	40	361	0.175	Set 2	open/eroded	
Lower Big Box Canyon	41	365	0.050	Set 4	dark	
Lower Big Box Canyon	42	368	0.050	Set 4	dark	
Lower Big Box Canyon	43	372	0.500	Set 1	dark	
Lower Big Box Canyon	44	374	0.215	Set 1	dark	
Lower Big Box Canyon	45	378	0.215	Set 1	dark	
Lower Big Box Canyon	46	381	0.140	Set 2	dark	

Site	Fracture (#)	Distance (mm)	App. Width (mm)*	Orientation (RHR)†	Fill	Notes
Lower Big Box Canyon	47	389	0.265	Set 1	dark red (hematite?)	anastamosing
Lower Big Box Canyon	48	399	0.050	Set 4	open	short
Lower Big Box Canyon	49	406	0.062	Set 4	dark/open	
Lower Big Box Canyon	50	408	0.050	Set 4	open/dark	
Lower Big Box Canyon	51	413	0.050	Set 4	dark	
Lower Big Box Canyon	52	421	0.140	Set 2	dark/open	
Lower Big Box Canyon	53	426	0.075	Set 2	dark	
Lower Big Box Canyon	54	428	0.075	Set 2	dark	
Lower Big Box Canyon	55	435	0.500	Set 1	dark	
Lower Big Box Canyon	56	438	0.095	Set 2	dark	
Lower Big Box Canyon	57	500	0.950	Set 2 (176, 72)	cataclasite	
Lower Big Box Canyon	58	505	0.620	Set 2	cataclasite	
Lower Big Box Canyon	59	510	0.950	Set 2	cataclasite	
Lower Big Box Canyon	60	516	0.095	Set 2	dark	
Lower Big Box Canyon	61	524	0.075	Set 2	dark	short
Lower Big Box Canyon	62	560	0.215	Set 1	dark	
Lower Big Box Canyon	63	572	0.140	Set 2	dark	
Lower Big Box Canyon	64	577	0.050	Set 2	dark	
Lower Big Box Canyon	65	592	0.115	Set 2	dark	
Lower Big Box Canyon	66	601	0.140	Set 2	dark	
Lower Big Box Canyon	67	606	0.050	Set 2	dark	short
Lower Big Box Canyon	68	608	0.140	Set 2	dark	short
Lower Big Box Canyon	69	609	0.075	Set 2	dark	short
Lower Big Box Canyon	70	612	0.050	Set 2	dark	short
Lower Big Box Canyon	71	627	0.265	Set 2	dark/open	
Lower Big Box Canyon	72	638	0.095	Set 2	dark	
Lower Big Box Canyon	73	657	0.095	Set 4	dark	
Lower Big Box Canyon	74	658	0.095	Set 1	dark	

Site	Fracture (#)	Distance (mm)	App. Width (mm)*	Orientation (RHR)†	Fill	Notes
Lower Big Box Canyon	75	660	0.175	Set 4	dark	
Lower Big Box Canyon	76	661	0.062	Set 4	dark	
Lower Big Box Canyon	77	666	0.050	Set 1	dark	
Lower Big Box Canyon	78	674	1.150	Set 1	dark cataclasite	cataclastic fill in set 2 cuts set 1
Lower Big Box Canyon	79	686	0.115	Set 1	dark	
Lower Big Box Canyon	80	707	0.750	Set 1	dark	
Lower Big Box Canyon	81	727	0.050	Set 1	dark	
Lower Big Box Canyon	82	728	0.075	Set 1	dark	
Lower Big Box Canyon	83	730	0.050	Set 2	dark	
Lower Big Box Canyon	84	734	0.095	Set 2	dark	
Lower Big Box Canyon	85	741	0.075	Set 2	dark	
Lower Big Box Canyon	86	743	0.062	Set 2	dark	
Lower Big Box Canyon	87	744	0.140	Set 2	dark	
Lower Big Box Canyon	88	756	0.500	Set 2	cataclasite (tan)	
Lower Big Box Canyon	89	761	0.265	Set 2	cataclasite (tan)	
Lower Big Box Canyon	90	763	0.620	Set 1	dark	
Lower Big Box Canyon	91	766	0.062	Set 1	dark	
Lower Big Box Canyon	92	770	0.400	Set 1	dark	
Lower Big Box Canyon	93	771	0.140	Set 1	dark	
Lower Big Box Canyon	94	780	0.215	Set 1	dark	
Lower Big Box Canyon	95	781	0.095	Set 1	dark	
Lower Big Box Canyon	96	784	0.140	Set 4	dark	
Lower Big Box Canyon	97	787	0.175	Set 4	dark	
Lower Big Box Canyon	98	799	0.095	Set 4	dark	
Lower Big Box Canyon	99	809	0.095	Set 1	dark	
Lower Big Box Canyon	100	821	0.330	Set 1	dark	
Lower Big Box Canyon	101	823	0.265	Set 1	dark	
Lower Big Box Canyon	102	842	0.095	Set 4	open	

Site	Fracture (#)	Distance (mm)	App. Width (mm)*	Orientation (RHR)†	Fill	Notes
Lower Big Box Canyon	103	844	2.650	Set 1	cataclasite	
Lower Big Box Canyon	104	853	0.215	Set 2	dark	
Lower Big Box Canyon	105	872	0.750	Set 1	dark cataclasite	
Lower Big Box Canyon	106	915	0.500	Set 2	dark	
Lower Big Box Canyon	107	921	0.075	Set 2	dark	short
Lower Big Box Canyon	108	984	0.500	Set 1	dark	
Lower Big Box Canyon	109	986	0.095	Set 1	dark	
Lower Big Box Canyon	110	1008	0.175	Set 4	cataclasite (tan)	
Lower Big Box Canyon	111	1013	2.150	Set 4	dark cataclasite	
Lower Big Box Canyon	112	1039	0.215	Set 2	dark	
Lower Big Box Canyon	113	1042	0.215	Set 2	dark	
Upper Little Box Canyon	1	27	0.050	Set 1	-	
Upper Little Box Canyon	2	28	0.050	Set 1	-	
Upper Little Box Canyon	3	29	0.050	Set 1	-	
Upper Little Box Canyon	4	30	0.050	Set 1	-	
Upper Little Box Canyon	5	31	0.050	Set 1	-	
Upper Little Box Canyon	6	32	0.050	Set 1	-	
Upper Little Box Canyon	7	33	0.050	Set 1	-	
Upper Little Box Canyon	8	33	0.050	Set 1	-	
Upper Little Box Canyon	9	34	0.050	Set 1	-	
Upper Little Box Canyon	10	36	0.050	-	-	
Upper Little Box Canyon	11	44	0.050	Set 1	-	
Upper Little Box Canyon	12	45	0.050	Set 1	-	
Upper Little Box Canyon	13	46	0.050	Set 1	-	
Upper Little Box Canyon	14	49	0.050	Set 1	-	
Upper Little Box Canyon	15	51	0.050	Set 1	-	
Upper Little Box Canyon	16	53	0.050	Set 1	-	

Site	Fracture (#)	Distance (mm)	App. Width (mm)*	Orientation (RHR)†	Fill	Notes
Upper Little Box Canyon	17	56	0.330	Set 1	-	
Upper Little Box Canyon	18	58	0.215	Set 1	-	
Upper Little Box Canyon	19	62	0.050	Set 1	-	
Upper Little Box Canyon	20	72	0.050	Set 1	-	
Upper Little Box Canyon	21	73	0.050	Set 1	-	
Upper Little Box Canyon	22	77	0.050	Set 1	-	
Upper Little Box Canyon	23	86	0.050	Set 1	-	
Upper Little Box Canyon	24	90	0.140	Set 1	open	
Upper Little Box Canyon	25	104	0.050	Set 1	-	
Upper Little Box Canyon	26	106	0.050	Set 1	-	
Upper Little Box Canyon	27	108	0.500	Set 1	calcite	
Upper Little Box Canyon	28	109	0.075	Set 2	open	
Upper Little Box Canyon	29	144	0.050	Set 1	-	
Upper Little Box Canyon	30	148	0.400	Set 1	calcite	
Upper Little Box Canyon	31	208	0.050	Set 1	-	
Upper Little Box Canyon	32	220	0.050	Set 1	-	
Upper Little Box Canyon	33	224	0.050	Set 1	-	
Upper Little Box Canyon	34	226	0.050	Set 1	-	
Upper Little Box Canyon	35	245	0.050	Set 1	-	
Upper Little Box Canyon	36	251	0.050	Set 2	-	
Upper Little Box Canyon	37	274	0.050	Set 1	-	
Upper Little Box Canyon	38	309	0.140	Set 1	-	
Upper Little Box Canyon	39	317	0.050	Set 1	-	
Upper Little Box Canyon	40	335	1.400	Set 1	cataclasite	
Upper Little Box Canyon	41	340	0.950	Set 1	cataclasite	
Upper Little Box Canyon	42	347	0.050	Set 1	-	
Upper Little Box Canyon	43	352	0.050	Set 2	-	
Upper Little Box Canyon	44	360	1.750	Set 2	cataclasite	

Site	Fracture (#)	Distance (mm)	App. Width (mm)*	Orientation (RHR)†	Fill	Notes
Upper Little Box Canyon	45	394	0.265	Set 3	open	
Upper Little Box Canyon	46	400	0.050	Set 2	-	
Upper Little Box Canyon	47	417	0.050	Set 2	open	
Upper Little Box Canyon	48	438	0.050	Set 4	open	
Upper Little Box Canyon	49	446	0.950	Set 3	open	
Upper Little Box Canyon	50	470	0.050	Set 3	-	
Upper Little Box Canyon	51	479	0.062	Set 1	open	
Upper Little Box Canyon	52	481	0.062	Set 1	open	
Upper Little Box Canyon	53	496	0.750	Set 3	cataclasite	
Upper Little Box Canyon	54	514	0.050	Set 1	-	
Upper Little Box Canyon	55	517	0.050	Set 3	-	
Upper Little Box Canyon	56	531	0.050	Set 1	-	
Upper Little Box Canyon	57	535	0.050	Set 1	-	
Upper Little Box Canyon	58	537	0.265	Set 1	-	
Upper Little Box Canyon	59	545	0.140	Set 1	open	
Upper Little Box Canyon	60	547	0.050	Set 1	-	
Upper Little Box Canyon	61	548	0.050	Set 1	-	
Upper Little Box Canyon	62	562	0.050	Set 1	-	
Upper Little Box Canyon	63	564	0.050	Set 1	-	
Upper Little Box Canyon	64	604	0.062	Set 1	open	
Upper Little Box Canyon	65	625	0.095	Set 2	open	
Upper Little Box Canyon	66	634	0.050	Set 1	-	
Upper Little Box Canyon	67	667	0.050	Set 1	-	
Upper Little Box Canyon	68	691	1.150	Set 1	cataclasite	
Upper Little Box Canyon	69	702	0.050	Set 1	-	
Upper Little Box Canyon	70	704	0.050	Set 1	-	
Upper Little Box Canyon	71	705	0.050	Set 1	-	
Upper Little Box Canyon	72	708	0.050	Set 1	-	

Site	Fracture (#)	Distance (mm)	App. Width (mm)*	Orientation (RHR)†	Fill	Notes
Upper Little Box Canyon	73	710	0.050	Set 1	-	
Upper Little Box Canyon	74	713	0.050	Set 1	-	
Upper Little Box Canyon	75	715	0.400	Set 1	cataclasite	
Upper Little Box Canyon	76	781	0.050	Set 1	-	
Upper Little Box Canyon	77	797	0.050	Set 1	-	
Upper Little Box Canyon	78	806	0.050	Set 2	-	
Upper Little Box Canyon	79	811	0.095	Set 1	-	
Upper Little Box Canyon	80	818	0.050	Set 1	-	
Upper Little Box Canyon	81	820	0.750	Set 1	cataclasite	
Upper Little Box Canyon	82	879	0.050	Set 1	-	
Upper Little Box Canyon	83	904	0.050	Set 4	-	
Upper Little Box Canyon	84	919	0.050	Set 3	-	
Upper Little Box Canyon	85	931	0.050	Set 1	-	
Upper Little Box Canyon	86	944	0.050	Set 2	-	
Upper Little Box Canyon	87	950	0.050	Set 3	open	
Upper Little Box Canyon	88	969	0.050	Set 1	-	
Upper Little Box Canyon	89	977	0.050	Set 4	-	
Upper Little Box Canyon	90	978	0.050	Set 1	open	
Upper Little Box Canyon	91	979	0.050	Set 1	-	
Upper Little Box Canyon	92	980	0.050	Set 1	-	
Upper Little Box Canyon	93	981	0.050	Set 1	-	
Upper Little Box Canyon	94	982	0.050	Set 1	-	
Upper Little Box Canyon	95	983	0.050	Set 1	-	
Upper Little Box Canyon	96	984	0.050	Set 1	-	
Upper Little Box Canyon	97	985	0.140	Set 3	-	
Upper Little Box Canyon	98	995	0.050	Set 4	open	
Upper Little Box Canyon	99	998	0.050	Set 3	-	
Upper Little Box Canyon	100	1000	0.050	Set 3	-	

Site	Fracture (#)	Distance (mm)	App. Width (mm)*	Orientation (RHR)†	Fill	Notes
Upper Little Box Canyon	101	1015	0.140	Set 3	open	
Upper Little Box Canyon	102	1020	0.050	Set 3	-	
Upper Little Box Canyon	103	1022	0.050	Set 3	-	
Upper Little Box Canyon	104	1025	0.050	Set 4	-	
Upper Little Box Canyon	105	1035	0.050	Set 1	-	
Upper Little Box Canyon	106	1045	0.050	Set 4	-	
Upper Little Box Canyon	107	1056	0.050	Set 1	-	
Upper Little Box Canyon	108	1063	0.050	Set 1	-	
Upper Little Box Canyon	109	1064	0.050	Set 1	-	
Upper Little Box Canyon	110	1065	0.050	Set 3	-	
Upper Little Box Canyon	111	1087	0.400	Set 3	dark	
Upper Little Box Canyon	112	1095	0.050	Set 3	closed	
Upper Little Box Canyon	113	1100	0.050	Set 3	open	
Upper Little Box Canyon	114	1108	0.050	Set 3	-	
Upper Little Box Canyon	115	1133	0.215	Set 1	cataclasite	
Upper Little Box Canyon	116	1135	0.500	Set 1	cataclasite	
Upper Little Box Canyon	117	1162	0.050	Set 1	-	
Upper Little Box Canyon	118	1166		Set 3	-	
Upper Little Box Canyon	119	1175	0.050	Set 3	-	
Upper Little Box Canyon	120	1177	0.050	Set 3	-	
Upper Little Box Canyon	121	1192	0.050	Set 1	-	
Upper Little Box Canyon	122	1195	0.050	Set 3	-	
Upper Little Box Canyon	123	1198	0.050	Set 1	-	
Upper Little Box Canyon	124	1215	0.050	Set 1	-	
Upper Little Box Canyon	125	1222	0.750	Set 1	cataclasite	
Upper Little Box Canyon	126	1233	0.330	Set 3	open	
Upper Little Box Canyon	127	1241	0.050	Set 1	-	
Upper Little Box Canyon	128	1256	0.400	Set 1		

Site	Fracture (#)	Distance (mm)	App. Width (mm)*	Orientation (RHR)†	Fill	Notes
Upper Little Box Canyon	129	1281	0.400	Set 3	cataclasite	
Upper Little Box Canyon	130	1326		Set 3	-	
Upper Little Box Canyon	131	1332	0.050	Set 4	-	
Upper Little Box Canyon	132	1339	0.050	Set 1	-	
Upper Little Box Canyon	133	1349		Set 3	-	
Upper Little Box Canyon	134	1361	0.050	Set 2	-	
Upper Little Box Canyon	135	1370	0.050	Set 4	-	
Upper Little Box Canyon	136	1380	0.400	Set 1	orange	
Upper Little Box Canyon	137	1389	0.950	Set 1	cataclastie, green	
Upper Little Box Canyon	138	1396	0.330	Set 1	cataclasite	
Upper Little Box Canyon	139	1402	0.050	Set 4	-	
Upper Little Box Canyon	140	1407	2.650	Set 1	cataclasite	
Upper Little Box Canyon	141	1429	0.050	Set 4	-	
Upper Little Box Canyon	142	1451	1.750	Set 3	cataclasite	
Middle Little Box Canyon		100				start of scan line
Middle Little Box Canyon	1	101	1.400	Set 1	hematite	
Middle Little Box Canyon	2	125	0.095		dark	
Middle Little Box Canyon	3	141	0.400	Set 1	hematite	
Middle Little Box Canyon	4	155	0.400		dark	
Middle Little Box Canyon	5	160	0.400		dark	
Middle Little Box Canyon	6	167	0.175		dark	
Middle Little Box Canyon	7	189	0.075		open	
Middle Little Box Canyon		190				transition to chlorite halo
Middle Little Box Canyon	8	192	0.095		open	chlorite
Middle Little Box Canyon	9	211	0.750		hematite	chlorite
Middle Little Box Canyon	10	217	2.150	Set 1	hematite banded	chlorite
Middle Little Box Canyon	11	243	0.620	Set 1	hematite and qtz	chlorite

Site	Fracture (#)	Distance (mm)	App. Width (mm)*	Orientation (RHR)†	Fill	Notes
Middle Little Box Canyon	12	253	0.175	Set 1	hematite	chlorite
Middle Little Box Canyon	13	260	1.150	Set 1	hematite	chlorite
Middle Little Box Canyon	14	270	0.050	Set 1	dark	chlorite
Middle Little Box Canyon	15	276	0.140		dark	leaving chlorite halo
Middle Little Box Canyon	16	278	0.085		dark	
Middle Little Box Canyon	17	282	0.265	Set 1	dark	
Middle Little Box Canyon	18	288	4.000	288, 78	cataclasite	
Middle Little Box Canyon	19	310	1.000	288, 78	cataclasite	
Middle Little Box Canyon	20	340	0.050		dark	
Middle Little Box Canyon	21	350	5.000	340, 16	dark, hematite	
Middle Little Box Canyon	22	405	0.095	Set 1	dark	
Middle Little Box Canyon	23	406	0.050	Set 1	dark	
Middle Little Box Canyon	24	476	1.150	272, 79	cataclasite	
Middle Little Box Canyon	25	500	0.050		dark	
Middle Little Box Canyon	26	536	0.050		dark	
Middle Little Box Canyon	27	537	0.050		dark	
Middle Little Box Canyon		540				transition to chlorite
Middle Little Box Canyon	28	568	0.050	Set 1	dark	chlorite
Middle Little Box Canyon	29	579	0.500	Set 1		chlorite
Middle Little Box Canyon	30	590	0.620	Set 1	hematite	chlorite
Middle Little Box Canyon	31	600	0.330	Set 1	hematite	chlorite
Middle Little Box Canyon	32	607	0.620	Set 1	hematite	chlorite
Middle Little Box Canyon	33	611	0.500	Set 1	hematite	chlorite
Middle Little Box Canyon	34	628	0.095	Set 1	hematite	chlorite
Middle Little Box Canyon	35	632	10.000	Set 1	cataclasite, hematite	chlorite
Middle Little Box Canyon	36	647	0.115	Set 1	hematite	chlorite
Middle Little Box Canyon	37	659	0.950	Set 1	hematite	chlorite
Middle Little Box Canyon	38	692	0.620	Set 1	hematite	chlorite

Site	Fracture (#)	Distance (mm)	App. Width (mm)*	Orientation (RHR)†	Fill	Notes
Middle Little Box Canyon		720				leaving chlorite halo
Middle Little Box Canyon	39	724	0.215		dark	
Middle Little Box Canyon	40	741	0.215		dark	
Middle Little Box Canyon		800				end of scan line
Lower Little Box Canyon	1	11	0.400		calcite	Chlorite
Lower Little Box Canyon	2	12	0.400		calcite	Chlorite
Lower Little Box Canyon	3	17	0.175		calcite, hematite	Chlorite
Lower Little Box Canyon	4	35	0.075		calcite	Chlorite
Lower Little Box Canyon	5	80	0.330		calcite, hematite	Chlorite
Lower Little Box Canyon	6	86	0.500		calcite, hematite	Chlorite
Lower Little Box Canyon	7	190	0.075		calcite	Chlorite
Lower Little Box Canyon	8	252	0.140		open	Chlorite
Lower Little Box Canyon	9	258	0.062		-	Chlorite
Lower Little Box Canyon		270				leaving chlorite halo
Lower Little Box Canyon	10	372	0.500	194, 64	calcite	
Lower Little Box Canyon	11	513	3.300	335, 56	calcite, hematite	
Lower Little Box Canyon	12	518	4.000	166, 69	calcite, hematite	
Lower Little Box Canyon	13	527	0.400	016, 82	calcite, hematite	
Lower Little Box Canyon	14	590	0.050		open	
Lower Little Box Canyon	15	630	0.620		hematite	
Lower Little Box Canyon	16	642	0.050		open	
Lower Little Box Canyon	17	644	0.050		open	
Lower Little Box Canyon	18	645	0.050	240, 71	open	
Lower Little Box Canyon	19	686	0.050	240, 71	open	
Lower Little Box Canyon	20	758	0.400	240, 71	hematite	
Lower Little Box Canyon	21	772	0.050	240, 71	open	
Lower Little Box Canyon	22	780	0.050		open	

Site	Fracture (#)	Distance (mm)	App. Width (mm)*	Orientation (RHR)†	Fill	Notes
Lower Little Box Canyon	23	782	0.050		open	
Lower Little Box Canyon	24	792	0.050		open	
Lower Little Box Canyon	25	794	0.050		open	
Lower Little Box Canyon		800				transition to chlorite
Lower Little Box Canyon	26	845	0.175	007, 79	calcite, hematite	Chlorite
Lower Little Box Canyon	27	878	0.750	029, 70	calcite, hematite	Chlorite
Lower Little Box Canyon	28	902	0.095		calcite	Chlorite
Lower Little Box Canyon	29	906	0.330		calcite	Chlorite
Lower Little Box Canyon	30	908	0.265		calcite	Chlorite
Lower Little Box Canyon	31	930	0.050		open	leaving chlorite halo
Lower Little Box Canyon	32	958	0.215		hematite	
Lower Little Box Canyon	33	978	0.095		open	
Lower Little Box Canyon	34	984	0.330	015, 69	open	
Lower Little Box Canyon	35	990	0.050		open	
Lower Little Box Canyon	36	1019	0.265	011, 86	calcite, hematite	
Lower Little Box Canyon		1020				transition to chlorite
Lower Little Box Canyon	37	1029	0.330	010, 90	calcite, hematite	Chlorite
Lower Little Box Canyon	38	1072	0.050		open	Chlorite
Lower Little Box Canyon	39	1074	0.620	017, 90	calcite, hematite	Chlorite
Lower Little Box Canyon	40	1089	0.050	017, 90	open	Chlorite
Lower Little Box Canyon	41	1094	0.095		dark gray	leaving chlorite halo
Lower Little Box Canyon		1100				
Lower Little Box Canyon	42	1256	0.050	019, 90	open	
Lower Little Box Canyon	43	1264	0.175		open	
Lower Little Box Canyon	44	1268	0.095	019, 90	dark gray	
Lower Little Box Canyon	45	1303	0.265		calcite, hematite	
Lower Little Box Canyon	46	1355	0.175		hematite	
Lower Little Box Canyon	47	1360	0.050		open	

Site	Fracture (#)	Distance (mm)	App. Width (mm)*	Orientation (RHR)†	Fill	Notes
Lower Little Box Canyon	48	1370	0.050		open	
Lower Little Box Canyon	49	1378	1.400		hematite	
Lower Little Box Canyon		1410				transition to chlorite
Lower Little Box Canyon	50	1418	1.750	301, 21	calcite, hematite	Chlorite
Lower Little Box Canyon	51	1439	0.140		calcite	Chlorite
Lower Little Box Canyon	52	1444	0.175		calcite	Chlorite
Lower Little Box Canyon	53	1515	0.500		calcite, hematite, qtz	Chlorite
Lower Little Box Canyon	54	1522	0.050		open	Chlorite
Lower Little Box Canyon	55	1527	0.050		open	Chlorite
Lower Little Box Canyon	56	1532	0.050		open	Chlorite
Lower Little Box Canyon	57	1546	0.050		open	leaving chlorite halo
Lower Little Box Canyon		1580				
Lower Little Box Canyon	58	1591	0.050		open	
Lower Little Box Canyon	59	1654	0.050		open	
Lower Little Box Canyon	60	1660	0.050		open	
Lower Little Box Canyon	61	1681	0.050		open	
Lower Little Box Canyon	62	1690	0.330		calcite	
Lower Little Box Canyon	63	1732	0.400		hematite	
Lower Little Box Canyon	64	1742	1.750		hematite	shear
Lower Little Box Canyon	65	1752	0.950		hematite	
Lower Little Box Canyon	66	1756	0.330		hematite	shear
Lower Little Box Canyon	67	1760	1.150		hematite	shear
Lower Little Box Canyon	68	1791	0.950		hematite	shear
Lower Little Box Canyon	69	1810	1.150	344, 22	hematite	shear
Lower Little Box Canyon	70	1830	2.150	344, 22	hematite	
Lower Little Box Canyon	71	1908	0.050	056, 80	open	
Lower Little Box Canyon	72	1982	0.500	051, 90	hematite	
Lower Little Box Canyon	73	1986	1.150		hematite	

Site	Fracture (#)	Distance (mm)	App. Width (mm)*	Orientation (RHR)†	Fill	Notes
Lower Little Box Canyon	74	2093	0.175		dark	
Lower Little Box Canyon	75	2111	0.330	046, 85	hematite	
Lower Little Box Canyon	76	2172	0.050	011, 85		
Lower Little Box Canyon	77	2174	0.050	011, 85		
Lower Little Box Canyon		2190				Chlorite
Lower Little Box Canyon	78	2366	0.620	007, 44	calcite, hematite	Chlorite
Lower Little Box Canyon	79	2374	0.330	shallow	open	Chlorite
Lower Little Box Canyon	80	2382	0.500	shallow	calcite, hematite	Chlorite
Lower Little Box Canyon	81	2436	0.950	062, 69	hematite	Chlorite
Lower Little Box Canyon	82	2475	0.950		hematite	Chlorite
Lower Little Box Canyon	83	2491	0.620		dark	leaving chlorite halo
Lower Little Box Canyon	84	2500	0.500		dark	
Lower Little Box Canyon	85	2501	0.500		dark	
Lower Little Box Canyon	86	2533	0.400		dark	
Lower Little Box Canyon	87	2543	0.140		dark	
Lower Little Box Canyon	88	2587	0.400		open	
Lower Little Box Canyon	89	2599	0.400	040, 90	open	
Lower Little Box Canyon	90	2603	0.265	040, 90	open	
Lower Little Box Canyon	91	2619	0.330	016, 83	open	
Lower Little Box Canyon	92	2624	0.400		open	
Lower Little Box Canyon	93	2625	0.140		open	Chlorite
Lower Little Box Canyon	94	2626	0.265		open	Chlorite
Lower Little Box Canyon	95	2654	0.500		dark	Chlorite
Lower Little Box Canyon	96	2720	0.750	355, 06	calcite, hematite	Chlorite
Lower Little Box Canyon	97	2749	2.150	005, 79	calcite, hematite	Chlorite
Lower Little Box Canyon	98	2789	0.500	351, 63	calcite, hematite	Chlorite
Lower Little Box Canyon	99	2811	0.265		open	Chlorite
Lower Little Box Canyon	100	2817	0.400		open	leaving chlorite halo

Site	Fracture (#)	Distance (mm)	App. Width (mm)*	Orientation (RHR)†	Fill	Notes
Lower Little Box Canyon		2830				
Lower Little Box Canyon	101	2869	1.400		cataclastic	
Lower Little Box Canyon	102	2876	0.620		dark	
Lower Little Box Canyon	103	2896	0.330	018, 75	calcite, hematite	
Lower Little Box Canyon	104	2898	0.175	018, 75	hematite	
Lower Little Box Canyon	105	2908	0.140	169, 60	unfilled, dark	
Lower Little Box Canyon	106	2912	0.140	169, 60	unfilled, dark	
Lower Little Box Canyon	107	2914	0.140	169, 60	unfilled, dark	
Lower Little Box Canyon	108	2930	0.400	005, 67	dark	
Lower Little Box Canyon	109	2948	2.650	345, 28	hematite	
Lower Little Box Canyon	110	2973	0.175	176, 77	dark	
Lower Little Box Canyon	111	2980	1.400	018, 64	hematite	
Lower Little Box Canyon	112	2991	0.140	019, 69	hematite	
Lower Little Box Canyon		3005				weak Chlorite
Lower Little Box Canyon	113	3017	0.500	231, 72	dark	weak Chlorite
Lower Little Box Canyon	114	3020	0.330	231, 72	dark	weak Chlorite
Lower Little Box Canyon	115	3022	1.150	231, 72	dark	weak Chlorite
Lower Little Box Canyon	116	3026	0.265	231, 72	dark	weak Chlorite
Lower Little Box Canyon	117	3036	0.500		dark	weak Chlorite
Lower Little Box Canyon	118	3038	0.620		dark	weak Chlorite
Lower Little Box Canyon	119	3040	0.050			weak Chlorite
Lower Little Box Canyon	120	3065	0.950		dark	weak Chlorite
Lower Little Box Canyon	121	3068	0.400		dark	weak Chlorite
Lower Little Box Canyon	122	3072	0.750		dark	weak Chlorite
Lower Little Box Canyon	123	3077	0.500		dark w pale interior	weak Chlorite
Lower Little Box Canyon	124	3095	0.950		dark, cataclasite	weak Chlorite
Lower Little Box Canyon	125	3099	0.140		dark	weak Chlorite
Lower Little Box Canyon	126	3100	0.140		dark	weak Chlorite

Site	Fracture (#)	Distance (mm)	App. Width (mm)*	Orientation (RHR)†	Fill	Notes
Lower Little Box Canyon	127	3107	0.095		dark	weak Chlorite
Lower Little Box Canyon	128	3112	1.150		dark	weak Chlorite
Lower Little Box Canyon	129	3126	1.150		calcite	weak Chlorite
Lower Little Box Canyon	130	3133	0.400		calcite	weak Chlorite
Lower Little Box Canyon	131	3140	0.265		dark	weak Chlorite
Lower Little Box Canyon	132	3156	0.215		dark	weak Chlorite
Lower Little Box Canyon	133	3169	0.500	000, 60	dark	weak Chlorite
Lower Little Box Canyon	134	3174	0.140		dark	weak Chlorite
Lower Little Box Canyon	135	3179	0.140		dark	weak Chlorite
Lower Little Box Canyon	136	3187	0.140		dark	weak Chlorite
Lower Little Box Canyon	137	3196	0.950		dark	weak Chlorite
Lower Little Box Canyon	138	3206	0.750		dark	weak Chlorite
Lower Little Box Canyon	139	3217	0.330	001, 65	dark	weak Chlorite
Lower Little Box Canyon	140	3233	0.265		dark	weak Chlorite
Lower Little Box Canyon	141	3237	0.750		dark	weak Chlorite
Lower Little Box Canyon	142	3242	0.140		dark	weak Chlorite
Lower Little Box Canyon	143	3248	0.050			weak Chlorite
Lower Little Box Canyon	144	3258	1.750		dark, cataclasite	weak Chlorite
Lower Little Box Canyon	145	3267	0.050		dark	weak Chlorite
Lower Little Box Canyon	146	3289	0.400		dark	Chlorite
Lower Little Box Canyon	147	3303	0.265		dark	Chlorite
Lower Little Box Canyon	148	3308	2.650	013, 90	calcite, hematite	Chlorite
Lower Little Box Canyon		3327				leaving chlorite halo
Lower Little Box Canyon	149	3332	0.330		dark	
Lower Little Box Canyon	150	3368	0.400		calcite, hematite	
Lower Little Box Canyon	151	3370	0.265		dark	
Lower Little Box Canyon	152	3373	0.115		dark	
Lower Little Box Canyon	153	3382	0.950		dark	

Site	Fracture (#)	Distance (mm)	App. Width (mm)*	Orientation (RHR)†	Fill	Notes
Lower Little Box Canyon	154	3394	0.950		irregular, cataclasite	
Lower Little Box Canyon	155	3396	0.050	221, 86		
Lower Little Box Canyon	156	3397	0.050	221, 86		
Lower Little Box Canyon	157	3410	0.095		dark	
Lower Little Box Canyon		3412				calcite vug to 342 cm
Lower Little Box Canyon	158	3420	4.000	353, 88	calcite, hematite	
Lower Little Box Canyon	159	3436	0.330		dark	
Lower Little Box Canyon	160	3442	0.620		he	
Lower Little Box Canyon	161	3446	1.750	006, 90	calcite, hematite	
Lower Little Box Canyon	162	3460	0.050			
Lower Little Box Canyon	163	3463	0.140		dark	
Lower Little Box Canyon	164	3466	0.215		calcite	
Lower Little Box Canyon	165	3472	0.050		dark	
Lower Little Box Canyon	166	3473	0.050		dark	
Lower Little Box Canyon	167	3474	0.050		dark	
Lower Little Box Canyon	168	3476	0.050		dark	
Lower Little Box Canyon	169	3482	0.050		dark	
Lower Little Box Canyon	170	3494	0.050		dark	
Lower Little Box Canyon	171	3495	0.050		dark	
Lower Little Box Canyon	172	3497	0.950		cataclastic	
Lower Little Box Canyon	173	3498	0.050		dark	
Lower Little Box Canyon	174	3499	0.050			
Lower Little Box Canyon	175	3500	0.500		dark	
Lower Little Box Canyon	176	3502	0.500		dark	
Lower Little Box Canyon	177	3507	0.620		dark	
Lower Little Box Canyon	178	3510	0.050			
Lower Little Box Canyon	179	3511	0.050			
Lower Little Box Canyon	180	3512	0.050			

Site	Fracture (#)	Distance (mm)	App. Width (mm)*	Orientation (RHR)†	Fill	Notes
Lower Little Box Canyon	181	3514	0.500		dark	
Lower Little Box Canyon	182	3519	0.500		dark	
Lower Little Box Canyon	183	3533	0.750	008, 80	dark, calcite	
Lower Little Box Canyon	184	3537	0.400		dark	
Lower Little Box Canyon	185	3539	0.265		dark	
Lower Little Box Canyon	186	3544	0.400		dark	
Dixie Comstock, South	1	1000	50.0	357, 52	qtz	
Dixie Comstock, South	2	1430	7.0	168, 82	qtz with calcite	start of stockwork
Dixie Comstock, South	3	1470	8.0	231, 51	calcite with minor qtz	
Dixie Comstock, South	4	1560	11.0	344, 87	qtz with calcite	end of stockwork zone
Dixie Comstock, South	5	1810	50.0	267, 16	calcite	actual thickness 0.8 cm
Dixie Comstock, South	6	2200	6.0	328, 39	qtz, gouge	
Dixie Comstock, South	7	2400	3.0	234, 53	calcite	
Dixie Comstock, South	8	2410	4.0	138, 87	qtz and calcite bands	
Dixie Comstock, South	9	2720	18.0	224, 59	calcite in qtz	
Dixie Comstock, South	10	2780	2.0	213, 57	banded qtz and calcite	
Dixie Comstock, South	11	3110	4.0	218, 67	qtz and calcite	
Dixie Comstock, South	12	3310	4.0	006, 44	qtz	shear zone, <1 cm offset
Dixie Comstock, South	13	3890	5.0	171, 65	calcite in gouge bands	
Dixie Comstock, South	14	4340	2.0	345, 90	gouge and calcite	
Dixie Comstock, South	15	4800	10.0	042, 43	gouge	
Dixie Comstock, South	16	4900	1.0	225, 70	calcite	
Dixie Comstock, South	17	5020	1.5	230, 82	calcite	
Dixie Comstock, South	18	5410	6.0	043, 87	qtz and calcite	
Dixie Comstock, South	19	5460	1.0	024, 40	calcite	
Dixie Comstock, South	20	5490	6.0	236, 74	calcite	
Dixie Comstock, South	21	5530	1.5	005, 87	calcite	

Site	Fracture (#)	Distance (mm)	App. Width (mm)*	Orientation (RHR)†	Fill	Notes
Dixie Comstock, South	22	5800	12.0	335, 88	qtz, calcite, hematite, gouge	6 increments
Dixie Comstock, South	23	6000	1.5	242, 55	calcite	
Dixie Comstock, South	24	6120	1.0	046, 79	calcite	
Dixie Comstock, South	25	6390	11.0	004, 62	qtz	vug is 0.6 cm wide
Dixie Comstock, South	26	6500	60.0	140, 74	calcite (brown bands)	
Dixie Comstock, South	27	6610	3.0	195, 78	calcite	
Dixie Comstock, South	28	6650	3.0	148, 70	calcite	
Dixie Comstock, South	29	6910	1.0	165, 64	calcite	
Dixie Comstock, South	30	7110	230.0	168, 65	fine grained gabbro, druzy qtz	stockwork to 734 cm, late calcite
Dixie Comstock, South	31	7420	3.0	050, 55	qtz vein	
Dixie Comstock, South	32	7440	7.0	156, 60	druzy qtz	
Dixie Comstock, South	33	7500	1.5	010, 52	qtz	wavy fracture walls
Dixie Comstock, South	34	7700	2.0	149, 72	druzy qtz in places	shear zone (small)
Dixie Comstock, South	35	8500	6.0	015, 58	qtz	
Dixie Comstock, South	36	9160	3.0	190, 54	qtz	transfer zone (fractures pinch out)
Dixie Comstock, South	37	9180	2.0	180, 36	qtz	transfer zone (fractures pinch out)
Dixie Comstock, South	38	9360	11.0	025, 66	qtz	
Dixie Comstock, South	39	9410	10.0	021, 81	qtz	calcite in vugs
Dixie Comstock, South	40	9900	2.0	000, 54	calcite	
Dixie Comstock, South	41	10090	2.0	315, 57	calcite and gouge	
Dixie Comstock, South	42	10600	1.0	002, 72	qtz	
Dixie Comstock, South	43	10740	7.0	337, 68	one generation of qtz	start of weak stockwork zone
Dixie Comstock, South	44	11010	80.0	019, 53	gabbro clasts and qtz	
Dixie Comstock, South	45	11340	1.0	081, 72	calcite	
Dixie Comstock, South	46	11510	1.0	359, 53	calcite	
Dixie Comstock, South	47	11550	2.0	007, 78	calcite	
Dixie Comstock, South	48	11660	1.0	000, 90	calcite	
Dixie Comstock, South	49	11970	2.0	323, 77	calcite	

Site	Fracture (#)	Distance (mm)	App. Width (mm)*	Orientation (RHR)†	Fill	Notes
Dixie Comstock, South	50	12230	70.0	141, 50	gouge	set of slicks, 15 to SE, calcite
Dixie Comstock, Middle	1	100	24.0	001, 29	qtz	veneer, true thickness 5 mm
Dixie Comstock, Middle	2	138	1.0	015, 84	qtz	
Dixie Comstock, Middle	3	148	4.0	336, 77	qtz	
Dixie Comstock, Middle	4	154	4.0	023, 74	qtz (cloudy and green)	
Dixie Comstock, Middle	5	164	1.0	329, 90	qtz	
Dixie Comstock, Middle	6	174	2.0	354, 59	qtz	
Dixie Comstock, Middle	7	180	2.0	168, 59	qtz	
Dixie Comstock, Middle	8	202	6.0	200, 30	qtz (coudy)	
Dixie Comstock, Middle	9	212	1.5	213, 67	qtz	
Dixie Comstock, Middle	10	235	1.0	028, 82	qtz	
Dixie Comstock, Middle	11	253	42.0	012, 79	qtz and clasts	
Dixie Comstock, Middle	12	321	2.0	166, 72	qtz	
Dixie Comstock, Middle	13	330	2.5	194, 61	qtz	
Dixie Comstock, Middle	14	343	8.0	217, 65	qtz	
Dixie Comstock, Middle	15	350	8.4	077, 13	qtz	true thickness = 3 mm
Dixie Comstock, Middle	16	376	3.0	250, 24	qtz	
Dixie Comstock, Middle	17	408	1.5	022, 80	qtz	covered until 456 mm
Dixie Comstock, Middle	18	456	4.0	275, 81	qtz	
Dixie Comstock, Middle	19	498	15.0	336, 78	qtz	
Dixie Comstock, Middle	20	516	1.5	199, 50	qtz	
Dixie Comstock, Middle	21	565	3.0	349, 50	qtz	
Dixie Comstock, Middle	22	578	2.5	025, 81	qtz	
Dixie Comstock, Middle	23	603	8.0	055, 88	qtz	
Dixie Comstock, Middle	24	650	12.0	236, 65	banded qtz	
Dixie Comstock, Middle	25	710	2.0	179, 63	qtz	
Dixie Comstock, Middle	26	714	5.0	030, 05	qtz	

Site	Fracture (#)	Distance (mm)	App. Width (mm)*	Orientation (RHR)†	Fill	Notes
Dixie Comstock, Middle	27	740	2.5	129, 60	qtz	
Dixie Comstock, Middle	28	760	4.0	034, 79	qtz	
Dixie Comstock, Middle	29	770	4.0	035, 81	qtz	
Dixie Comstock, Middle	30	798	2.0	013, 90	qtz	
Dixie Comstock, Middle	31	812	2.0	179, 83	qtz	
Dixie Comstock, Middle	32	856	1.0	048, 64	qtz	
Dixie Comstock, Middle	33	858	3.0	201, 68	qtz	
Dixie Comstock, Middle	34	865	1.0	011, 81	qtz	
Dixie Comstock, Middle	35	938	2.0	185, 75	qtz	
Dixie Comstock, Middle	36	990	2.5	020, 60	qtz	
Dixie Comstock, Middle	37	994	1.0	019, 64	qtz	
Dixie Comstock, Middle	38	1005	3.0	230, 63	qtz	
Dixie Comstock, Middle	39	1043	13.0	170 61	qtz and clasts	
Dixie Comstock, Middle	40	1078	12.0	041, 90	banded qtz	
Dixie Comstock, Middle	41	1110	1.0	011, 90	qtz	
Dixie Comstock, Middle	42	1124	5.0	010, 68	qtz and clasts	
Dixie Comstock, Middle	43	1150	12.0	032, 50	qtz and clasts	
Dixie Comstock, Middle	44	1190	6.0	177, 71	qtz	
Dixie Comstock, Middle	45	1200	12.0	163, 74	qtz with medial line and clasts	
Dixie Comstock, North	1	190	22.0	028, 79	cloudy qtz and clasts	
Dixie Comstock, North	2	510	1.0	022, 89	gouge and qtz	
Dixie Comstock, North	3	540	1.0	036, 72	qtz	
Dixie Comstock, North	4	812	1.5	012, 77	qtz with porosity	
Dixie Comstock, North	5	902	1.5	024, 75	qtz with euhedral lining	
Dixie Comstock, North	6	1070	6.0	012, 82	microstockwork	qtz on qtz and clasts, late calcite
Dixie Comstock, North	7	1406	2.0	350, 80	cloudy qtz	
Dixie Comstock, North	8	1412	1.0	177, 82	cloudy qtz	

Site	Fracture (#)	Distance (mm)	App. Width (mm)*	Orientation (RHR)†	Fill	Notes
Dixie Comstock, North	9	1450	1.0	053, 80	cloudy qtz	
Dixie Comstock, North	10	1480	28.0	037, 86	cloudy qtz and clasts	sigmoid with left lateral offset
Dixie Comstock, North	11	1526	4.0	356, 82	qtz with medial line	
Dixie Comstock, North	12	1700	1.0	229, 71	qtz	
Dixie Comstock, North	13	1810	1.0	042, 69	qtz	
Dixie Comstock, North	14	2250	1.0	026, 77	cataclastic?	
Dixie Comstock, North	15	2366	2.0	042, 70	calcite	
Dixie Comstock, North	16	2710	4.0	015, 78	qtz	
Dixie Comstock, North	17	3080	1.5	005, 70	qtz and gouge	
Dixie Comstock, North	18	3590	6.0	346, 32	qtz and calcite	
Dixie Comstock, North	19	4500	3.0	004, 39	qtz	
Dixie Comstock, North	20	4800	6.0	008, 40	qtz	true thickness 0.3 cm
Dixie Comstock, North	21	4940	8.0	008, 39	qtz	
Dixie Comstock, North	22	5350	1.0	352, 46	qtz and calcite	
Dixie Comstock, North	23	5860	2.0	002, 59	qtz	
Dixie Comstock, North	24	6000	1.0	042, 80	qtz and calcite	
Dixie Comstock, North	25	6400	1.0	209, 81	qtz	
Dixie Comstock, North	26	6450	1.5	004, 59	qtz	
Dixie Comstock, North	27	6500	3.0	024, 82	qtz	
Dixie Comstock, North	28	6554	1.5	045, 78	qtz	
Dixie Comstock, North	29	6766	2.0	060, 58	qtz	
Dixie Comstock, North	30	6800	1.0	214, 84	qtz	
Dixie Comstock, North	31	6904	2.0	222, 90	qtz	
Dixie Comstock, North	32	7120	1.0	015, 78	qtz	
Dixie Comstock, North	33	7140	1.0	059, 65	qtz	
Dixie Comstock, North	34	7380	1.5	182, 87	qtz	
Dixie Comstock, North	35	7530	9.0	033, 65	qtz	open space is <0.2 cm wide
Dixie Comstock, North	36	7640	19.0	023, 59	cloudy qtz and clasts	

Site	Fracture (#)	Distance (mm)	App. Width (mm)*	Orientation (RHR)†	Fill	Notes
Dixie Comstock, North	37	7670	2.0	018, 78	qtz	
Dixie Comstock, North	38	7680	3.0	019, 85	qtz and medial line	
Dixie Comstock, North	39	7700	5.0	068, 78	qtz	cut by previous fracture
Dixie Comstock, North	40	7740	5.5	033, 51	qtz	true thickness = 0.3
Dixie Comstock, North	41	8850	4.0	024, 42	qtz and calcite blebs	
Dixie Comstock, North	42	8880	4.0	023, 47	qtz with calcite blebs	
Dixie Comstock, North	43	9000	2.0	011, 53	qtz	

J. Appendix: Stable Isotope Composition of Calcite, Dixie and Buena Vista Valleys

Table J.1. Sample Area and Identification, Material, and Stable Isotope Composition

Area	Sample Name*	Description	$\delta^{13}C$ (‰, PDB)	$\delta^{18}O$ (‰, PDB)	$\delta^{18}O$ (‰, SMOW)
Cottonwood Range Front	052715-4A	Boyer carbonate or fumarole relic	-2.9	-30.1	-0.1
Cottonwood Range Front	052715-4B	platy, travertine and sediment	1.4	-15.8	14.7
Cottonwood Range Front	052715-4B dupe	platy, travertine and sediment	1.4	-15.7	14.7
Cottonwood Range Front	052715-5	botryoidal vein in breccia	1.4	-15.2	15.2
Cottonwood Range Front	052715-5 dupe	botryoidal vein in breccia	1.5	-15.1	15.4
Dixie Comstock	052615-4	large blocky vertical vein and breccia	-6.1	-34.3	-4.4
Dixie Comstock	052615-4 dupe	large blocky vertical vein and breccia	-6.0	-34.2	-4.3
Dixie Comstock	052615-5	bladed calcite in fault breccia	-5.6	-32.2	-2.3
Dixie Comstock	052615-6A	bladed calcite from a vertical vein	-5.8	-33.9	-4.0
Dixie Comstock	052615-6A dupe	bladed calcite from a vertical vein	-5.8	-33.7	-3.8
Dixie Comstock	052615-6B	blocky vug fill	-6.0	-34.9	-5.1
Dixie Comstock	052815-1	calcite and barite zone	-5.7	-24.0	6.2
Dixie Comstock	052815-3A	partially calcified gabbro	-5.6	-20.0	10.3
Dixie Comstock	float	bladed calcite, silica cemented	-5.1	-30.4	-0.5
Dixie Meadows	052615-3C	bladed calcite, silica cemented	-4.3	-24.3	5.8
Kyle Hot Springs	053015-1	travertine and sediment from active spring	3.6	-18.2	12.2
Senator Fumaroles	052715-1A	lower fumarole, west side	-3.3	-33.5	-3.6
Senator Fumaroles	052715-1A dupe	lower fumarole, west side	-2.7	-33.2	-3.3
Senator Fumaroles	052715-1B	lower fumarole, near main vent	-3.2	-33.5	-3.6
Senator Fumaroles	052715-2	fault parallel calcite cemented breccia	-1.5	-27.0	3.1

* dupe = duplicate

K. Appendix: Fluid Inclusion Microthermometry, 072013-7

Fluid inclusion microthermometry was conducted on a thick section (~60 μm) of sample 072013-7. The thick section was bonded with super glue and cured at <60 °C. Sample petrography and photomicrographs of fluid inclusions were collected on the full thick section. The slide was then scored, broken, and the super glue was dissolved in acetone to separate rock chips from the glass. Homogenization temperatures for fluid inclusions in seven different assemblages (sites) were measured in the Fluid Inclusions Laboratory at the Bureau of Economic Geology, using a FLUID INC.-adapted USGS-type gas-flow heating/freezing stage mounted on an Olympus BX 51 microscope equipped with a 40X objective, 15X oculars, and up to 2X magnifier, with a maximum magnification of 80X. Homogenization was verified by cooling the chip below inferred homogenization temperatures to observe bubble growth or super-cooled nucleation.

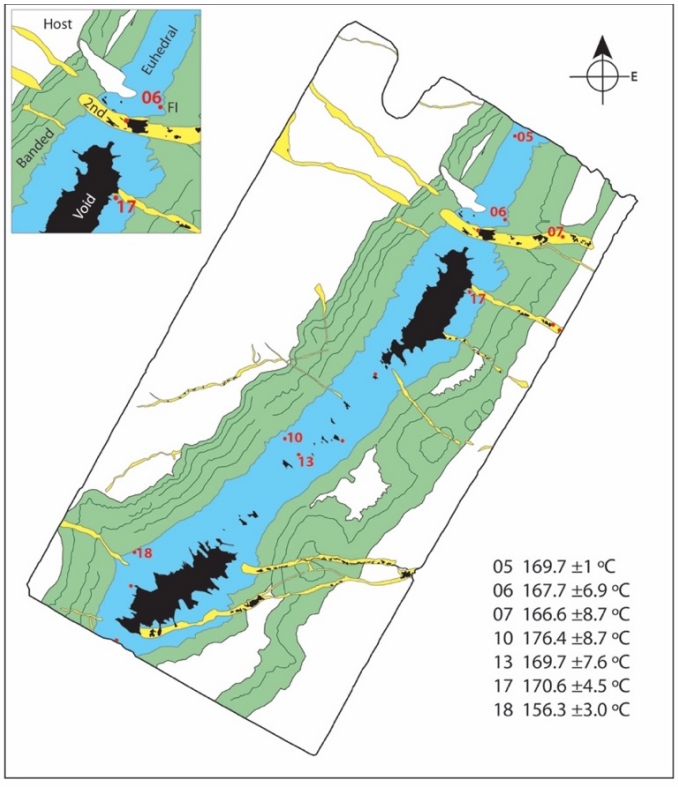

Figure K.1. Trace map of quartz vein textures and fluid inclusion analysis sites for sample 072013-7.

Table K.1. Homogenization Temperatures by Site, Sample 072013-7

Site	5	6		7	10			13	15	17		18
Homogenization Temperatures (°C)*	167.9	156.0	167.2	154.5	162.1	169.3	182.2	153.0	*226.6*	164.4	172.4	153.6
	169.6	158.6	168.5	163.0	163.0	169.8	182.3	165.0		165.2	172.5	153.8
	170.0	165.0	174.0	166.7	167.6	174.0	183.5	166.2		166.2	172.7	154.5
	170.2	165.7	175.0	167.5	167.8	176.1	183.7	166.5		166.4	172.8	158.5
	170.7	166.0	184.7	181.4	167.8	178.0	183.7	167.6		166.8	173.0	161.0
	188.6	166.5	*220.0*	*215.0*	168.0	179.0	183.8	168.0		167.0	177.5	*170.5*
		166.5	*221.0*	*217.8*	168.2	180.1	184.3	169.4		168.8	182.2	*186.5*
		167.0	*234.0*		168.2	180.8	192.0	174.3		170.6	*198.5*	*211.0*
					168.5	181.8	196.4	175.2		170.6	*202.0*	
								179.3		171.2		
								182.2				
Median	170.0	166.5		166.7	178.0			168.0	-	170.6		154.5
Mean	169.7	167.7		166.6	176.4			169..7	-	170.6		156.3
Std Dev	1.0	6.9		8.7	8.7			7.6	-	4.5		3.0

* *Red italicized* numbers denote outliers or poorly behaved inclusions that are not included in site statistics.

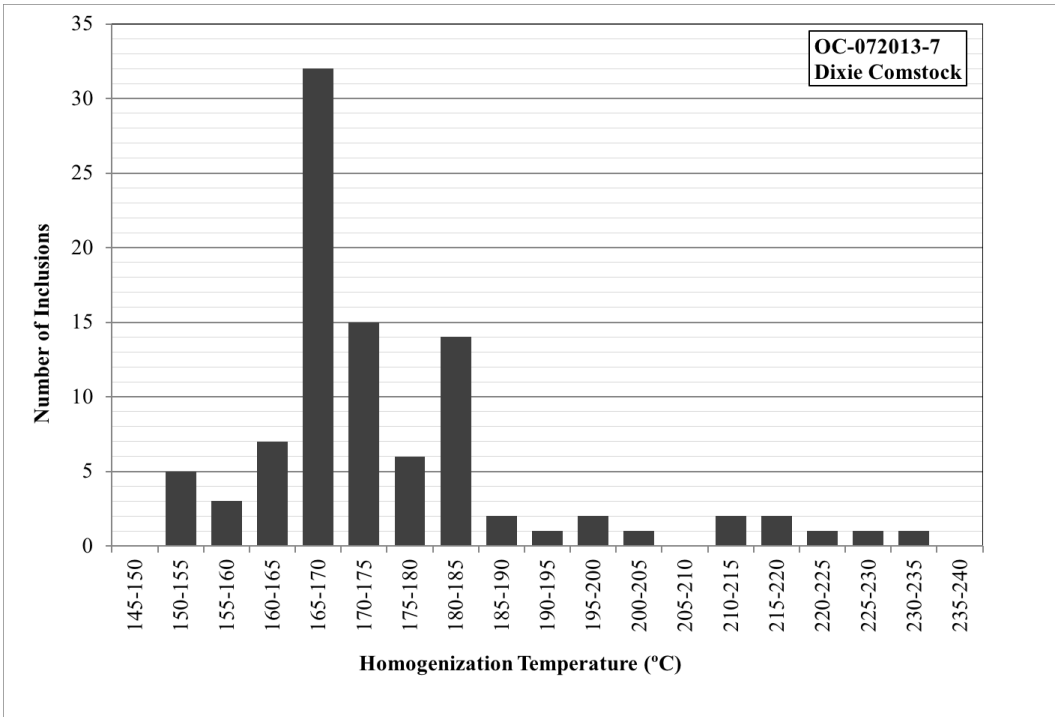

Figure K.2. Histogram showing all homogenization temperatures for sample 072013-7.

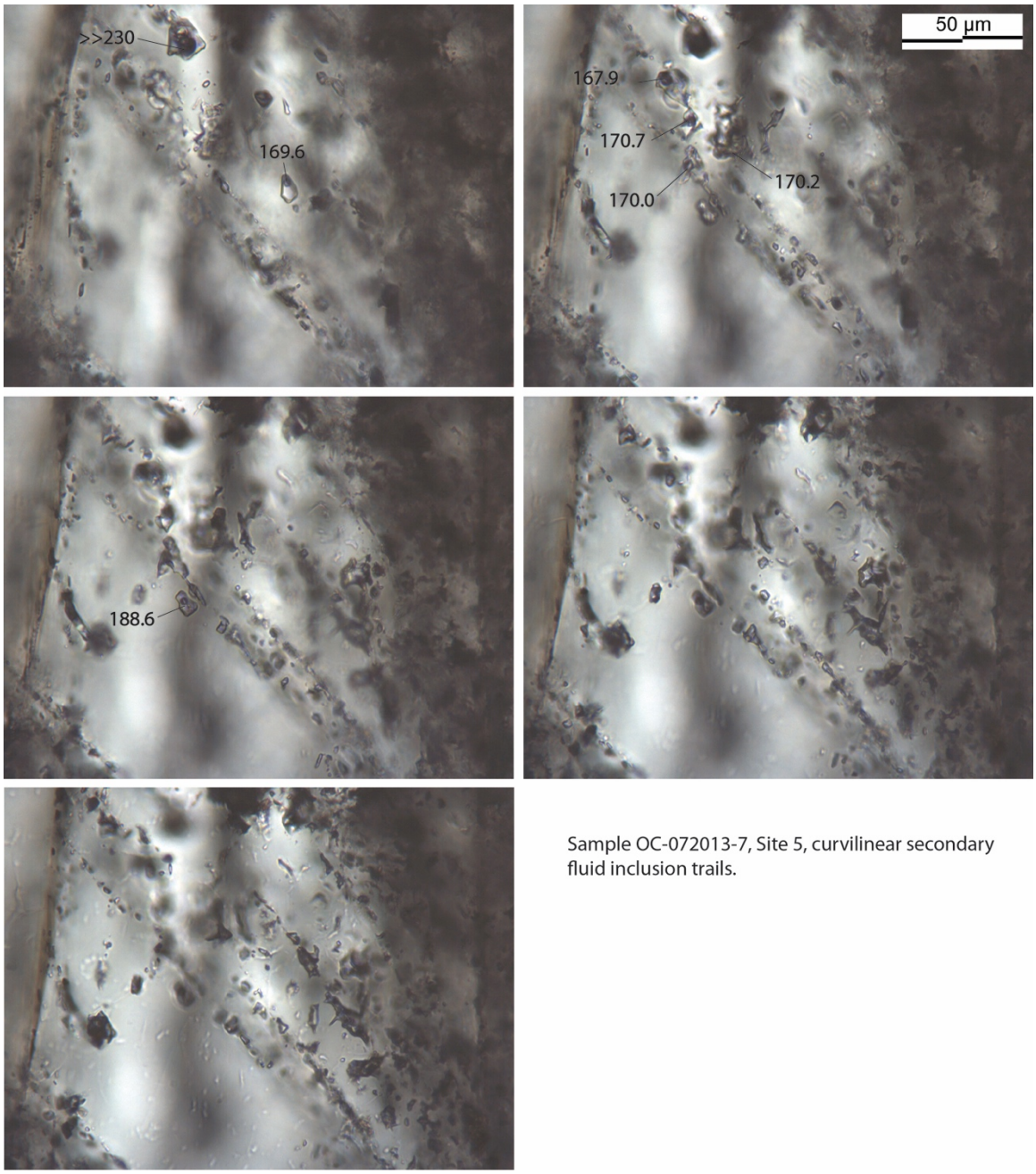

Figure K.3. Photomicrograph of fluid inclusions, site 5, sample 072013-7.

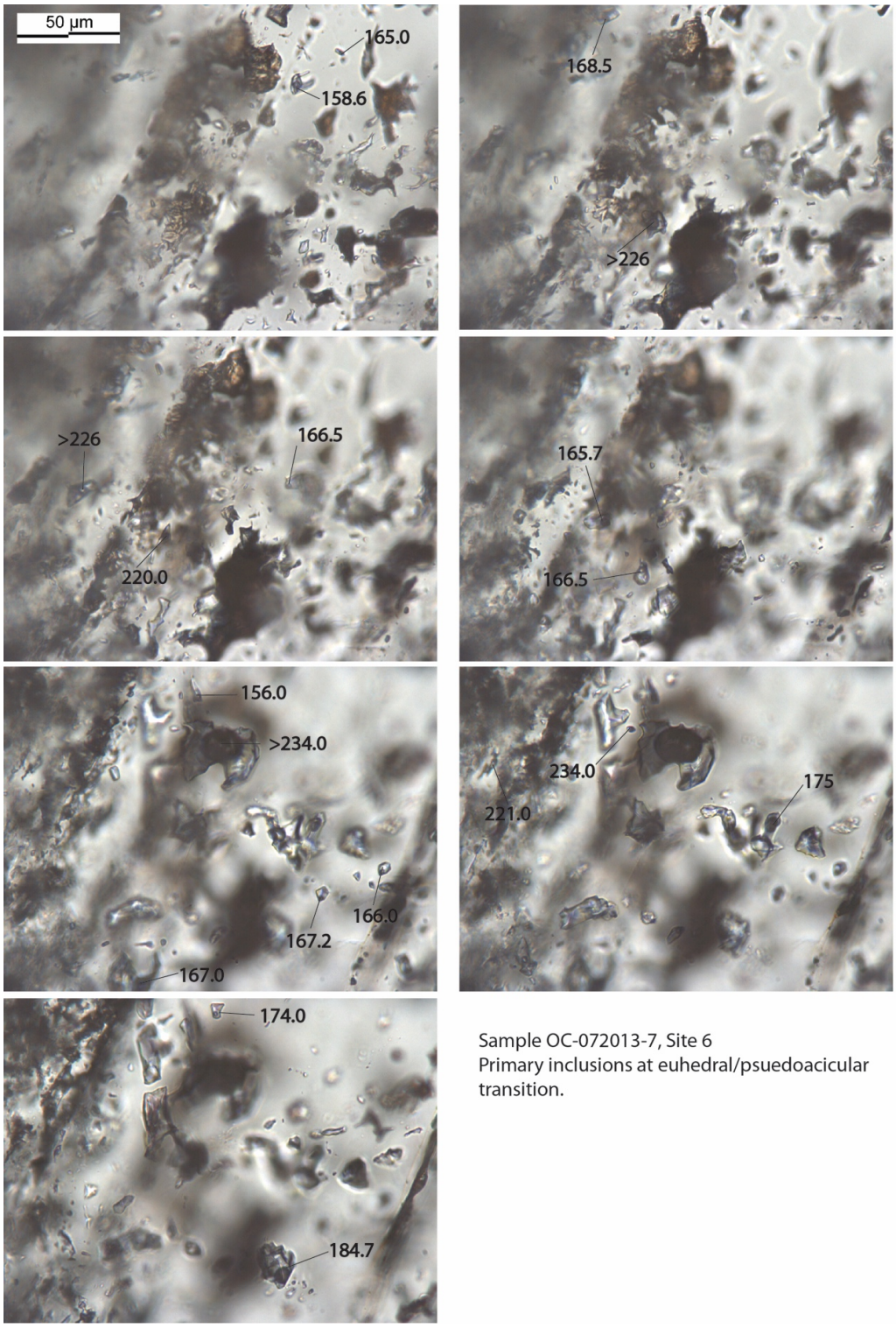

Sample OC-072013-7, Site 6
Primary inclusions at euhedral/psuedoacicular transition.

Figure K.4. Photomicrograph of fluid inclusions, site 6, sample 072013-7.

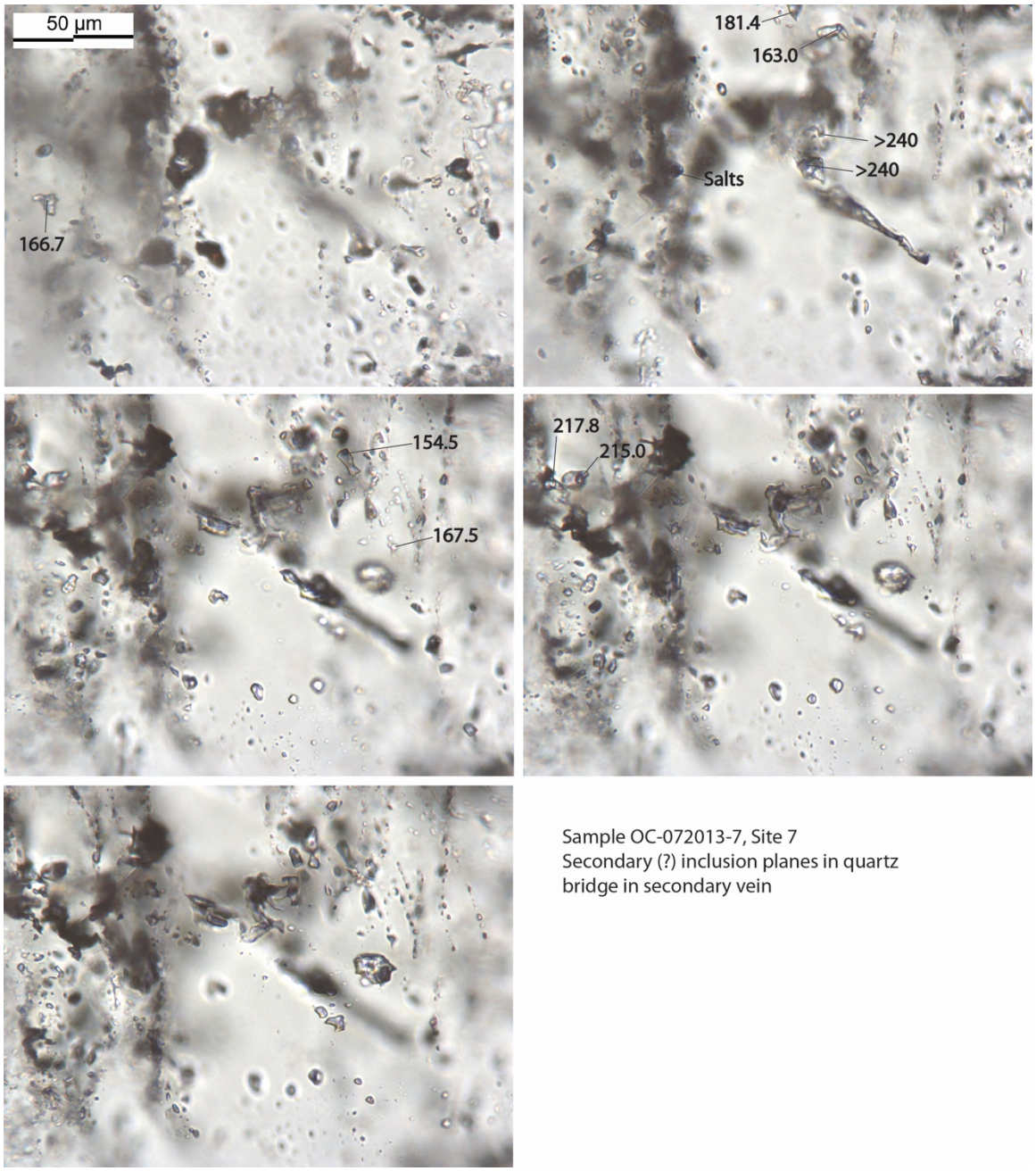

Figure K.5. Photomicrograph of fluid inclusions, site 7, sample 072013-7.

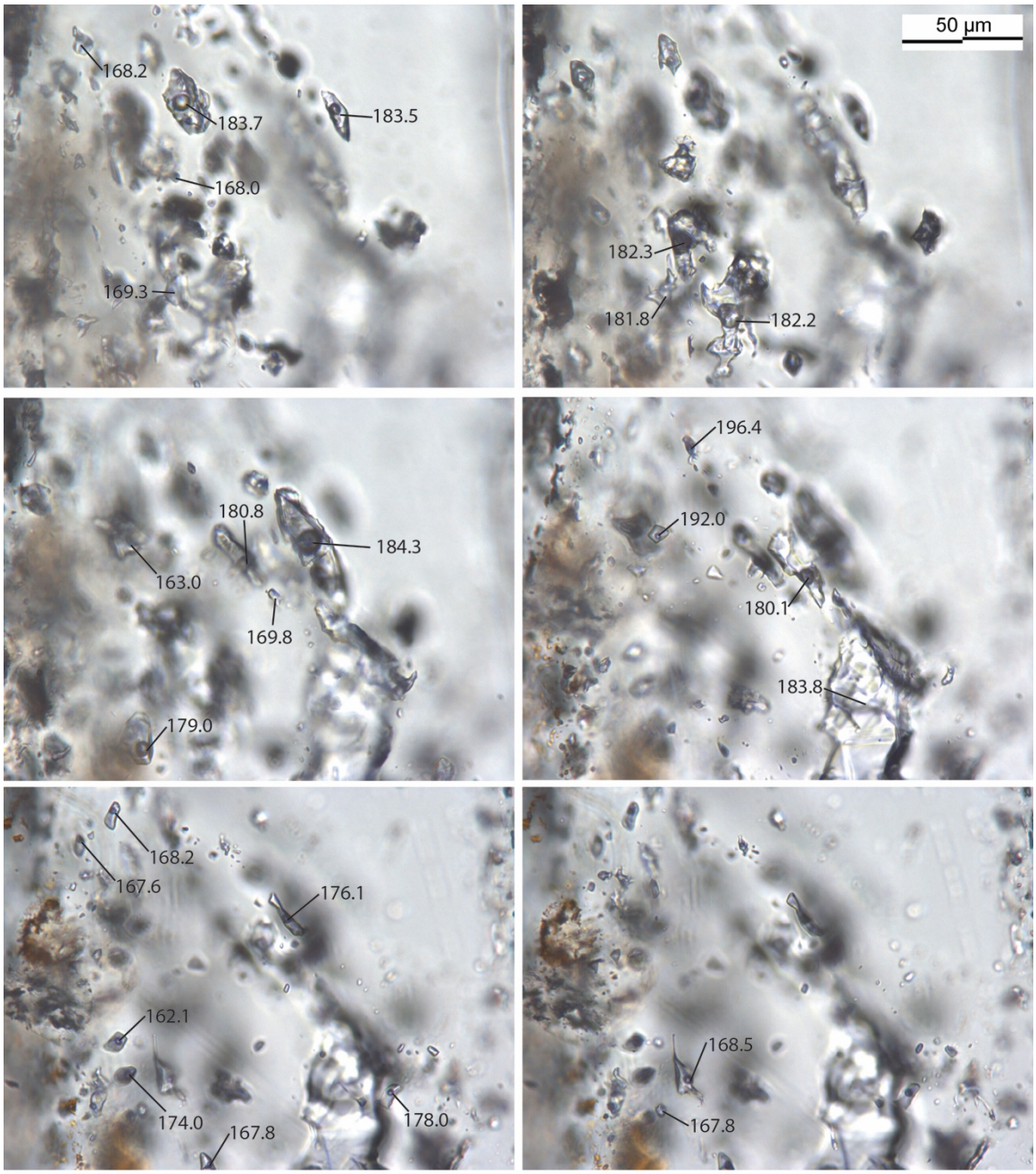

Sample OC-072013-7, Site 10
Primary inclusions near base of euhedral zone.

Figure K.6. Photomicrograph of fluid inclusions, site 10, sample 072013-7.

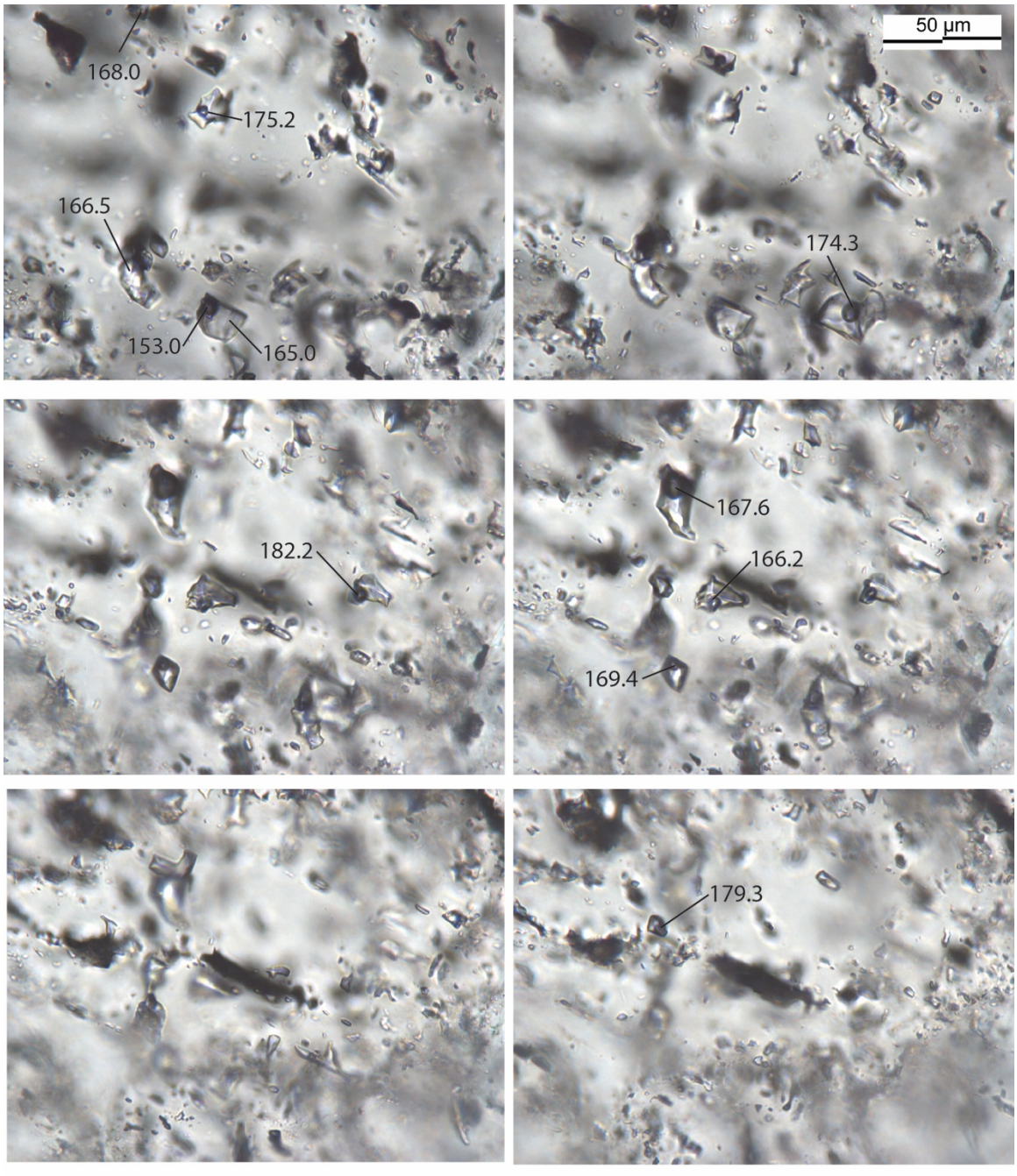

Figure K.7. Photomicrograph of fluid inclusions, site 13, sample 072013-7.

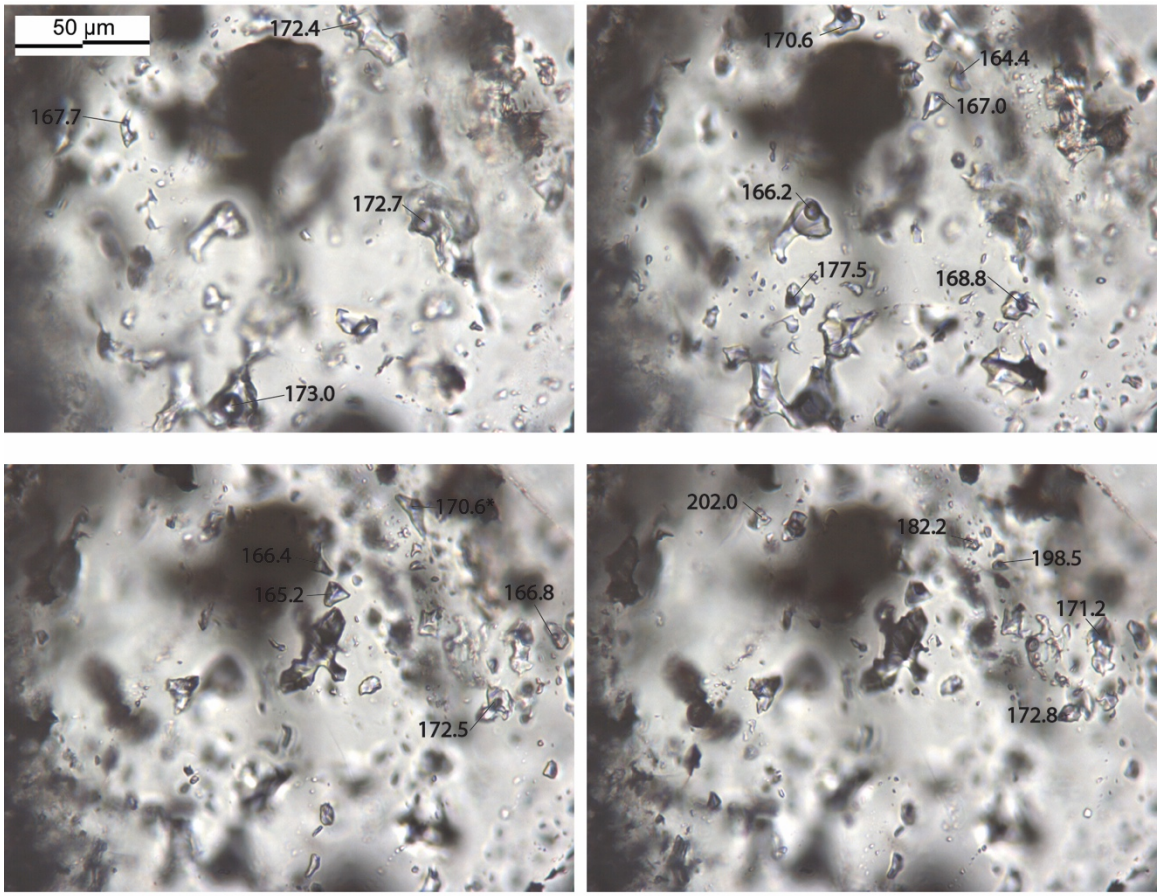

Figure K.8. Photomicrograph of fluid inclusions, site 17, sample 072013-7.

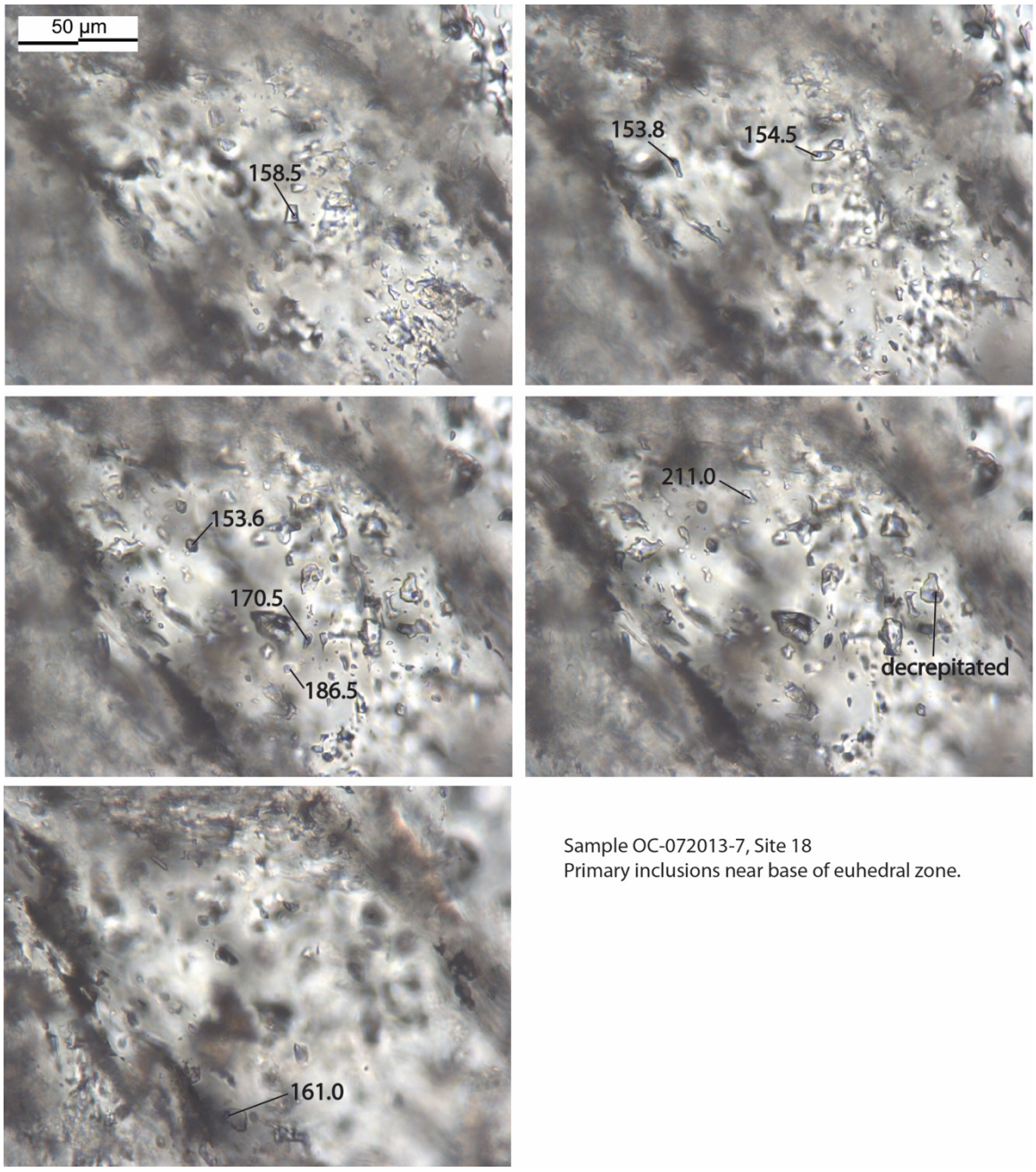

Figure K.9. Photomicrograph of fluid inclusions, site 18, sample 072013-7.

References Cited

Anders, M. H., Schneider, J. R., Scholz, C. H., and Losh, S., 2013, Mode I microfracturing and fluid flow in damage zones: the key to distinguishing faults from slides: Journal of Structural Geology, v. 48, p. 113-125.

Anderson, O. L., and Grew, P. C., 1977, Stress corrosion theory of crack propagation with applications to geophysics: Review of Geophysics and Space Physics, v. 15, no. 1, p. 77-104.

Anderson, T. R., and Fairley, J. P., 2008, Relating permeability to the structural setting of a fault-controlled hydrothermal system in southeast Oregon, USA: Journal of Geophysical Research, v. 113, no. B5.

Atkinson, B. K., 1979a, A fracture mechanics study of subcritical tensile cracking of quartz in wet environments: Pure and Applied Geophysics, v. 117, p. 1011-1024.

Atkinson, B. K., 1979b, Technical note: fracture toughness of Tennessee sandstone and Carrara marble using the double torsion testing method: Int J Rock Mech Min Sci & Geomech, v. 16, p. 49-53.

-, 1980, Stress corrosion and the rate-depedent tensile failure of a fine-grained quartz rock: Tectonophysics, v. 65, p. 281-290.

Atkinson, B. K., 1982, Subcritical crack propagation in rocks: theory, experimental results and applications: Journal of Structural Geology, v. 4, no. 1, p. 41-56.

-, 1984, Subcritical crack growth in geological materials: Journal of Geophysical Research, v. 89, no. B6, p. 4077.

Atkinson, B. K., and Meredith, P. G., 1981, Stress corrosion cracking of quartz: a note on the influence of chemical environment: Tectonophysics, v. 77, p. T1-T11.

Atkinson, B. K., and Meredith, P. G., 1987, Experimental fracture mechanics data for rocks and minerals, *in* Atkinson, B. K., ed., Fractures Mechanics of Rock: London, Academic Press, p. 477-525.

Backeberg, N. R., Rowe, C. D., and Barshi, N., 2016, Alteration-weakening leading to localized deformation in a damage aureole adjacent to a dormant shear zone: Journal of Structural Geology, v. 90, p. 144-156.

Balme, M. R., Rocchi, V., Jones, C., Sammonds, P. R., Meredith, P. G., and Boon, S., 2004, Fracture toughness measurements on igneous rocks using a high-pressure, high-temperature rock fracture mechanics cell: Journal of Volcanology and Geothermal Research, v. 132, no. 2-3, p. 159-172.

Baud, P., Zhu, W., and Wong, T.-f., 2000, Failure mode and weakening effect of water on sandstone: Journal of Geophysical Research, v. 105, no. B7, p. 16371.

Becker, S. P., Eichhubl, P., Laubach, S. E., Reed, R. M., Lander, R. H., and Bodnar, R. J., 2010, A 48 m.y. history of fracture opening, temperature, and fluid pressure; Cretaceous Travis Peak Formation, East Texas Basin: Geological Society of America Bulletin, v. 122, no. 7-8, p. 1081-1093.

Beeler, N. M., and Hickman, S. H., 2004, Stress-induced, time-dependent fracture closure at hydrothermal conditions: Journal of Geophysical Research - Solid Earth, v. 109, no. B2, p. B02211.

Bell, J. W., Caskey, S. J., Ramelli, A. R., and Guerrieri, L., 2004, Pattern and rates of faulting in the Central Nevada Seismic Belt, and paleoseismic evidence for prior beltlike behavior: Bulletin of the Seismological Society of America, v. 94, no. 4, p. 1229-1254.

Bell, J. W., and Katzer, T., 1990, Timing of late Quaternary faulting in the 1954 Dixie Valley earthquake area, central Nevada: Geology, v. 18, no. 7, p. 622.

Benoit, D., 1992, A case history of injection through 1991 at Dixie Valley, Nevada, Geothermal Resources Council Transactions, Volume 16, p. 611-620.

Bense, V. F., Gleeson, T., Loveless, S. E., Bour, O., and Scibek, J., 2013, Fault zone hydrogeology: Earth-Science Reviews, v. 127, p. 171-192.

Berger, B. R., and Bethke, P. M., 1985, Geology and geochemistry of epithermal systems, Littleton, CO, Society of Eoconomic Geologists, Reviews in Economic Geology, 296 p.

Berkowitz, B., 2002, Characterizing flow and transport in fractured geological media: a review: Advances in Water Resources, v. 25, p. 861-884.

Berry, G. W., Grim, P. J., and Ikelman, J. A., 1980, Thermal springs list for the United States, Key to Geophysical Records Documentation (KGRD): Springfield, Virginia, NOAA/EDIS, p. 67.

Bertani, R., 2005, World geothermal power generation in the period 2001–2005: Geothermics, v. 34, no. 6, p. 651-690.

-, 2012, Geothermal power generation in the world 2005–2010 update report: Geothermics, v. 41, p. 1-29.

Blackwell, D. D., Golan, B., and Benoit, D., 2000, Temperatures in the Dixie Valley, Nevada geothermal system: GRC Transactions, v. 24, p. 223-228.

Blackwell, D. D., Smith, R. P., and Richards, M. C., 2007, Exploration and development at Dixie Valley, Nevada: summary of DOE studies, 32nd Workshop on Geothermal Reservoir Engineering: Stanford University, Stanford, California.

Blanpied, M. L., Lockner, D. A., and Byerlee, J. D., 1995, Frictional slip of granite at hydrothermal conditions: Journal of Geophysical Research, v. 100, no. B7, p. 13045.

Blanpied, M. L., Marone, C. J., Lockner, D. A., Byerlee, J. D., and King, D. P., 1998, Quantitative measure of the variation in fault rheology due to fluid-rock interactions: Journal of Geophysical Research, v. 103, no. B5, p. 9691.

Blenkinsop, T. G., 2008, Relationships between faults, extension fractures and veins, and stress: Journal of Structural Geology, v. 30, no. 5, p. 622-632.

Blenkinsop, T. G., and Sibson, R. H., 1992, Aseismic fracturing and cataclasis involving reaction softening within core material from the Cajon Pass drill hole: Journal of Geophysical Research - Solid Earth, v. 97, no. B4, p. 5135-5144.

Bourne, S. J., and Willemse, E. J. M., 2001, Elastic stress control on the pattern of tensile fracturing around a small fault network at Nash Point, UK: Journal of Structural Geology, v. 23, p. 1753-1770.

Brantley, S. L., 1992, The effect of fluid chemistry on quartz microcrack lifetimes: Earth and Planetary Science Letters, v. 113, no. 1, p. 145-156.

Brantley, S. L., Evans, B., Hickman, S. H., and Crerar, D. A., 1990, Healing of microcracks in quartz: implications for fluid flow: Geology, v. 18, no. 2, p. 136.

Brantut, N., Heap, M. J., Meredith, P. G., and Baud, P., 2013, Time-dependent cracking and brittle creep in crustal rocks: a review: Journal of Structural Geology, v. 52, p. 17-43.

Brodsky, E. E., Gilchrist, J. J., Sagy, A., and Collettini, C., 2011, Faults smooth gradually as a function of slip: Earth and Planetary Science Letters, v. 302, no. 1-2, p. 185-193.

Brown, S. R., and Bruhn, R. L., 1996, Formation of voids and veins during faulting: Journal of Structural Geology, v. 18, no. 5, p. 657-671.

Brown, W. F., and Strawley, J. E., 1966, Plane strain crack toughness testing of high strength metallic materials, ASTM STP 410, p. 129.

Browne, P. R. L., 1978, Hydrothermal alteration in active geothermal fields: Annual Review of Earth and Planetary Sciences, v. 6, p. 229-250.

Bruhn, R. L., Parry, W. T., Yonkee, W. A., and Thompson, T., 1994, Fracturing and hydrothermal alteration in normal fault zones: Pure and Applied Geophysics, v. 142, no. 3/4, p. 609-644.

Caine, J. S., 1999, The architecture and permeability structure of brittle fault zonesUniversity of Utah, 134 p.

Caine, J. S., Bruhn, R. L., and Forster, C. B., 2010, Internal structure, fault rocks, and inferences regarding deformation, fluid flow, and mineralization in the seismogenic Stillwater normal fault, Dixie Valley, Nevada: Journal of Structural Geology, v. 32, no. 11, p. 1576-1589.

Caine, J. S., Evans, J. P., and Forster, C. B., 1996, Fault zone architecture and permeability structure: Geology, v. 24, no. 11, p. 1025-1028.

Candela, T., and Renard, F., 2012, Segment linkage process at the origin of slip surface roughness: evidence from the Dixie Valley fault: Journal of Structural Geology, v. 45, p. 87-100.

Caskey, J., 2002, Historic faulting, chronostratigraphy, and paleoseismicity of the Central Nevada Seismic Belt, Field guide, 2002 Pacific Cell Friends of the Pleistocene Field Trip, September 20-22, 2002, 122 p.

Caskey, S. J., 2000, Active faulting and stress redistribution in the Dixie Valley, Beowawe, and Bradys geothermal fields: implications for geothermal exploration in the Basin and Range, 25th Workshop on Geothermal Reservoir Engineering: Stanford University, Stanford, California.

Caskey, S. J., and Ramelli, A. R., 2004, Tectonic displacement and far-field isostatic flexure of pluvial lake shorelines, Dixie Valley, Nevada: Journal of Geodynamics, v. 38, no. 2, p. 131-145.

Caskey, S. J., Wesnousky, S. G., Zhang, P., and Slemmons, D. B., 1996, Surface faulting of the 1954 Fairview Peak (Ms 7.2) and Dixie Valley (Ms 6.8) earthquakes, central Nevada: Bulletin of the Seismological Society of America, v. 86, no. 3, p. 761-787.

Chandler, M. R., Meredith, P. G., Brantut, N., and Crawford, B. R., 2016, Fracture toughness anisotropy in shale: Journal of Geophysical Research - Solid Earth, v. 121, no. 3, p. 1706-1729.

Charles, R. J., 1958, Dynamic fatigue of glass: Journal of Applied Physics, v. 29, p. 1657-1662.

Chen, X., Eichhubl, P., and Olson, J. E., 2017, Effect of water on critical and subcritical fracture properties of Woodford shale: Journal of Geophysical Research - Solid Earth, v. 122, p. 2736-2750.

Chen, X., Eichhubl, P., Olson, J. E., and Dewers, T. A., submitted, Salinity and pH dependent fracture mechanical properties of shales, implications for long-term seal integrity of CO2 storage: International Journal of Greenhouse Gas Control.

Chester, F. M., and Chester, J. S., 1998, Ultracataclasite structure and friction processes of the Punchbowl fault, San Andreas system, California: Tectonophysics, v. 295, p. 199-221.

Chester, F. M., Evans, J. P., and Biegel, R. L., 1993, Internal structure and weakening mechanisms of the San Andreas Fault: Journal of Geophysical Research, v. 98, p. 771–786.

Chester, F. M., and Logan, J. M., 1986, Implications for mechanical properties of brittle faults from observations of the Punchbowl fault zone, California: PAGEOPH, v. 124, no. 1/2, p. 79-106.

Childs, C., Manzocchi, T., Walsh, J. J., Bonson, C. G., Nicol, A., and Schöpfer, M. P. J., 2009, A geometric model of fault zone and fault rock thickness variations: Journal of Structural Geology, v. 31, no. 2, p. 117-127.

Cox, S. F., 2005, Coupling between deformation, fluid pressure, and fluid flow in ore-producing hydrothermal systems at depth in the crust, Economic Geology 100th Anniversary Volume, Society of Economic Geology, p. 39-75.

Cox, S. F., Knackstedt, M. A., and Braun, J., 2001, Principles of structural control on permeability and fluid flow in hydrothermal systems, *in* Richards, J. P., and Tosdal, R. M., eds., Structural Controls on Ore Genesis, Volume 14: Littleton, Colorado, Society of Economic Geologist, p. 1-24.

Crafford, A. E. J., 2007, Geologic Map of Nevada: U.S. Geological Survey Data Series 249.

Crider, J. G., 2015, The initiation of brittle faults in crystalline rock: Journal of Structural Geology, v. 77, p. 159-174.

Crider, J. G., and Peacock, D. C. P., 2004, Initiation of brittle faults in the upper crust: a review of field observations: Journal of Structural Geology, v. 26, p. 691-707.

Curewitz, D., and Karson, J. A., 1997, Structural settings of hydrothermal outflow: Fracture permeability maintained by fault propagation and interaction: Journal of Volcanology and Geothermal Research, v. 79, no. 3, p. 149-168.

Davatzes, N. C., and Aydin, A., 2003, Overprinting faulting mechanisms in high porosity sandstones of SE Utah: Journal of Structural Geology, v. 25, no. 11, p. 1795-1813.

Davatzes, N. C., Aydin, A., and Eichhubl, P., 2003a, Overprinting faulting mechanisms during the development of multiple fault sets in sandstone, Chimney Rock fault array, Utah, USA: Tectonophysics, v. 363, no. 1-2, p. 1-18.

Davatzes, N. C., Eichhubl, P., and Aydin, A., 2003b, Fault seal and conduit dichotomy; impact of deformation mechanism and fault geometry: Annual Meeting Expanded Abstracts - American Association of Petroleum Geologists, v. 12, p. 36-36.

-, 2005, Structural evolution of fault zones in sandstone by multiple deformation mechanisms; Moab Fault, southeast Utah: Geological Society of America Bulletin, v. 117, no. 1-2, p. 135-148.

Davatzes, N. C., and Hickman, S. H., The feedback between stress, faulting, and fluid flow: lessons from the Coso Geothermal Field, CA, USA, *in* Proceedings World Geothermal Congress, Bali, Indonesia, 25-29 April 2010, p. 1-15.

del Potro, R., and Hürlimann, M., 2009, The decrease in the shear strength of volcanic materials with argillic hydrothermal alteration, insights from the summit region of Teide stratovolcano, Tenerife: Engineering Geology, v. 104, no. 1-2, p. 135-143.

Demarest, H. H., Jr., 1976, Application of stress corrosion to geothermal reservoirs, informal report LA-6148-Ms, Los Alamos Scientific Laboratory, p. 4.

Dempsey, D. E., Rowland, J. V., Zyvoloski, G. A., and Archer, R. A., 2012, Modeling the effects of silica deposition and fault rupture on natural geothermal systems: Journal of Geophysical Research - Solid Earth, v. 117, no. 5.

Dilek, Y., and Moores, E. M., 1995, Geology of the Humboldt igneous complex, Nevada, and tectonic implications for the Jurassic magmatism in the Cordilleran orogen, *in* Miller, D. M., and Busby, C., eds., Jurassic Magmatism and Tectonics of the North American Cordillera: Boulder, Colorado, Geological Society of America Special Paper 299, p. 229-248.

Dove, P. M., 1995, Geochemical controls on the kinetics of quartz fracture at subcritical tensile stresses: Journal of Geophysical Research - Solid Earth, v. 100, no. B11, p. 22349-22359.

Eichhubl, P., and Boles, J. R., 2000, Rates of fluid flow in fault systems; evidence for episodic rapid fluid flow in the Miocene Monterey Formation, coastal California: American Journal of Science, v. 300, no. 7, p. 571-600.

Eichhubl, P., Davatzes, N. C., and Becker, S. P., 2009, Structural and diagenetic control of fluid migration and cementation along the Moab fault, Utah: AAPG Bulletin, v. 93, no. 5, p. 653-681.

Eichhubl, P., Taylor, W. L., Pollard, D. D., and Aydin, A., 2004, Paleo-fluid flow and deformation in the Aztec Sandstone at the Valley of Fire, Nevada; evidence for the coupling of hydrogeologic, diagenetic, and tectonic processes: Geological Society of America Bulletin, v. 116, no. 9-10, p. 1120-1136.

Engelder, T., Fischer, M. P., and Gross, M. R., 1993, GSA Short Course Notes: Geological Aspects of Fracture Mechanics, Boston, MA, GSA Division of Structural Geology and Tectonics.

Erarslan, N., 2016, Microstructural investigation of subcritical crack propagation and Fracture Process Zone (FPZ) by the reduction of rock fracture toughness under cyclic loading: Engineering Geology, v. 208, p. 181-190.

Escartin, J., Hirth, G., and Evans, B., 2001, Strength of slightly serpentinized peridotites: implications for the tectonics of oceanic lithosphere: Geology, v. 29, no. 11, p. 1023-1026.

Evans, A. G., 1972, A method for evaluating the time-dependent failutre characteristics of brittle materials - and its application to polycrystalline alumina: Journal of Materials Science, v. 7, p. 1137-1146.

Evans, J. P., 1990, Thickness-displacement relationship for faults: Journal of Structural Geology, v. 12, no. 8, p. 1061-1065.

Fabre, G., and Pellet, F., 2006, Creep and time-dependent damage in argillaceous rocks: International Journal of Rock Mechanics and Mining Sciences, v. 43, no. 6, p. 950-960.

Facca, G., and Tonani, F., 1967, The self-sealing geothermal field: Bulletin Volcanologique, v. 30, no. 1, p. 271-273.

Faulds, J. E., Coolbaugh, M. F., Vice, G. S., and Edwards, M. L., 2006, Characterizing structural controls of geothermal fields in the northwestern Great Basin: a progress report: Geothermal Resources Council Transactions, v. 30, p. 69-76.

Faulkner, D. R., Mitchell, T. M., Rutter, E. H., and Cembrano, J., 2008, On the structure and mechanical properties of large strike-slip faults, *in* Wibberley, C. A. J., Kurz, W., Imber, J., Holdsworth, R. E., and Collettini, C., eds., The internal structure of fault zones: implications for mechanical and fluid-flow properties, Volume 299: London, Geological Society, p. 139-150.

Feng, X.-T., and Ding, W., 2007, Experimental study of limestone micro-fracturing under a coupled stress, fluid flow and changing chemical environment: International Journal of Rock Mechanics and Mining Sciences, v. 44, no. 3, p. 437-448.

Feng, X.-T., Ding, W., and Zhang, D., 2009, Multi-crack interaction in limestone subject to stress and flow of chemical solutions: International Journal of Rock Mechanics and Mining Sciences, v. 46, no. 1, p. 159-171.

Finzi, Y., Hearn, E. H., Lyakhovsky, V., and Gross, L., 2011, Fault-zone healing effectiveness and the structural evolution of strike-slip fault systems: Geophysical Journal International, v. 186, no. 3, p. 963-970.

Fournier, R. O., 1985, The behavior of silica in hydrothermal solutions, *in* Berger, B. R., and Bethke, P. M., eds., Geology and Geochemistry of Epithermal Systems, Volume 2, p. 45-61.

Fournier, R. O., and Rowe, J. J., 1977, The solubility of amorphous silica in water at high temperature and high pressures: American Mineralogist, v. 62, p. 1052-1056.

Freiman, S. W., Wiederhorn, S. M., and Mecholsky, J. J. J., 2009, Environmentally enhanced fracture of glass: a historical perspective: Journal of the American Ceramic Society, v. 92, no. 7, p. 1371-1382.

Fuller, E. R., 1979, An evaluation of double-torsion testing - analysis, *in* Freiman, S. W., ed., Fracture Mechanics Applied to Brittle Materials, ASTM STP 678, American Society for Testing and Materials, p. 3-18.

Funatsu, T., Seto, M., Shimada, H., Matsui, K., and Kuruppu, M., 2004, Combined effects of increasing temperature and confining pressure on the fracture toughness of clay bearing rocks: International Journal of Rock Mechanics and Mining Sciences, v. 41, no. 6, p. 927-938.

Gherardi, F., Xu, T., and Pruess, K., 2007, Numerical modeling of self-limiting and self-enhancing caprock alteration induced by CO2 storage in a depleted gas reservoir: Chemical Geology, v. 244, no. 1-2, p. 103-129.

Gonsior, Z. J., and Dilles, J. H., 2008, Timing and evolution of Cenozoic extensional normal faulting and magmatism in the southern Tobin Range, Nevada: Geosphere, v. 4, no. 4, p. 687-712.

Gratier, J. P., 2011, Fault permeability and strength evolution related to fracturing and healing episodic processes (years to millenia): the role of pressure solution: Oil and Gas Science and Technology, p. 1-16.

Gratier, J. P., and Gueydan, F., 2006, Deformation in the presence of fluids and mineral reactions: effect of fracturing and fluid-rock interaction on seismic cycles, p. 319-356.

Griffith, W. A., Sanz, P. F., and Pollard, D. D., 2009, Influence of outcrop scale fractures on the effective stiffness of fault damage zone rocks: Pure and Applied Geophysics, v. 166, no. 10-11, p. 1595-1627.

Guilbert, J. M., and Park, C. F., Jr, 1986, The Geology of Ore Deposits, New York, W. H. Freeman and Company, 985 p.

Haas, J. L., Jr., 1971, The effect of salinity on the maximum thermal gradient of a hydrothermal system at hydrostatic pressure: Economic Geology and the Bulletin of the Society of Economic Geologists, v. 66, no. 6, p. 940-946.

Hadizadeh, J., and Law, R. D., 1991, Technical note: water-weakening of sandstone and quartzite deformed at various stress and strain rates: Int J Rock Mech Min Sci & Geomech. Abstr., v. 28, no. 5, p. 431-439.

Hao, R.-q., Li, J.-t., Cao, P., Liu, B., and Liao, J., 2015, Test of subcritical crack growth and fracture toughness under water-rock interaction in three types of rocks: Journal of Central South University, v. 22, no. 2, p. 662-668.

Hashiba, K., and Fukui, K., 2016, Time-dependent behaviors of granite: loading-rate dependence, creep, and relaxation: Rock Mechanics and Rock Engineering, v. 49, no. 7, p. 2569-2580.

Heap, M. J., Kennedy, B. M., Pernin, N., Jacquemard, L., Baud, P., Farquharson, J. I., Scheu, B., Lavallée, Y., Gilg, H. A., Letham-Brake, M., Mayer, K., Jolly, A. D., Reuschlé, T., and Dingwell, D. B., 2015, Mechanical behaviour and failure modes in the Whakaari (White Island volcano) hydrothermal system, New Zealand: Journal of Volcanology and Geothermal Research, v. 295, p. 26-42.

Hedderly-Smith, D. A., 1997, A geochemical examination of the Dixie Valley fault, Nevada: implications for the propogation and behavior of seismogenic normal faults, PhD: The University of Utah, 322 p.

Hedenquist, J. W., and Henley, R. W., 1985, Hydrothermal eruptions in the Waiotapu Geothermal System, New Zealand: their origin, associated breccias, and relation to precious metal mineralization: Economic Geology, v. 80, p. 1640-1668.

Henley, R. W., and Ellis, A. J., 1983, Geothermal systems ancient and modern: a geochemical review: Earth-Science Reviews, v. 19, p. 1-50.

Henley, R. W., Truesdell, A. H., and Barton, P. B., Jr., 1984, Fluid-mineral equilibria in hydrothermal systems, *in* Robertson, J. M., ed., Reviews in Economic Geology, Volume 1: Chelsea, MI, Society of Economic Geologists, p. 267.

Heynekamp, M. R., Goodwin, L. B., Mozley, P. S., and Haneberg, W. C., 1999, Controls on fault-zone architecture in poorly lithified sediments, Rio Grande Rift, New Mexico: implications for fault-zone permeability and fluid flow, *in* Haneberg, W. C., Mozley, P. S., Moore, J. C., and Goodwin, L. B., eds., Faults and Subsurface Fluid Flow in the Shallow Crust: Washington, DC, American Geophysical Union, p. 27-49.

Hickman, S., Zoback, M., and Benoit, R., Tectonic controls on reservoir permeability in the Dixie Valley, Nevada, Geothermal Field, *in* Proceedings 23rd Workshop on Geothermal Reservoir Engineering, Stanford University, Stanford, CA, 1998.

Hickman, S. H., Barton, C. A., Zoback, M. D., Morin, R., Sass, J., and Benoit, R., 2007, In-situ stress and fracture permeability along the Stillwater Fault Zone, Dixie Valley, Nevada: International Journal of Rock Mechanics & Mining Sciences, v. 34, no. 3-4.

Hillier, S., 1999, Use of an air brush to spray dry samples for X-ray powder diffraction: Clay Minerals, v. 34, p. 127-135.

Hoek, E., and Brown, E. T., 1997, Practical estimates of rock mass strength: International Journal of Rock Mechanics & Mining Sciences, v. 34, no. 8, p. 1165-1186.

Holder, J., Olson, J. E., and Philip, Z., 2001, Experimental determination of subcritical crack growth parameters in sedimentary rock: Geophysical Research Letters, v. 28, no. 4, p. 599-602.

Howald, T., Person, M., Campbell, A., Lueth, V., Hofstra, A., Sweetkind, D., Gable, C. W., Banerjee, A., Luijendijk, E., Crossey, L., Karlstrom, K., Kelley, S., and Phillips, F. M., 2015, Evidence for long timescale (>10^3 years) changes in hydrothermal activity induced by seismic events: Geofluids, v. 15, p. 252-268.

Hudson, M. R., and Geissman, J. W., 1991, Paleomagnetic evidence for the age and extent of middle Tertiary counterclockwise rotation, Dixie Valley region, west central Nevada: Journal of Geophysical Research, v. 96, no. B3, p. 3979-4006.

Hull, J., 1988, Thickness-displacement relationships for deformation zones: Journal of Structural Geology, v. 10, p. 431-435.

Ikari, M. J., Saffer, D. M., and Marone, C., 2009, Frictional and hydrologic properties of clay-rich fault gouge: Journal of Geophysical Research, v. 114, no. B5, p. 18.

Jamtveit, B., Putnis, C. V., and Malthe-Sørenssen, A., 2008, Reaction induced fracturing during replacement processes: Contributions to Mineralogy and Petrology, v. 157, no. 1, p. 127-133.

John, D. A., 1995, Tilted middle Tertiary ash-flow calderas and subjacent granitic plutons, southern Stillwater Range, Nevada: cross sections of an Oligocene igneous center: GSA Bulletin, v. 107, no. 2, p. 180-200.

Johnson, D. A., and Barton, M. D., 2000, Time-space development of an extern brine-dominated, igneou-driven hydrothermal system: Humboldt Mafic Compex, Western Nevada, Part I, *in* Dilles, J. H., Barton, M. D., Johnson, D. A., Proffett, J. M., and Einaudi, M. T., eds., Contrasting styles of intrusion-associated hydrothermal systems, Volume 32, Society of Economic Geologists, p. 127-143.

Karfakis, M. G., and Akram, M., 1993, Effects of chemical solutions on rock fracturing: International Journal of Rock Mechanics & Mining Sciences, v. 30, no. 7, p. 1253-1259.

Kennedy-Bowdoin, T., Silver, E. A., Martini, B. A., and Pickles, W. L., 2004, Geothermal prospecting using hyperspectral imaging and field observations, Dixie Meadows, NV, Geothermal Resources Council 2004 Annual Meeting: Palm Springs, CA, p. 10.

Kim, Y.-S., Peacock, D. C. P., and Sanderson, D. J., 2004, Fault damage zones: Journal of Structural Geology, v. 26, no. 3, p. 503-517.

Kistler, R. W., and Speed, R. C., 2000, Open-File Report 00-217 40 Ar/39Ar, K-Ar, Rb-Sr whole rock and mineral ages, chemical composition, strontium, oxygen and hydrogen isotopic systematics of Jurassic Humboldt Lopolith and Permian (?) and Triassic Koipato Group rocks, Pershing and Churchill Counties, Nevada, p. 14.

Kobayashi, R., Matsuki, K., and Otsuka, N., 1986, Size effect in the fracture toughness of Ogino Tuff: Int J Rock Mech Min Sci & Geomech, v. 23, p. 13-18.

Kumar, R., 2010, Effect of chemical environments on subcritical crack growth in geological materials, Masters of Science in Engineering: The University of Texas at Austin, 108 p.

Lajtai, E. Z., and Bielus, L. P., 1986, Stress corrosion cracking of Lac du Bonnet Granite in tenstion and compression: Rock Mechanics and Rock Engineering, v. 19, p. 71-87.

Lamb, A., Kratt, C., and Calvin, W., 2011, Geothermal exploration using hyperspectral analysis over Dixie and Fairview Valleys, Nevada: GRC Transactions, v. 35, p. 867-871.

Laubach, S. E., Eichhubl, P., Hargrove, P., Ellis, M. A., and Hooker, J. N., 2014, Fault core and damage zone fracture attributes vary along strike owing to interaction of fracture growth, quartz accumulation, and differing sandstone composition: Journal of Structural Geology, v. 68, p. 207-226.

Laubach, S. E., Eichhubl, P., Hilgers, C., and Lander, R. H., 2010, Structural diagenesis: Journal of Structural Geology, v. 32, no. 12, p. 1866-1872.

Lester, D. R., Ord, A., and Hobbs, B. E., 2012, The mechanics of hydrothermal systems: II. Fluid mixing and chemical reactions: Ore Geology Reviews, v. 49, p. 45-71.

Lindgren, W., 1933, Mineral Deposits, New York, McGraw Hill, 930 p.

Lockner, D., 1993, Room temperature creep in saturated granite.: J Geophys Res, v. 98, p. 475-487.

Lockner, D. A., Morrow, C., Moore, D., and Hickman, S., 2011, Low strength of deep San Andreas fault gouge from SAFOD core.: Nature.

Lopez, D. L., and Williams, S. N., 1993, Catastrophic volcanic collapse: relation to hydrothermal processes: Science, v. 260, no. 5115, p. 1794-1796.

Lowell, R. P., van Cappellen, P., and Germanovich, L. N., 1993, Silica precipitation in fractures and the evolution of permeability in hydrothermal uplfow zones: Science, v. 260, no. 5105, p. 192-194.

Lutz, S. J., Caskey, S. J., Mildenhall, D. D., Browne, P. R. L., and Johnson, S. D., 2002, Dating sinter deposits in northern Dixie Valley, Nevada-the paleoseismic record and implications for the Dixie Valley geothermal system, 27th Workshop on Geothermal Reservoir Engineering: Stanford University.

Lutz, S. J., and Hulen, J. B., 2000, Mapping and characterization of hydrothermal alteration associated with the Dixie Valley geothermal system, Nevada, Department of Energy, p. 225-230.

Lutz, S. J., and Moore, J. M., 1996, Alteration mineralogy of the Dixie Valley Geothermal System, Nevada: GRC Transactions, v. 20, p. 353-362.

MacNamee, A. F., 2015, Thermochronometric investigation of structural evolution and geothermal systems in extensional settings, Dixie Valley, Nevada, MS: The University of Texas at Austin, 180 p.

Major, J. R., Eichhubl, P., Dewers, T. A., and Olson, J. E., 2018, Effect of CO2 –brine–rock interaction on fracture mechanical properties of CO 2 reservoirs and seals: Earth and Planetary Science Letters, v. 499, p. 37-47.

Meredith, P. G., and Atkinson, B. K., 1985, Fracture toughness and subcritical crack growth during high-temperature deformation of Westerly granite and Black gabbro: Physics of the Earth and Planetary Interiors, v. 39, p. 33-51.

Michalske, T. A., and Freiman, S. W., 1982, A molecular interpretation of stress corrosion in silica: Nature, v. 295, no. 11, p. 511-512.

Micklethwaite, S., 2009, Mechanisms of faulting and permeability enhancement during epithermal mineralisation; Cracow goldfield, Australia: Journal of Structural Geology, v. 31, no. 3, p. 288-300.

Micklethwaite, S., Sheldon, H. A., and Baker, T., 2010, Active fault and shear processes and their implications for mineral deposit formation and discovery: Journal of Structural Geology, v. 32, no. 2, p. 151-165.

Mitchell, T. M., and Faulkner, D. R., 2009, The nature and origin of off-fault damage surrounding strike-slip fault zones with a wide range of displacements: A field study from the Atacama fault system, northern Chile: Journal of Structural Geology, v. 31, no. 8, p. 802-816.

Moir, H., Lunn, R. J., Micklethwaite, S., and Shipton, Z. K., 2013, Distant off-fault damage and gold mineralization: the impact of rock heterogeneity: Tectonophysics, v. 608, p. 461-467.

Moore, D. E., Morrow, C. A., and Byerlee, J. D., 1983, Chemical reactions accompanying fluid flow through granite held in a temperature gradient: Geochimica et Cosmochimica Acta, v. 47, no. 3, p. 445-453.

Morrow, C. A., Moore, D. E., and Lockner, D. A., 2001, Permeability reduction in granite under hydrothermal conditions: Journal of Geophysical Research - Solid Earth, v. 106, no. B12, p. 30551-30560.

Myers, R., and Aydin, A., 2004, The evolution of faults formed by shearing across joint zones in sandstone: Journal of Structural Geology, v. 26, no. 5, p. 947-966.

Nara, Y., and Kaneko, K., 2005, Study of subcritical crack growth in andesite using the double torsion test: International Journal of Rock Mechanics & Mining Sciences, v. 42, p. 521-530.

Nara, Y., Kashiwaya, K., Nishida, Y., and Ii, T., 2017a, Influence of surrounding environment on subcritical crack growth in marble: Tectonophysics, v. 706-707, p. 116-128.

Nara, Y., Morimoto, K., Hiroyoshi, N., Yoneda, T., Kaneko, K., and Benson, P. M., 2012, Influence of relative humidity on fracture toughness of rock: implications for subcritical crack growth: International Journal of Solids and Structures, v. 49, p. 2471-2481.

Nara, Y., Nakabayashi, R., Maruyama, M., Hiroyoshi, N., Yoneda, T., and Kaneko, K., 2014, Influences of electrolyte concentration on subcritical crack growth in sandstone in water: Engineering Geology, v. 179, p. 41-49.

Nara, Y., Tanaka, M., and Harui, T., 2017b, Evaluating long-term strength of rock under changing environments from air to water: Engineering Fracture Mechanics, v. 178, p. 201-211.

Nara, Y., Yamanaka, H., Oe, Y., and Kaneko, K., 2013, Influence of temperature and water on subcritical crack growth parameters and long-term strength for igneous rocks: Geophysical Journal International, v. 193, no. 1, p. 47-60.

Nasseri, M. H. B., Tatone, B. S. A., Grasselli, G., and Young, R. P., 2009, Fracture toughness and fracture roughness interrelationship in thermally treated Westerly Granite: Pure and Applied Geophysics, v. 166, no. 5-7, p. 801-822.

Nelson, E. P., Kullman, A. J., Gardner, M. H., and Batzle, M., 1999, Fault-fracture networks and related fluid flow and sealing, Brushy Canyon Formation, west Texas, *in* Haneberg, W. C., Mozley, P. S., Moore, J. C., and Goodwin, L. B., eds., Faults and Subsurface Fluid Flow in the Shallow Crust, Volume 113: Washington, D.C., American Geophysical Union, p. 69-81.

Nishimoto, S., and Yoshida, H., 2010, Hydrothermal alteration of deep fractured granite: effects of dissolution and precipitation: Lithos, v. 115, no. 1-4, p. 153-162.

Nortje, G. S., Oliver, N. H. S., Blenkinsop, T. G., Keys, D. L., McLellan, J. G., and Oxenburgh, S., 2011, New faults v. fault reactivation; implications for fault cohesion, fluid flow and copper mineralization, Mount Gordon fault zone, Mount Isa District, Australia: Geological Society Special Publications, v. 359, p. 287-311.

Nosker, S. A., 1981, Stratigraphy and structure of the Sou Hills, Pershing County, Nevada, PhD: University of Nevada, Reno, 70 p.

NREL, Geothermal Prospector, https://maps.nrel.gov/geothermal-prospector, accessed 11-2-2016

Okaya, D. A., and Thompson, G. A., 1985, Geometry of Cenozoic extensional faulting: Dixie Valley, Nevada: Tectonics, v. 4, no. 1, p. 107-125.

Olsen, M. P., Scholz, C. H., and Léger, A., 1998, Healing and sealing of a simulated fault gouge under hydrothermal conditions: implications for fault healing: Journal of Geophysical Research, v. 103, no. B4, p. 7421.

Olson, J. E., 1993, Joint pattern development: effects of subcritical crack growth and mechanical crack interaction: Journal of Geophysical Research, v. 98, no. B7, p. 12,251-212,265.

-, 2004, Predicting fracture swarms - the influence of subcritical crack growth and the crack-tip process zone on joint spacing in rock, *in* Cosgrove, J. W., and Engelder, T., eds., The initiation, propagation, and arrest of joints and other fractures, Volume 231: London, Geological Society, p. 73-88.

Ord, A., Hobbs, B. E., and Lester, D. R., 2012, The mechanics of hydrothermal systems: I. Ore systems as chemical reactors: Ore Geology Reviews, v. 49, p. 1-44.

Page, B. M., 1965, Preliminary geologic map of a part of the Stillwater Range, Churchill County, Nevada, scale 1:125,000

Parry, W. T., and Bruhn, R. L., 1990, Fluid pressure transients on seismogenic normal faults: Tectonophysics, v. 179, p. 335-344.

Parry, W. T., Hedderly-Smith, D., and Bruhn, R. L., 1991, Fluid inclusions and hydrothermal alteration on the Dixie Valley Fault, Nevada: Journal of Geophysical Research, v. 96, no. B12, p. 19733.

Pletka, B. J., Fuller, E. R., Jr., and Koepke, B. G., 1979, An evaluation of double-torsion testing - experimental, *in* Freiman, S. W., ed., Fracture Mechanics Applied to Brittle Materials, ASTM STP 678, American Society for Testing and Materials, p. 19-37.

Pola, A., Crosta, G. B., Fusi, N., and Castellanza, R., 2014, General characterization of the mechanical behaviour of different volcanic rocks with respect to alteration: Engineering Geology, v. 169, p. 1-13.

Power, W. L., and Tullis, T. E., 1989, The relationship between slickenside surface in fine-grained quartz and the seismic cycle: Journal of Structural Geology, v. 11, no. 7, p. 879-893.

-, 1992, The contact between opposing fault surfaces at Dixie Valley, Nevada, and implications for fault mechanics: Journal of Geophysical Research, v. 97, no. B11, p. 15425.

Reid, M. E., Sisson, T. W., and Brien, D. L., 2001, Volcano collapse promoted by hydrothermal alteration and edifice shape, Mount Rainier, Washington: Geology, v. 29, no. 9, p. 779-782.

Rijken, M. C. M., 2005, Modeling naturally fractured reservoirs: from experimental rock mechanics to flow simulation, Ph.D.: The University of Texas at Austin, 239 p.

Robb, L., 2005, Introduction to Ore-Forming Processes, Malden, MA, Blackwell Publishing, 373 p.

Rostom, F., Royne, A., Dysthe, D. K., and Renard, F., 2012, Effect of fluid salinity on subcritical crack propagation in calcite: Tectonophysics, v. 583, p. 68-75.

Rudnicki, J. W., 1980, Fracture mechanics applied to the earth's crust: Annual Review of Earth and Planetary Sciences, v. 8, p. 489-525.

Sano, O., and Kudo, Y., 1992, Relation of fracture resistance to fabric for granitic rocks: PAGEOPH, v. 138, no. 4, p. 657-677.

Sano, O., Kudo, Y., and Mizuta, Y., 1992, Experimental determination of elastic constants of Oshima granite, Barre granite, and Chelmsford granite: Journal of Geophysical Research - Solid Earth, v. 97, no. B3, p. 3367-3379.

Savage, H. M., and Brodsky, E. E., 2011, Collateral damage: evolution with displacement of fracture distribution and secondary fault strands in fault damage zones: Journal of Geophysical Research - Solid Earth, v. 116, no. B3.

Schmidt, K. M., and Montgomery, D. R., 1995, Limits to relief: Science, v. 270, p. 617-620.

Schmidt, R. A., 1975, Fracture-toughness testing of limestone, SESA Spring Meeting: Chicago, IL.

Schwering, P. C., 2013, Geophysical modeling of the Dixie Meadows Geothermal prospect: dual analysis of gravity and magnetic data towards identifying structural controls, M.S.: University of Nevada, Reno, 83 p.

Seront, B., Wong, T.-F., Caine, J. S., Forster, C. B., Bruhn, R., L., and Fredrich, J. T., 1998, Laboratory characterization of hydromechanical properties of a seismogenic normal fault system: Journal of Structural Geology, v. 20, no. 7, p. 865-881.

Sheldon, H. A., and Micklethwaite, S., 2007, Damage and permeability around faults; implications for mineralization: Geology, v. 35, no. 10, p. 903-906.

Sibson, R. H., 1996, Structural permeability of fluid-driven fault-fracture meshes: Journal of Structural Geology, v. 18, no. 8, p. 1031-1042.

Siler, D. L., Hinz, N. H., and Faulds, J. E., 2018, Stress concentrations at structural discontinuities in active fault zones in the western United States: implications for permeability and fluid flow in geothermal fields: GSA Bulletin, v. 130, no. 3-4.

Sillitoe, R. H., 2010, Porphyry copper systems: Economic Geology, v. 105, p. 3-41.

Simmons, S. F., White, N. C., and John, D. A., 2005, Geological characteristics of epithermal precious and base metal deposits: Economic Geology 100th Anniversary Volume, p. 485-522.

Siratovich, P. A., Heap, M. J., Villeneuve, M. C., Cole, J. W., and Reuschle, T., 2014, Physical property relationships of the Rotokawa Andesite, a significant geothermal reservoir rock in the Taupo Volcanic Zone, New Zealand: Geothermal Energy, v. 2, no. 10, p. 31.

Sleep, N. H., and Blanpied, M. L., 1992, Creep, compaction and the weak rheology of major faults: Nature, v. 359, p. 687–692.

Solum, J. G., Davatzes, N. C., and Lockner, D. A., 2010, Fault-related clay authigenesis along the Moab Fault; implications for calculations of fault rock composition and mechanical and hydrologic fault zone properties: Journal of Structural Geology, v. 32, no. 12, p. 1899-1911.

Sonnenthal, E., Spycher, N., Callahan, O., Cladouhos, T., and Petty, S., 2012, A Thermal-Hydrological-Chemical Model for the Enhanced Geothermal System Demonstration Project at Newberry Volcano, Oregon, Proceedings, Thirty-Seventh

Workshop on Geothermal Reservoir Engineering, Volume 37: Stanford University, Stanford University.

Sornette, D., 1999, Earthquakes: from chemical alteration to mechanical rupture: Physics Reports, v. 313, no. 5, p. 237-292.

Speed, R. C., 1976, Geologic map of the Humboldt Lopolith and surrounding terrane, Nevada: The Geological Society of America, Map and Chart Series MC-14

Summers, R., Winkler, K., and Byerlee, J., 1978, Permeability changes during the flow of water through Westerly Granite at temperatures of 100 degrees -400 degrees C: Journal of Geophysical Research, v. 83, no. B1, p. 339-344.

Swanson, M. T., 1989, Sidewall ripouts in strike-slip faults: Journal of Structural Geology, v. 11, no. 8, p. 993-948.

-, 2005, Geometry and kinematics of adhesive wear in brittle strike-slip fault zones: Journal of Structural Geology, v. 27, no. 5, p. 871-887.

Swanson, P. L., 1984, Subcritical crack growth and other time- and environment-dependent behaviors in crustal rocks: Journal of Geophysical Research, v. 89, no. B6, p. 4137-4152.

Takahashi, H., and Abé, H., 1987, Fracture mechanics applied to hot, dry rock geothermal energy, *in* Atkinson, B. K., ed., Fracture Mechancis of Rock: London, Academic Press, p. 241-276.

Taron, J., and Elsworth, D., 2009, Thermal-hydrologic-mechanical-chemical processes in the evolution of engineered geothermal reservoirs: International Journal of Rock Mechanics & Mining Sciences, v. 46, p. 855-864.

-, 2010, Coupled mechanical and chemical processes in engineered geothermal reservoirs with dynamic permeability: International Journal of Rock Mechanics and Mining Sciences, v. 47, no. 8, p. 1339-1348.

Tenthorey, E., Cox, S. F., and Todd, H. F., 2003, Evolution of strength recovery and permeability during fluid-rock reaction in experimental fault zones: Earth and Planetary Science Letters, v. 206, p. 161-172.

Thompson, A. J. B., and Thompson, J. F. H., 1996, Atlas of Alteration, Vancouver, Canada, Mineral Deposits Division of the Geological Association of Canada, MDD Special Publication, 119 p.

Thompson, G. A., and Burke, D. B., 1973, Rate and direction of spreading in Dixie Valley, Basin and Range Province, Nevada: Geological Society of America Bulletin, v. 84, no. 2, p. 627-632.

Thompson, G. A., Meister, L. J., Herring, A. T., Smith, T. E., Burke, D. B., Kovach, R. L., Burford, R. O., Salehi, A., and Wood, M. D., 1967, Geophysics, study of Basin-

Range structure, Dixie Valley region, Nevada. U.S. Air Force Cambridge Research Labs. Spec. Rept. 66-848.

Tosdal, R. M., Dilles, J. H., and Cooke, D. R., 2009, From source to sinks in auriferous magmatic-hydrothermal porphyry and epithermal deposits: Elements, v. 5, no. 5, p. 289-295.

USGS, and NBMG, Quaternary fault and fold database for the United States, https://earthquake.usgs.gov/hazards/qfaults/, accessed Jan 5, 2010

Vanderburg, W. O., 1940, Reconnaissance of mining districts in Churchill County, Nevada: United States Department of the Interior, Information Circular, IC 7093, 57 p.

Vikre, P. G., 1993, Gold mineralization and fault evolution at the Dixie Comstock Mine, Churchill County, Nevada: Economic Geology, v. 89, no. 4, p. 707-719.

Wallace, R. E., 1984, Patterns and timing of Late Quaternary faulting in the Great Basin Province and relation to some regional tectonic features: Journal of Geophysical Research - Solid Earth, v. 89, no. B7, p. 5763-5769.

Wallace, R. E., and Whitney, R. A., 1984, Late Quaternary history of the Stillwater Seismic Gap, Nevada: Bulletin of the Seismological Society of America, v. 74, no. 1, p. 301-314.

Watters, R. J., Zimbelman, D. R., Bowman, S. D., and Crowley, J. K., 2000, Rock mass strength assessment and significance to edifice stability, Mount Rainier and Mount Hood, Cascades Range volcanoes: Pure and Applied Geophysics, v. 157, p. 957-976.

Watterson, J., Childs, C., and Walsh, J. J., 1998, Widening of fault zones by erosion of asperities: Geology, v. 26, p. 71-74.

Waza, T., Kurita, K., and Mizutani, H., 1980, The effect of water on the subcritical crack growth in silicate rocks: Tectonophysics, v. 67, p. 25-34.

White, D. E., 1981, Active geothermal systems and hydrothermal ore deposits: 75th Anniversary Volume, Economic Geology, p. 392-423.

White, M. D., and others, 2016, Benchmark Problems of the Geothermal Technologies Office Code Comparision Study, Pacific Northwest National Laboratory, Richland, WA, US Department of Energy, 190 p.

White, N. C., and Hedenquist, J. W., 1990, Epithermal environments and styles of mineralization: variations and their causes, and guidelines for exploration: Journal of Geochemical Exploration, v. 36, p. 445-474.

Whitten, C. A., 1957, Geodetic measurements in the Dixie Valley area: Bulletin of the Seismological Society of America, v. 47, no. 4, p. 321-325.

Wiederhorn, S., 1967, Influence of water vapor on crack propagation in soda-lime glass: J Am Cream Soc, v. 50, p. 407-414.

Wiederhorn, S., and Johnson, H., 1973, Effect of electrolyte pH on crack propagation in glass: J. Am. Ceram. Soc., v. 56, p. 192-197.

Wiederhorn, S. M., 1974, Subcritical crack growth in ceramics, *in* Bradt, R. C., Hasselman, D. P. H., and Lange, F. F., eds., Fracture Mechanics of Ceramics, Volume 2: New York, Plenum Press, p. 549-580.

Wilden, R., and Speed, R. C., 1974, Geology and mineral deposits of Churchill County, Nevada.

Wilkins, J. S., 1980, Slow crack growth and delayed failure of granite: Int J Rock Mech Min Sci & Geomech, v. 17, p. 365-369.

Williams, D. P., and Evans, A. G., 1973, A simple method for studying slow crack growth: JTEVA, v. 1, no. 4, p. 264-270.

Wilson, J. E., Chester, J. S., and Chester, F. M., 2003, Microfracture analysis of fault growth and wear processes, Punchbowl Fault, San Andreas system, California: Journal of Structural Geology, v. 25, p. 1855-1873.

Wintsch, R. P., Cristoffersen, R., and Kronenberg, A. K., 1995, Fluid–rock reaction weakening of fault zones: Journal of Geophysical Research, v. 100, p. 13021-13032.

Wong, L., Maruvanchery, V., and Liu, G., 2016, Water effects on rock strength and stiffness degradation: Acta Geotechnica, v. 11, p. 713-737.

Wong, T.-f., and Zhu, W., 1999, Brittle faulting and permeability evolution: hydromechanical measurement, microstructural observation, and network modeling, *in* Haneberg, W. C., Mozley, P. S., Moore, J. C., and Goodwin, L. B., eds., Faults and subsurface fluid flow in the shallow crust: Washington, DC :, American Geophysical Union, p. 83-100.

Woodcock, N. H., Dickson, J. A. D., and Tarasewicz, J. P. T., 2007, Transient permeability and reseal hardening in fault zones: evidence from dilation breccia textures: Geological Society, London, Special Publications, v. 270, no. 1, p. 43-53.

Wyering, L. D., Villeneuve, M. C., Wallis, I. C., Siratovich, P. A., Kennedy, B. M., Gravley, D. M., and Cant, J. L., 2014, Mechanical and physical properties of hydrothermally altered rocks, Taupo Volcanic Zone, New Zealand: Journal of Volcanology and Geothermal Research, v. 288, p. 76-93.

Yasuhara, H., 2005, Fault zone restrengthening and frictional healing: The role of pressure solution: Journal of Geophysical Research, v. 110, no. B6.

Zhang, P., Slemmons, D. B., and Mao, F., 1991, Geometric pattern, rupture termination and fault segmentation of the Dixie Valley-Pleasant Valley active normal fault system, Nevada, U.S.A.: Journal of Structural Geology, v. 13, no. 2, p. 165-176.

Zoback, M. L., Anderson, R. E., and Thompson, G. A., 1981, Cainozoic evolution of the state of stress and style of tectonism of the Basin and Range Province of the Western United States: Philosophical Transactions of the Royal Society of London. Series A, v. 300, no. 1545, p. 407-434.

Vita

Owen Callahan was born in southeastern Ohio in 1979 and grew up in the Midwest. He graduated valedictorian of Carbondale Community High School, Carbondale, Illinois, in 1998. He earned a Bachelor of Arts from Hampshire College, Amherst, Massachusetts, in 2003, and a Master of Science in geology from Western Washington University, Bellingham, Washington, in 2007. Shortly thereafter he began working in the geothermal energy industry on projects across the western US, including flagship DOE Engineered Geothermal System research at the Geysers, California, in Dixie Valley, Nevada, and at Newberry Volcano, Oregon. He returned to graduate school in 2012 as a William C. Powers Graduate Fellow at The University of Texas at Austin, earning his PhD in geology in 2018.

Owen lives with his wife, Amy, and their two boys.

Permanent address (or email): owen.callahan@gmail.com
This dissertation was typed by the author.